Aim & Scope
The journal publishes original papers in the extensive field of Electrical-Electronics and Computer engineering. It accepts contributions which are fundamental for the development of electrical engineering, computer engineering and its applications, including overlaps to physics. Manuscripts on both theoretical and experimental work are welcome. Review articles and letters to the editors are also included.

Application areas include (but are not limited to): Electrical & Electronics Engineering, Computer Engineering, Software Engineering, Biomedical Engineering, Electrical Power Engineering, Control Engineering, Signal and Image Processing, Communications & Networking, Sensors, Actuators, Remote Sensing, Consumer Electronics, Fiber-Optics, Radar and Sonar Systems, Artificial Intelligence and its applications, Expert Systems, Medical Imaging, Biomedical Analysis and its applications, Computer Vision, Pattern Recognition, Robotics, Industrial Automation.

Balkan Journal of Electrical & Computer Engineering

An International Peer Reviewed, Indexed and Open Access Journal

BAJECE

CONTENTS

BALKAN

JOURNAL OF
ELECTRICAL & COMPUTER ENGINEERING
(An International Peer Reviewed, Indexed and Open Access Journal)

Research Article

Advancing Sentiment Analysis during the Era of Data-Driven Exploration via the Implementation of Machine Learning Principles

Ali A. H. Karah Bash and Ergun Ercelebi

Abstract— **As a result of the rapid expansion in digital communication, information technology has seamlessly integrated into our everyday existence. It's nearly inconceivable to envision life without the presence of social media. The modern era of communications and networks encompasses not just entertainment instruments, but also contemporary means for users to share crucial data, viewpoints, and concepts. Certain data and information are of such significance that they are vital for analysis and the extraction of essential data that can subsequently be employed in decision support systems. This study examines sentiment polarity analysis through the utilization of the Naive Bayes approach. Naive Bayes is a supervised machine learning model employed for the prediction and analysis of data obtained from external sources. In the training phase, the dataset is categorized into three different groups: small, medium, and large. Additionally, both positive and negative dictionaries are obtained. As for the testing phase, two dataset categories are employed. To gauge the performance of the Naive Bayes algorithm in sentiment analysis, evaluation metrics like accuracy, precision, recall, and the F1 score are utilized. These assessment metrics are computed across three varied categories of positive and negative reviews. The experimental outcomes proved that the Naive Bayes approach is superior and the most effective technique for sentiment analysis.**

Based on the findings, it can be stated that the Naive Bayes classifier delivers a high level of accuracy when analyzing the positive and negative polarity of the data. Additionally, this method requires less time to generate high-quality results.

Index Terms— **Sentiment Analysis, Favorable Polarity, Unfavorable Polarity, Naive Bayes Technique, Machine Learning, Guided Training.**

I. INTRODUCTION

THE sentiment analysis is not a recent domain; rather, its examination and evolution commenced during the early 1990s and persists into the present [1,2]. The ongoing scholarly attention dedicated to this realm underscores its significance within our societal landscape, where sentiment analysis has emerged as a prevalent tool within networks and communication systems. Its application extends to the scrutiny of data, facilitating the extraction of novel insights utilized for analytical and statistical purposes [3].

Recent investigations have extended beyond the boundaries of individual sentiment analysis methodologies, combining machine learning and artificial intelligence to examine a variety of data sources. These investigations delve into the field of predictive analysis, leveraging the subject matter of artificial intelligence and machine learning models to predict outcomes with high accuracy [4].

Furthermore, sentiment analysis techniques are used to unpack the complexities of textual content sourced from communication systems and the broad reach of the Internet. This results in new data containing texts rich in intrinsic informational value, which then becomes raw material for machine learning algorithms [5]. It is worth noting that sentiment analysis should focus on revealing hidden emotional secrets, dividing feelings into positive and negative feelings, and including feelings that extend from anger and joy to sadness, fear, and vitality [6, 7].

Nevertheless, it is important to emphasize that the purpose of employing sentiment analysis techniques is not direct decision-making, but rather data analysis, thereby reinforcing the foundation upon which machine learning methodologies foresee emotional outcomes [8].

The main focal point of this study revolves around the execution of a classification algorithm aimed at discerning positive and negative sentiments within reviews. To fulfil this objective, we employed the Naive Bayes methodology, utilizing the bag-of-words to train the classifier.

Subsequently, the aim of this research is to conduct a series of experiments to meticulously assess the effectiveness of the Naive Bayes approach in identifying positive and negative sentiments within reviews.

Furthermore, an integral aspect of this investigation entails an exploration into the impact of data pre-processing, feature selection, and data curation on the accuracy of the Naive Bayes algorithm.

The organization of this manuscript is outlined as follows: Section 1 introduces the subject matter. Section 2 introduces

Ali A. H. Karah Bash, Department of Electric and Electronic Engineering, Hasan kalyoncu University, Gaziantep 27310, Turkey, (e-mail: ali_karabash2016@yahoo.com).

https://orcid.org/0000-0002-6513-9180

Ergun Ercelebi, Department of Electric and Electronic Engineering, Gaziantep University, Gaziantep 27310, Turkey, (e-mail: ergun.erceleb@gmail.com).

https://orcid.org/0000-0002-4289-7026

the background of sentiment analysis and the Naive Bayes method. Section 3 details the materials and methodologies employed in the research. Section 4 comprehensively presents the findings and subsequent discourse. Ultimately, Section 5 encapsulates the concluding remarks.

II. BACKGROUND

The study published in 2021 by Manitosh, employed an ensemble learning technique for sentiment analysis using textual data. However, it is found unsuitable for sentiment classification within the domain of textual sentiment analysis [9].

In a publication from 2021, Ayushi and Sanjukta introduced a rule-based methodology for sentiment analysis, employing Natural Language Processing (NLP) techniques that encompass stemming, tokenization, part-of-speech tagging, and machine learning-based parsing for text mining [10].

In the paper [11], the researchers conducted a meta-analysis concerning the immune system's reaction to perturbations in the presence of artificial intelligence and extensive data frameworks. The study focused on analysing the sentiments expressed by individuals through social media data, while also undertaking a comparative evaluation of diverse machine learning methodologies.

In the referenced study, the scholars employed machine learning techniques to conduct sentiment analysis, operating at both sentence and perspective levels. Their findings revealed variations in the efficacy of the methodologies employed, emphasizing the challenges in drawing definitive conclusions based on the existing state-of-the-art approaches [12].

In a publication from the year 2021, the researchers employed text-mining methodologies for the generation and manipulation of variables. Subsequently, a supervised probabilistic machine learning algorithm was utilized to categorize tweets into positive and negative sentiments. The authors then conducted two distinct experiments to comprehensively assess the effectiveness of their model [13].

The researchers delved into the progression of sentiment analysis, considering the emergence of text processing techniques and the shift from rule-based to statistical text comprehension. This exploration included a comparative analysis of benchmark performance across diverse applications and datasets, utilizing state-of-the-art models [14].

Within the study documented in [15], a comparative assessment was conducted on the efficacy of five distinct machine-learning techniques for sentiment analysis. These techniques encompass Support Vector Machine (SVM), Logistic Regression, Naive Bayes, Random Forest, and K-Nearest Neighbor. The evaluation was carried out utilizing a publicly accessible dataset sourced from kaggle.com.

In the publication referenced as [16], the authors comprehensively addressed the progression of the sentiment analysis workflow. Their inquiry encompassed an exploration into prevalent supervised machine learning methodologies, including multinomial naive Bayes, Bernoulli naive Bayes, logistic regression, support vector machine, random forest, K-nearest neighbour, decision tree, and deep learning techniques.

In a distinct publication denoted as [17], the authors directed their attention toward the scrutiny of online application reviews. Their primary objective revolved around discerning the polarity – positive or negative – of these reviews. To achieve this, the authors commenced their analysis by subjecting the data to preliminary processing, involving both data cleaning and the elimination of stop words.

In prior research endeavours, techniques were employed to enhance comprehension of work content. This involved the amalgamation of rule-based strategies and publicly available machine learning models, empowering analysts to efficiently pinpoint significant elements within extensive document collections [18].

Furthermore, in the study outlined in [19], traditional classifiers and deep neural networks, along with hybrid amalgamations thereof, underwent experimentation. The purpose was to fine-tune pertinent parameters with the aim of attaining optimal classification accuracy on a labelled movie review corpus.

III. MATERIALS AND METHODS

In contemporary society, access to the Internet has become a basic necessity, performing a myriad of roles ranging from information retrieval to engaging with social media platforms. Prominent companies such as Amazon, Adidas, and Nike are now proactively soliciting consumer input, with the goal of anticipating demands and forecasting upcoming purchasing trends. This sector delves into a carefully designed methodology aimed at extracting valuable consumer insights, a practice that some companies leverage by developing software to discern consumer preferences and thus monetize this data. This section provides a comprehensive explanation of the proposed methodology, its systematic implementation process, and a detailed presentation of the project functions. The overall breakdown of sentiment analysis implementation includes distinct phases including preprocessing, training, and testing.

A. System Prerequisites

Table 1 presents identifying details of the software and hardware used in this work. The software is compatible with a variety of operating systems, including all versions of Windows as well as the PC software platform. The application runs on a personal computer (PC) equipped with a computer software platform, appropriately dimensioned random access memory (RAM), a capable hard disk (HD), and central processing unit (CPU).

B. Dataset Compilation and Pre-processing

User feedback stands as a pivotal metric driving the enhancement of service quality and the refinement of deliverables. Blogs, review platforms, data repositories, and microblogs collectively offer valuable insights into the reception of products and services. Within this study, the

dataset pertinent to sentiment analysis encompassing both positive and negative sentiments has been sourced from [20–22]. Moreover, we employed the dataset accessible via the following online link: https://www.cs.uic.edu/~liub/FBS.

This dataset comprises two distinct classes representing (positive and negative) polarities and incorporates expansive dictionaries for both positive and negative sentiments (comprising more than 2000 words each). The primary aim of the pre-processing phase is to meticulously extract the dataset's distinctive features, which subsequently serve as fundamental elements during the training phase.

TABLE I
SOFTWARE AND HARDWARE REQUIREMENTS.

SOFTWARE	Operational system	compatibility includes Windows 7, Windows Vista, and Windows 8
	Programming Language	computer software platform
HARDWARE	CPU	Any Intel processor is suitable.
	RAM	At least 4 GB or higher.
	Processing Speed	Core i5 or higher
	Hard Disk	Requires a minimum of 100 GB or more of storage capacity.

1.1.   pre-processing

The comprehensive depiction of the entire pre-processing process is presented in Figure 1. The sequence commences with the integration of a dataset containing both affirmative and negative reviews, subsequently reorganized into a singular array. Subsequent stages involve the elimination of special characters and numerical elements through a structured elimination process. These parcels are systematically organized into word structures within distinct classes, with each word being allocated an independent array cell. To exemplify, consider the sentence "I like you," which is organized as depicted in Figure 2.

The pre-processing procedure comprises several key stages, as detailed below:
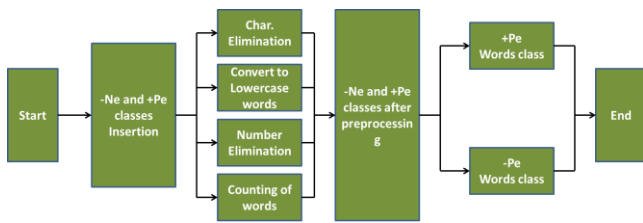
Fig.1. pre-processing steps
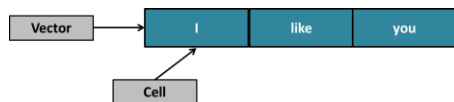
Fig. 2. Sentences representation as vector and cell in this work.

1.1.1   Removal of Special Characters

The process of removing special characters involves examining both the positive and negative class datasets. It initiates by scanning for specific characters like (@, #, $, % ^, &, (,), _, <, >, =!) within each word, sentence, and paragraph. Subsequently, these special characters are removed from both the negative and positive dataset classes, as demonstrated in the following example:

Before applying the special characters elimination process: "I @@ like to * e ^^ at && some %$ food &". After applying the special characters elimination process: "I like to eat some food".

1.1.2   Lowercase Conversion

The conversion of all letters within the negative and positive classes to lowercase is undertaken upon completion of the special character elimination. This conversion is facilitated by invoking a dedicated computer software platform function, illustrated as follows:

- Before Lowercase Conversion:
  "He like gOing TO The School In thE Afternoon. He is solving H.W."
- After Lowercase Conversion:
  "he like going to the school in the afternoon. he is solving hw."

1.1.3   Removal of Numerical Characters

The inclusion of numerical values in the dataset reviews does not convey positive or negative emotions, and it merely adds to the dataset's length without providing any advantages. As a result, it is necessary to remove these numbers to reduce the dataset's size, as illustrated in the following example:

- Before Number Elimination:
  "He is 0 going 77 to 78 the 32 school 84 for studying789."
- After Number Elimination:
  "He is going to the school for studying."

1.1.4   Word Count

The word count process involves comparing words from the positive/negative classes within the dataset against those existing in the dictionary. Repeated word occurrences are counted and stored in a new package for testing. Subsequently, probabilities (prior probability, conditional probability, and posterior probability) are computed. The following illustrates the word count procedure:

- Before Word Count:
  "He loves some foods. He loves playing tennis. He likes swimming. He likes me."
- After Word Count:
  [4, 2, 0, 0, 0, 2, 0, 0…]

1.2.   Training Stage

A comprehensive dataset containing positive and negative words is harnessed to train the system. The system then seeks to create a frequency distribution function, with the aim of identifying the most relevant terms.

Following this, the system proceeds to evaluate the terms to determine the polarity of statements, discerning whether they convey a negative or positive connotation. Terms accumulated from the preceding stages are enlisted for system training.

For this training endeavour, the Naive Bayes approach is adopted, facilitating the system's ability to discern sentiments—whether they are positive or negative—markedly illustrated in Figure 3.
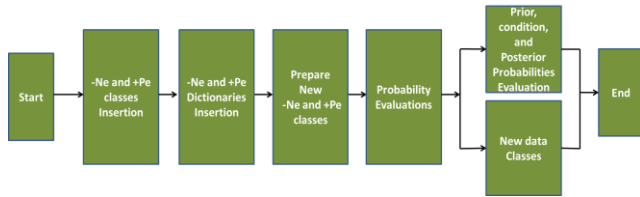
Fig.3. Training stages in this work.

The dataset is partitioned into three distinct categories: small, medium, and large. Moreover, both positive and negative dictionaries are procured, serving as a basis for comparison against the words within the positive and negative classes. This comparison is employed to construct respective positive and negative bags of words.

In the testing phase, a bag of words is utilized, comprising the shared terms between the positive and negative classes within the dataset and dictionaries. Consequently, residual words exclusive to individual classes are omitted from this bag.

1.3. The Proposed Algorithm

Naive Bayes represents a machine learning algorithm suitable for a range of classification tasks, including document classification and sentiment prediction, among others. Its label "Naive" originates from the inherent indirect relationship between the features, where altering the value of one feature does not directly impact the others, a characteristic ingrained in the Naive Bayes algorithm. This method is rooted in Bayes' Theorem [19], underpinning its classification approach.

Notably, the Naive Bayes approach offers simplicity in construction and remarkable efficiency, especially when handling extensive datasets. The underlying formula employed within the Naïve Bayes algorithm is provided below.

$$P_{(C|X)} = \frac{P_{(X|C)}P_{(C)}}{P_{(X)}} \qquad (1)$$

Where $P_{(C|X)}$ is conditional probability, $P_{(X|C)}$ is the class prior probability $P_{(C)}$ and $P_{(X)}$ are predictor prior probability.

Figure 4 illustrates the overarching schematic of the envisaged system. The developed system is implemented using computer software platform and is bifurcated into two principal components: the training segment and the testing segment. Further elaboration of the training component can be garnered through examination of the algorithmic code.
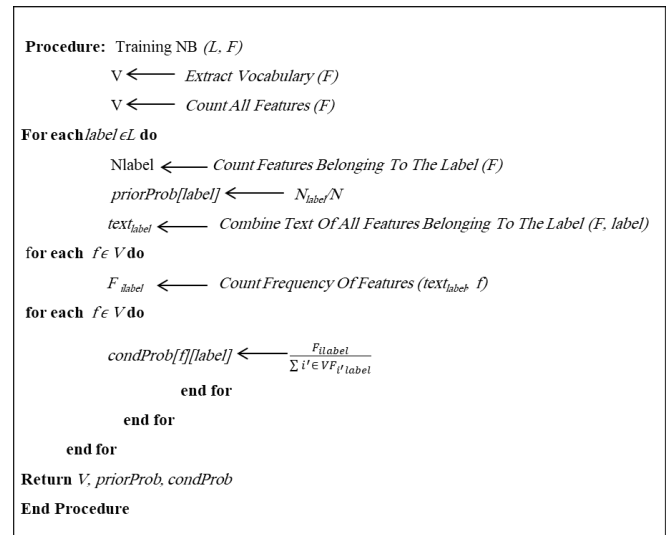
Fig.4. The code schematic of the proposed system in this work.

The Bayes algorithm is recognized for its directness and efficiency, consistently yielding precise outcomes. Thus, the probabilistic supervised technique, Naive Bayes, is harnessed to prognosticate positive and negative emotions. This is achieved by computing the probability associated with dataset classes.

Three distinct probabilities (prior, conditional, and posterior) necessitate computation. The prior probability is assessed by incorporating prior knowledge pertaining to positive/negative dataset classes, employing the subsequent formula:

$$\text{Positive prior prob.} = \frac{No\_of\_positive\_reviews}{No\_of\_classes} \qquad (2)$$

$$\text{Negative prior prob.} = \frac{No\_of\_negative\_reviews}{No\_of\_classes} \qquad (3)$$

The conditional probability is construed as the likelihood probability value assigned to each word within the dataset's classes, specifically within the confines of negative and positive classes, expressed as the ensuing formula (1).

The posterior probability entails a connection between the prior and conditional probabilities, and its computation is determined through the subsequent relationship:

$$\text{Posterior prob.} = \text{prior prob. X conditional prob.} \qquad (4)$$

1.4. Testing Phase

The process of testing is illustrated in Figure 5. The algorithm initiates by incorporating both positive and negative reviews into the testing segment of the simulation. Subsequently, pre-processing procedures are executed on these reviews, involving a comparison of all words within the reviews with the respective positive and negative word repositories.
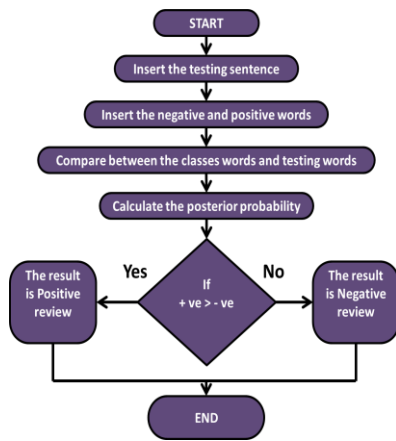
Fig.5. The Testing procedure in this work.

Specific linguistic elements such as negations and adverbs are gathered and employed for juxtaposition with evaluation reviews, thereby augmenting the likelihood of categorizing them as either negative or positive. This augmentation contributes to an overall enhancement in the effectiveness and precision of the process. The resultant lexicon is subsequently harnessed to compute three distinct probabilities: prior, conditional, and posterior.

The procedure encompasses the computation of prior probabilities using Equations 2 and 3, leveraging historical data and their impact on testing reviews. Further, conditional probabilities (defined by Equation 1) are calculated, expressing the likelihood of a variable's value given knowledge of another variable's outcome. These probabilities collectively determine the positive and negative posterior probabilities through the application of Equation 4.

These resultant values are stored within novel packages, utilized for the purpose of making comparative assessments that culminate in the ultimate determination of sentiment polarity (positive/negative). The outcomes of these comparisons find their place within the dataset package, serving as the foundational framework for sentiment classification. Should the positive probability eclipses the negative counterpart, the sentiment is classified as positive; conversely, it is categorized as negative. In instances where the positive and negative probabilities are equal, a neutral sentiment is indicated. The procedural depiction is provided through the algorithmic representation, facilitating the categorization of document sentiment, as depicted in Figure 6.
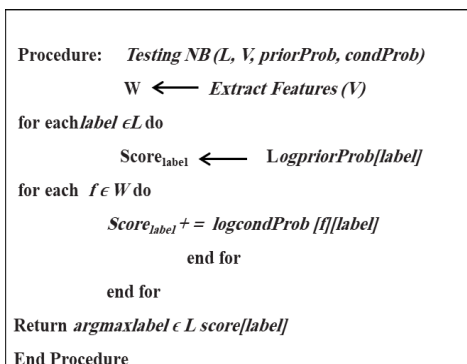
Fig.6. Code algorithm of testing procedure in this work.

IV. RESULT AND DISCUSSION

This section provides an elaborate account of the comprehensive experimental outcomes derived from the implementation of the Naive Bayes algorithm. The experiments encompass three distinct datasets of reviews, comprising 50, 100, and 200 reviews, respectively. Notably, each dataset encompasses an equal distribution of positive and negative reviews.

A. Performance Metric

The evaluation metrics commonly employed to assess the efficacy of classification algorithms encompass precision metrics such as accuracy, precision, recall, and the F1 score. Moreover, it is imperative to consider computational resource costs, a crucial aspect often taken into account during classifier construction.

Table 2 elucidates the metrics utilized for calculating precision, encompassing accuracy, and the F1 score. The confusion matrix presents the actual and predicted label distributions, with each row indicating the predicted label and each column denoting the actual label of the sentence. The True Positive (TP) represents the count of sentences that are correctly classified as positive (both actual and predicted labels are positive). The True Negative (TN) signifies the count of sentences that are accurately classified as negative (both actual and predicted labels are negative).

False Positive (FP) indicates the quantity of sentences falsely predicted as positive, when in reality they are negative. Conversely, False Negative (FN) quantifies the number of sentences falsely predicted as negative, while they are actually positive.

TABLE 2
CONFUSION MATRIX FOR THE BINARY CLASSIFIER.

		Actual	
		Positive	Negative
Estimated	Positive	TP	FP
	Negative	FN	TN

The accuracy formula, as represented by Equation 5, showcases the ratio of correctly predicted answers, encompassing both True Positives (TP) and True Negatives (TN), in relation to the total number of answers.

In addition, precision and recall are utilized as alternative performance metrics. Precision, captured by Equation 6, quantifies the count of accurately classified positive answers derived from the classifier.

$$Accuracy = \frac{(T_N + T_P)}{(T_N + T_P + F_N + F_P)} \tag{5}$$

$$\mathrm{Pr}ecision = \frac{T_P}{(F_P + T_P)} \tag{6}$$

Recall quantifies a classifier's proficiency in correctly identifying the potential positive answers within the anticipated responses. This computation is expressed mathematically through Equation 7.

While a higher precision value corresponds to improved

recall, attaining elevated levels of both precision and recall concurrently in practical contexts is exceedingly challenging. Thus, striking a balance between these two metrics becomes imperative. The F1 score, constituting the harmonic mean of precision and recall, offers a means to assess this equilibrium. Mathematically, the F1 score is determined as follows:

$$\mathrm{Re}\,call = \frac{T_P}{(F_N + T_P)} \quad (7)$$

$$F_1 = \frac{2x\,\mathrm{Re}\,callx\,\mathrm{Pr}\,ecision}{\mathrm{Re}\,call + \mathrm{Pr}\,ecision} \quad (8)$$

B. Dataset and Pre-processing

In this study, the dataset utilized is sourced from [23]. This dataset encompasses distinct classes of positive and negative polarities and is presented as a unified package, devoid of partitioning into separate positive and negative subsets [23–25].

The preparation of this dataset entails several stages. The initial phase involves the incorporation of both positive and negative classes into the dataset. Subsequently, these positive and negative classes are consolidated within a single array, a process constituting the second step.

In the third step, the dataset undergoes a treatment wherein special characters and numerical values, such as (#, $, %, &, ^, *, (,), -,:, 9, 5, 654), are removed. Following this, the array is organized such that each word within the classes occupies an individual cell, denoting the fourth step. The final step is executed to eliminate any vacant cells present within the array [26].

For the development of the network, a set of 200 negative and 200 positive reviews was employed as input data. The negative word classes exhibit a minimum size of 204 and a maximum size of 1644, whereas the positive word classes range from a minimum of 219 to a maximum of 1975 words. The initial phase of the project involved importing these classes into computer software platform and subsequently initiating pre-processing on both positive and negative categories. The cumulative word count across all classes is tabulated in Table 3. Furthermore, the count of negative words, both with and without repetition, is provided in the same table. Similarly, the count of positive words, considering both repetition and non-repetition, is also pivotal for sentiment analysis and is outlined in Table 3.

TABLE 3
THE TERMS WITHIN THE CATEGORIES, BOTH THE NEGATIVE AND POSITIVE WORDS CONSIDERING REPETITION AND NON-REPETITION.

Total number of words in the classes	Negative words		positive words	
	With repetition	Without repetition	With repetition	Without repetition
163322	78737	9090	84585	9470

C. Training Stage

To establish the proficiency of the system in discerning positive and negative emotions, the Naive Bayes method was iterated ten times during the learning process. In this endeavor, the word dictionaries for positive and negative sentiment

encompassed a total of 3004 words, with 1502 words allocated to each polarity. Prior probability calculations, achieved through Equations 2 and 3, were performed for all instances of negative and positive polarities. The outcomes of these calculations are meticulously documented in Table 4. Similarly, posterior and conditional probabilities, computed using equations (4 and 1) respectively, were determined for all instances of negative and positive polarity, with detailed results featured in Table 4.

TABLE 4
ASSESSMENT OF PRIOR, CONDITIONAL, AND POSTERIOR PROBABILITIES.

	Negative Polarity	Positive Polarity
prior probability value	0.500	0.500
conditional probabilities value	0.500	6.11688e-05
posterior probabilities value	0.0003368	3.05844e-05

D. Testing Stage

In the testing phase, testing reviews are initially input as one or more paragraphs. Subsequently, these reviews undergo preprocessing, involving the removal of special characters and numbers, followed by the conversion of all words to lowercase. The processed reviews are then organized into sentences within a testing array through sentence segmentation. A comparison of these sentences with the bag of words is performed, and outcomes are stored in the testing database. Binary values (zeros and ones) are assigned based on word matches between the testing reviews and the bag of words. To evaluate the efficiency of the proposed method, experiments are conducted three times with 50 and 100 reviews.

For the testing results involving 50 reviews, the system's performance is analyzed using a smaller dataset comprising 25 positive and 25 negative reviews. The first dictionary group correctly identifies 75 positive and 80 negative reviews out of 100 each. Subsequent dictionary groups also achieve progressively better results, culminating in 90 positive and 89 negative reviews correctly identified. These outcomes are summarized in Table 5.

Similarly, testing results are conducted for a dataset of 100 reviews (50 positive and 50 negative). Employing the first dictionary group, 90 positive and 82 negative reviews are correctly identified. Successive dictionary groups yield improved results, with the final group correctly identifying 95 positive and 92 negative reviews. These results are presented in Table 5.

TABLE 5
RESULT OF TESTING STAGE FOR 50 AND 100 REVIEWS

Total no. of testing reviews for positive and negative	Dictionary size	No. of positive reviews correctly identified in entirety	No. of negative reviews correctly identified in entirety.
50 reviews	1000	75	80
	2000	80	83
	3000	80	84
	4000	90	89
100 reviews	1000	90	82
	2000	89	85
	3000	93	90
	4000	95	92

E. Evaluations of Accuracy, Precision, Recall and F1

The evaluation of accuracy entails assessing the closeness between calculated values and their true counterparts, while the percent error quantifies the error ratio relative to the actual value, presented as a scaled factor of 100. This measure contributes to appraising work efficiency and enables the comparison of results in experimental contexts.

The assessment of accuracy spans three distinct review groups, engaged in both training and testing phases, illuminating the impact of varying review quantities on sentiment analysis. Additionally, diverse dictionary sizes are investigated to showcase the effectiveness and efficiency of the Naive Bayes algorithm in sentiment analysis as depicted in Figure 7.

Accuracy Evaluations

	0	1000	2000	3000	4000
Accuracy of 100 reviews	0	0.89	0.91	0.94	0.96
Accuracy of 50 reviews	0	0.84	0.87	0.9	0.92
Accuracy of 25 reviews	0	0.76	0.82	0.84	0.88
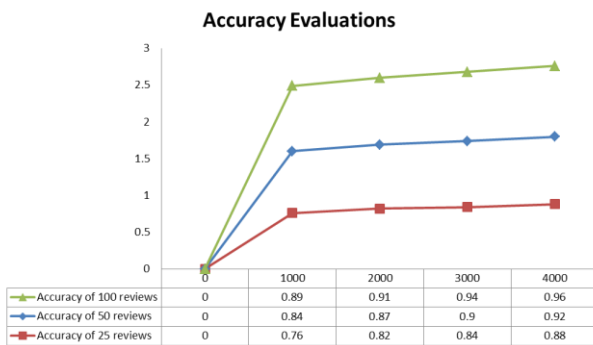
Fig. 7. Accuracy evaluation for 25, 50, and 100 reviews.

Precision, a metric gauging measurement consistency, is determined through the calculation of the standard deviation within a dataset. It provides insight into the precision of positive or negative responses within reviews of the corresponding polarity. The maximum precision value signifies the minimal occurrence of false estimations as depicted in Figure 8.

Precision Evaluations

	0	1000	2000	3000	4000
Precition of 100 reviews	0	0.87	0.89	0.93	0.94
Precition of 50 reviews	0	0.81	0.85	0.89	0.91
Precition of 25 reviews	0	0.81	0.84	0.85	0.88
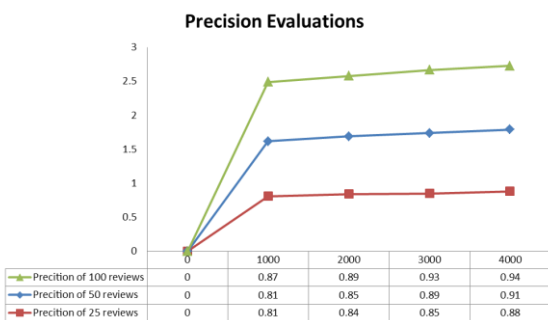
Fig. 8. Precision evaluation for 25, 50, and 100 reviews.

Figure 9 illustrates the Recall values corresponding to review quantities of 25, 50, and 100. Recall, also known as sensitivity, reveals the ratio of correctly predicted positive or negative reviews to the total reviews within the original dataset. This metric underscores the Naive Bayes method's capability to anticipate the maximum achievable count of

positive or negative reviews within the anticipated set.

Recall Evaluations

	0	1000	2000	3000	4000
Recall of 100 reviews	0	0.87	0.89	0.93	0.94
Recall of 50 reviews	0	0.88	0.89	0.92	0.94
Recall of 25 reviews	0	0.77	0.8	0.82	0.89
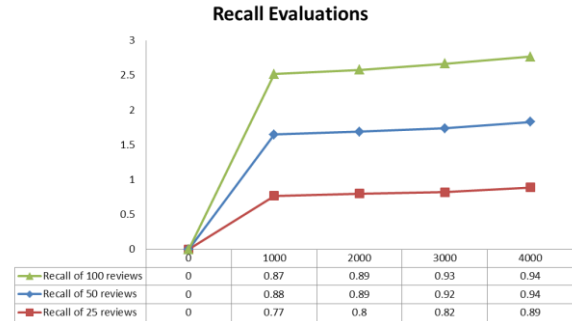
Fig. 9. Recall evaluation for 25, 50, and 100 reviews.

Recognizing the inherent difficulty of simultaneously optimizing recall and precision within real-world contexts, the F1 score is computed to achieve equilibrium between these two metrics. Functioning as a combination of precision and recall, the F1 score accommodates both false positive and false negative reviews, as illustrated in Figure 10.

F1 Score Evaluations

	0	1000	2000	3000	4000
F1 Score for 100 reviews	0	0.88	0.9	0.93	0.96
F1 Score for 50 reviews	0	0.84	0.87	0.9	0.92
F1 Score for 25 reviews	0	0.79	0.82	0.83	0.88
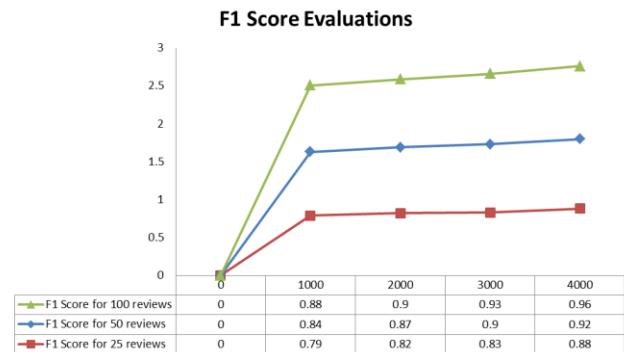
Fig. 10. F1 Score evaluation for 25, 50, and 100 reviews.

As Table 4 reveals, the visual representations elucidate that smaller review sets and a limited dictionary vocabulary result in diminished accuracy values, whereas larger review sets and a comprehensive dictionary lead to enhanced accuracy (approximately ranging from 76% to 96%). The highest level of accuracy is achieved with 4000 informative dictionary words and 100 training reviews. This trend is mirrored in the precision figure, wherein smaller review sets and datasets yield an 81% precision rate, which progressively rises to around 94% with augmented review quantities and expanded dictionary sizes. The pinnacle precision is realized with a dictionary comprising 4000 words and 100 training reviews. Additionally, heightened review quantities and the inclusion of informative dictionary words correspondingly contribute to elevated recall and F1 scores in the figures. With 4000 informative dictionary words and 100 training reviews, recall reaches approximately 94%, and the F1 score approaches 96%.

F. Analysis of Time

The analysis of time, as succinctly presented in Table 6, offers valuable insights into the temporal aspects of the training phase within this study. Particularly noteworthy is the

observation that a reduced volume of reviews coupled with a diminished count of informative words in the dictionary or bag led to a modest requirement of approximately 50 minutes for the Naive Bayes algorithm to complete its training. Conversely, an elevation in the count of informative words contained within the dictionary engendered a commensurate augmentation in the duration of the training process. To illustrate, the utilization of a dictionary encompassing four thousand words necessitated an extended training period of roughly one and a half hours for the proposed systems. In a similar vein, when contending with a corpus of 100 reviews and a quota of 1000 informative words held within the bag, the proposed classifier expended a comparable time span of approximately one and a half hours; this temporal demand increased proportionally as the word count within the bag expanded.

Of notable significance is the circumstance where the management of a collection comprising 200 reviews, interwoven with a dictionary harboring 4000 informative words, prompted the proposed Naive Bayes classifier to commandeer a training interval of 5 hours and 10 minutes. This underscores the discernible reality that while an augmentation in the number of reviews and a proliferation of dictionary size can bestow a boon upon enhanced accuracy and precision, this marked improvement is coupled with the trade-off of heightened temporal investment. Hence, the imperative of striking equilibrium between optimal performance and judicious time efficiency takes center stage as a pivotal deliberation.

TABLE 6
ANALYSIS OF THE TIME IN THIS WORK IN DIFFERENT DICTIONARIES.

Reviews No.	Dictionary word			
	1000	2000	3000	4000
25	33 min	40 min	50 min	1 h
50	1h.30min	2h.12min	2h.55min	3h.15min
100	3h.25min	3h.50min	4h.20min	5h.20min

In the comparison between the Naive Bayes method employed in this article and the Support Vector Machine (SVM) method as utilized in reference [1], it was observed that the method used in this study demonstrates high efficiency even when utilizing relatively small positive and negative dictionaries. Furthermore, when comparing the method applied in Reference [27], it was observed that the approach employed in our article operates with high efficiency and expeditiously performs sentiment analysis.

V.   CONCLUSION

Due to its wide range of applications, sentiment analysis remains a highly active research area for numerous scholars. In our study, we employed the Naive Bayes approach for sentiment analysis across various dataset categories because of is a simple and effective method. The system classifies and determines the polarity of the text into positive and negative classes. This classifier utilizes a dataset that is integrated into a machine-learning framework. The experimental findings demonstrate that the Naive Bayes classifier yields highly

satisfactory results. In this work, the Naive Bayes classifier underwent training and testing with three various numbers of review sets and dictionary sizes. In the first scenario, an accuracy of 0.88 % was attained using 50 training reviews and a 4000-word dictionary. In the second scenario, where 100 training reviews and the same 4000-word dictionary were used, the accuracy increased to 0.92 %. In the third scenario, with 200 training reviews and the same 4000-word dictionary, an accuracy of 0.96 % was achieved. Furthermore, this approach is also characterized by its efficiency in reaching decisions within a shorter timeframe.

REFERENCES

[1] R. Singh and R. Singh, "Applications of sentiment analysis and machine learning techniques in disease outbreak prediction–A review," Mater. Today Proc., vol. 81, pp. 1006–1011, 2023.

[2] G. Gupta et al., "DDPM: A Dengue Disease Prediction and Diagnosis Model Using Sentiment Analysis and Machine Learning Algorithms," Diagnostics, vol. 13, no. 6, p. 1093, 2023.

[3] E. M. Mercha and H. Benbrahim, "Machine learning and deep learning for sentiment analysis across languages: A survey," Neurocomputing, vol. 531, pp. 195–216, 2023.

[4] H. Rahman, J. Tariq, M. A. Masood, A. F. Subahi, O. I. Khalaf, and Y. Alotaibi, "Multi-tier sentiment analysis of social media text using supervised machine learning," Comput. Mater. Contin, vol. 74, pp. 5527–5543, 2023.

[5] M. Costola, O. Hinz, M. Nofer, and L. Pelizzon, "Machine learning sentiment analysis, COVID-19 news and stock market reactions," Res. Int. Bus. Financ., vol. 64, p. 101881, 2023.

[6] Y. Wang et al., "Supervised Gradual Machine Learning for Aspect-Term Sentiment Analysis," Trans. Assoc. Comput. Linguist., vol. 11, pp. 723–739, 2023.

[7] M. A. Jassim, D. H. Abd, and M. N. Omri, "A survey of sentiment analysis from film critics based on machine learning, lexicon and hybridization," Neural Comput. Appl., vol. 35, no. 13, pp. 9437–9461, 2023.

[8] S. Ghosh et al., "'Do we like this, or do we like like this?': Reflections on a Human-Centered Machine Learning Approach to Sentiment Analysis," in International Conference on Human-Computer Interaction, Springer, 2023, pp. 63–82.

[9] Y. N. Prajapati, U. Sesadri, T. R. Mahesh, S. Shreyanth, A. Oberoi, and K. P. Jayant, "Machine Learning Algorithms in Big Data Analytics for Social Media Data Based Sentimental Analysis," Int. J. Intell. Syst. Appl. Eng., vol. 10, no. 2s, pp. 264–267, 2022.

[10] A. Mitra and S. Mohanty, "Sentiment Analysis Using Machine Learning Approaches," in Emerging Technologies in Data Mining and Information Security: Proceedings of IEMIS 2020, Volume 2, Springer, 2021, pp. 63–68.

[11] S. Qaiser, N. Yusoff, M. A. Remli, and H. K. Adli, "A comparison of machine learning techniques for sentiment analysis," Turkish J. Comput. Math. Educ., 2021.

[12] J. Srivastava and N. Katiyar, "Machine Learning Technique for Target-Based Sentiment Analysis," in Micro-Electronics and Telecommunication Engineering, Springer, 2021, pp. 161–169.

[13] M. Hayouni and S. Baccar, "Sentiment analysis using machine learning algorithms," 2021.

[14] A. A. Ansari, "Evolution of Sentiment Analysis: Methodologies and Paradigms," Trends Data Sci. Appl. Theory Pract., pp. 147–174, 2021.

[15] M. H. I. Ahmad Hapez, N. L. Adam, and Z. Ibrahim, "Performance analysis of machine learning techniques for sentiment analysis," in Advances in Visual Informatics: 7th International Visual Informatics

Conference, IVIC 2021, Kajang, Malaysia, November 23–25, 2021, Proceedings 7, Springer, 2021, pp. 205–213.

[16] V. Umarani, A. Julian, and J. Deepa, "Sentiment analysis using various machine learning and deep learning Techniques," J. Niger. Soc. Phys. Sci., pp. 385–394, 2021.

[17] A. Bhardwaj and P. Srivastava, "A machine learning approach to sentiment analysis on web based feedback," in Applications of Artificial Intelligence and Machine Learning: Select Proceedings of ICAAAIML 2020, Springer, 2021, pp. 127–139.

[18] I. I. Mestric, A. Kok, G. Valiyev, M. Street, and P. Lenk, "Aspect Level Sentiment Analysis Methods Applied to Text in Formal Military Reports," Inf. Secur., vol. 46, no. 3, pp. 227–238, 2020.

[19] A. Mehta, Y. Parekh, and S. Karamchandani, "Performance evaluation of machine learning and deep learning techniques for sentiment analysis," in Information Systems Design and Intelligent Applications: Proceedings of Fourth International Conference INDIA 2017, Springer, 2018, pp. 463–471.

[20] O. Iparraguirre-Villanueva et al., "The public health contribution of sentiment analysis of Monkeypox tweets to detect polarities using the CNN-LSTM model," Vaccines, vol. 11, no. 2, p. 312, 2023.

[21] B. Gokulakrishnan, P. Priyanthan, T. Ragavan, N. Prasath, and As. Perera, "Opinion mining and sentiment analysis on a twitter data stream," in International conference on advances in ICT for emerging regions (ICTer2012), IEEE, 2012, pp. 182–188.

[22] F. Hallsmar and J. Palm, "Multi-class sentiment classification on twitter using an emoji training heuristic." 2016.

[23] B. Gokulakrishnan, P. Priyanthan, T. Ragavan, N. Prasath, and As. Perera, "Opinion mining and sentiment analysis on a twitter data stream," in International conference on advances in ICT for emerging regions (ICTer2012), IEEE, 2012, pp. 182–188.

[24] Z. Ke, H. Xu, and B. Liu, "Adapting BERT for continual learning of a sequence of aspect sentiment classification tasks," arXiv Prepr. arXiv2112.03271, 2021.

[25] O. Iparraguirre-Villanueva et al., "The public health contribution of sentiment analysis of Monkeypox tweets to detect polarities using the CNN-LSTM

[26] F. Hallsmar and J. Palm, "Multi-class sentiment classification on twitter using an emoji training heuristic." 2016.

[27] Sharma, D., & Sabharwal, M, "Sentiment analysis for social media using SVM classifier of machine learning. " Int J Innov Technol Exploring Eng (IJITEE), 2019, 8(9), 39-47.

BIOGRAPHIES

Ali A. H. Karah Bash achieved his B.S. degree in Computer and Information Engineering from University of Mosul, situated in Mosul, Iraq, in 2006. Subsequently, he embarked on a scholarly trajectory, attaining both Master's and Doctoral degrees in Electrical and Electronics Engineering from Gaziantep University, Turkey, in 2014 and 2022, correspondingly. His scholarly interests revolve around embedded systems, signal and image processing, as well as artificial neural networks. Importantly, he is associated with the ORCID ID (0000-0002-6513-9180).

Ergun ERÇELEBI attained his B.S. degree in Electrical and Electronics Engineering from METU, located in Gaziantep, Turkey, in 1990. Following this, he pursued his academic journey and secured both M.S. and Ph.D. degrees in Electrical and Electronics Engineering from Gaziantep University, Turkey, in 1992 and 1999, respectively. From 2011 onward, he has held the esteemed position of Professor within the Electrical and Electronics Engineering Department at the University of Gaziantep in Turkey. Subsequently, in 2014, he assumed the role of department head. His academic pursuits center around embedded systems, signal processing, and artificial neural networks. Notably, his ORCID ID is (0000-0002-4289-7026).

Investigation of Near Shading Losses in Photovoltaic Systems with PVsyst Software

İsmail Kayri

Abstract—**Shading in photovoltaic systems is known to cause serious energy losses. However, predicting how much shading photovoltaic systems in living spaces will experience throughout the year and the resulting energy loss is not easy. In this study, the effects of near shading on the system efficiency of photovoltaic systems have been investigated with PVsyst software. Instead of standard shading elements, a mosque with a complex architecture was chosen to test the drawing capabilities of the software. A 20 kWp PV power plant is assumed to be installed in three different locations in the courtyard of the mosque. In Scenario-1, 2, and 3, the modules are located in the west, east, and north directions of the mosque, respectively. The annual energy production values obtained in these scenarios have been compared with the reference scenario without shading. According to the results, the annual production in the scenario without near shading was realized as 28.84 kWh. In Scenario-1, 2, and 3, the annual production was 20.43 kWh, 21.46 kWh, and 19.05 kWh, respectively. In the content of the study, sample geometries of shading for all scenarios are presented comparatively for critical dates. In addition, monthly energy production, performance ratio values, and loss diagrams have been presented comparatively.**

Index Terms— **PVsyst software, shading losses, PV efficiency, renewable energy**

I. INTRODUCTION

ELECTRIC POWER generation with photovoltaic (PV) systems has many advantages in terms of sustainability. For this reason, it is becoming more and more ambitious to replace conventional methods. However, power generation with PV plants is characterized by many uncertainties [1]. The most effective variable in the conversion of solar energy into electrical energy is undoubtedly the amount of radiation reaching the earth from the sun. Many studies have been conducted to determine the solar energy potential, and these studies continue to be conducted. While some of these studies focused on a global scale [2-5], some of them on regional case studies [6-9] that aimed to address more accurate results.

İsmail Kayri, is with Department of Electrical and Electronics Engineering, University of Batman, Batman, Turkey, (e-mail: ismail.kayri@batman.edu.tr).

https://orcid.org/0000-0002-4973-641X

It is not impossible to increase the energy conversion rate of a PV module that has been produced and put into use. This is because the catalog information provided by module manufacturers for their products is determined according to some ambient data considered as Standard Test Conditions (STC). It is possible to increase the energy conversion rate of PV cells by controlling the cell temperature in the P-N junction region using various passive or active cooling methods. In this field, there are many theoretical or experimental active cooling studies [10-13] using only air or phase change materials (PCM), active cooling studies using only water [14-16], and many theoretical or experimental active cooling studies [17-20] by adding various nanofluids to water at certain ratios.

The location where the PV plant is installed and the direction that the modules are placed can have a strong impact on the shading of the modules. Mistakes at this stage can cause critical reductions in system efficiency. In addition, it can cause fluctuations in the I-V curves of the modules and even lead to overheating and damage to the energy generating cells during periodic partial shading [21]. Figure 1 shows the factors that cause partial shading in PV modules, their consequences, and some methods to mitigate these problems [21].

There are many studies in the literature [21-24] that address the effects of partial shading and provide recommendations for its mitigation. However, these proposals often lead to extra costs, system installation difficulties, or other power quality related issues according to today's technology.

In fact, during the design of a photovoltaic power system, locations are carefully selected to avoid shading. The spacing between PV panels chassis must be configured to prevent mutual shading of modules, particularly during peak power generation hours. However, systems installed in building-integrated PV applications or grid-connected or stand-alone domestic PV applications, especially in urban environments, are exposed to many near shading elements. Shading can eliminate the benefit of all methods to increase efficiency. It can even result in a PV application producing significantly less power than it could generate, without the user being aware of it.

It is not easy to predict shading losses by observation. This is because the sun moves from east to west throughout a day. Accordingly, the form and effecting level of the shadow cast by objects on PV arrays constantly changes. In addition, the solar elevation angle (αs) of the sun varies throughout the year. Therefore, for example, a PV module that is not shaded in the summer in the northern hemisphere may be shaded in the fall and winter when the solar elevation angle is low.
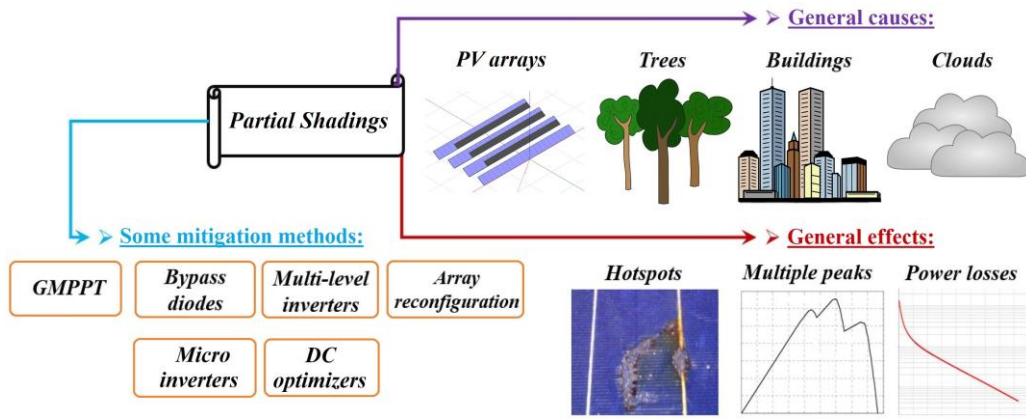
Fig. 1. Causes, possible effects and mitigation methods of partial shading in PV modules

Knowing the effect of near shading elements in advance generally provides two benefits. Firstly, the feasible amount of energy produced by a PV system with a certain installed power can be determined. Another is that the array location where the lowest shading losses occur can be determined. In recent years, many PV design and simulator software such as PVsyst, HomerPro, PV case, SolarPro, pvPlanner, PV F-Chart, RETScreen, HelioScope and similar ones have been developed that can perform these operations and much more. These software's generally provide comprehensive identification, evaluation and optimization of the technical and financial feasibility of potential renewable energy and energy efficiency projects to measuring and verifying the actual performance of the systems [25].

When the problems discussed above and in previous studies in this field are evaluated together, it has been seen that studies examining the effects of near shading on the efficiency of PV power plants in detail using PV design software are limited. Additionally, no studies have been conducted on buildings with complex architecture as shading elements and there is no study in the literature addressing the performance of solar simulation software in performing complex shading analyzes caused by such structures. In this study, the efficiency analysis of near

shading on a PV system is considered as a case study. While carrying out this case analysis, it was aimed to deeply explain many issues, such as the configuration of the PV power plant, the determination and drawing of near shading elements, and the calculation and interpretation of efficiency losses caused by long-term shading, with the simulation software used.

II. Materials and Methods

A. PVsyst simulation software

The analyses in this study were performed with the PVsyst simulation software, which is widely used in industrial and educational fields. PVsyst software is frequently used in studies on determination PV potential of various regions [26, 27], in the design and performance analysis of grid-connected or standalone PV power plants [28, 29], and in the analysis of shading events [30, 31]. The PVsyst 7.4 [32] software produced by PVsyst SA was used in the designs and simulations made in the present study. The trial version of this software gives users the right to use all its features free of charge for 1 month.

B. Determining location for simulation

Batman province, located in the Southeastern Anatolia Region of Turkey, was chosen for the simulation study.
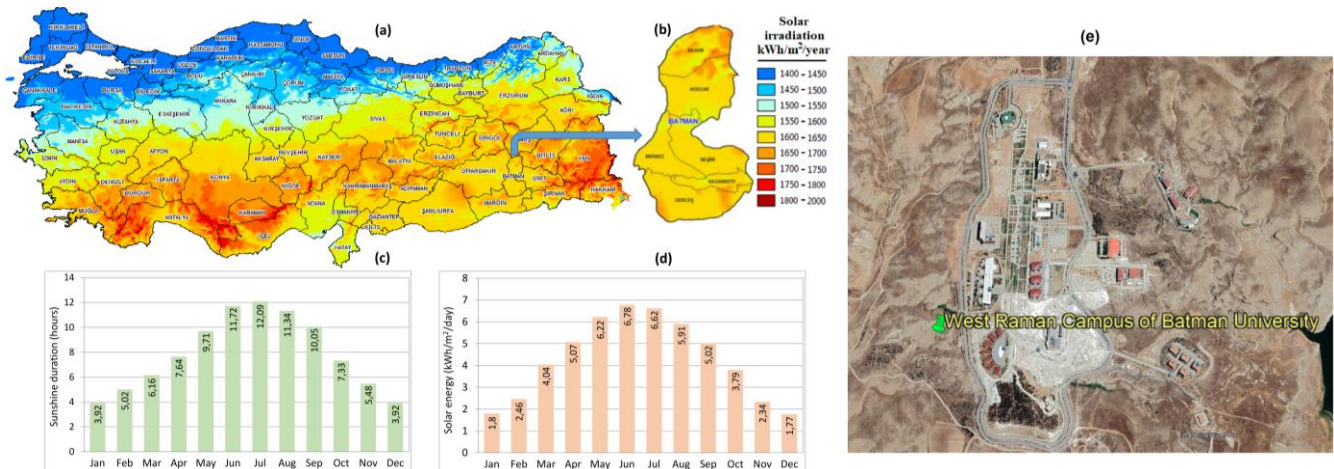
Fig. 2. Solar energy potential of Batman province; a) Turkey's solar energy potential view; b) Batman's solar energy atlas; c) Sunshine duration average by month; d) Solar energy average by month; e) Satellite view of the location of the PV system

Batman is among the provinces with the highest solar energy potential in Turkey, with an annual sunshine duration of approximately 2850 hours and a radiation energy of 1600-1650 kWh/m^2/year. The annual total precipitation of Batman province, which is located at an altitude of 550 meters, is 490 mm. The average air temperature in summer is 28.56 °C and it is under the influence of a continental climate. In Figure 2 [33], details of the monthly solar energy potential of Batman province are presented. The location of the PV power plant designed for the simulation study is at Batman University West Raman Campus, at 37°47'9.45" north latitude and 41°3'45.06" east longitude. The satellite image of West Raman campus is given in Figure 2(e).

C. Procedures followed and strategies applied in the study

One of the consistent ways to evaluate the effects of near shading on efficiency in PV power plants and the performance of the simulation software used in this regard is to conduct a case analysis. Because the area covered by the power plants and the diversity of near shading elements make it very difficult to develop a general opinion on such problems. In this context, first of all, a PV power plant was designed with PVsyst software. The shading elements in the environment where the designed power plant will operate were determined, and these were designed in 3D with the opportunities offered by the software. The results of the annual energy production were obtained if the designed PV power plant had no shading. Scenarios were determined to be tested at various points of the designed 3D structure in order to provide partial shading of the PV power plant with the same features. The annual energy production values of unshaded and different shading scenarios were compared.

1) Geographic location parameters

The necessary operations to determine the location where the PV power plant to be simulated will be operated are carried out in the "geographical site parameters" module in the PVsyst software. West Raman campus was selected as the location from the interactive map. PVsyst software uses the OpenStreetMap infrastructure in the maps module. The map of the selected region is shown in Figure 3.
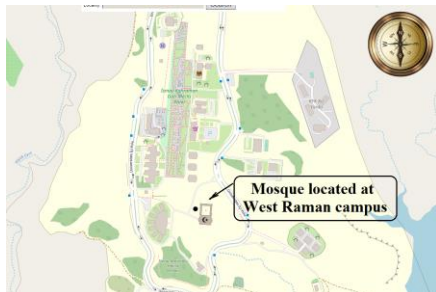
Fig. 3. Map of the West Raman campus

In Figure 3, the mosque located on the campus was chosen as the near shading element. PV simulation software generally provides convenience in drawing basic elements such as buildings, roofs, trees, electric poles and various geometric shapes in shading analyses. However, the ability to draw objects with complex structures depends on the capabilities of the

software. Another purpose of this study is to discuss the 3D drawing capabilities of the software used.

According to the data provided by the software, the latitude, longitude and altitude information of the selected location are 37.7857°N, 41.0650°E and 615 m, respectively. The time zone of Batman province is +3. The database of PVsyst software includes meteo tables of many institutions such as Meteonorm, NASA-SSE, PVGIS, NREL, Solcast, Solar Anywhere®. When the meteo tables of different institutions for the geographical location where the PV power plant will be installed are examined, it is seen that the data closest to Turkey's local meteorological office is provided by Meteonorm. Therefore, Meteonorm 7.3 data was used in the simulations. Meteonorm 7.3 data used in the simulations are presented in Table I.

TABLE I
METEONORM DATA FOR BATI RAMAN LOCATION

Months	Global horizontal irradiation	Horizontal diffuse irradiation	Temp.	Wind velocity	Relative humidity
	kWh/m^2/mth	kWh/m^2/mth	°C	m/s	%
January	55.80	27.8	2.00	2.51	72.0
February	75.80	40.5	4.60	2.79	67.8
March	121.2	63.5	9.80	2.89	61.2
April	148.8	75.6	13.9	2.89	61.9
May	192.5	86.4	19.7	3.01	46.9
June	215.0	76.3	26.9	3.90	26.9
July	215.7	71.6	31.9	3.69	22.4
August	196.3	67.8	31.1	3.20	22.6
September	159.8	48.8	24.9	3.10	26.6
October	113.6	50.9	18.7	2.49	41.8
November	71.90	33.5	9.70	2.39	60.8
December	54.20	29.8	4.40	2.40	48.4
Year	1620.6	672.5	16.5	2.94	46.6

The values in Table I should be considered as the average of the days in each month. Horizontal diffuse irradiation (HDI) value represents the amount of irradiation that does not come directly from the sun, but is scattered by molecules and particles in the atmosphere. Global horizontal irradiation (GHI) value expresses the total irradiation incident on the horizontal surface. GHI is the sum of direct normal irradiation (DNI), HDI and ground-reflected irradiation (GRI) values. It can be seen that both irradiation and other meteorological parameters of Meteonorm are quite close to the values presented in Figure 2.

2) Design of PV power plant

Within the scope of the simulation study, it was deemed appropriate to design a 20 kWp PV power plant. The PV power plant was designed as grid-connected, and it was assumed that all of the generated energy would be injected into the energy grid. The construction used in the designed PV power plant was mounted at a fixed angle throughout the year. The tilt and azimuth angles were optimized for annual yield. In the orientation module, which is one of the main parameters in the PVsyst software, the tilt and azimuth angles of the designed power plant were optimized for the highest efficiency. The optimizations made are shown in Figure 4. In the relevant location, the optimum tilt angle was found to be 32°, and the optimum azimuth angle was 0°. According to the optimization

results, the transposition factor (TF) was found to be 1.14. The TF value expresses the increase in the radiation level coming to the PV system surface due to the optimization made. In this case, thanks to the optimization of tilt and azimuth angles, the annual solar potential value reaching the surface of the solar modules in the relevant region has increased to 1845 kWh/m².
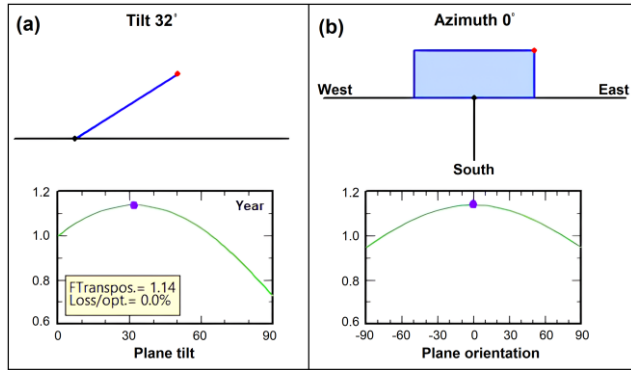
Fig. 4. Orientation of PV arrays a) Optimization of tilt angle; b) Optimization of azimuth angle

A grid-connected PV system basically has two components. While one of these is PV modules, the other is inverters. In the simulation study, 250 Wp Bereket brand PV modules based on polycrystalline silicon technology were used. A 20 kWp power plant requires the use of 80 PV modules. In this case, the total module area is 133 m². In Table II, the basic characteristics of the PV module used are presented for standard test conditions (STC).

TABLE II
TECHNICAL SPECIFICATIONS OF THE PV MODULE USED (AT STC)

Brand	Bereket Solar
Model	Poly 250 Wp 60 cells
Nominal power	250 Wp ±3%
Number of cells	60x1
Length×width×thickness	1665×1001×42 mm
Weight	18.5 kg
Short circuit current (I_{sc})	8.7 A
Open circuit voltage (V_{oc})	37.8 V
Maximum power point current (I_{mpp})	8.2 A
Maximum power point voltage (V_{mpp})	30.5 V
temperature coefficient	-0.42 %/°C
Diode saturation current	0.161 nA
Diode quality factor	0.99 /K

A PV module consists of the connection of many cells in series or parallel. In this way, the current, voltage and power values that the modules can offer can be determined. PV modules have a nonlinear structure and behave differently than a typical voltage and current source. A number of test studies are carried out by manufacturers to determine the behavior of PV modules under different loads and operating conditions. The results of these test studies must be included in the catalog information of the PV modules. Because these values have critical importance in the design of PV arrays that make up the

power plants and in the selection of inverters. Generally, curves of current-voltage (I-V), power-voltage (P-V), efficiency-irradiation and efficiency-temperature characteristics of modules are used in the design of PV systems. These data of the Bereket brand module used in the simulation study are presented in Figure 5.
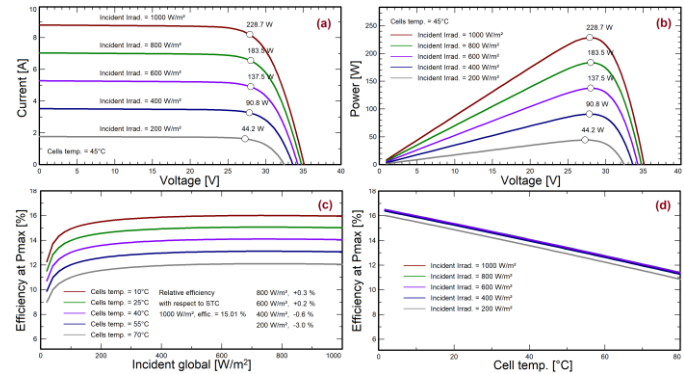
Fig. 5. Characteristic curves of the module used a) I-V curve b) P-V curve c) Efficiency-Irradiance curve d) Efficiency-Temperature curve

PV systems produce energy in the form of direct current. Before the generated energy is injected into the grid, voltage and frequency harmony must be ensured. This process is provided by inverters. In PV power plants, array inverters can be used for each array, or a common central inverter can be used for all arrays. A 20 kW inverter was chosen to convert the energy produced by the PV power plant, designed as 20 kWp, into AC form. The features of the inverter used are given in Table III.

TABLE III
TECHNICAL SPECIFICATIONS OF THE INVERTER USED

Brand	ABB
Model	TRIO-20.0-TL-OUTD-400
Height×width×thickness	1061×702×292 mm
Weight	70.0 kg
Grid voltage	400 V
Nominal AC power	20.0 kVA
Minimum MPP voltage	200 V
Minimum voltage for P_{nom}	440 V
Nominal MPP voltage	620 V
Maximum MPP voltage	950 V
Maximum current per MPPT	23.3 A
Maximum efficiency	98.16%
Frequency	50 Hz

Inverters generally operate with high efficiency under appropriate loads and operating conditions. However, the voltage value of PV modules also affects their efficiency. The efficiency of the inverter used under different operating voltages according to the input power is shown in Figure 6.

Inverters generally operate with high efficiency under appropriate loads and operating conditions. However, the voltage value of PV modules also affects their efficiency. The efficiency of the inverter used under different operating voltages according to the input power is shown in Figure 6.
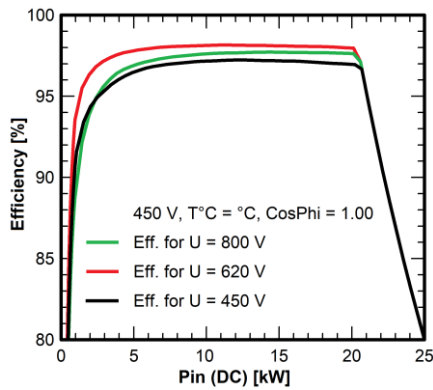
Fig. 6. Power and efficiency curves of the inverter used

According to Figure 6, the ABB Trio 20 kW inverter offers an efficiency of 95% and above at all operating voltages, but not below 200 V. However, the power values converted by inverters are also extremely effective on their efficient operation. Therefore, when configuring PV arrays, attention should be paid to ensure that the array parameters are compatible with the selected inverter.

TABLE IV
CRITICAL I-V VALUES OF PV ARRAYS AND VERIFICATION OF INVERTER COMPATIBILITY

Modules in series: 20, Module in parallel: 4, Plane irradiance: 1000 W/m^2	
V_{mpp} (60 °C)	518 V
V_{mpp} (20 °C)	626 V
V_{oc} (-10 °C)	847 V
I_{mpp} (STC)	32.8 A
I_{sc} (STC)	34.8 A
Operating power (STC)	19.3 kW
Array nominal power (STC)	20.0 kW
P_{nom} raito	1.00
Overload loss	0.0%

A total of 80 polycrystalline modules worth 250 Wp should be used in a power plant with a power of 20 kWp. These modules are configured as 4 arrays of 20 modules each for best efficiency. According to this configuration, the "voltage and current values" of the PV power plant at some critical operating

temperatures and the findings regarding the verification of the compatibility between the "arrays and the inverter" are presented in Table IV.

The reason for connecting modules in series in PV arrays is to increase the voltage value. However, two factors limit the voltage value. One of these is the operating voltage range of the inverter, and the other is the absolute maximum PV voltage value. The absolute maximum PV voltage value is also a limit for the PV array and is 1000 V according to the IEC 60038 standard. In the PV power plant designed in Figure 7, the output energy produced by the inverter according to the array power and I-V curves and limit values are presented according to various operating conditions of the PV power plant.
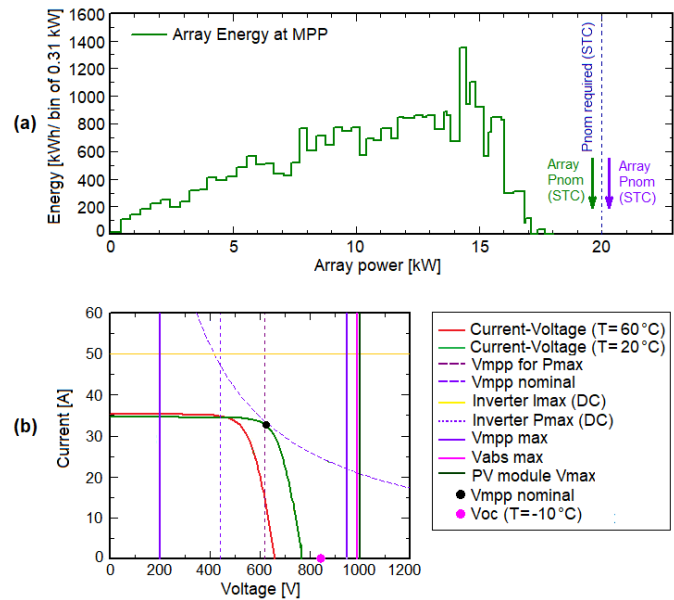
Fig. 7. Verification of inverter selection for the designed PV power plant a) Inverter output energy according to array power; b) I-V curves of the PV power plant and limit values of the system

3) Location of the power plant and its 3D model

The 20 kWp PV power plant, all elements of which are determined above, will be located close to the mosque on the West Raman campus. The satellite image of the mosque and its geometric dimensions when viewed from the west are presented in Figure 8.
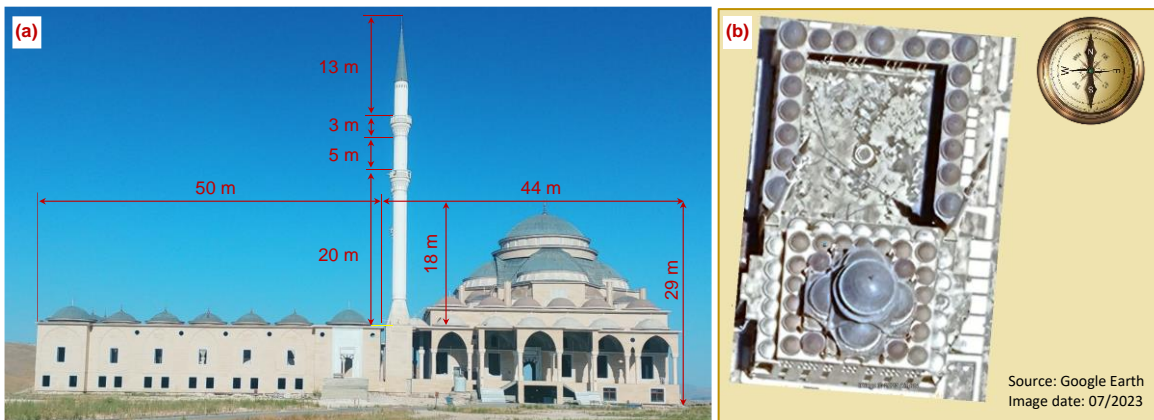
Fig. 8. Various images of the mosque a) Photograph and measurements of the western facade of the mosque b) Satellite image of the mosque

PVsyst software can reveal the effects of near shading elements on PV power plants. In order to do this, near shading elements must be drawn in 3D. The software allows the drawing of buildings, roofs, electricity pylons, cables, trees and many other objects around the PV plant in a very easy way. However, in order to draw structures with different architectures, geometric shapes such as rectangular prisms, cylinders and triangular prisms must be brought together. Mosques usually have a specific architecture that includes structures such as domes and minarets. Figure 9(a) shows the 3D model of the mosque created via the software. This model was created using the Construction/Perspective module under the "Near Shadings" section of the PVsyst software.

The 3D model seen in Figure 9(a) was created by combining many parallelepipeds, octagonal prisms and square pyramids

with appropriate dimensions. While creating the model, only shadows that may occur on the PV system were taken into account. The sections in the middle of the architectural structure have nothing to do with shading. That's why the details of these sections are not drawn. While placing the model on the plane, its azimuth angle with the south-north direction was taken into consideration.

In the designed PV power plant, performance losses due to shading were evaluated for 3 different scenarios. The performance of the PV plant in the absence of any near shading elements was accepted as reference. The results of 3 different scenarios were compared with these reference values. Figure 9(b) and (c) show the locations of PV arrays without shading and the PV power plant for 3 different scenarios.
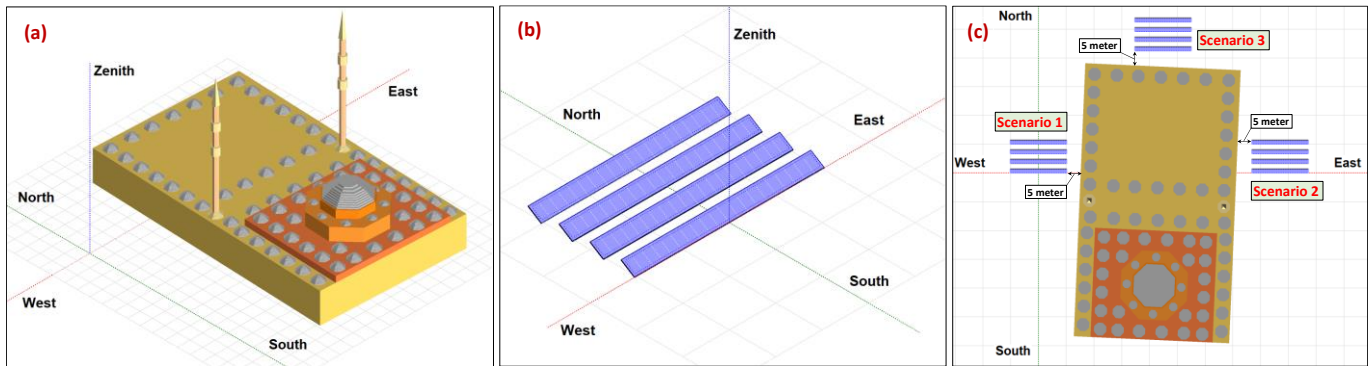
Fig. 9. a) 3D model of the architectural structure; b) Image of the PV power plant without shading; c) Position of the power plant for 3 different scenarios

Four tables were used in the designed PV power plant. The distance between the tables is important for the modules to shade each other. The distance between the tables is determined as two times the height of the shed as a general approach. However, in locations where the latitude angle is greater, increasing this distance will increase the efficiency of the system. However, in cases where there is no space restriction in the location where the power plant is installed, it would be meaningful to choose a larger distance between the tables to reduce shading losses during periods when the sun elevation angle is low. There may be a height difference between the sheds in the PV system. In this case, this parameter must also be specified in the software. In this case analysis, there is no slope in the land structure of the relevant location. These parameters and other information about the power plant are presented in Table V.

TABLE V
THE SIMULATION PARAMETERS OF COLLECTOR FIELD IN SHEDS

Basic parameters		Sheds sizes	
Nb. of sheds	4	Module sizes	1.001×1.665 m
Pitch N-S	3.34 m	Orientation	Portrait
Misalign	0.00 m	Nb. of modules in length	20
Shed to shed slop	0.0°	Nb. of modules in height	1
Shed tilt	32.0°	Modules X spacing	0.02 m
Azimuth	0.0°	Modules Y spacing	0.02 m
Baseline slope	0.0°	Table area	33.97 m²
Number of modules	4×20 = 80	Shed area	133.3 m²

III. RESULTS AND DISCUSSIONS

PVsyst software can analyze a designed PV system in 3 ways. These are "no shadings", "linear shadings" and "according to module strings". When a PV system is analyzed according to "no shadings", it is assumed that the system is not exposed to any near and/or distant shading elements. This approach is generally used when a quick assessment is desired but does not produce realistic results. When the designed system is analyzed according to "linear shadings", it is assumed that there is a linear relationship between the shaded area on the system surface and system performance. For example, when 20% of the PV system is shaded, the losses due to shading are calculated as 20%. Similarly, when, for example, 5% of a system is shaded, losses are calculated as 5%. This approach is more realistic than "no shadings", but it does not fully reflect the response of PV modules to shading. Because, depending on whether the cells in the panel are connected in series or parallel, even shading 20% of the surface of a panel may cause the array in which the panel is located to not produce any energy. The most realistic approach to calculating the response of PV panels and arrays to shading is "according to module strings". Therefore, in this study, all simulations were carried out according to this approach in order to address the effects of shading in the most sensitive way.

In order to compare the performance of the PV system according to the 3 determined shading scenarios and to interpret the effects of shading, it would be useful to present some of the outputs of the reports produced by the software together

visually. In this section, firstly, the shading geometry that occurs on the system on different days of the year is presented. Then, produced energy values, performance ratios and loss diagrams are presented for different scenarios.

A. Shading geometry and its resultant efficiency loss

The solar elevation angle changes with respect to the PV plane throughout a day. In addition, the maximum angle of incidence of the sun changes throughout the year. For example, the maximum sun elevation angle is approximately 29° for Batman on December 21, when the longest night is experienced, while this angle is approximately 76° on June 21, when the longest day is experienced. Due to the shadow length of the objects, the greatest shading losses will occur on December 21. Therefore, December 21 was preferred to show some critical shading geometries that occur in the determined scenarios. In Figure 10, critical shading geometries are given for the situation where there are no shading elements and for 3 different shading scenarios.
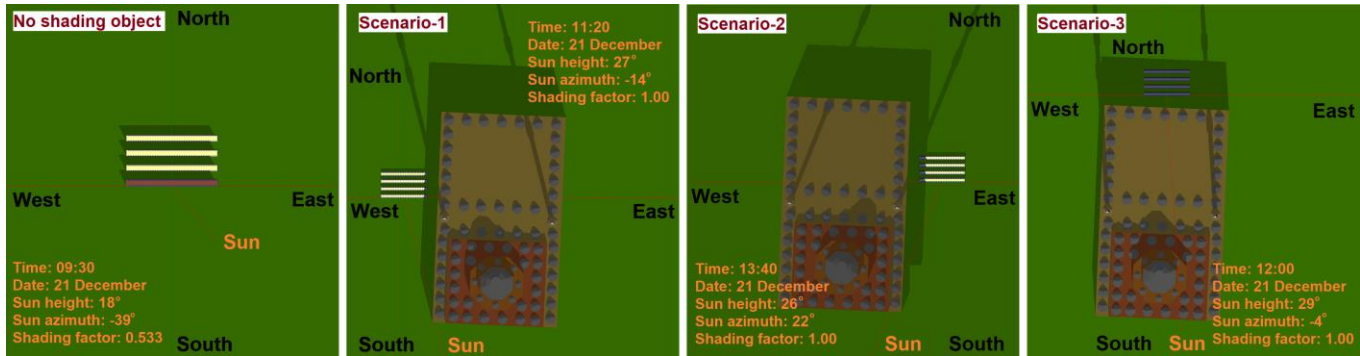
Fig. 10. Critical shading geometries for all scenarios

PVsyst software can show the shading status for specified periods on any day of the year in the shading animation module. Shading animation was performed for all scenarios on December 21, when the shadow length was highest. Accordingly, in the absence of near shading elements, low levels of shading occurred until 09:30 in the morning and from 14:30 in the afternoon. Shading events here occur due to the modules shading each other. In Scenario-1, the shading factor on the panels is 1.00 until 11:20. Due to the current array layout, the PV system starts producing energy after this time. In Scenario-2, the shading factor on the PV system is 1.00 after 13:40, and no energy can be produced after this time. On the same date, PV modules are exposed to radiation only for a very short time in the morning and evening for the placement in Scenario-3. In this scenario, full shading occurs even when the sun angle is at its highest value of 29°. In Scenario-3, very little energy can be produced throughout the day. In Figure 11, the variation of beam and electrical loss according to hours in the 3D shading analysis performed for all scenarios is presented.

When Figure 11 is examined, in the absence of near shading elements, shading losses were limited to 2% even on December 21. In Scenario-1, shading, which had a great impact especially in the morning hours, caused a beam loss of 14.1% during one day. In Scenario-2, shading, which was especially effective in the afternoon, caused a beam loss of 12.2% throughout the day. The most critical loss rate occurred in Scenario-3, as expected. The PV system was exposed to a very low beam during the day in Scenario-3. Complete shading occurred for almost the entire day. The electrical loss values in the graphs in Figure 11 are calculated relative to the energy value produced by the PV system during the relevant day. Since almost no energy is produced in Scenario-3, the electrical loss rate due to shading is calculated to be very low.

B. Energy produced and performance ratios of the system

One of the most important parameters of a grid-connected PV plant is its annual energy production. In grid-connected systems, the distribution of annual production by months may also be important in terms of energy management. PVsyst software provides the energy production graph of a designed PV power plant. Energy production graphs for all scenarios were created separately in the software, and these graphs are presented together in Figure 12.

When Figure 12 is examined, it is seen that there is a serious decrease in energy production in Scenario-3, especially in January, February, November and December. The reason for this is that the beam value suffers great losses during these months due to the architectural structure. As a matter of fact, Figure 11 shows the dramatic change in beam loss in the 3D shading analysis conducted for November 21. Considering all the data in Figure 12 together, the annual energy productions for "no near shadings", Scenario-1, Scenario-2 and Scenario-3 are calculated as 28.84, 20.43, 21.46 and 19.05 kWh, respectively.
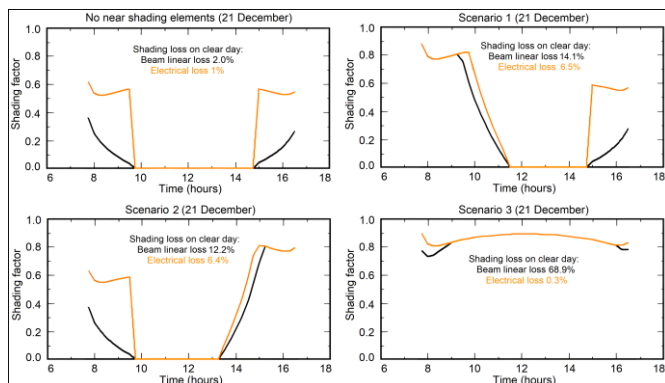
Fig. 11. Variation of beam and electrical loss throughout the day for all scenarios
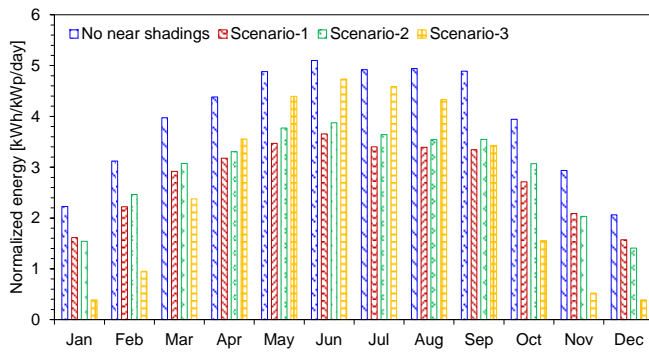
Fig. 12. Average daily energy production for all scenarios

Performance Ratio (PR) is expressed as the ratio of the energy produced by the PV system to the energy that the same system can produce in the STC state. The PR value does not depend on the efficiency of the PV modules used but is an important indicator that takes all losses into account in the designed system. The monthly average PR values of all simulated scenarios throughout the year are presented in Figure 13.

When all the data in Figure 13 are examined together, the annual values of PR for "no near shadings", Scenario-1, Scenario-2 and Scenario-3 are calculated as 0.797, 0.565, 0.593 and 0.526, respectively. In the PV system where there is no shading element, the highest PR value was obtained since there were no beam and electrical losses due to external shading. The reason why PR is less than 1.00 in this scenario is the optical, array and system losses that occur during the operation of the PV power plant. The lowest annual average PR rate occurred in Scenario-3. However, the PR value of Scenario-3 is not much lower than Scenario-2 and Scenario-3. This is because in Scenario-3, the PV plant achieves relatively high PR values in the summer months when irradiance is high.
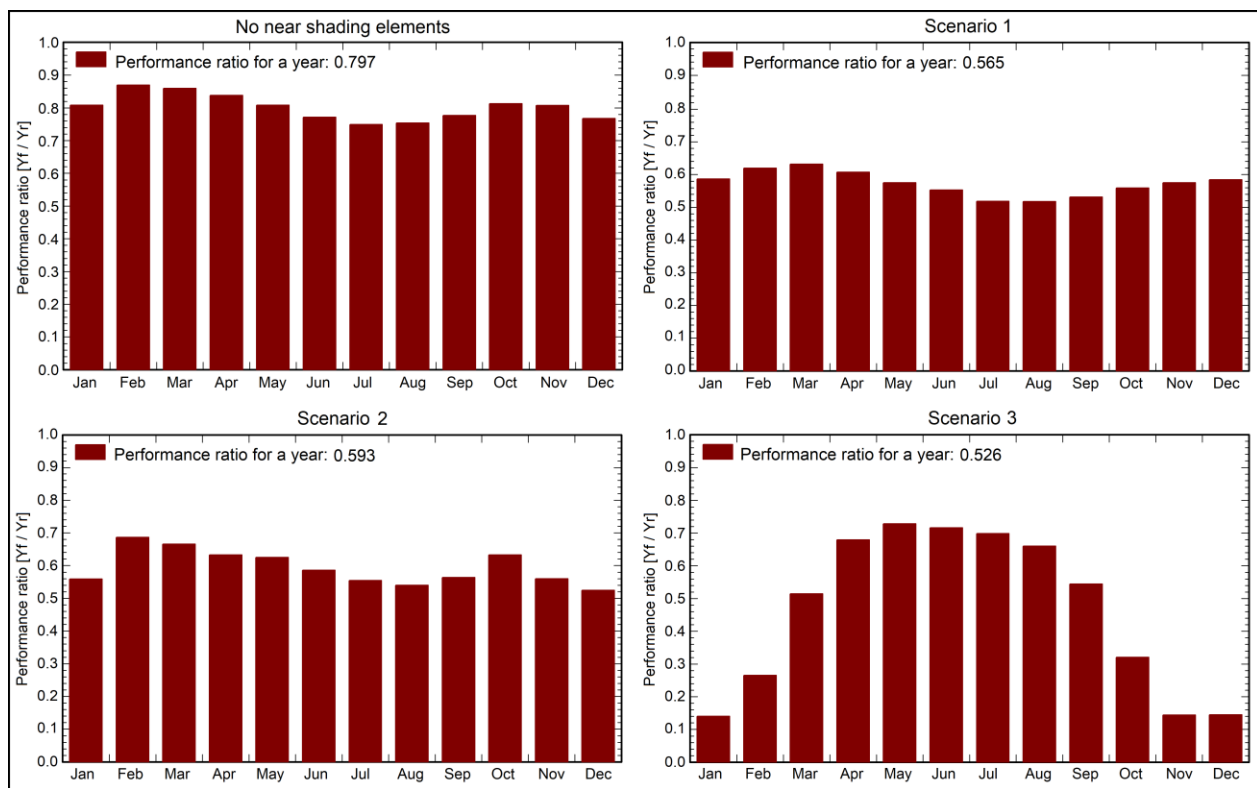
Fig. 13. Monthly average PR graphs for all scenarios

C. Analyzing loss diagrams

Sankey diagrams are very useful for understanding the lost energy values when the PV power plant operates in different scenarios. PVsyst software provides these visual diagrams as a report for each simulated variant. A typical Sankey diagram in PV systems shows the impact level of all variables that have a negative and positive effect between the solar radiation value arriving at a certain plane and the AC energy value injected into the grid. In Figure 14, loss diagrams for all scenarios are presented together, and losses due to shading are highlighted.

For all scenarios in Figure 14, the annual global horizontal radiation value at the location where the power plant is installed is 1621 kWh/m². The tilt angle of 32°, which is the optimum value for Batman province, increased the amount of energy coming to the surface of the modules by 11.7%. In the scenario where there are no near shading elements, a 2.2% loss occurred due to the panels shading each other. In Scenario-1, 2 and 3, irradiance losses due to near shading are 16.6%, 15.5% and 32%, respectively. Near shading analyses were performed according to the "according to strings" approach, which is the most realistic approach. According to this approach, the electrical loss values caused by the shading effect for all scenarios were found to be 1.6%, 18.4%, 15.6% and 5.4%, respectively. It is not a contradiction that the electrical losses in Scenario-3 are low. This is because the electrical losses include the losses caused in PV arrays by partial shading in the presence of radiation.
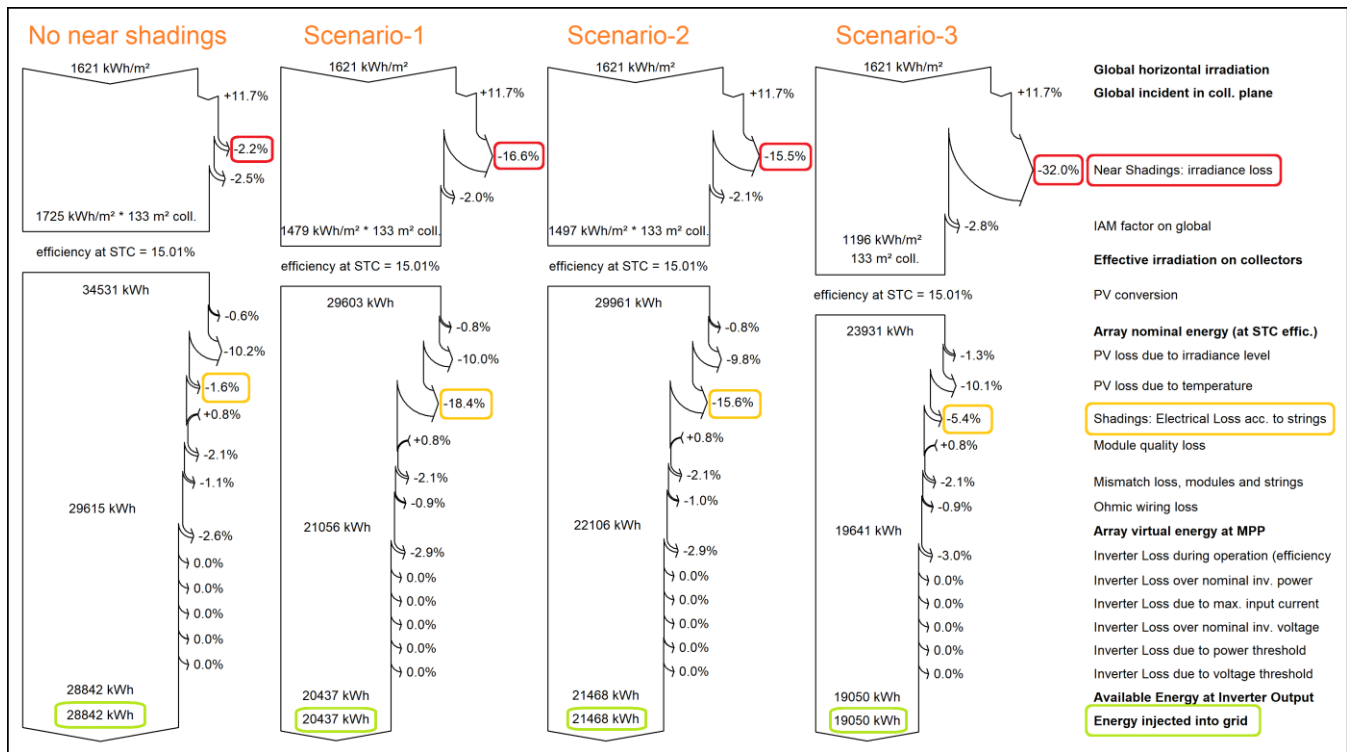
Fig. 14. Sankey diagrams of energy conversion for all scenarios

IV. CONCLUSIONS

In this study, the effects of near shading on the efficiency and operation of the PV systems, especially in cases where the usage area is limited, were investigated with the PVsyst software. Buildings with roofs, trees, overhead transmission lines, electricity pylons and similar structures are generally considered as near shading elements. 3D drawings of these structures can be easily added in desired dimensions via PVsyst software. However, shading elements can sometimes be unique. In this study, a mosque with an original architecture was chosen instead of standard shading elements. The 3D drawing of the mosque was created using the auxiliary drawing tools in the software. It is thought that a PV power plant with a power of 20 kWp will be installed in 3 different locations that are considered suitable in the courtyard of the mosque. The power plant, located in these 3 different locations, is shaded by the domes and minarets of the mosque throughout the year. Annual energy production values of 3 different scenarios were compared with the reference scenario without shading elements. According to the simulation results, in the scenario where there is no near shading element, annual production was 28.84 kWh. In Scenario-1, 2 and 3, the modules are located in the west, east and north directions of the mosque, respectively. In Scenario-1, 2 and 3, annual production was 20.43 kWh, 21.46 kWh and 19.05 kWh, respectively. In the content of the study, sample geometries of shading for all scenarios are presented comparatively for critical dates. In addition, monthly energy production, PR values and loss diagrams are given comparatively.

It has been observed that the PVsyst software used in the present case study plays a user-friendly role at all points, from problem creation to solution. The software is equipped with capabilities to answer many of the problems that may be encountered both in professional business life and in academic studies. It offers many 3D objects ready for shading analysis. Although the software allows drawing detailed architectural structures, it has been determined that drawing them is not as easy as in 3D design software. 3D scenes such as 3DS, DAE, PVC and H2P can be imported in the Construction / Perspective interface. However, it has been seen that it does not directly support the files of software commonly used in 3D drawing, such as SolidWorks and AutoCAD. It is thought that the direct import of file formats of this and similar software will make a significant contribution to the PVsyst software at this point.

In this study, a mosque with a complex architectural structure was chosen as the shading element. However, the effect of shading caused by other architectural structures with a similarly complex structure can also be investigated. Only PVsyst software was used within the scope of the study. The capabilities of other solar energy software can be examined under equal shading conditions, or comparative studies can be carried out to compare their capabilities. PVsyst software does not recognize all file types drawn in other software. To achieve this, third party software can be developed that allows PVsyst software to import any 3D drawing file type.

REFERENCES

[1] I. Kayri and M. T. Gencoglu, "Predicting power production from a photovoltaic panel through artificial neural networks using atmospheric indicators," *Neural Comput. Appl.*, vol. 31, no. 8, pp. 3573–3586, 2019.

[2] A. Korfiati *et al.*, "Estimation of the global solar energy potential and photovoltaic cost with the use of open data," *Int J Sustain Energy Plan Manag*, vol. 9, pp. 17–30, 2016.

[3] E. Dupont, R. Koppelaar, and H. Jeanmart, "Global available solar energy under physical and energy return on investment constraints," *Appl. Energy*, vol. 257, no. 113968, p. 113968, 2020.

[4]   R. Prăvălie, C. Patriche, and G. Bandoc, "Spatial assessment of solar energy potential at global scale. A geographical approach," *J. Clean. Prod.*, vol. 209, pp. 692–721, 2019.

[5]   R. Dutta, K. Chanda, and R. Maity, "Future of solar energy potential in a changing climate across the world: A CMIP6 multi-model ensemble analysis," *Renew. Energy*, vol. 188, pp. 819–829, 2022.

[6]   İ. Kayri, M. T. Gençoğlu, and M. Kayri, "Batman İli Güneş Enerjisi Potansiyelinin Belirlenmesine Yönelik Deneysel Bir Çalışma," in *1st International Engineering and Technology Symposium (1st IETS)*, Batman, Türkiye, May 03-05, 2018, pp. 646–654.

[7]   L. Cheng *et al.*, "Solar energy potential of urban buildings in 10 cities of China," *Energy (Oxf.)*, vol. 196, no. 117038, p. 117038, 2020.

[8]   D. F. Silalahi, A. Blakers, M. Stocks, B. Lu, C. Cheng, and L. Hayes, "Indonesia's vast solar energy potential," *Energies*, vol. 14, no. 17, p. 5424, 2021.

[9]   F. Mansouri Kouhestani, J. Byrne, D. Johnson, L. Spencer, P. Hazendonk, and B. Brown, "Evaluating solar energy technical and economic potential on rooftops in an urban setting: the city of Lethbridge, Canada," *Int. J. Energy Environ. Eng.*, vol. 10, no. 1, pp. 13–32, 2019.

[10] S. Nižetić, M. Jurčević, D. Čoko, and M. Arıcı, "A novel and effective passive cooling strategy for photovoltaic panel," *Renew. Sustain. Energy Rev.*, vol. 145, no. 111164, p. 111164, 2021.

[11] J. G. Hernandez-Perez, J. G. Carrillo, A. Bassam, M. Flota-Banuelos, and L. D. Patino-Lopez, "Thermal performance of a discontinuous finned heatsink profile for PV passive cooling," *Appl. Therm. Eng.*, vol. 184, no. 116238, p. 116238, 2021.

[12] E. Özbaş, "A novel design of passive cooler for PV with PCM and two-phase closed thermosyphons," *Sol. Energy*, vol. 245, pp. 19–24, 2022.

[13] M. Krstic *et al.*, "Passive cooling of photovoltaic panel by aluminum heat sinks and numerical simulation," *Ain Shams Eng. J.*, no. 102330, p. 102330, 2023.

[14] İ. Kayri, "The effects of coolant mass flow rate and atmospheric indicators in a PV/T system with experimental and ANN's models," *Sustain. Energy Grids Netw.*, vol. 36, no. 101189, p. 101189, 2023.

[15] M. Firoozzadeh, M. Lotfi, A. H. Shiravi, and M. Rajabzadeh Dezfuli, "An experimental study on using water streaks and water film over PV module to enhance the electrical efficiency," *Environ. Sci. Pollut. Res. Int.*, 2023.

[16] S. Panda, B. Panda, C. Jena, L. Nanda, and A. Pradhan, "Investigating the similarities and differences between front and back surface cooling for PV panels," *Mater. Today*, vol. 74, pp. 358–363, 2023.

[17] A. Aydın, İ. Kayri, and H. Aydin, "Determination of the performance improvement of a PV/T hybrid system with a novel inner plate-finned collective cooling with Al2O3 nanofluid," *Energy Sources Part A*, vol. 44, no. 4, pp. 9663–9681, 2022.

[18] M. Javidan and A. J. Moghadam, "Effective cooling of a photovoltaic module using jet-impingement array and nanofluid coolant," *Int. Commun. Heat Mass Transf.*, vol. 137, no. 106310, p. 106310, 2022.

[19] A. Aydın, İ. Kayri, and H. Aydin, "Electrical and thermal performance enhancement of a photovoltaic thermal hybrid system with a novel inner plate-finned collective cooling with different nanofluids," *Int J Green Energy*, pp. 1–15, 2023.

[20] R. Salehi, A. Jahanbakhshi, J. B. Ooi, A. Rohani, and M. R. Golzarian, "Study on the performance of solar cells cooled with heatsink and nanofluid added with aluminum nanoparticle," *International Journal of Thermofluids*, vol. 20, no. 100445, p. 100445, 2023.

[21] K. Osmani, A. Haddad, H. Jaber, T. Lemenand, B. Castanier, and M. Ramadan, "Mitigating the effects of partial shading on PV system's performance through PV array reconfiguration: A review," *Therm. Sci. Eng. Prog.*, vol. 31, no. 101280, p. 101280, 2022.

[22] A. G. Olabi *et al.*, "Artificial neural networks applications in partially shaded PV systems," *Therm. Sci. Eng. Prog.*, vol. 37, no. 101612, p. 101612, 2023.

[23] D. J. K. Kishore, M. R. Mohamed, K. Sudhakar, and K. Peddakapu, "Swarm intelligence-based MPPT design for PV systems under diverse partial shading conditions," *Energy (Oxf.)*, vol. 265, no. 126366, p. 126366, 2023.

[24] S. Sarwar *et al.*, "A novel hybrid MPPT technique to maximize power harvesting from PV system under partial and Complex Partial Shading," *Appl. Sci. (Basel)*, vol. 12, no. 2, p. 587, 2022.

[25] D. D. Milosavljević, T. S. Kevkić, and S. J. Jovanović, "Review and validation of photovoltaic solar simulation tools/software based on case study," *Open Phys.*, vol. 20, no. 1, pp. 431–451, 2022.

[26] B. Belmahdi and A. E. Bouardi, "Solar potential assessment using PVsyst software in the northern zone of morocco," *Procedia Manuf.*, vol. 46, pp. 738–745, 2020.

[27] Q. A. Alabdali and A. M. Nahhas, "Simulation study of grid connected photovoltaic system using PVsyst Software: analytical study for Yanbu and Rabigh Regions in Saudi Arabia," *Am J Energy Res*, vol. 9, pp. 30–44, 2021.

[28] N. A. Matchanov, K. O. Seok, A. A. Mirzaev, M. A. Malikov, and D. S. Saidov, "Study of energy yield on grid connected micro-inverter type 2.24 kW PV system using PVsyst simulation software," *Appl. Sol. Energy*, vol. 56, no. 4, pp. 263–269, 2020.

[29] R. Kumar, C. S. Rajoria, A. Sharma, and S. Suhag, "Design and simulation of standalone solar PV system using PVsyst Software: A case study," *Mater. Today*, vol. 46, pp. 5322–5328, 2021.

[30] E. D. Chepp, F. P. Gasparin, and A. Krenzinger, "Accuracy investigation in the modeling of partially shaded photovoltaic systems," *Sol. Energy*, vol. 223, pp. 182–192, 2021.

[31] E. D. Chepp, F. P. Gasparin, and A. Krenzinger, "Improvements in methods for analysis of partially shaded PV modules," *Renew. Energy*, vol. 200, pp. 900–910, 2022.

[32] *PVsyst 7.4.* (2023), PVsyst SA. Accessed: Jul. 13, 2023. [Online]. Available: https://www.pvsyst.com/download-pvsyst/

[33] MENR (2023), Ministry of Energy and Natural Resources of Türkiye, Solar Energy Potential Atlas. Accessed: Dec. 12, 2023. [Online]. Available: https://gepa.enerji.gov.tr/MyCalculator/pages/72.aspx

BIOGRAPHIES

İsmail Kayri received his Ph.D. degree in Electrical and Electronics Engineering from Fırat University, Elazığ in 2017. He has been working as an assistant professor at Batman University, Department of Electrical and Electronics Engineering, since 2018. Between 2006 and 2017, he taught many courses on the production, transmission and distribution of electrical energy at Batman University, the Faculty of Electrical and Electronics Engineering and Faculty of Technical Education. He conducts research on renewable and sustainable energy sources. His work focuses on photovoltaic systems. He conducts studies on the behavior of photovoltaic systems under real-world conditions.

Research Article

Multiple Physics Design of Induction Motor

Serhat Dogan and Yasemin Oner

Abstract—**Today, induction motors which have a widespread usage network are constantly developed by manufacturers. It is frequently used in heavy industry, mines, household appliances and consumer electronics due to its cheap maintenance, efficiency, effective torque and easy control features. Designers go to increase productivity with various analysis methods. Moreover, designers want to check the manufacturability of their desired machines. In this study, the multi-physics design of an induction motor is discussed. Electromagnetic, thermal, modal and stress analyzes are carried out in the design. Various analysis methods are discussed for electromagnetic and thermal analysis. In this article, Finite Element Analysis (FEA) method is used for electromagnetic and thermal analysis. In addition, the components required in multi physics design are emphasized. Electronics Desktop, Ansys Workbench Steady-State Thermal, Modal and Static Structural software are used in the analysis. In this study, the necessary analyzes for the design of an induction motor are carried out.**

Index Terms—**Induction motor analysis, multiple physics design, electromagnetic analysis, thermal analysis, modal analysis, stress analysis, finite element analysis, coupling maxwell and steady-state thermal.**

I. INTRODUCTION

INDUCTION MOTORS are widely used today. Compared with other motors, it has always had a development area, as it has features such as high torque, low cost, robustness and low maintenance. Due to its wide usage area in the industry, it creates negativity regarding energy consumption. Therefore, studies on these motors are mostly focused on efficiency [1-3]. The efficiency is usually improved to reduce electrical losses. The losses generally occur in the stator core, stator winding, rotor core and rotor bars. These losses are stated as the main cause of temperature. In other words, reducing these losses during the development phase will also reduce the temperature. Therefore, the temperature distribution of the machine to be analyzed is important for designers. Designers often focus on thermal analysis. Because they want the

SERHAT DOGAN, is with Department of Electrical & Electronics Engineering University of Dicle, Diyarbakir, Turkey, (e-mail: serhat.dogan@dicle.edu.tr).

https://orcid.org/0009-0007-8047-1337

YASEMIN ONER, is with Department of Electrical Engineering University of Yıldız Technical, Istanbul, Turkey, (e-mail: yoner@yildiz.edu.tr).

https://orcid.org/0000-0002-5310-6875

isolation classes to be determined according to the temperature values and distributions. Further, they want to create integrity in the motor design stages by performing modal and stress analyzes structurally.

In this study, the FEA method is used for electromagnetic analysis. The FEA method has several advantages compared to the Magnetic Equivalent Circuit (MEC) and Lumped Parameter Model (LPM) methods. The FEA method facilitates the analysis of complex geometries. Analyzes are performed by creating small mesh or part structures on the geometry. Analysis can be used in one, two or three-dimensional systems.

The simplified magnetic equivalent circuit of a machine is extracted with the MEC method. Elements in this circuit are compared to electrical equivalent circuit elements. Magnetic motor force, flux and reluctance elements in the magnetic equivalent circuit are compared to the voltage source, current and resistance elements in the electrical equivalent circuit, respectively. It is difficult to obtain the magnetic equivalent circuit on machines with complex geometries. However, it saves time compared to the FEA method. Moreover, it gives outputs closer to the experimental results. Regarding MEC analysis, Sudhoff aims to extract magnetic equivalent circuits of magnetic power circuits in his study [4].

The LPM method makes matching of different physical larges by analogy. This simplifies the behaviour of fragmented structures in the simulation. This method is used in various systems such as electrical, mechanical or heat transfer. It enables the simplification of components used in circuits, such as in electrical and electronic systems.

The LPM method creates an affinity between electrical and thermal systems [5]. Therefore, a close relationship can be established between electrical equivalent circuit parameters and real machine behaviour [6]. In the literature, FEA and LPM methods have been widely compared. For example, E. Ravaioli reports that the LPM method gives faster results than FEA analysis in nonlinear systems [7]. In fact, with this method, the mechanical components in the machine are assimilated to electrical circuit elements. The LPM method also helps to find losses in electromagnetic analysis.

Lumped Parameter Thermal Network (LPTN), Computational Fluid Dynamics (CFD) and FEA methods are mostly used for thermal analysis. The LPTN method is associated with the theory of heat transfer. This method takes advantage of the analogy between thermal and electrical circuits. In thermal analysis, simulation is likened to resistor and capacitor elements. While the capacitor element acts as

energy storage, it helps to resolve transient behaviour. On the other hand, the resistor element refers to the heat transfer over the system. Its function is conduction, heat dissipation, and radiation events, and it helps to analyze steady-state temperatures [8].

With the LPTN method, the heat flows in the machine can be estimated. It enables the analysis of transient and steady states. In addition, the specific temperature of the machine components can be determined. [9, 10]. In order to obtain correct results, the mesh structure should be properly detailed [11]. As a result, comprehensive heat dissipation is obtained. Thermal analysis is performed with Ansys Steady-State Thermal software.

A negative situation that occurs in induction motors is vibrations. Depending on the duration and amplitude of these vibrations, structural changes such as bearing disintegration or fan friction may occur in the machine. Modal analyzes are performed to observe the changes in the machine. With the modal analysis, the dynamic properties of the system can be determined under the determined frequency conditions of a system. Due to the electrical frequency effect, the stator structure of the induction motor should be examined. Vibrations occur as a result of various losses [12]. The modal analysis allows to improve the dynamic characteristics of the structure. Almost all systems produce large amplitude vibration at the resonant frequency [13]. If the frequency applied to the motor is close to or compatible with the motor's frequency, the motor can pass in the resonance state. As a result, vibration and noise occur [14]. The natural frequency of the machine should be examined to eliminate these negative effects [15]. Ansys Modal software is used for modal analysis.

In addition to modal analysis, stress analysis should also be performed. It can be determined how a load exerting pressure on the machine shaft affects the rotor core and shaft. Stress analysis is performed to determine the deformations in the rotor structure. Ansys Static Structural software is used for this.

In this study electromagnetic, thermal, modal and stress analyzes are carried out, respectively. The geometry obtained by electromagnetic analysis is also used in later analyses.

II. METHODOLOGY

The FEA method is used for electromagnetic and thermal analysis. Electronics Desktop software uses equations obtained by J. C. Maxwell in 1864. Maxwell rearranged the laws of Gauss, Faraday and Ampere. These are the laws of electromagnetic induction, Ampere's law, and electric and magnetic fields, respectively. The edited statements are given below:

$$\nabla \times \mathbf{E} = \frac{\partial \mathbf{B}}{\partial t} \tag{1}$$

$$\nabla \times \mathbf{H} = J + \frac{\partial \mathbf{D}}{\partial t} \tag{2}$$

$$\nabla . \mathbf{D} = \rho \tag{3}$$

$$\nabla . \mathbf{B} = 0 \tag{4}$$

Maxwell also added the expression $\partial D/\partial t$ to Ampere's law. The displacement expression is used for the estimation of electromagnetic waves. The above equations are in SI units. H and E express the magnetic and electric field strength in (ampere/m) and (volt/m) units. B and D express the magnetic and electric density in (weber/m^2) and (coulomb/m^2) units. It is also called B magnetic induction and D electrical displacement. Other expressions J and ρ are electric current and volume charge density, respectively. Its units are (ampere/m^2) and (coulomb/m^3).

Understanding the types of heat transfer will facilitate how thermal analysis is performed. Heat transfer is an energy process that occurs due to temperature differences. According to the law of thermodynamics, if a system loses energy, it is taken up by the environment. The same is true for vice versa. Namely, different structures transform into another form of energy without losing their energy [16]. This refers to the conservation of energy. Heat transfer phenomena generally take place in the form of conduction, convection and radiation.

- Conduction

The transfer of heat energy from a high point to a low point in a solid, liquid or gaseous medium is defined as conduction. The ability of the object to transfer heat in conduction is defined as thermal conductivity. In Fourier's law, the thermal conduction equation is expressed as:

$$q = -k\nabla T \tag{5}$$

$$q = -k\frac{dT}{dx} \tag{6}$$

where q is the heat flux density (W/m^2); k is the material conductivity W/(m.°K) or W/(m.°C) and dT/dx is the temperature gradient (°K/m). The heat transfer coefficient between the two materials is defined as h. The heat transfer coefficient expresses the power per unit area-Kelvin in SI unit.

$$h = \frac{W}{m^2 K} \tag{7}$$

- Convection

Convection, unlike conduction, refers to the spread of heat transfer from one point to another by the movement of fluids. It usually takes place in liquid and gaseous environments. In Newton's law of cooling, it is expressed as:

$$Q = hA(T - T_f) \tag{8}$$

where Q is the heat transferred per unit time; A is the area of the object (m^2); h, heat transfer coefficient (W/m^{2}K); T indicates the surface temperature of the object (°K or °C) and finally T_f indicates the liquid temperature (°K or °C).

- Radiation

The realization of heat transfer through electromagnetic waves is defined as a radiation event. Heat dissipation by radiation can occur in solid, liquid and gas environments. Radiation emission is expressed as follows according to Stefan Boltzman's law.

$$E_b = \sigma_b A T^4 \tag{9}$$

where E_b is the energy dissipated per unit time; T is the absolute temperature of the surface and σ_b is the Stefan-Boltzman constant and its value is 5.67×10^{-8} (W/m^{2}K^4).

Finally, the following equations are used for modal and stress analysis in FEA, respectively.

$$[M][\ddot{U}] + [K][x] = 0 \tag{10}$$

$$[K]\{x\} = \{F\} \tag{11}$$

where [M] is the mass matrix, [Ü] is the 2nd time derivative of [X] (displacement), [K] is the stiffness matrix (constant) and [F] is the force vector.

III. ELECTROMAGNETIC ANALYSIS

For thermal analysis, it is necessary to find electrical losses. In this study, an electromagnetic analysis of a 1.1 kW machine is carried out. The induction motor is 2-pole, 380 V (AC), 50 Hz, star connected and nominal speed is 1450 rpm. The analysis was carried out under constant power and full-load. In addition, the stator and rotor slot numbers are 36 and 28, respectively.
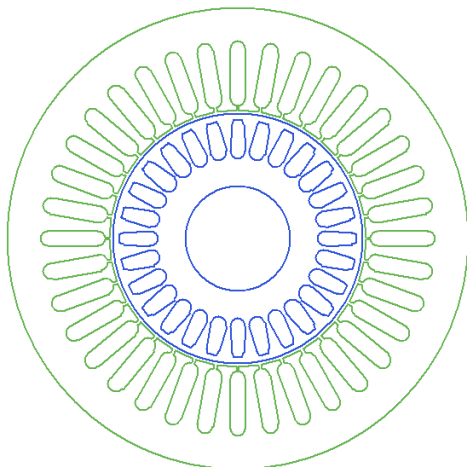
Fig. 1. 2D geometry of induction machine

Fig. 1 is the two-dimensional geometry of the machine. RMxprt software is used here. Magnetic analysis of the machine is performed with Electronics Desktop software. With magnetic analysis, it can be determined whether the machine is saturated or not.
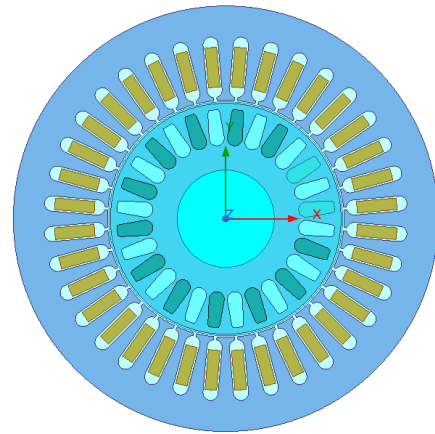
Fig. 2. Maxwell 2D representation of the machine

The magnetic flux density and flux distribution obtained according to the electromagnetic analysis are shown in the figures below. According to the results, while the maximum magnetic flux density is 1.87 Tesla, the magnetic flux value is found to be 0.0118 Weber/meter.
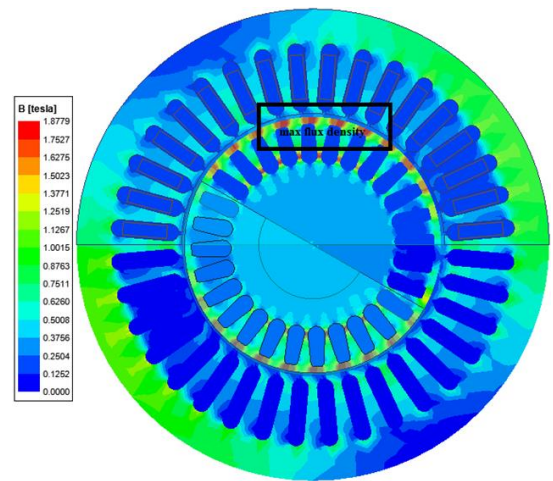
Fig. 3. Magnetic flux density distribution
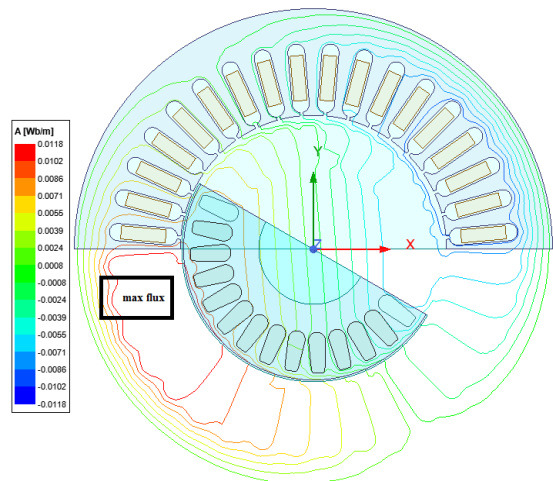
Fig. 4. Magnetic flux distribution

In the analysis, the average moment value is found as 3.91 Nm. Likewise, the current drawn by each phase is 3.08 A, in a steady state. Then, core, winding and rotor bars losses, which are critical, is calculated. The main factor causing temperature is usually losses. In addition, friction and wind losses also affect the temperature distribution. The Electronics Desktop software is used to find the stator and rotor core losses. The losses in the stator and rotor core are taken into account with the Electronics Desktop software. In addition, the eddy loss values of the rotor aluminum bars are calculated because of the thick cross-section. The total core losses consist of stator and rotor losses. When the steady state is examined, the average loss value is 19.44 W, while the average stator and rotor eddy losses are 5.65 W. It is determined that most of the eddy losses occur in the rotor bars.

IV.   THERMAL ANALYSIS

The heat dissipation of a machine is an important parameter for determining the insulation class. In the basic insulation classes, the ambient temperature is taken as 40 °C. The three-dimensional geometry of the machine is obtained with Electronics Desktop Maxwell 3D software.
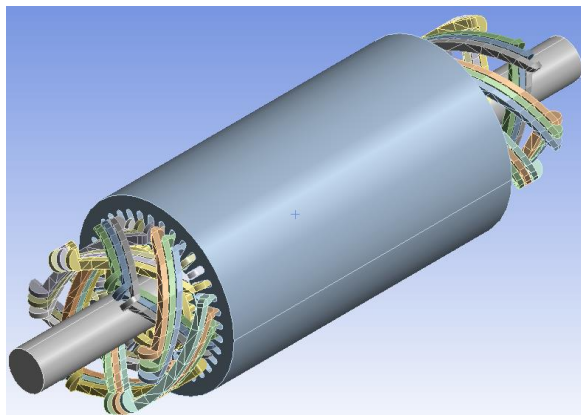
Fig. 5. Geometry of induction motor

Steel alloy M19_24G material is used in the stator, rotor cores. However, the rotor shaft was chosen from steel material and its magnetic effect was neglected while analyzing. The stator windings are made of copper. Rotor bars are aluminum. The properties of the materials used in this analysis are shown in Table 1.

TABLE I
MATERIAL PROPERTIES

Material	Thermal conductivity [W/m².°C]	Specific temperature [J/kg.°C]	Density [kg/m³]
Steel M19_24G	45.0	481.0	7872.0
Copper	400.0	385.0	8933.0
Aluminum	237.5	951.0	2689.0
Air	0.026	1007.0	1.1614

The specific temperature value is the energy required to enhance the heat of a material by one degree. If attention is paid, the thermal conductivity value of air is quite low compared to other materials. Therefore, it negatively affects the heat dissipation between the rotor and the stator. Advanced cooling systems are used to reduce this negative effect.

In order to use electrical losses in thermal analysis, Electronics Desktop Maxwell and Steady-State Thermal software are coupled in the Ansys Workbench program. Then, the mesh structure of the geometry used is extracted as seen in Fig. 6.

Fig. 6. Mesh structure of the mechanical model

The heat generation values of the stator and rotor cores are calculated separately in order to conclude the losses accurately. The heat generation value is the electrical losses per unit cubed on the core. In other words, it is the conversion of any form of energy into thermal energy. Usually, these forms of energy are electrical, mechanical or chemical. Temperature distributions are found with these losses. The highest and lowest heat generation values are found in the stator and rotor cores. The heat generation value of each rotor bar is calculated in the software. However, the heat generation value of the total rotor bars is indicated here. The highest values in the rotor core are the rotor bars. The lowest values are the rotor core. In the stator core, on the other hand, it is observed that the heat generation values are high near the windings.
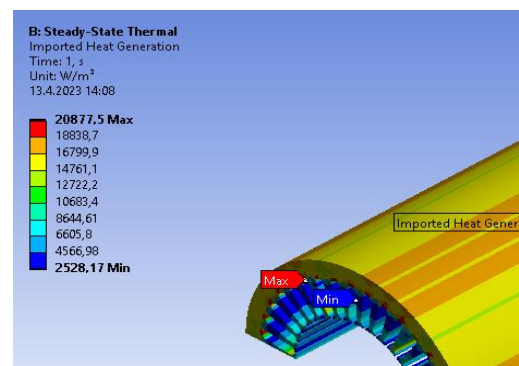
Fig. 7. Heat generation values of the stator core
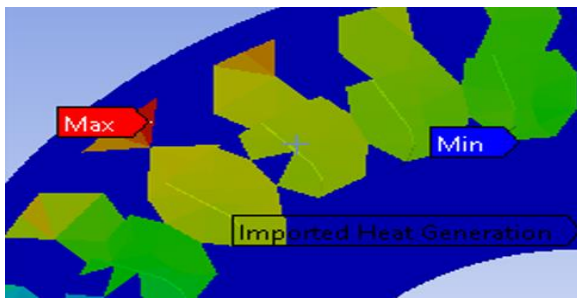
Fig. 8. Heat generation values of the rotor core

Losses per volume are obtained from heat generation values. These losses are listed in Table 2.

TABLE II
VOLUME LOSS DENSITIES

Structure	Total loss [W/m^3]	Scaling factor
Stator	10.9351	1.02266
Stator windings	43.5337	1.00
Rotor	0.438306	1.01047
Rotor bars	82.9701	0.999

Another important point in thermal analysis is boundary conditions. Material properties contribute to the determination of boundary conditions. There are two important components for determining the temperature dispersion: the heat dissipation and the heat source. The boundary conditions are as follows:

TABLE III
BOUNDARY CONDITIONS

Parameters		
Temperature source	Electrical losses	
	Ambient temperature [40 °C]	Thermal conductivity coefficient [45 W/m^2.°C]
Convection		

In the analysis, the heat generation values obtained from the stator and rotor structures are combined as a single structure as in Fig. 9. It is previously stated that the thermal conductivity coefficient for the M19_24G steel material is 45 W/m^2°C. For this reason, the same value is also used in the boundary conditions.
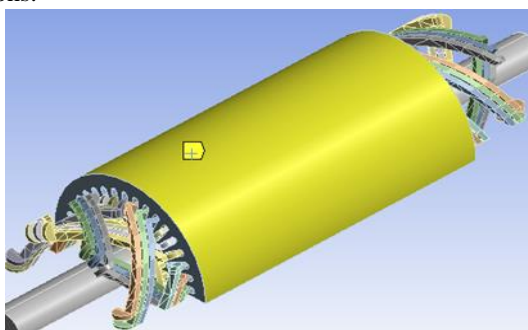
Fig. 9. Stator surface heat dissipation heat

Heat dissipation takes place through the stator surface. In other words, it is known that the cooling effect is effective on the stator surface. Therefore, the yellow region in Fig. 9 is determined as the boundary condition. The environment temperature is taken as 40 °C according to the determination of the insulation classes.

By establishing the boundary conditions, the temperature distribution is obtained, aligning with the results of the thermal analysis. In Fig. 10, while the maximum temperature value is 102.42 °C, the minimum temperature value is 95.015 °C.
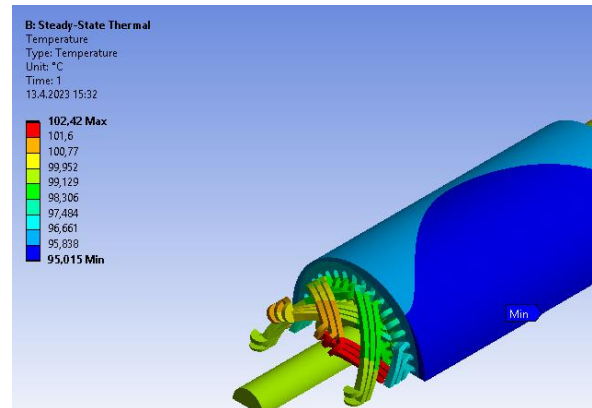
Fig. 10. Temperature dispersion

Fig. 11. Side section temperature dispersion

Fig. 11 is the side section of the machine structure. The highest values occurred in the stator windings. It is observed that the temperature distributions towards the stator surface decrease. Because of the air gap between the rotor and the stator, high-temperature values only show their effect on the windings. The temperature values around the rotor and shaft are lower compared to those around the windings. If a material with a higher thermal conductivity coefficient is selected in these analyses, the temperature distribution would change positively.

V. STRUCTURAL ANALYSIS

The natural frequency of the system is tried to be found by using the stator structure. The analysis is carried out in a condition where the stator core is kept stationary and free vibration. The stator core is shown in Fig. 12. The structural properties of the stator core are shown in Table 4. Here, young and volume modulus are values formed under hardness and pressure, respectively.

TABLE IV
STRUCTURAL PROPERTIES OF THE MATERIAL

Properties	Values
Density	7.85×10^{-6} [kg/mm^3]
Young module	2×10^5 MPa
Poisson ratio	0.3
Volume module	1.667×10^5 MPa
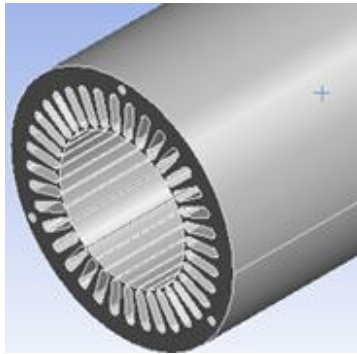
Fig. 12. Stator structure for modal analysis
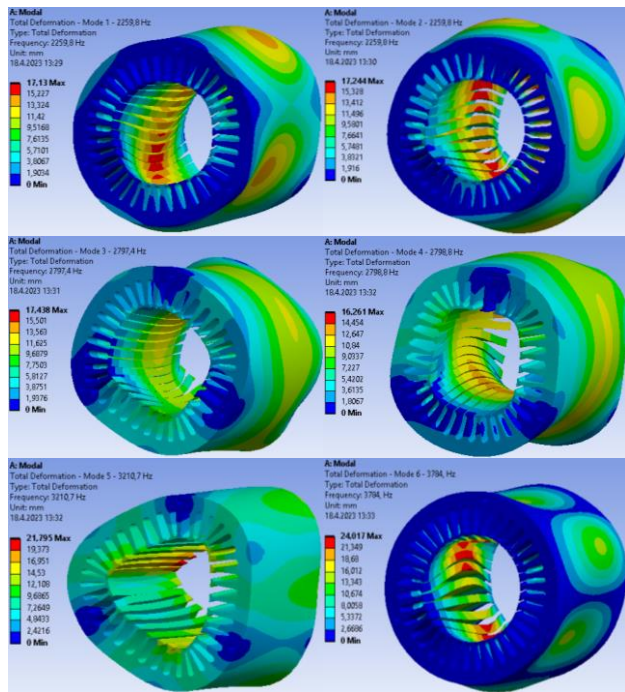
Fig. 13. Total deformation changes by modal analysis

According to the modal analysis, the natural frequencies of the system are found as 2259.8, 2797.4, 2798.8, 3210.7, and 3784.0 Hz. Images of the total deformation are shown in Fig. 13. When the results are examined, it is seen that the deformation ratio increase with the increase of the natural frequency value. The lowest deformation rate is 2259.8 Hz, while the highest deformation rate is 3784 Hz. Deformation rates occurred at high levels in the middle parts of the stator teeth.

In the electromagnetic analysis, the torque generated by the motor shaft is found as 3.91 Nm. In the stress analysis, it has been revealed how this moment value causes deformation in the rotor and shaft structure. For this, mechanical changes are applied to the rotor shaft. Fig. 14 shows the changes made to the motor shaft. There are two bearings and gears here. The boundary conditions required for the stress analysis are given in Fig. 14 and Table 5.
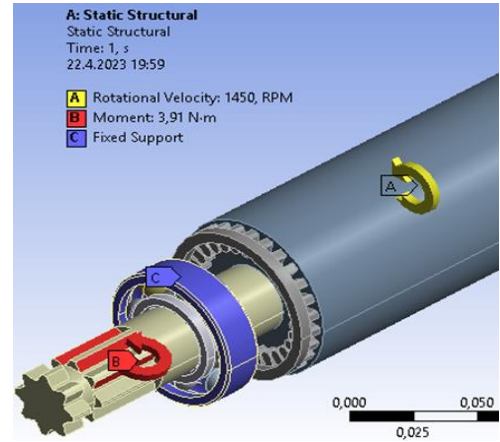
Fig. 14. Boundary conditions for stress analysis

TABLE V
BOUNDARY CONDITIONS FOR STRESS ANALYSIS

Parameters	Values
Rotation speed and direction	1450 rpm and counterclockwise
Applied torque and direction	3.91 Nm and counterclockwise
Fixed supports	The outer ring of the bearings

Looking at the stress analysis results in Fig. 15, it is seen that a maximum deformation of 0.0189 mm occurred in the middle parts of the rotor core. When this ratio is compared with the rotor diameter, it is determined that it is equal to a small value of 0.0144%. In the bearing and gear areas exposed to loads, there is almost no deformation effect.
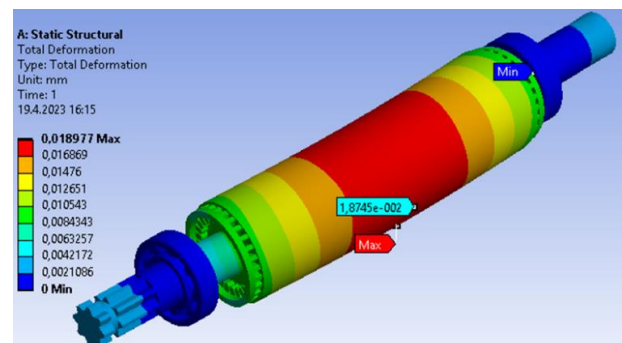
Fig. 15. Stress analysis results

VI. CONCLUSION

In this study, a multi physics design of a 1.1 kW induction motor is carried out. The parameters required at each design stage are emphasized. More focused on electromagnetic and thermal analysis. According to the literature, FEA is chosen as the analysis method.

Electronics Desktop software is used for electromagnetic analysis. In addition, the three-dimensional geometry of the machine is obtained from Electronics Desktop Maxwell 3D software. By calculating the electrical losses, the heat generation values required for the thermal analysis are calculated. Heat production values are used in thermal analysis by coupling Electronics Desktop Maxwell and Steady-State Thermal software in the Ansys Workbench program.

It is emphasized on which parameters the boundary conditions required for performing thermal analyzes depend. In the analysis made according to the heat production values of the induction machine, the temperature values of the materials in the stator and rotor structures are obtained. The highest temperatures occur in the stator windings, while the lowest temperatures occur on the stator core surface.

Structurally, modal and stress analyzes are carried out. In these analyzes, Ansys Modal and Static Structural software are used, respectively. The natural frequencies of the stator are obtained. Further, the total deformations caused by the natural frequencies are determined. In the stress analysis, the deformations caused by the load applied to the rotor shaft in the rotor structure are examined.

In this study, the points to be considered in the multiple physics design of an induction motor are emphasized. Moreover, the analysis that should be carried out in the process up to the production state is examined.

REFERENCES

[1] V. Anand, B.S. Ram, "A comprehensive investigation of the design of solar-powered induction motor-driven electric vehicle." Materials Today: Proceedings 2022;56 pp.3682-3686.

[2] M.Y. Mohamed, S.A.A. Maksoud, M. Fawzi, A.E. Kalas, "Effect of poles, slots, phases number and stack length changes on the optimal design of induction motor. " Nineteenth International Middle East Power Systems Conference (MEPCON) 2014 pp.66-471.

[3] M.J. Akhtar, R.K. Behera, "Optimal design of stator and rotor slot of induction motor for electric vehicle applications." IET Electr. Syst. Transp. 2019;9 pp.35-43.

[4] S.D. Sudoff, *Power Magnetic Devices: a Multi-Objective Design Approach*, John Wiley & Sons, 2014.

[5] P. Cabral, A. Adouni, "Induction Motor Thermal Analysis Based on Lumped Parameter Thermal Network." KnE Engineering 2020;5(6) pp.451–464.

[6] M. Amrhein, P.T. Krein, "Induction Machine Modeling Approach Based on 3-D Magnetic Equivalent Circuit Framework." IEEE Transactions on Energy Conversion 2010;25(2) pp.339-347.

[7] E. Ravaioli, B. Auchmann, M. Maciejewski, H.H.J. Kate, A.P. Verweij, "Lumped-Element Dynamic Electro-Thermal model of a superconducting magnet." Cryogenics 2016;80(3) pp.346-256.

[8] F. Graffeo, S. Vaschetto, A. Miotto, F. Carbone, A. Tenconi, A. Cavagnino, "Lumped-Parameters Thermal Network of PM Synchronous Machines for Automotive Brake-by-Wire Systems." Energies 2021;14(18) pp.5652.

[9] D. Liang, "A Hybrid Lumped-Parameter and Two-Dimensional Analytical Thermal Model for Electrical Machines." IEEE Transactions on Industry Applications 2021;57(1) pp.246-258.

[10] D.A. Staton, DA, A. Cavagnino, "Convection Heat Transfer and Flow Calculations Suitable for Electric Machines Thermal Models" IEEE Transactions on Industrial Electronics 2008;55(10) pp.3509-3516.

[11] Y. Yang, B. Bilgin, M. Kasprzak, S. Nalakath, H. Sadek, M. Preindl, J. Cotton, N. Schofield, A. Emadi, "Thermal management of electric machines." IET Electr. Syst. Transp. 2017;7 pp.104-116.

[12] S. Bhadouria, B.N. Agrawal, S.K. Singh, P.K.S, Nain, "Study and Modal Analysis of Induction Motor by Using ANSYS." In: R.M. Singari, P.K. Kankar, G. Moona, (eds) Advances in Mechanical Engineering and Technology. Lecture Notes in Mechanical Engineering, Springer 2022.

[13] M.L. Chandravanshi, A.K. Mukhopadhyay, "Modal Analysis of Structural Vibration." Proceedings of the ASME 2013 International Mechanical Engineering Congress and Exposition 2013;14.

[14] Y. Li, J. Du, J. Xia, "Vibration and Modal Analysis of Small Induction Motor." Proceedings of the International Conference on Advances in Mechanical Engineering and Industrial Informatics 2015 pp.903-907.

[15] L. Xiao-hua, H. Su-rong, L. Liang-zi, "Calculation and analysis of vehicle vibration and noise of permanent magnet synchronous motor applied in electric vehicle [J]." Electric Machines and Control 2013;17(8) pp.37-42.

[16] I.V. Lienhard, V.J.H. Lienhard, *A Heat Transfer Textbook*, Phlogiston Press, 2020.

BIOGRAPHIES

SERHAT DOĞAN received a B.Sc. degree in Electrical & Electronics Engineering from Fırat University, Elazığ, Turkey, in 2017. He worked as Wireline Logging Engineer at TPIC until 2020. He started his M.Sc. Electrical Engineering at Yıldız Technical University, Istanbul, Turkey, in 2021. He is currently Research Assistant at Dicle University. His areas of interest are electrical machines and power electronics.
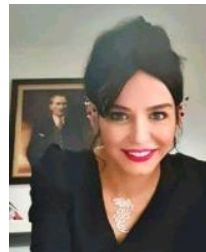
YASEMİN ÖNER received the B.Eng., M.Sc., and Ph.D. degrees in electrical engineering from Yıldız Technical University, Istanbul, Turkey, in 2007, 2009, and 2013, respectively. She is currently Prof. Dr. at Yıldız Technical University. Her research interests include analytical solutions for electrical machines.

Research Article

A Sensorless MPPT Approach For PV Pump System Used BLDC Motor

Yunus Atagun, Resat Celikel

Abstract—PV irrigation systems have begun to be used intensively today, as energy needs increase. In Partially Shaded Conditions (PSC), the efficiency of the PV system decreases significantly, and traditional Maximum Power Point Tracking (MPPT) algorithms become insufficient. On the other hand, traditional MPPT algorithms require sensors to measure the current and voltage of the PV system. In this study, a sensorless hybrid MPPT algorithm is proposed to reduce system costs and enable operation without the need for PV system data. A simulation study was conducted in the MATLAB/Simulink environment to examine the PV system. The proposed algorithm has been tested under four different PSC scenarios. PV system power, motor speed, and currents were examined under each condition. The high maximum power tracking performance of the proposed algorithm is demonstrated through simulation results. In the steady state, the lowest MPPT efficiency was 95.66%, whereas the highest MPPT efficiency was 99.9%. The MPPT algorithm completed in less than 2 seconds, with the first stage taking 1.3 seconds to reach most of the maximum PV system power. The second stage of the MPPT algorithm was used to achieve maximum power in a narrower area.

Index Terms—PV pump, BLDC, Partial shading, MPPT, Sensorless algorithm.

I. INTRODUCTION

FOSSIL FUELS, which are used extensively in energy production, are decreasing. At the same time, energy production costs continue to increase. On the other hand, consumption of fossil fuels causes significant environmental problems. For these reasons, interest in renewable energy sources is increasing day by day [1]. Solar energy has an important place among renewable energy sources. Photovoltaic (PV) irrigation systems have been increasing in importance in recent years. It offers an important alternative solution,

Yunus Atagun, is with Department of Mechatronic Engineering Firat University, Elazig, Turkey, (e-mail: yunusatgn23@gmail.com).
https://orcid.org/0009-0006-0039-5972

Resat Celikel, is with Department of Mechatronic Engineering Firat University, Elazig, Turkey, (e-mail: rcelikel@firat.edu.tr).
https://orcid.org/ 0000-0002-9169-6466

especially in agricultural irrigation, in places where there is no energy network and energy delivery is costly.

Solar energy has an important place among renewable energy sources. Photovoltaic (PV) irrigation systems have been increasing in importance in recent years. It offers an important alternative solution, especially in agricultural irrigation, in places where there is no energy network and energy delivery is costly.

Many different types of motors are used in photovoltaic irrigation systems, such as synchronous reluctance motor (SynRM), permanent magnet synchronous motor (PMSM), induction motor and brushless direct current motor (BLDC) [2-6]. BLDC motors are used as a better alternative to the induction motor in PV fed water pumping systems. This motor is compact, robust and efficient compared to the AC motor. Additionally, a BLDC motor has many advantages such as reliability, low maintenance, easy to drive and simple control. Therefore, BLDC motors have received increasing attention in water pumping systems in recent years due to their superior features. [7]. DC-DC converters are used in traditional PV pump systems. In [8], the MPPT technique without a DC-DC converter was developed for a PV pump system using a BLDC motor. In [9], a PV irrigation system was created by connecting a PMSM motor directly to the DC line of the inverter. However, DC-DC converters are used in many conventional PV water pump systems with MPPT algorithms.

PV panels operate with very low efficiency. Therefore, various Maximum Power Point Tracking (MPPT) algorithms and methods have been developed to obtain maximum power from PV panels [10, 11]. In the literature, two important atmospheric conditions that are effective in obtaining energy from PV power systems have been examined. These atmospheric conditions are known as uniform solar radiation and partial shading conditions (PSC). Perturb&Observe (P&O), Incremental Conductivity (InC), 0.8VoC and derivatives of these methods are used extensively under uniform radiation conditions [12, 13]. However, to achieve higher efficiency and lower power ripple, optimization-based MPPT algorithms such as artificial intelligence-based [14], Particle Swarm Optimization (PSO) and Gray Wolf Optimization (GWO) have been developed [15, 16]. Today, similar MPPT algorithms continue to be developed.

Conventional algorithms are ineffective in operating under atmospheric conditions under PSC. Because, Local MPP and Global MPP points are created in the system which is operated

under PSC. The MPPT algorithms need to find the GMPP. This is a complex and quite difficult process. For this purpose, various optimization and artificial intelligence-based MPPT algorithms along with derivatives of conventional MPPT algorithms have been developed. Some of the algorithms that have a lot of space in the literature can be examined as; a hybrid method including the particle swarm optimization (PSO) and search-skip-judge algorithms [17], Asymmetrical interval type-2 fuzzy logic control [18], a dynamic particles MPPT method [19] , MPPT Method Based on Inflection Voltages [20], Deep reinforcement learning approach MPPT [21], Artificial neural network based modified incremental conductance algorithm [22], Variable step size P&O MPPT controller by applying Ө modified krill herd algorithm [23], Chaotic Flower Pollination Algorithm (C-FPA) [24], improved sparrow search algorithm (ISSA) [25], Modified Butterfly Optimization Algorithm [26], Improved Team Game Optimization Algorithm [27], Harris hawk optimization (HHO) [28], Manta ray foraging optimization (MRFO) [29], and Salp Swarm Optimization (SSO) [30]. However, the literature is not limited to this algorithms; it is possible to examine many more studies.

Apart from this, scanning-based algorithms, which form the basis of P&O and InC algorithms, also find their place in the literature. The most important feature of these algorithms is their simple structure and applicability. A very recently developed two-level Voltage partitioning method appears to work with high efficiency [31]. Voltage partitioning and scanning techniques are fundamentally very similar. Scanning algorithms are especially concentrated on finding the voltage value at the GMPP point [32-34]. One of the newest of these algorithms is the voltage scanning algorithm and stands out with its high performance [35].

While the radiation value on photovoltaic panels may be uniform, the radiation values falling on each panel may be different due to natural events such as cloud shadowing and different external factors. In this case, each panel produces voltage in relation to the radiation value on itself. As a result, different maximum power points occur under different shading conditions. These points must be determined in order to obtain maximum efficiency from the system.

In recent years, there has been an increase in research into obtaining maximum efficiency from photovoltaic irrigation systems operating under PSC. In these studies, one or more of the current, voltage and speed parameters of the motor side are measured. At the same time, one or more of the current, voltage and radiation values are measured on the PV side [36-38]. Different motor types and MPPT algorithms have been used in PV pump systems operating under PSC. These MPPT algorithms are implemented using analytical or intelligent methods. In these studies, the advantages of BLDC motors such as easy driving technique and simple controllability were utilized [39-42]. Sensors are a significant cost in PV systems. For this reason, research on sensorless MPPT algorithms has recently been concentrated. Generally, algorithms without current sensors come to the fore, because the voltage of the PV system can be measured with simpler and lower-cost methods.

In some of these algorithms, the current estimation of the PV system is made by using DC-DC converter and in others by using the load data [43-46].

Obtaining maximum power from a PV system under partial shading conditions generally requires complex and difficult algorithms. This reveals the need for advanced microcontrollers and increases the system cost. Although voltage division algorithms are simple, they require PV panel parameters. Small changes in panel data or uncertain parameters limit system efficiency. The proposed algorithm stands out because it is both simple and does not require panel data, and its application is very simple. On the other hand, measuring current and voltage increases the system cost. Especially at high current values, both installation and sensor costs increase. Since panel currents and voltages are not measured in the proposed algorithm, a more compact structure is achieved and the system cost is reduced.

In this study, a hybrid MPPT algorithm was created by combining the voltage scanning algorithm with a modified P&O algorithm. PV irrigation system consists of ZETA DC-DC converter, BLDC motor and PV panels. In this algorithm, the back EMF and mechanical power of the motor are approximately calculated by using the speed and current information of the motor. The back EMF of the motor was scanned and mechanical power was approximately obtained. The maximum power value obtained from the scan is not accurate and has determined the area of maximum power. The data in the first stage formed the input data of the MPPT algorithm in the second stage. The second step used the motor speed and current information and determined the exact value of the maximum power point in the MPP region obtained in the first step. The most important advantage of this method is that only motor data is used. None of the current, voltage and radiation values of the PV system were used. Thus, the overall cost of the system is reduced. On the other hand, there are no complex operations in the algorithm. Implementation of the algorithm can be easily done.

II. PV PUMP SYSTEM MODELING

A. PV System

Figure 1 shows a PV cell model consisting of a well-known diode, a current source, and 2 resistors. The output current produced here is expressed as seen in the equations between equation 1 and equation 3.

$$I = I_{PV} - I_D - I_{R_P} \qquad (1)$$

$$I = I_{PV} - I_0 \left[exp\left(\frac{V+R_S I}{a}\right) - 1 \right] - \frac{V+R_S I}{R_P} \qquad (2)$$

$$a = \frac{N_S nkT}{q} \qquad (3)$$

where I_0 refers to the reverse saturation current or leakage current of the diode. a is the ideality factor, N_s is the number of series-connected cells, n is the diode ideality constant, k is the Boltzmann constant (1.3806503x10-23 J/K), T is the cell

temperature (Kelvin), and q is the electron charge (1.60217646x10-19 C). The current generated by the PV cell by the effect of light is present in Equation 4.
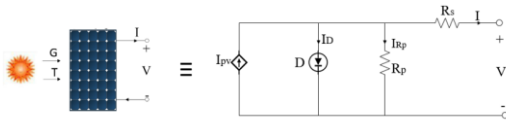
Fig.1. Electrical equivalent circuit model of a PV cell

$$I_{PV} = \left(I_{PV,n} + K_I(T - T_n)\right)\frac{G}{G_n} \qquad (4)$$

where $I_{PV,n}$ refers to the current generated for 25 °C and 1000 W/m², T_n refers to the nominal temperature (Kelvin), G refers to the radiation value on the panel surface (W/m²), and G_n refers to the nominal radiation value (W/m²). The saturation current of the diode (I_0) is given in Equation 5.

$$I_0 = \frac{I_{SC,n}+K_I(T-T_n)}{\exp\left(\frac{V_{OC,n}+K_V(T-T_n)}{a}\right)-1} \qquad (5)$$

where $I_{SC,n}$ is the nominal short-circuit current, $V_{OC,n}$ is the nominal open-circuit voltage, K_I is current coefficient, and K_V is voltage coefficient. If the radiation value on each panel in a PV array is the same, it is in uniform radiation. However, if the radiation values on the panels are different, partial shading conditions occur. While only one maximum power point occurs in uniform insolation, more than one maximum power point will occur in operation under PSC. Some of these points are LMPP and one of them is GMPP. In this study, the P-V graph formed in the case of uniform radiation and PSC is seen in Figure 2. The PV system consists of six series connected panels. The voltage produced by a panel at its maximum power point is 35.3V, its current is 4.39A and its power is 154.967W. Accordingly, the maximum power that the PV system can produce is given as 929.8W.
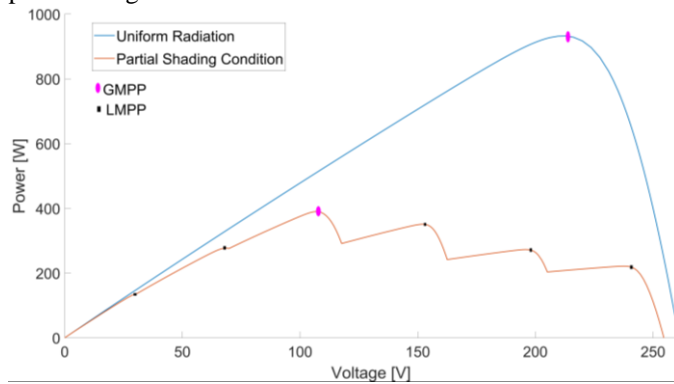
Fig.2. Uniform Radiation and P-V graph formed in case of PSC

B. DC-DC converter

The first stage is a DC-DC converter which used to operate the PV irrigation system at maximum power point. In this study, the zeta converter, which is widely used in PV systems, was used as the DC-DC converter. Zeta converter is a fourth order DC-DC converter that operates by increasing or decreasing input voltage. The Zeta converter consists of components such

as input inductor L_1, output inductor L_2 and intermediate capacitor C_1. Duty cycle D is estimated with the equation given in Equation 6.

$$D = \frac{V_{dc}}{V_{dc}+V_{mpp}} \qquad (6)$$

$$I_{dc} = \frac{P_{mpp}}{V_{dc}} \qquad (7)$$

$$L_1 = \frac{DV_{mpp}}{f_{sw}\Delta I_{L1}} \qquad (8)$$

$$L_2 = \frac{(1-D)V_{dc}}{f_{sw}\Delta V_{C1}} \qquad (9)$$

$$C_1 = \frac{DI_{dc}}{f_{sw}\Delta V_{C1}} \qquad (10)$$

where V_{dc} is the average value of the output voltage of the Zeta converter. The estimate of the average current I_{dc} flowing through the inverter is given in equation 7. After D and I_{dc} estimation L_1, L_2 and C_1 estimation are given between equations 8 and 10.

C. BLDC motor

BLDC motors are widely used due to their long life, ability to operate at high speeds, high moment and high efficiency. There is a three-phase winding on the stator of the BLDC motor. There are permanent magnets in its rotor. Motor windings are energized with a three-phase inverter. Six-step switching is used as the switching technique. When the six-step switching technique is applied to the windings, two phase windings will be energized at any time. According to the results obtained in this case, the mathematical equations of the BLDC motor using the six-step switching technique are similar to the conventional DC motor. BLDC motor shows approximately DC motor characteristics. Accordingly, the mechanical power of the motor Pmech and the power Pdc at the output of the DC-DC converter can be approximately equal when losses of motor, pump and inverter are ignored. The mechanical power of the motor is given in Equation 11. Where, Ia indicates the current of the motor and is approximately the same as Idc calculated in Equation 12. DC link power is calculated in Equation 13. where, Vdc shows the DC link voltage of the inverter.

$$P_{mech=}E_z.I_a \qquad (11)$$

$$I_{dc} = \frac{I_{a\_ph}+I_{b\_ph}+I_{c\_ph}}{2} \qquad (12)$$

$$P_{dc=}V_{dc}.I_{dc} \qquad (13)$$

$$E_z.I_a \cong V_{dc}.I_{dc} \qquad (14)$$

$$E_z = k.\omega \qquad (15)$$

According to equation 14 it can be $I_{dc} \cong I_a$. If the speed and current of the motor are known, E_z is calculated according to equation 15. Here, if $E_z.I_a \cong V_{dc}.I_{dc}$ then it can be $E_z \cong V_{dc}$. If the DC-DC converter duty cycle D is known, V_{pv} can be predicted as in equation 16.

$$V_{dc} \cong V_{pv}\left(\frac{D}{1-D}\right) \tag{16}$$

III. SENSORLESS MPPT METHOD

In PV systems, temperature and radiation changes change the value of the power obtained from the panel. Increases in temperature and decreases in radiation value reduce the maximum power obtained from the panel. On the other hand, the voltage value at which maximum power will be achieved varies due to different radiation values falling on the panels. For this reason, various algorithms must be used to obtain maximum power under both uniform radiation and partial shadowing conditions.

The main purpose of the proposed MPPT method is to estimate the maximum power point by measuring only the motor current and speed without measuring the current and voltage of the PV system. Thus, a significant advantage will be achieved in system cost. Generally, current and speed values of the motor must be obtained to control. Speed data can be estimated using sensorless control techniques. However, it is assumed that speed is measured in this study. First of all, as seen in Equation 11, the mechanical power of motor is obtained from the product of the back emf and the motor current. Accordingly, obtaining maximum mechanical power from the motor will approximately mean drawing maximum power from the PV system. Since there is a motor, DC-DC converter and inverter in the system, the efficiency of the system is not fully known. Because efficiency of the system will vary at different motor speeds and switching frequencies. For this purpose, a two-stage MPPT algorithm has been proposed, first approximately

estimating the region of the MPP and then reaching the exact value.

In the first stage, the increasing back emf value with a small increase amount is given as the input reference. Since the speed and parameters of the motor are known, the motor back emf is calculated and the voltage of the motor and therefore the inverter input voltage is determined approximately. Depending on the increasing reference voltage value, a PI controller determines the duty cycle for switching the DC-DC converter and the motor is accelerated by increasing the voltage. The output voltage of the DC-DC converter is actually the same as the DC link voltage of the inverter and is calculated approximately. Using Equation 16, the input voltage of the DC-DC converter, that is, the voltage produced by the PV system, is obtained approximately. As the motor accelerates, its mechanical power will increase and the power value to be transferred by the PV system will change. The mechanical power of the motor will be calculated instantly and the maximum generated power will be recorded using sampling blocks and the GMPP point will be determined approximately. When the maximum input voltage to be applied to the motor is reached, the second stage MPPT algorithm is started. In the second stage, the initial duty cycle value was determined by using duty cycle obtained at the maximum power value in the first stage. Here, the maximum power point is found with the modified P&O algorithm using the motor's current and speed values, and the motor continues to operate at this point. The flow chart of the proposed algorithm can be seen in Figure 3.
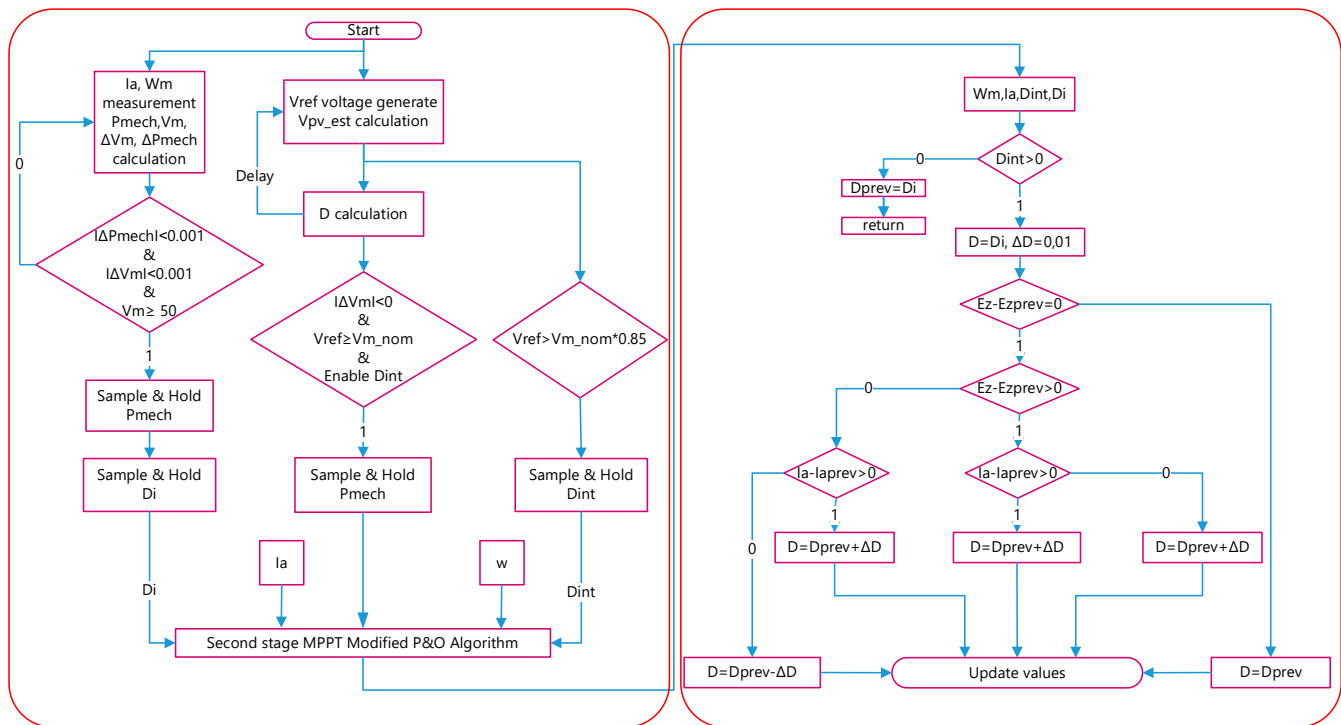
Fig.3. Flow chart of the proposed algorithm

IV.   SIMULATION AND RESULTS

The simulation study has been performed by using MATLAB/Simulink. The MATLAB/Simulink blocks of simulation are shown in Figure 4. The water pump shows a non-linear load characteristic with high inertia. For this reason, the BLDC motor accelerates slower and different load torque occurs on the motor at different speed values. This behavior causes difficulties in the operation of MPPT algorithms. Since maximum power is obtained at different voltage levels, especially in partial shading conditions, it becomes difficult to accelerate the motor. In the simulation study, in order to create the torque characteristic of the non-linear pump load, the load torque of the motor was created to vary with the square of the speed. The proposed algorithm has been tested under four different PSCs, as depicted in Figure 5. In these PSCs, maximum power was generated at different voltage points, and the proposed algorithm was tested in various regions. Four different PSCs were created to test the proposed algorithm. The voltage level at which maximum power occurs in each of these atmospheric conditions is located in different regions. The created PSCs and their maximum power under these conditions are illustrated in Figure 5.
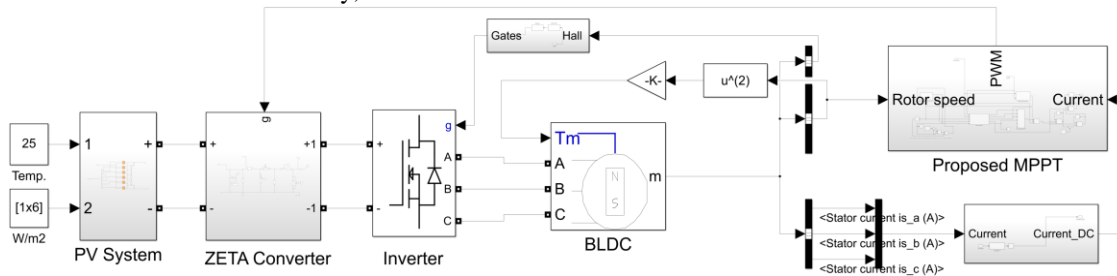
Fig.4. MATLAB/Simulink blocks of PV pump system
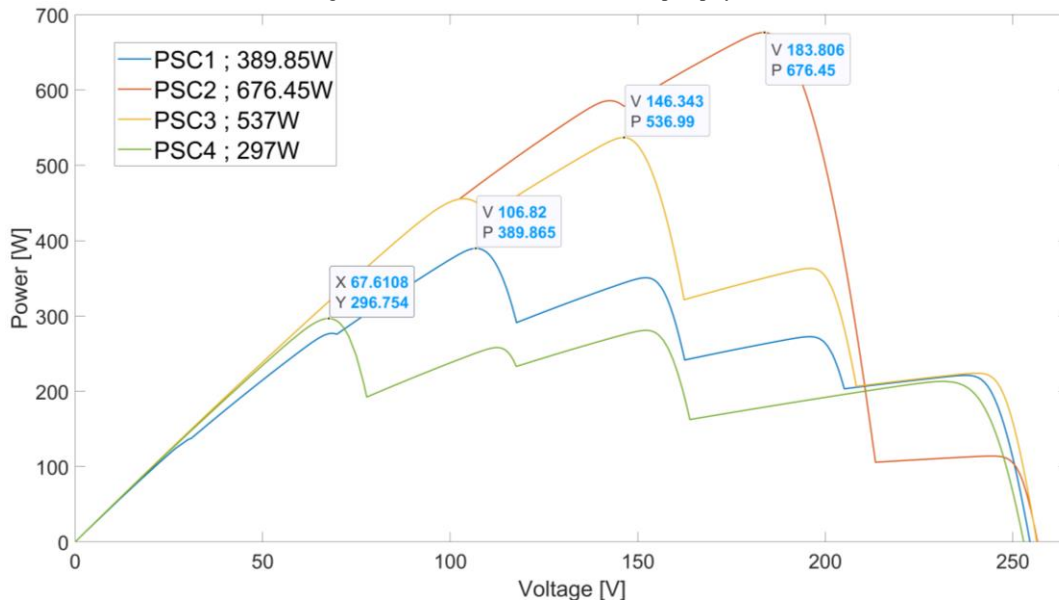
Fig.5. PV graph for four different PSC cases used in the simulation

Figure 6 shows the motor speeds and power of the PV system for four different PSC cases. Accordingly, the first stage MPPT algorithm was completed in 1.3 s, and the second stage MPPT started. When the power values obtained from the PV system were examined, a PV power of 389.683W was under PSC1 and the MPPT efficiency has been obtained as 99.95% in a steady state. When the PV system operated under PSC2, the power of the PV system measured as 647.114W, and the MPPT efficiency was found to be 95.66%. MPPT efficiencies under PSC3 and PSC4 conditions were obtained as 99.9% and 99.7%, respectively.

When the obtained results were examined, it was observed that the proposed algorithm worked only under PSC2 conditions with slightly lower efficiency than other conditions. Indeed, this efficiency value is at an acceptable level; however, very high efficiency has been achieved under other conditions. An important advantage of the proposed algorithm is its ability to the need for current and voltage information from the PV system, and PV system parameters are not required. The most important advantage of the scanning algorithm is its ability to approximately determine the power of the PV system using motor data. Figure 7 shows the current and voltages of the PV system. Accordingly, it can be seen that the completion of MPPT in Stage 2 does not depend on a specific period of time. However, at steady state is achieved in less than 2 seconds for all scenarios.
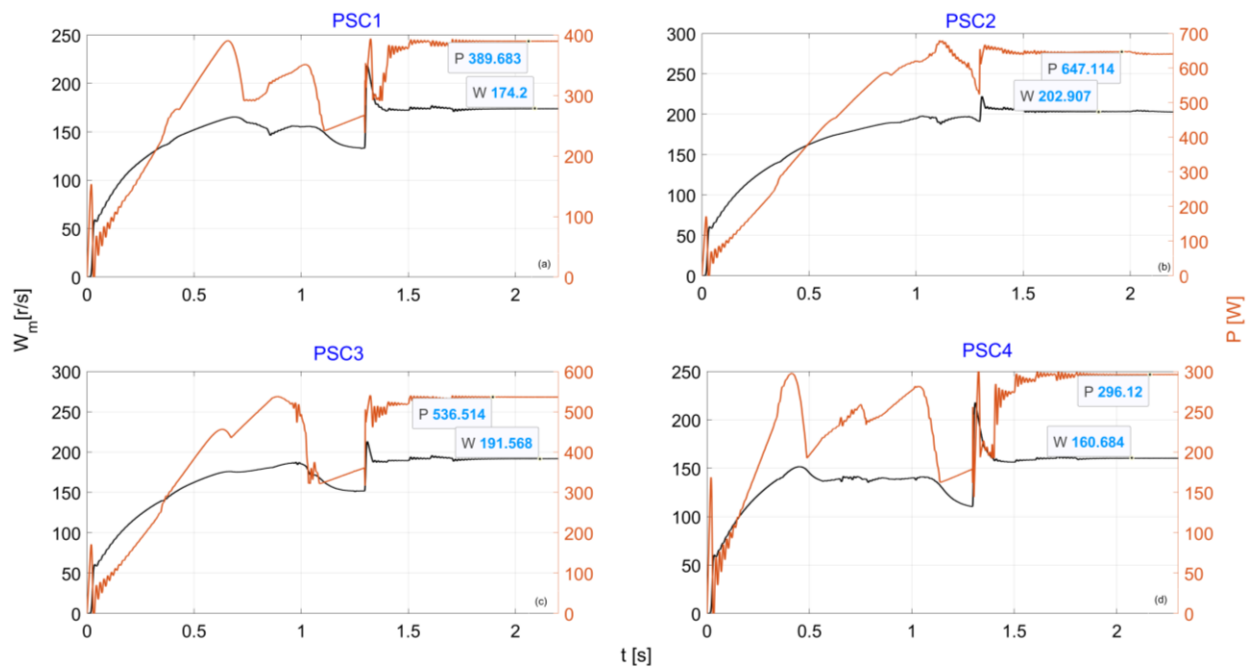
Fig.6. PV Powers and motor speeds obtained using the proposed algorithm a) PSC1 b)PSC2 c)PSC3 d)PSC4
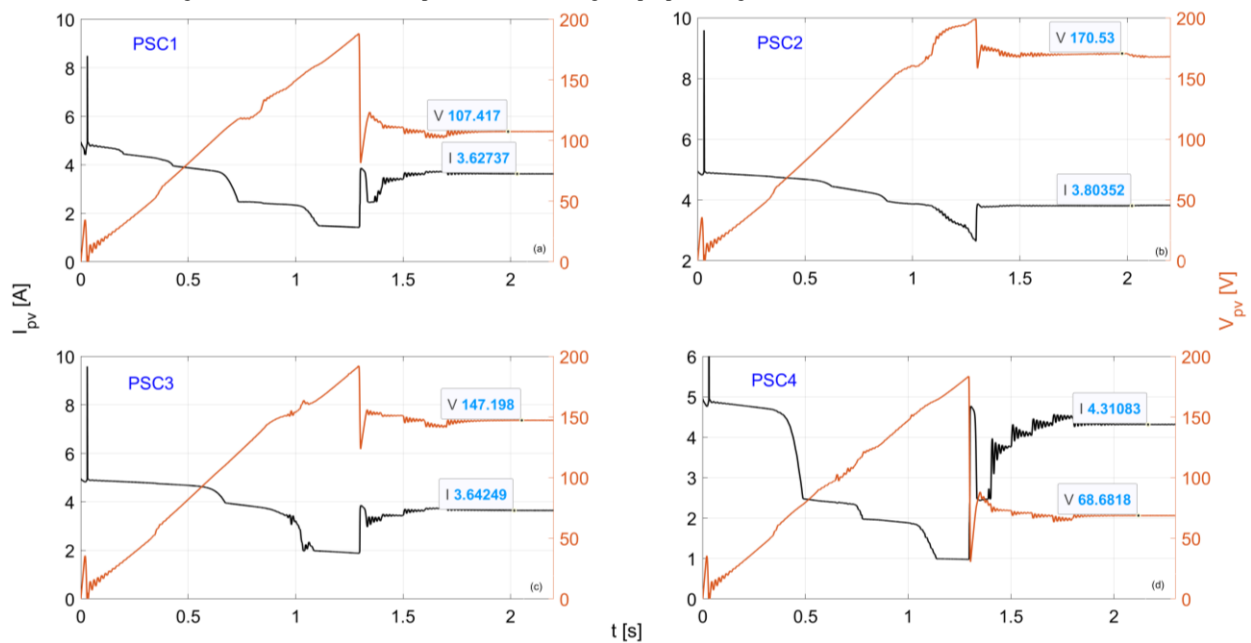
Fig.7. PV voltage currents obtained using the proposed algorithm a) PSC1 b)PSC2 c)PSC3 d)PSC4

Figure 8 illustrates the duty cycles occurring in four different PSC situations. This duty cycle is produced as a result of the operation of the MPPT algorithm. The duty cycle adjusts the voltage of the DC-DC converter. Although the running time of the MPPT algorithm appears to be long, it is not actually very long because the pump connected to the motor has a moment of inertia, slowing down the acceleration of the motor. If the motor could act as a resistive load, this scanning process could be completed much faster.
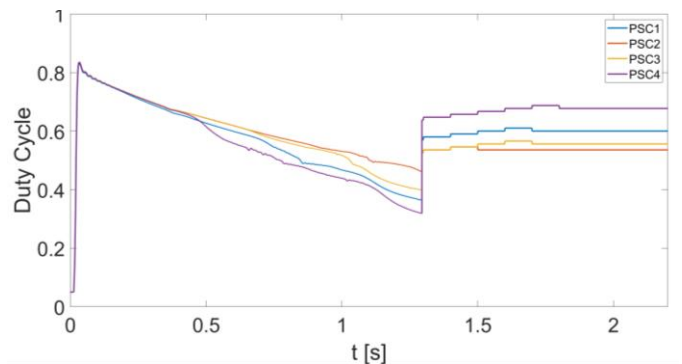
Fig.8. Duty cycles obtained using the proposed algorithm

In Figure 9, motor phase currents are shown for four different PSC conditions. When MPPT moves to the second stage, it is observed that the motor current remains approximately constant or undergoes small changes because the second stage operates in a very narrow area. This situation is evident when examining the change in duty cycles in Figure 8.In fact, this indicates that the efficiency of the MPPT continuous state is high and the tracking efficiency is also high. This is because when the first stage is completed, the maximum PV power has been greatly approached.
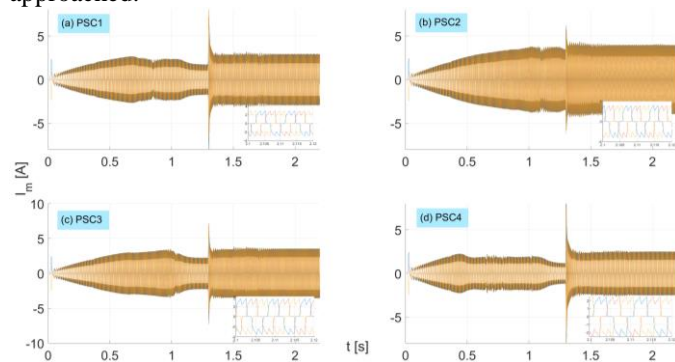
Fig.9. Motor phase currents obtained using the proposed algorithm

Since the proposed algorithm is a two-level hybrid MPPT algorithm, the first level detects the voltage region while the second level provides maximum power. The algorithm used at the second level in this study can be implemented with simple and low-level microcontrollers. More efficient and faster algorithms can be developed at the second level by using artificial intelligence-based, fuzzy-based and optimization-based algorithms. The most important problem here will be the use of complex algorithms that will increase the system cost. Because it will be necessary to use high-level microcontrollers and the system cost will increase. Additionally, it would be very difficult to develop these algorithms for nonlinear load. However, nonlinear loads can be driven more easily by using adaptive MPPT algorithms. In future studies, adaptive MPPT methods that adapt quickly to variable load conditions and have a simple structure can be developed to achieve higher efficiency. In this study, engine speed information was obtained assuming a sensor was used. Nowadays, a lot of research is being done on sensorless controls of BLDC motors. There are effective speed control applications by measuring only current and back-emf information. Therefore, in ongoing studies, a lower-cost system can be obtained by speed detection without using an engine speed sensor. In addition, malfunctions and maintenance costs arising from the speed sensor may be minimal.

V. CONCLUSION

In this study, a hybrid MPPT algorithm was developed for the PV pump system. In this system, BLDC is used as the motor. The output of the PV system is connected to a DC-DC ZETA converter. The converter output creates the input voltage of the inverter. The operation of the PV pump system was examined through simulation in the MATLAB/Simulink environment. The simulation study demonstrated that the proposed hybrid MPPT algorithm works with high efficiency under partial shading conditions. While the lowest MPPT efficiency was 95.66%, the highest efficiency was 99.9%. When the literature is examined, it is seen that the current and voltage information of the PV system is used for MPPT in photovoltaic pump systems using BLDC motors. In addition, system efficiency in PSC cases is also an important research topic. The fact that the proposed MPPT algorithm does not require information about the PV system is a significant advantage. The MPPT algorithm was carried out in two stages, using only motor current and speed information without measuring the current and voltage of the PV system. Thus, it is aimed to reduce the system cost. This study contributes significantly to the literature as a sensorless MPPT technique. However, this algorithm can be further improved. In future studies, especially the two-stage MPPT algorithm will be implemented in a single stage using artificial intelligence techniques. In addition, using artificial intelligence-based methods instead of the modified P&O algorithm used at the second level will significantly increase MPPT performance.

REFERENCES

[1] A. Gundogdu, H. Kizmaz, R. Celikel, M. Yilmaz, 2023. "Speed sensorless Adaptive Power Control for photovoltaic-fed water pump using Extended Kalman–Bucy filter." Energy Reports, Vol.10, 2023, pp.1785-1795.,

[2] R. Celikel, G. Boztas, O. Aydogmus. "A system identification-based MPPT algorithm for solar photovoltaic pumping system under partial shading conditions." Energy Sources, Part A: Recovery, Utilization, and Environmental Effects, Vol. 44, No. 2, 2022, pp. 5199-5214.

[3] R. Kumar, B. Singh. "BLDC motor-driven solar PV array-fed water pumping system employing zeta converter." IEEE Transactions on Industry Applications, Vol.52, No.2, 2016, pp. 2315-2322.

[4] K. Khan, S. Shukla, B. Singh. "Improved performance design realization of a fractional kilowatt induction motor with predictive current control for water pumping." IEEE Transactions on Industry Applications, Vol. 56, No.4, 2020, pp.4575-4587.

[5] G. Boztas, O. Aydogmus, H. Guldemir, "Design and implementation of a high-efficiency low-voltage synchronous reluctance motor." Electrical Engineering, Vol.10, No.2, 2020, pp. 717-725.

[6] R. Antonello, M. Carraro, A. Costabeber, F. Tinazzi, M. Zigliotto, "Energy-efficient autonomous solar water-pumping system for permanent-magnet synchronous motors." IEEE Transactions on Industrial Electronics, Vol.64, No.1, 2016, pp. , 43-51.

[7] R. Kumar, B. Singh. "Solar PV powered-sensorless BLDC motor driven water pump." IET Renewable Power Generation, Vol.13,No.3, 2019, pp.389-398.

[8] R. Kumar, B. Singh. "Single stage solar PV fed brushless DC motor driven water pump." IEEE Journal of Emerging and Selected Topics in Power Electronics, Vol. 5, No 3, 2017, pp.1377-1385.

[9] O. Aydogmus. "Design of a solar motor drive system fed by a direct-connected photovoltaic array." Advances in Electrical and Computer Engineering, Vol.12,No.3, 2012, pp. 53-58.

[10] A. Gupta, Y.K. Chauhan, K. Pachauri. "A comparative investigation of maximum power point tracking methods for solar PV systems." Solar Energy ,Vol.136, 2016, pp.236-253,

[11] T. Esram, P.L. Chapman. "Comparison of photovoltaic array maximum power point tracking techniques," IEEE Trans Energy Conversion, Vol.22, 2007, pp.439-449, 10.1109/TEC.2006.874230.

[12] R. Celikel, A. Gundogdu. "Comparison of PO and INC MPPT methods using FPGA in-the-loop under different radiation conditions. Balkan Journal of Electrical and Computer Engineering, Vol.9, No.22,2021, pp.114-122.

[13] Z. Bi, J. Ma, K.L. Man, J.S. Smith, Y. Yue. H. Wen. "An Enhanced 0.8VOC-Model-Based Global Maximum Power Point Tracking Method for Photovoltaic Systems," IEEE Transactions on Industry Applications, Vol.56, 2020, pp.6825-6834, doi:0.1109/TIA.2020.3019364.

[14] A. A. Kulaksız, R. Akkaya. "A genetic algorithm optimized ANN-based MPPT algorithm for a stand-alone PV system with induction motor drive." Solar Energy, Vol.86, No.9, 2012, pp.2366-2375.

[15] H. Renaudineau, F. Donatantonio, J. Fontchastagner, G. Petrone, G. Spagnuolo, J. P. Martin, S. Pierfederici. "A PSO-based global MPPT technique for distributed PV power generation." IEEE Transactions on Industrial Electronics, Vol.62, No.2, 2014, pp.1047-1058.

[16] S. Mohanty, B. Subudhi, P. K. Ray. A new MPPT design using grey wolf optimization technique for photovoltaic system under partial shading conditions. IEEE Transactions on Sustainable Energy, Vol.7, No.1, 2015, pp.181-188.

[17] M. Kermadi, Z. Salam, J. Ahmed, E.M. Berkouk, "An effective hybrid maximum power point tracker of photovoltaic arrays for complex partial shading conditions," IEEE Transactions on Industrial Electronics, Vol.66, 2018, pp. 6990-7000.

[18] V. Pallavi, R. Gar, P. Mahajan, "Asymmetrical interval type-2 fuzzy logic control based MPPT tuning for PV system under partial shading condition," ISA transactions, Vol. 100, 2020, pp. 251-263,

[19] Z. Zhao, R. Cheng, B. Yan, J. Zhang, Z. Zhang, M. Zhang, L.L. Lai, "A dynamic particles MPPT method for photovoltaic systems under partial shading conditions," Energy Conversion and Management, Vol. 220 , 2020.

[20] Z. Kesilmiş, , M.A. Karabacak, M. Aksoy, "A Novel MPPT Method Based on Inflection Voltages," Journal of Cleaner Production, Vol.266, 2020, pp.121473.

[21] L. Avila, M.D. Paula, M. Trimboli, I. Carluchod, "Deep reinforcement learning approach for MPPT control of partially shaded PV systems in Smart Grids," Applied Soft Computing, Vol.97, 2020, 106711.

[22] K. Punitha, D. Devaraj, S. Sakthivel, "Artificial neural network based modified incremental conductance algorithm for maximum power point tracking in photovoltaic system under partial shading conditions," Energy, Vol.62, 2013, pp.330-340.

[23] M.A. Ziad, N.V. Quynhc, S. Dadfar, H. Nakamuraf, "Variable step size perturb and observe MPPT controller by applying θ-modified krill herd algorithm-sliding mode controller under partially shaded conditions," Journal of Cleaner Production, Vol.271, 2020, 122243.

[24] D. Yousri, T.S. Babu, D. Allam, V. K. Ramachandaramurthy, M.B. Etiba, "A novel chaotic flower pollination algorithm for global maximum power point tracking for photovoltaic system under partial shading conditions," IEEE Access. Vol.7, 2019, pp.121432-121445.

[25] J. Yuan, Z. Zhao, Y. Liu, B. He, L. Wang, B. Xie, Y. Gao, "DMPPT Control of Photovoltaic Microgrid Based on Improved Sparrow Search Algorithm," IEEE Access, Vol.9, 2021, pp.16623-16629.

[26] S. Immad, S. Mekhilef, T. K. Soon, "Maximum Power Point Tracking using Modified Butterfly Optimization Algorithm for Partial Shading, Uniform Shading and Fast Varying Load Conditions," IEEE Transactions on Power Electronics, Vol.36, 2021, pp.5569-5581.

[27] S., Immad, S. Mekhilef, T.K. Soon, "Improved Team Game Optimization Algorithm Based Solar MPPT with Fast Convergence Speed and Fast Response to Load Variations," IEEE Transactions on Industrial Electronics, Vol.68, 2020, pp.7093 –7103.

[28] M. Majad, A.F. Mirza, Q. Ling. "Harris hawk optimization-based MPPT control for PV Systems under Partial Shading Conditions." Journal of Cleaner Production, Vol.27, 2020, 122857.

[29] A. Fathy, R. Hegazy, D. Yousri. "A robust global MPPT to mitigate partial shading of triple-junction solar cell-based system using manta ray foraging optimization algorithm," Solar Energy, Vol.207, 2020, pp.305-316.

[30] A.F. Mirza, M. Mansoor, Q. Ling, B. Yin, M.Y. Javed. "A Salp-Swarm Optimization based MPPT technique for harvesting maximum energy from PV systems under partial shading conditions," Energy Conversion and Management, Vol.209, 2020, 112625.

[31] M. A. Karabacak, Z. Kesilmiş, M. Aksoy, "A novel two-stage MPPT method based on inflection voltages." Energy Sources, Part A: Recovery, Utilization, and Environmental Effects, Vol.44, No.1, 2022, pp.591-612.

[32] M. E. Başoğlu. "An enhanced scanning-based MPPT approach for DMPPT systems." International Journal of Electronics, Vol.105, No.12, 2018, pp.2066-2081.

[33] Y. H. Liu, J. H. Chen, J. W. Huang. "Global maximum power point tracking algorithm for PV systems operating under partially shaded conditions using the segmentation search method." Solar Energy, Vol.103, 2014, pp.350-363.

[34] V. Jately, S. Bhattacharya, B. Azzopardi, A. Montgareuil, J, Joshi, S. Arora.). "Voltage and current reference based MPPT under rapidly changing irradiance and load resistance." IEEE Transactions on Energy Conversion, Vol.36, No.3, 2021, pp.2297-2309.

[35] R. Celikel, M. Yilmaz, A. Gundogdu. "A voltage scanning-based MPPT method for PV power systems under complex partial shading conditions." Renewable Energy, Vol.184, 2022, pp.361-373.

[36] K. Astitva, et al. "Grey Wolf Optimization Inspired Maximum Power Extraction from SPV System for Water Pumping Application." 2022 International Conference for Advancement in Technology (ICONAT). IEEE, 2022.

[37] H. K. V. Gadiraju, V. R. Barry, R. K. Jain. "Improved Performance of PV Water Pumping System Using Dynamic Reconfiguration Algorithm Under Partial Shading Conditions." CPSS Transactions on Power Electronics and Applications, Vol.7, No.2, 2022, pp.206-215.

[38] M. Kashif, B. Singh. "Modified Active-Power MRAS Based Adaptive Control With Reduced Sensors for PMSM Operated Solar Water Pump." IEEE Transactions on Energy Conversion, Vol.38, No.1, 2022, pp.38-52.

[39] S. G. Malla, P. Malla, J. M. R. Malla, R. Singla, P. Choudekar, R. Koilada, M. K. Sahu. ""Whale optimization algorithm for PV based water pumping system driven by BLDC motor using sliding mode controller." IEEE Journal of Emerging and Selected Topics in Power Electronics, Vol.10, No.4, 2022, pp.4832-4844.

[40] A. Mudlapur, V. V. Ramana, R. V. Damodaran, V. Balasubramanian, S. Mishra. Effect of partial shading on PV fed induction motor water pumping systems. IEEE Transactions on Energy Conversion, Vol.34, No.1, 2018, pp.530-539.

[41] A. Ammar, K. Hamraoui, M. Belguellaoui, A. Kheldoun. "Performance enhancement of photovoltaic water pumping system based on BLDC Motor under partial shading condition." Engineering Proceedings, Vol.14, No.1, 2022.

[42] J. Arfaoui, H. Rezk, M. Al-Dhaifallah, F. Elyes, M. Abdelkader. "Numerical performance evaluation of solar photovoltaic water pumping system under partial shading condition using modern optimization.",- Mathematics, Vol.7, No.11, 2019, pp. 1123.

[43] X. Li, H. Wen, Y. Hu, L. Jiang. "Drift-free current sensorless MPPT algorithm in photovoltaic systems." Solar Energy, Vol.177, 2019, pp.118-126.

[44] H. Phillips-Brenes, R. Pereira-Arroyo, R. Rímolo-Donadío, M. Muñoz-Arias. "Current-Sensorless Control Strategy for the MPPT of a PV Cell: An Energy-Based Approach." International Journal of Photoenergy, 2022.

[45] D. Cortes-Vega, H. Alazki, J. L. Rullan-Lara. "Current Sensorless MPPT Control for PV Systems Based on Robust Observer." Applied Sciences, Vol.12, No.9, 2022, pp.4360.

[46] É. A. Tonolo, J. W. M. Soares, E. F. R. Romaneli, A. A. Badin.Current "Sensorless MPPT with a CCM Interleaved Boost Converter for Renewable Energy System." IEEE Transactions on Power Electronics, Vol.37, No.9, 2022, pp.11296-11304.

BIOGRAPHIES

Yunus Atagün was born in 1993. He received the B.S. degrees in mechatronic engineering from the University of Firat,Elazig,Turkey.He is studying for his master's deegre in mechatronic engineering at Firat University.His research interests include renewable energy and MPPT.

Resat Celikel was born in 1980. He received the B.S., M.S., and Ph.D. degrees from Firat University, Elazig, Turkey. He has been an Associate Professor with Firat University. His current research interests include BLDC motors, flywheel energy storage, FPGA, renewable energy, and MPPT.

Multimodal Emotion Recognition using Bi-LG-GCN for MELD Dataset

Hussein Farooq Tayeb Al-Saadawi, Resul Daş

Abstract—Emotion recognition through multimodal data can significantly enhance human interactions. We introduce the Multimodal Emotion Lines Dataset (MELD) and present a novel method, Bi-LG-GNN, which capitalizes on diverse emotion labeling across text, audio, and visuals. This research emphasizes detecting concealed affective computing states within textual and audio data, contributing to emotion recognition and sentiment analysis. The quality and consistency of the data undergo improvements via meticulous pre-processing techniques, which encompass noise elimination, normalization, and linguistic adjustments. These interventions specifically aim to address linguistic discrepancies and reduce background noise in the discourse. To extract salient features, we employ the Kernel Principal Component Analysis (K-PCA), aiming to derive meaningful attributes from each modality and to encode labels for array values. We introduce a Bi-LG-GCN-based architecture meticulously designed for multimodal emotion recognition, which effectively amalgamates data from diverse modalities. This Bi-LG-GCN system interprets the enhanced multi-modal data representations, producing synthetic samples that capture multimodal relationships. As a result, it allows for precise emotion recognition and prediction on multimodal datasets. When tested on the MELD dataset, the results were remarkable, showing accuracy (80%), F1-score (81%), precision (81%), and recall (81%). The implemented pre-processing and feature extraction phases substantially elevate the quality and discrimination of input representations. Our Bi-LG-GCN approach, accentuated by its ability to synthesize multimodal data, surpasses existing methods, showcasing its significant practical value.

Index Terms—Bimodal emotion recognition, text and speech recognition, Multimodal Emotion Lines Dataset (MELD), Bilateral gradient graph convolutional network (Bi-LG-GCN), Affective computing identification.

I. INTRODUCTION

Emotions are central to how humans interact. With more multimedia data available, our understanding of computer recognition of these emotions has greatly improved. Expression of emotions, whether written or spoken, deeply influences behavior and markedly affects decision-making, learning, and cognitive functions. In contemporary periods, the domain of artificial intelligence has strived to develop platforms proficient in comprehending and expressing emotions, progress majorly influenced by innovations in affective computing. Audio and written content integration has evolved, enhancing

user experience and comprehension. As a result, dealing with singular modes of texts without this combination has become even more tedious and intricate [1]. The integration of audio and written content has improved, enhancing user comprehension and experience. Consequently, handling text without this combination has become more cumbersome and complex, underscoring the importance of bimodal content [2]. Challenges persist in communication via speech, including variability in the precision of emotional speech detection and a shortage of foundational understanding centered on emotions. Such dimensions are quintessential for articulating intent, interpreting social cues, and nurturing profound connections. Traditionally, emotion discernment predominantly relied upon facial lines [3]. Humans employ many means for emotional conveyance, encompassing gestures, postural indications, tonal variations, and facial nuances. A comprehensive approach that contemplates these diverse indicators is essential for precise emotion discernment and assimilation [4]. Stemming from this understanding, multimodal emotion recognition has emerged as a captivating field. It involves aggregating and examining emotional indicators from multiple channels. A more holistic and accurate representation of human emotions can be achieved by amalgamating information from varied sources, such as facial cues, vocal rhythms, physical gestures, and physiological responses. This interdisciplinary domain, converging research from affective computing, voice analytics, computer visualizations, and machine intelligence, endeavors to formulate algorithms and models adept at adeptly processing and interpreting multimodal emotional stimuli [5].

Improving human-computer interaction is an important factor behind multimodal emotion detection. To provide more individualized and interesting encounters, emotionally intelligent systems can modify their behavior and replies according to the user's emotional state [6]. Similarly, multimodal emotion recognition may be used in healthcare applications to assess a patient's emotional health and provide important insights for individualized care and treatment. Multimodal emotion recognition faces a variety of difficulties. It is a challenging effort to integrate and synchronize data from several modalities, each with distinct properties and noise sources [7]. Deep learning algorithms have been developed to mix data from many modalities efficiently. Because emotional displays can vary greatly across people, creating solid models that can generalize across diverse people and cultural backgrounds is another difficulty. Further obstacles come from the subjectivity and context-dependence of emotions, which individual experiences may impact.

While GCNs, or Graph Convolutional Networks, have proven

Hussein Farooq Tayeb Al-Saadawi is with the Department of Software Engineering, Technology Faculty, Firat University, Elazig, 23119 TÜRKİYE. Email: husseinftayeb@gmail.com

Resul Daş is with the Department of Software Engineering, Technology Faculty, Firat University, Elazig, 23119 TÜRKİYE. Email: rdas@frat.edu.tr

indispensable for visually understanding intricate systems through graphs, the importance of textual data in human interactions cannot be overlooked, especially in the realm of sentiment analysis. Graphs, as outlined by the rising popularity of infographics and knowledge graphs, can convey information efficiently[8]. On the other hand, textual data plays a significant role in sentiment analysis, as evidenced by the work of Mucahit Pinar Savci et al.[9]. Their research, which focused on evaluating deep learning and machine learning methods using e-commerce corpora in different languages, emphasized the power of pre-trained language models in discerning various sentiments. As for emotion extraction from speech, Pulatov et al., [10] present a notable advancement by employing dual feature extraction techniques, combining CNNs, MFCC, and Speech2Vec. While their methodology displays impressive accuracy enhancements on two renowned datasets, the omission of 10-fold cross-validation might prompt questions on generalizability. Nevertheless, their findings, suggesting the potential integration of diverse features and modalities, significantly enrich the current understanding of Speech Emotion Recognition research. Therefore, while graphical representation simplifies our comprehension of complex systems, textual data analysis remains crucial for understanding human emotions and intentions. Future studies might explore how integrating these two domains—graphical and textual—can bring more holistic insights across various sectors. Multimodal emotion identification has a lot of potential despite the difficulties in several areas. It may benefit from affective computing, human-robot interaction, virtual reality, gaming, market research, and psychology. Researchers and practitioners may design intelligent systems that are more sympathetic, intuitive, and responsive by analyzing and interpreting the intricate interplay of emotional signals [11]. There are many different ways that people might express and interpret their emotions. It tries to give a comprehensive knowledge of human emotions by including a variety of modalities. By developing emotionally intelligent systems, the discipline has the potential to transform human-computer interaction, healthcare, and other industries completely. We proposed a bi-lateral gradient graph convolutional network (Bi-LG-GCN) method to recognize the emotions of human beings.

A. Contributions

- We provide the MELD dataset, which was utilized for accurate emotion categorization on both textual and audio modalities.
- To improve the multimodal dataset's quality and consistency, we use pre-processing techniques (linguistic and normalization).
- We apply K-PCA as a feature extraction method to get specific characteristics from each modality.
- To assess the effectiveness of our suggested strategy, we carry out thorough metrics such as accuracy, precision, recall, and f1-score using the multimodal dataset.

The following sections of the paper are written as follows: Section 2 contains reviews of the relevant literature. Section 3 explains the proposed approach, Section 4 discusses the findings, and Section 5 presents the conclusion.

II. BACKGROUND

The field of research into understanding human emotions is rapidly growing and attracting the attention of both industries as it delves deep beyond facial expressions and body language to explore how emotions resonate within the nuances of our spoken words. Emotion, an intricate aspect of human communication, is pivotal in conveying sentiments, thoughts, and intentions. Our speech encodes information through elements like text meaning, speech rate, rhythm, pitch, volume, voice quality, articulation, duration, and inflection. Accordingly, the research objectives outlined of [12], a novel multi-modal approach for recognizing human emotions was introduced. The proposed method employed a deep learning architecture, specifically the "3D-Convolutional Neural Network (3D-CNN)," to extract spatiotemporal features from both electroencephalogram (EEG) signals and facial recordings. Then, a mix of data enhancement and ensemble learning approaches was presented to obtain the final fusion projections. The suggested scheme's multi-modality fusion was accomplished using data and score fusion approaches. The "3D-CNN output characteristics of the face chunks were then classified using the Support Vector Machine (SVM) classifier". In a parallel vein, wi and Liang [13] proposed a fusion-based approach to detect emotions in affective speech. This method integrated acoustic-prosodic information and semantic labels with multiple classifiers.

The text serves as a cornerstone in emotion recognition, crucial for enhancing human interaction within affective computing systems across languages. Mucahit Soylu et al.,[14] delved into attitude markers (AMs) in academic writing by English and Turkish authors. They identified 'significance' as a key functional category and 'adjective' as the top form. Their innovative approach, incorporating Java for data cleaning and a radial knowledge graph for visualization, offers promising avenues for emotion recognition in diverse linguistic landscapes. A key component of their methodology was the MDT technique, which is responsible for selecting the most suitable classifier based on recognition confidence. This work, although focused primarily on audio and semantic information, highlighted the effectiveness of using multimodal data and sophisticated classifiers for enhanced emotion recognition. They emphasized the synergistic effects of combining distinct data types, achieving an impressive recognition accuracy of up to 85.79% when considering the personality traits of speakers. Building on the exploration of acoustic features, Jin et al. [15] centered on the fusion of features from both acoustic and lexical levels to enhance emotion recognition in speech. At the acoustic level, a gamut of features, including intensity, F0, and others, was extracted, with novel representations such as Gaussian supervectors introduced. The lexical dimension saw the proposal of the "emotion vector" (eVector) feature, which was predicated on emotion lexicons, giving words weights based on their emotion-expressive inclination. Applied to

the USC-IEMOCAP database, the study demonstrated that the late fusion of both these feature realms culminated in a four-class emotion recognition accuracy of 69.2%. This further solidified the potential of combining various feature sets to hone the precision of emotion recognition, marking it as a noteworthy contribution to the field. The researchers in [16] introduced a new approach for multimodal emotion recognition utilizing raw waveforms and cross-modal attention mechanisms. By integrating raw audio processing through a one-dimensional convolutional model and establishing a cross-modal attention network between audio and text features, they optimized their emotion detection system. This approach showed that features extracted from raw audio, when coupled with a cross-modal attention mechanism, can effectively capture the interplay between audio and textual cues, enhancing emotion classification capabilities.

The investigators of [17] presented an innovative emotion detection system according to various expressions and other modalities of the face, Galvanic Skin Response (GSR), and electroencephalogram (EEG). Emotional Analysis Databases for variable numbers of emotional classes, four on a median, including angry, disgusted, fearful, joyful, neutral, sad, and confused [18]. In natural deceptive facial expressions, the suggested model demonstrated the benefit of detecting the proper state of emotions. In the study by [19], a method for multi-modal emotion detection was introduced, which harnesses speech-visual correlation features. This approach utilized two-dimensional convolutional neural networks (2D-CNN) to extract speech characteristics and 3D-CNN for visual attributes. During multi-modal fusion, a feature correlation analysis technique was employed to analyze both audio and visual data. Results from experiments performed on diverse datasets show that the approach is comparable to other cutting-edge algorithms in terms of recognition effectiveness. The focus is on deploying deep learning methodologies to discern underlying emotional tones in textual data. A notable advancement in this domain is the Emo2Vec model, which, when integrated with Logistic Regression and GloVe, demonstrates competitive performance in emotion detection. Ragheb et al. have made a significant contribution by developing a learning-based model that recognizes six emotions as described by Paul Ekman; their method employs a two-phase approach of encoding and classification, utilizing tokenization, encoders, and Bi-LSTM units trained via average stochastic gradient descent [20]

According to Lian et al., [21], they proposed "domain adversarial neural networks (DANN) for emotion detection. The main objective was to forecast emotion categories and develop a common representation where speaker's identity could not be discriminated". The depictions of different speakers were closer together thanks to their use of this technique. Using unlabeled data during the training phase, they reduced the effect of low-resource sample collections. The researchers of [22] introduced a deep learning (DL) based method for accessing and combining text and perceptual data to classify emotions. To extract acoustic characteristics from unprocessed audio, they added a DCNN layer after using a SincNet layer based on a customizable sinc value with band-

pass filtering. When compared to performing convergence over the raw voice signal, the method develops filter banks modified for the recognition of emotions and provides superior aspects. To infer N-gram level association on hidden models derived from the Bi-RNN, they used two parallel streams for text analysis "(a DCNN and a Bidirectional RNN followed by a DCNN)" with cross attentiveness. The researchers of [23] demonstrated M3ER, a learning-based approach for emotion identification from several input modalities. Their system incorporated inputs from many co-occurring models and is more resistant to any of the sensors are noisy various approaches than previous methods. "M3ER model an innovative, data-driven multiplicative fusion strategy" for combining the models, which learns to enhance the extra accurate cues. M3ER was resistant to sensor noise by incorporating a check step that used Canonical Correlational Assessment to distinguish between ineffective and effective models.

Liu et al., in their study [24], proposed utilizing deep canonical correlation analysis (DCCA) for recognizing emotions across multiple modalities. DCCA primarily functions by independently transforming each modality and then correlating the varied modalities into a unified hyperspace, adhering to predefined canonical statistical constraints. The efficacy of DCCA was assessed across five different datasets. The research results revealed that DCCA obtained state-of-the-art detection accuracy rates across all datasets. Mittal et al. introduced "EmotiCon," a learning-based system designed for identifying perceived emotions from photos and video clips by considering context [25]. This approach incorporates three different perspectives of context for emotion detection. The initial interpretation was based on the use of various senses for emotion identification. In the second analysis, they obtained semantic information from the input image and used a self-attention-based CNN" to encode the information. At last, depth maps were employed to simulate the third interpretation, which was connected to socio-dynamic interactions and agent proximity. They showed the effectiveness of their network by running tests on datasets. The researchers [26] suggested an innovative cross-representation speech model for detecting emotions on "wav2vec 2.0 voice characteristics and also trained a CNN-based model to distinguish emotions from text data extracted with Transformer-based models. A score fusion method was used to merge the speech-based and text-based findings".Authors of [27] developed a method for multimodal emotion identification named "deep generalized canonical correlation analysis with an attention mechanism (DGCCA-AM)." The model established multimodal adaptive fusion with a focus system, extending the usual "canonical correlation analysis (CCA) from two modalities" to arbitrarily numerous modalities. According to Zhang [28] suggested a deep automated encoder-based expression-EEG interaction multi-modal recognition of emotions approach. In the beginning, a decision tree was used as a feature-based selection approach. The solution vector values were then examined to establish the expression classification for the test sample based on the facial expression characteristics detected by sparse

representation. The bimodal deep automated encoder was then used to combine the EEG. The 3rd layer of BDAE extracts characteristics for the supervised training phase. To complete the categorization, the LIBSVM classifier was employed.

An approach to identifying age, gender, and state of mind from audio was developed by Zaman et al. [29]. All audio recordings in our system were transformed into 20 statistical attributes, and the transformed numerical dataset was utilized to build several prediction models in order to achieve the goal. "Kneatest neighbors (KNN), XGBoost, AdaBoost, and Decision Tree, Artificial neural networks (ANN), Naive Bayes, and Support vector machine (SVM)." The authors of I will schedule some time for us to connect.[30] suggested an innovative emotion-relevant crucial subnetwork identification method and examined 3 EEG functional connectivity network features. On three open emotion EEG databases, the identifying capacity of the EEG connectivity characteristics in emotion detection was examined. By single-channel analysis, the strength feature surpassed the state-of-the-art differential entropy feature in the accuracy of classification. The findings from the study demonstrated that each of the five emotions had different functional conjunction characteristics. The researchers [31] proposed a deep multi-task learning system that analyzed emotions simultaneously. A video's multi-modal inputs provide unique and distinct information, and they typically do not contribute equally to decision-making. They suggested a context-level inter-modal attention method for evaluating an utterance's sentiment and conveying emotions at the same time. They tested the suggested method for multi-modal sentiment and evaluation of emotions using the CMU-MOSEI database.

According to Nemati et al. [32] they suggested an integrated multimodal data fusion approach in which the audio and visual models were fused using a latent space linear map, and their presented characteristics into the cross-modal space were fused with the textual modality using a Dempster-Shafer (DS) theory-based evidential fusion approach.." The suggested technique outperformed "both decision-level and non-latent space fusion approaches when tested on DEAP dataset." The HED dataset was created by Fang et al. of [33] as a sizable multimodal emotion dataset to aid in the emotion detection challenge. The method for multimodal emotion recognition was then suggested. The "HED" dataset was far bigger than previous datasets and comprises emotion-aligned face, body, and text samples that express many emotions, including happiness, sadness, disgust, anger, and fear. The researchers of [34] utilized Muse-CaR, a vehicle review database, to make continuous emotional predictions. To do this, they initially extract handmade characteristics and complex depictions from several modes. They next used the "Long Short-Term Memory (LSTM) recurrent neural network and the self-attention system to represent the sequence's complicated temporal relationships. The Concordance Correlation Coefficient (CCC) loss was used to direct the model's learning of local fluctuations as well as the global trend of emotion". At last, two fusion procedures, early fusion and late fusion, were used to improve the model's

performance even more by complementing information from various modalities.

To enhance the efficiency of the emotional identification framework, researchers presented a multimodal emotion detection model based on voice and text [35]. Additionally, the study confirmed that the intersection of sentiment analysis of textual data and the domain of artificial intelligence yields effective outcomes for classification and prediction. Various neural network architectures, including CNN, LSTM, and GRU, have demonstrated their efficacy in this regard [36]. To learn acoustic emotion features, "CNN and LSTM (long short-term memory) were combined in the form of binary channels; in the meantime, an effective Bi-LSTM (bidirectional long short-term memory) network" was used to record textual elements. In addition, a Deep Neural Network (DNN) was employed to classify and gain knowledge of the fusion characteristics. The results of both voice and text emotion analysis were used to establish the final emotional state. The authors of [37] introduced the Visual Aspects Attention Network, or VistaNet, which integrates text and visual elements. They demonstrated that, in many situations, visuals support text in emotion identification, emphasizing significant elements of an entity rather than conveying emotions independent of the text. As a result, rather than using visual data as features, VistaNet uses visual information as alignment to highlight the relevant phrases in a text using attention.

III. METHODOLOGY

Leveraging bimodal datasets in affective computing is gaining traction due to its ability to enhance human inter-actions and multiple use cases. Discerning emotions with multimodal information significantly elevates the caliber of human engagements. This approach is drawing widespread attention and is under exploration in various domains. By amalgamating details from sources such as facial cues, vocal nuances, gestures, and physiological indicators, multimodal emotion detection offers a deeper understanding of emotional states. This is particularly salient in areas like healthcare, gaming, virtual reality, and human-machine interfaces [38]. We compiled the MELD dataset for this specific emotion detection purpose. Data preprocessing was executed with normalization techniques and linguistic methodologies. Kernel Principal Component Analysis (K-PCA) was introduced for feature derivation. Subsequently, we employed the proposed Bi-Lateral Gradient Graphical Conventional Network (Bi-LG-GCN) algorithm for emotion discernment. The results were assessed based on metrics including accuracy, precision, recall, f1-score, Mean Squared Error (MSE), and Mean Absolute Error (MAE). The comprehensive methodological approach is illustrated in Figure 1.

A. Data collection

In our daily interactions, emotions are frequently communicated and understood through a mix of signals from various modalities. Figure 2 provides a glimpse into multimodal
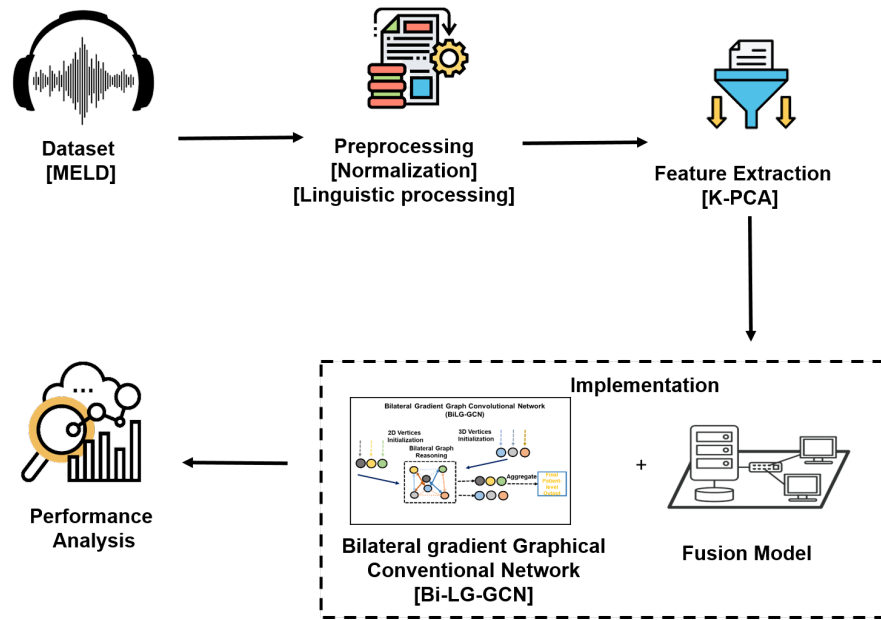
Fig. 1. Multimodal Emotion Recognition using Bi-LG-GCN system

databases that accumulate both auditory and textual information. Given the significance of reliable data, many researchers have dedicated efforts to identify nuanced emotions, be it manifestly or in more subtle forms. These feelings typically originate from three main channels: text, voice, and visuals. As we embark on this data-gathering phase, it's pivotal to pinpoint the specific type of data to collect and the sources from which they'll be procured. The method of data collection can differ based on the application's nature [8]. A prime illustration of this is the MELD dataset, which was crafted by enhancing the core affective computing dataset.
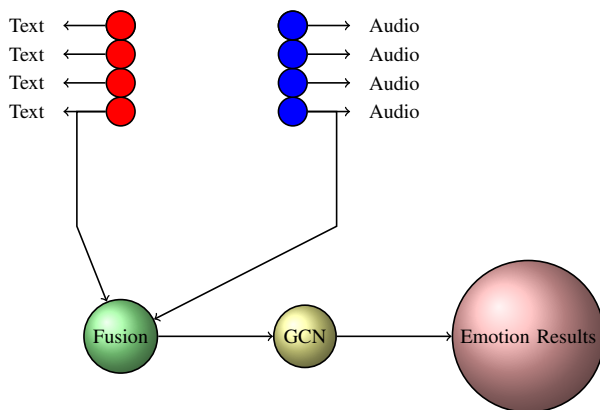
Fig. 2. Design for Combining Multiple Text and Audio Datasets

The MELD was developed by improving and expanding upon the original Emotion Lines dataset. This multimodal dataset includes audio and visual media and text and consists of the same conversation examples found in Emotion Lines. For the purpose of multimodal emotion identification, we only employ the text and audio modalities. The dataset makes available more than 1400 conversations and 13000 utterances

from the Friends TV series. The discussions included a number of speakers. Each remark in a discourse is given an identity according to one of the seven emotions: fear, anger, surprise, sorrow, neutral, disgust, and joy. Additionally, the dataset annotates each utterance's emotion (positive, negative, and neutral). The dataset was collected from (https://www.kaggle.com/datasets/zaber666/meld-dataset).

B. Data preprocessing

Once the data has been collected, the primary task is to refine it for training the Bi-LG-GCN. This refinement may require feature extraction or modifications to account for variations in speaker attributes or recording quality. Such adjustments are crucial, particularly when dealing with datasets comprising both text and audio, to guarantee consistent normalization and effective language processing.

1) Normalization: Normalization describes standardizing and modifying input data from numerous modalities (text input, voice) to a single scale or range. This approach tries to eliminate differences and disparities between modalities, allowing for optimal emotional information integration and comparison. By normalizing the data, information acquired from diverse modalities may be treated similarly and merged in a meaningful way. This normalization process improves the accuracy and reliability of the emotion detection system, allowing for more robust and precise recognition and interpretation of human emotions across many modalities.

2) Linguistic processing: Linguistic processing is the computerized examination and interpretation of linguistic information with the purpose of identifying and detecting emotions in a multimodal environment. Enhancing the durability and precision of identifying emotional systems entails synthesizing emotional information from many language modalities. To evaluate linguistic elements like emotions, semantic content,

and structural patterns, this discipline utilizes techniques from Machine learning, AI, and the processing of natural language. The objective is to enhance human emotion interpretation and processing across several modalities, enabling more precise and thorough emotion detection[39].

C. Feature extraction using Kernel Principle Component Analysis (K-PCA)

Feature extraction is the process of extracting significant features from large amounts of data. It involves evaluating many modalities and translating raw input signals into compact and useful summaries that incorporate relevant emotional cues. These retrieved properties are input for machine learning algorithms to classify emotions. In our work, we proposed Kernel Principle Component Analysis (K-PCA) for feature extraction. For reducing the dimension of vast quantities of data, PCA is a popular multimodal estimate technique. Typically, dimensionality reduction is done by randomly selecting the linear relationship between the parameters. However, as was previously said, conventional PCA offers linear dimensional reduction. For mapping a non-linear process in a data set, KPCA is still a more effective method. Contrary to other non-linear techniques, the ability of the kernel algorithm to run without any non-linear optimization is essential. This approach includes altering the input variables and using them as independent PC parameters. Kaiser-Meyer-Olkin (KMO) [40] is one of the most often used statistics for determining the amount of data in any factor analysis (FA), a quick explanation of the procedure to establish KPCA for feature extraction is provided with Eq. 1.

$$KMO = \frac{\sum \sum q_{ji}^2}{\sum \sum q_{ji}^2 + \sum \sum b_{ji}^2} \tag{1}$$

Where q_{ji} is the correlation value between variables j and i, and b_{ji} is their partial correlation value. Considering that the non-linear change $\phi(w)$ from the initial in sample covariance matrix D in F space should meet the Eq. 3, the projected novel characteristics have zero mean Eq. 2:

$$\frac{1}{M} \sum_{j=1}^{M} \Phi\left(\Phi(W_j)\right) = 0 \tag{2}$$

$$D = \frac{1}{M} \sum_{j=1}^{M} (\phi(W_j) \cdot (\phi(W_j))^S) \tag{3}$$

If the kernel function is formatted as follows Eq. 4:

$$l(W_j, W_i) = \varnothing(W_j)^S \varnothing W_i \tag{4}$$

$$L_{\mathrm{bl}}^2 = \lambda_l M L_{\mathrm{bl}} \tag{5}$$

$$L_{ji} = l(W_j, W_i) \tag{6}$$

Where $\mathbf{b}_l$ is an N-dimensional column vector and $\mathbf{b}_{lj}^{'s}$ as follows in the Eq. 7:

$$\mathbf{b}_l = [b_{l1}, b_{l2}, \ldots, b_{lM}]^S \tag{7}$$

The theory b_{lis} is solvable by the Eq. 8

$$L_{bl} = \lambda_l M_{b_l}, \tag{8}$$

and the corresponding kernel primary components can be determined by the Eq. 9

$$z_l(W) = \varnothing(W)^S \quad u_l = \sum_{j=1}^{M} b_{lj} \cdot \ell(W, W_j) \tag{9}$$

If the predicted dataset $\{\varphi(w_j)\}$ does not have a zero mean, the kernel matrix L can be replaced with the Gram matrix $\tilde{L}$. The Gram matrix is denoted by Eq. 10 :

$$\tilde{L} = L - 1_M L - L1_M + 1_M LM \tag{10}$$

Where 1_M is the $M \times M$ matrix with all components equivalent to $\frac{1}{M}$. The positive aspect of kernel approaches is that it is not essential to calculate $\{\varphi(w_j)\}$ explicitly; the kernel matrix may be rapidly established from the training dataset $\{w_j\}$ in Eq. 11.

$$k(W, Z) = \exp\left(-\frac{1}{2\sigma^2} \|W - Z\|^2\right) \tag{11}$$

In our work, KPCA analyzes and understands human emotions by combining numerous sources of data. KPCA is a dimensionality reduction approach that converts the data provided into a lower-dimensional space while retaining vital details. KPCA can manage nonlinear interactions between modalities by utilizing a kernel function. This method attempts to find the fundamental trends and patterns in multimodal data, enabling more accurate and robust emotion identification across several modalities improving human emotion comprehension and interpretation.

D. Implementation of Bilateral gradient graphical Conventional Network (Bi-LG-GCN)

An innovative method for multimodal emotion identification is the bi-lateral gradient graph convolutional network (Bi-LG-GCN). Emotion recognition is the process of identifying and labeling the emotions that are sent by humans through a variety of modalities such as audio and text. The Bi-LG-GCN needs the advantage of graph convolutional networks (GCNs) to detect the complex relationships between multiple modalities and increase recognition of emotional performance. Figure 3 shows the GCN architecture.

The input data to the Bi-LG-GCN consists of various modalities, each represented as a graph. The nodes in each graph represent the individual samples in the dataset, while the edges among the nodes record the relationships between them. In the context of multimodal emotion detection, the nodes may represent distinct face, voice characteristics, or textual information, and the edges could reflect similarities between them. The Bi-LG-GCN's primary concept is to efficiently capture multimodal interactions by combining local and global information from graphs. A bilateral gradient approach that makes use of the advantages of both local and global graph convolution processes achieves this. While the global graph
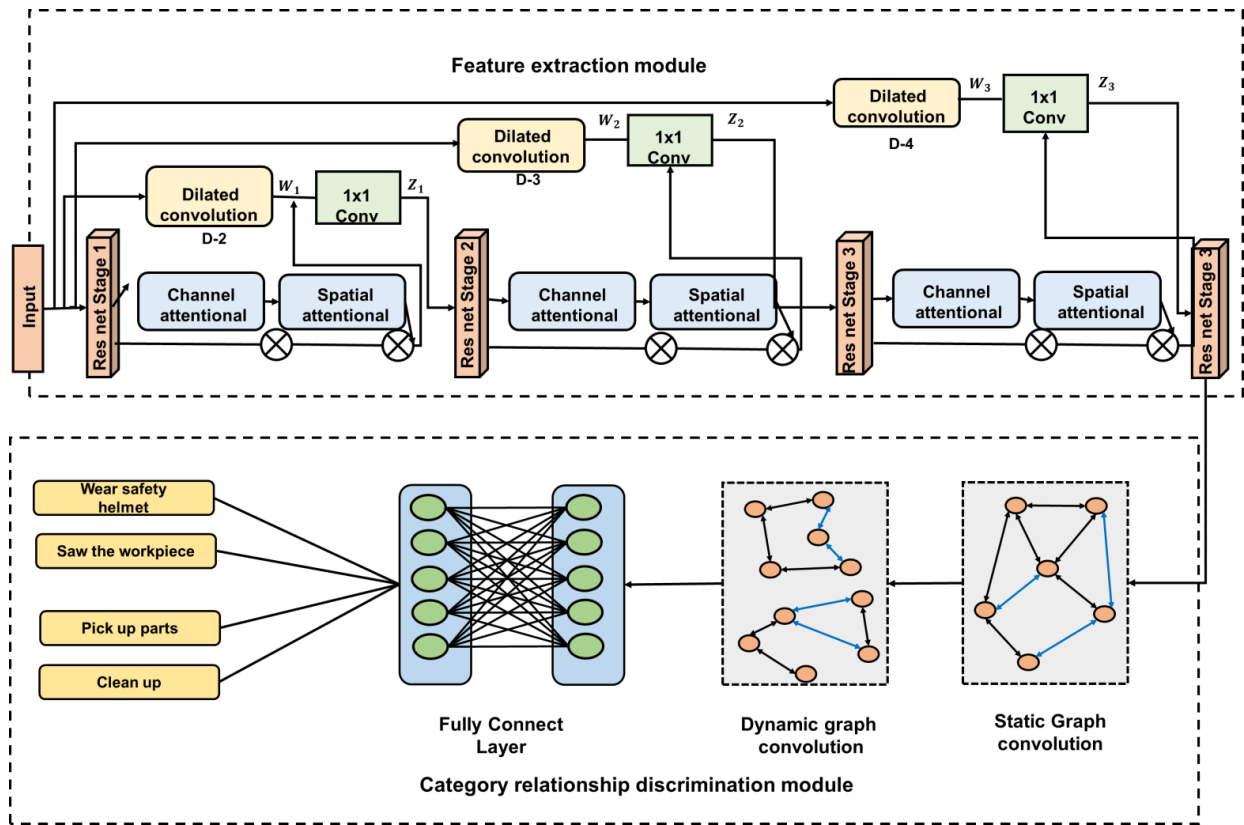
Fig. 3. GCN Architecture

convolution covers the general framework of the network and captures global interactions, the local graph convolution concentrates on gathering information about each node's nearest area.

Bi-LG-GCN can be represented as follows:

Local graph convolution in the Eq. 12:

$$g_j k = \text{ReLU}\left(V_k \cdot Y_j + \sum_{j \in M_j} \alpha_{ji} \cdot Y_i\right) \quad (12)$$

A hidden instance of the ith node after the lth local convolution of the graph layer is denoted by the symbol g_j^k in this equation. The kth local convolution layer's weight matrix is denoted by V_k, while the ith node's surrounding nodes are represented by M_j. The attention-related elements that control the information flow between the nodes are illustrated by the α_{ji}. Global graph convolution in the Eq. 13:

$$g_j h = \text{ReLU}\left(V_h \cdot g_j k + \sum_{j \in w} \beta_{ji} \cdot g_i k\right) \quad (13)$$

After global graph convolution, g_j delivers the hidden representation of the ith node. W is for the set of all nodes in the graph, V_h stands for the weight matrix of the global convolution layer, and β_{ji} stands for the attention coefficients that capture the global connections between nodes. The bilateral gradient technique combines the local and global representations to generate the final node representations. It is achieved using an iterative optimization procedure that updates the attention coefficients α_{ij} and β_{ij} while minimizing the loss function.

Overall, the Bi-LG-GCN offers a strong foundation for multimodal emotion recognition by effectively capturing the intricate interactions between various modalities. The bi-lateral gradient approach combines local neighborhood information and the global graph structure to combine local and global information, improving the accuracy of recognized emotion. By adopting this methodology, not only can the accuracy of emotion classification tools be enhanced, but the broader domain of multimodal emotion recognition could also witness significant advancements.

IV. RESULT EVALUATION

Result evaluation in our context relies on accuracy, precision-recall, and the F1-score metrics. While accuracy offers a general overview, precision and recall prioritize positive predictions. The F1-score strikes a balance. The method employs Bi-LG-GCN for multimodal emotion recognition, assessing performance with these metrics to ensure precise emotion detection across diverse data sources.

A. Experimental setup

We designed our experimental setup based on a combination of both hardware and software configurations tailored for efficient and taxing machine learning applications. The experiments were performed on a Windows 11 operating system.

The chosen programming environment is Python 3.11, which supports the deployment of PyTorch 2.0. We also incorporated the use of Colab Google software to complement the setup. The underlying hardware and software infrastructure ensures the seamless implementation and execution of our technique.

TABLE I
HARDWARE AND SOFTWARE CONFIGURATION

Component	Specification
OS	Windows 11
Processor	11th Gen Intel(R) Core(TM) i7-11370H @ 3.30GHz
Memory (RAM)	16.0 GB
Storage	SSD
Graphics Card	GPU 0 Intel(R) Iris(R) Xe Graphics
	GPU 1 NVIDIA GeForce RTX 3050 Ti Laptop GPU
Network Adapter	Ethernet (Turk Telecom) TTNET 24Mbps
Software	Pytorch 2.0
	Python 3.11
	Colab Google
Total Processing Time	(h, m, s): 00, 21, 31

B. Existing methods

A crucial aspect of classification involves evaluating the models to gauge their precision and dependability in classifying data. Examining the performance metrics helps pinpoint the optimal model for classification assignments. Insights from model training and testing play a pivotal role in evaluating their efficacy. For the performance assessment of classification models, the confusion matrix is a standard tool. This matrix encompasses four components: true positive (TP), true negative (TN), false positive (FP), and false negative (FN). Using the confusion matrix, we can derive various performance metrics like accuracy, precision, recall, F1-score, etc., as illustrated in the color-coded axis above. Model predictions undergo testing and training processes, categorizing outcomes into the following segments: **True Positive** - A successful classification of an actual positive outcome, **False Negative** - An erroneous classification where a positive outcome is predicted as negative, **False Positive** - A misclassification where a negative outcome is predicted as positive, and **True Negative** - A successful classification of an actual negative outcome [10]. To provide a clearer visualization of these categorizations, the following Table II shows how TP, FP, TN, and FN are represented.

TABLE II
REPRESENTATION OF TP, FP, TN, AND FN EXPLANATION MATRIX

	Predicted Positive	Predicted Negative
Actual Positive	True Positive (TP)	False Positive (FP)
Actual Negative	False Negative (FN)	True Negative (TN)

The accuracy, f1-score, precision, and recall metrics are used in this section to assess the performance of the sug-

gested technique Bi-LG-GCN. For calculating accuracy and f1-score, we compare the Bi-LG-GCN with Dialogue Contextual Reasoning Networks (DialogueCRN) [41], Multimodal fused Graph Convolutional Networks (MMGCN), and Graph network-based Multimodal Fusion Technique [41]. For calculating precision and recall, we compare the Bi-LG-GCN with Support Vector Machine (SVM) [33], CentralNet, and Low-rank Multimodal Fusion (LMF).

C. Comparison phase

The degree of accuracy reflects how effectively these systems can identify and categorize emotions. It assesses how well the system can correlate the observed multimodal input data with the relevant emotional states, indicating how well it can decode and identify human emotions. Table III and Figure 4 show the accuracy comparison of the suggested Bi-LG-GCN and alternative procedures. Whereas Dialogue CRN, MMGCN, and Graph MFT only succeed with 65.31, 65.56, and 67.90% accuracy, respectively, the suggested technique Bi-LG-GCN achieves 80% accuracy. The Bi-LG-GCN achieved higher accuracy than the other methods. The accuracy value is expressed in the following Eq. 14.

$$\text{Accuracy} = \frac{\text{True Positives} + \text{True Negatives}}{\text{Total Number of Instances}} \quad (14)$$

TABLE III
COMPARISON OF ACCURACY

Methods	Accuracy (%)
DialogueCRN	65.31
MMGCN	65.56
GraphMFT	67.9
Bi-LG-GCN	80
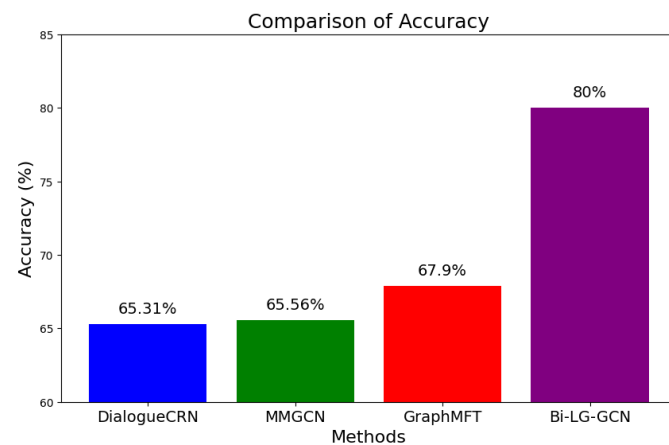
Fig. 4. Accuracy comparison of Bi-LG-GCN with existing methods

The effectiveness of a model that attempts to identify and categorize emotions utilizing different forms of media combines recall and precision into a single measurement that

considers the precision and comprehensiveness of emotion forecasts. The overall ability to capture emotions across several modalities is greater when the F1 score is higher. The F1 score comparison of the suggested and other approaches is displayed in Table IV and Figure 5. Whereas DialogueCRN, MMGCN, and GraphMFT only succeed at 65.34, 65.71, and 68.07%, respectively, the suggested technique Bi-LG-GCN achieves 81% accuracy. Comparing the Bi-LG-GCN method to other conventional approaches provides a higher F1 score. The F1-score with the Eqn. 15 is described below.

$$\text{F1-score} = \frac{2 \times (\text{Precision} \times \text{Recall})}{\text{Precision} + \text{Recall}} \qquad (15)$$

TABLE IV
COMPARISON OF F1-SCORE

Methods	F1-Score (%)
DialogueCRN	65.34
MMGCN	65.71
GraphMFT	68.07
Bi-LG-GCN	81
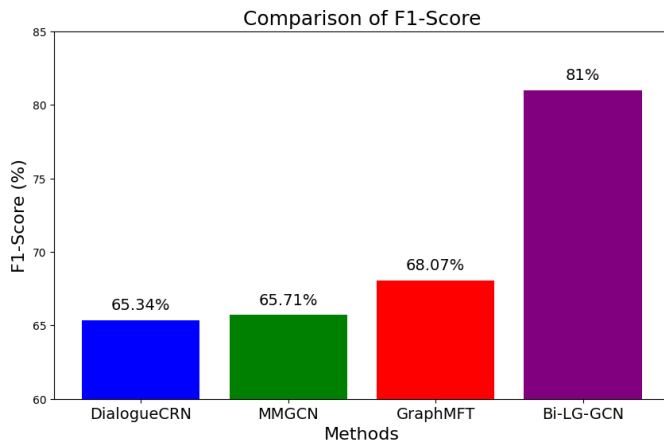
Fig. 5. F1-score comparison of Bi-LG-GCN with existing methods

Precision is the ability to reliably and accurately recognize particular emotions from various signals; it calculates the percentage of emotions that were properly categorized out of all the emotions a system predicts. The system is more accurate at recognizing the desired emotions when the precision is higher since a lower percentage of false positives is shown. Precision is a key indicator of how well multimodal emotion recognition systems execute. Table V and Figure 6 demonstrate the precision comparison between the suggested and alternative procedures. A precision value of 81% is achieved by the recommended technique, Bi-LG-GCN, as opposed to merely 66%, 80%, and 73% for SVM, CentralNet, and LMF. The Bi-LG-GCN concept offers a high precision value when compared to earlier techniques. The following equation is used to determine the precision value with the Eqn. 16.

$$\text{Precision} = \frac{TP}{TP + FP} \qquad (16)$$

TABLE V
COMPARISON OF PRECISION

Methods	Precision (%)
SVM	66
CentralNet	80
LMF	73
Bi-LG-GCN	81
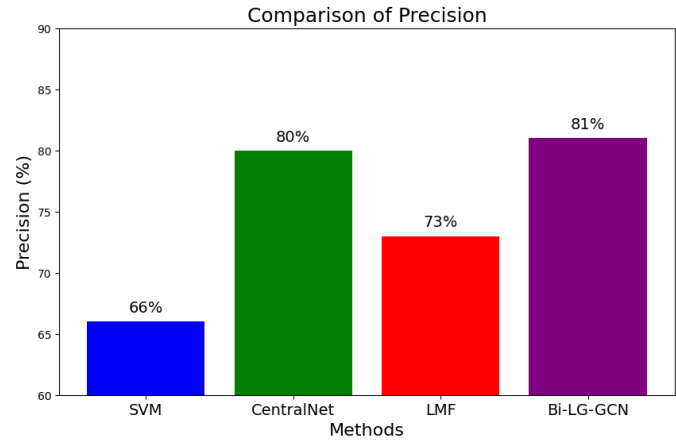
Fig. 6. Precision comparison of Bi-LG-GCN with existing methods

Recall is a characteristic of a system that enables it to identify and classify emotions through multiple modalities consistently. The efficacy of the system in accurately discerning emotions from diverse data inputs is quantified by the ratio of genuinely positive emotions it has identified. Table VI and Figure 7 illustrate the recall distinctions between the proposed and other methods. The suggested method, Bi-LG-GCN, attains a recall score of 81%, which surpasses the scores of 65%, 79%, and 69% achieved by SVM, CentralNet, and LMF respectively. Consequently, Bi-LG-GCN outperforms conventional methods in terms of recall with the Eqn. 17. The ensuing formula determines the recall metric.
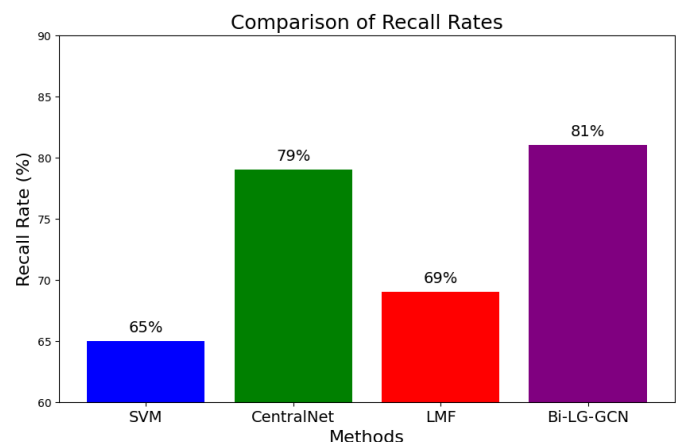
Fig. 7. Recall comparison of Bi-LG-GCN with existing methods

$$\text{Recall} = \frac{TP}{TP + FN} \qquad (17)$$

TABLE VI
COMPARISON OF RECALL

Technique	Recall Rate (%)
SVM	65
CentralNet	79
LMF	69
Bi-LG-GCN	81

In comparing the results, it becomes evident that Bi-LG-GCN demonstrates superior recall capabilities over other evaluated techniques. This dominance in performance reinforces the potential of Bi-LG-GCN for applications that prioritize recall. Furthermore, the detailed evaluation as per the provided formula offers a comprehensive perspective on the recall differences among these methods.

V. CONCLUSION

In our study, we proposed a novel method, a bi-lateral gradient graph convolutional network (Bi-LG-GCN) for multimodal emotion recognition. To recognize multimodal emotions using Bi-LG-GNN, we collected the MELD dataset using textual and audio modalities. And applied linguistic and normalization pre-processing methods to improve the standard and standardization of both datasets. As a feature extraction technique, we used K-PCA to extract certain traits from each modality. The experiment is done on various parameters such as "accuracy (80%), precision (81%), recall (81%), F1-score (81%)" using Bi-LG-GCN for the MELD dataset. Several existing methods were used in the comparing phase. The experiment showed our proposed Bi-LG-GCN method performed efficiently when compared to earlier techniques. Its performance may be impacted by the quantity and caliber of multimodal input, which may result in unreliable emotion predictions. The approach may also have trouble generalizing to various cultural and linguistic environments, which makes it challenging to use in real-world situations involving a range of emotional expressions. For better user experiences, more studies can examine real-time emotion identification, cross-domain generalization, and its incorporation into virtual assistants and emotion-aware systems.

REFERENCES

[1] P. Savci and B. Das, "Comparison of pre-trained language models in terms of carbon emissions, time and accuracy in multi-label text classification using AutoML," *Heliyon*, vol. 9, no. 5, p. e15670, 2023-05-01. [Online]. Available: https://www.sciencedirect.com/science/article/pii/S2405844023028773

[2] M. Aydogan, "A hybrid deep neural network-based automated diagnosis system using x-ray images and clinical findings," *International Journal of Imaging Systems and Technology*, vol. 33, no. 4, pp. 1368–1382, 2023, _eprint: https://onlinelibrary.wiley.com/doi/pdf/10.1002/ima.22856. [Online]. Available: https://onlinelibrary.wiley.com/doi/abs/10.1002/ima.22856

[3] D. Dupré, E. G. Krumhuber, D. Küster, and G. J. McKeown, "A performance comparison of eight commercially available automatic classifiers for facial affect recognition," *PLOS ONE*, vol. 15, no. 4, p. e0231968, 2020, publisher: Public Library of Science. [Online]. Available: https://journals.plos.org/plosone/article?id=10.1371/journal.pone.0231968

[4] E. Cameron and M. Green, *Making Sense of Change Management: A Complete Guide to the Models, Tools and Techniques of Organizational Change*. Kogan Page Publishers, 2019. [Online]. Available: https://www.example.com/your-book-url

[5] W. Zehra, A. R. Javed, Z. Jalil, H. U. Khan, and T. R. Gadekallu, "Cross corpus multi-lingual speech emotion recognition using ensemble learning," *Complex & Intelligent Systems*, vol. 7, no. 4, pp. 1845–1854, 2021. [Online]. Available: https://doi.org/10.1007/s40747-020-00250-4

[6] A survey of emotion recognition methods with emphasis on e-learning environments | journal of network and computer applications. [Online]. Available: https://dl.acm.org/doi/10.1016/j.jnca.2019.102423

[7] S. K. Yadav, K. Tiwari, H. M. Pandey, and S. A. Akbar, "A review of multimodal human activity recognition with special emphasis on classification, applications, challenges and future directions," *Knowledge-Based Systems*, vol. 223, p. 106970, 2021. [Online]. Available: https://www.sciencedirect.com/science/article/pii/S0950705121002331

[8] R. Das and M. Soylu, "A key review on graph data science: The power of graphs in scientific studies," *Chemometrics and Intelligent Laboratory Systems*, vol. 240, p. 104896, 2023-09-15. [Online]. Available: https://www.sciencedirect.com/science/article/pii/S0169743923001466

[9] P. Savci and B. Das, "Prediction of the customers' interests using sentiment analysis in e-commerce data for comparison of arabic, english, and turkish languages," *Journal of King Saud University - Computer and Information Sciences*, vol. 35, no. 3, pp. 227–237, 2023-03-01. [Online]. Available: https://www.sciencedirect.com/science/article/pii/S131915782300054X

[10] I. Pulatov, R. Oteniyazov, F. Makhmudov, and Y.-I. Cho, "Enhancing speech emotion recognition using dual feature extraction encoders," *Sensors*, vol. 23, no. 14, p. 6640, 2023-01, number: 14 Publisher: Multidisciplinary Digital Publishing Institute. [Online]. Available: https://www.mdpi.com/1424-8220/23/14/6640

[11] M. Egger, M. Ley, and S. Hanke, "Emotion recognition from physiological signal analysis: A review," *Electronic Notes in Theoretical Computer Science*, vol. 343, pp. 35–55, 2019. [Online]. Available: https://www.sciencedirect.com/science/article/pii/S157106611930009X

[12] E. S. Salama, R. A. El-Khoribi, M. E. Shoman, and M. A. W. Shalaby, "A 3d-convolutional neural network framework with ensemble learning techniques for multi-modal emotion recognition," *Egyptian Informatics Journal*, vol. 22, no. 2, pp. 167–176, 2021. [Online]. Available: https://www.sciencedirect.com/science/article/pii/S1110866520301389

[13] C.-H. Wu and W.-B. Liang, "Emotion recognition of affective speech based on multiple classifiers using acoustic-prosodic information and semantic labels," *T. Affective Computing*, vol. 2, pp. 10–21, 2011. [Online]. Available: https://ieeexplore.ieee.org/document/5674019

[14] M. Soylu, A. Soylu, and R. Das, "A new approach to recognizing the use of attitude markers by authors of academic journal articles," *Expert Systems with Applications*, vol. 230, p. 120538, 2023-11. [Online]. Available: https://linkinghub.elsevier.com/retrieve/pii/S0957417423010400

[15] Speech emotion recognition with acoustic and lexical features. [Online]. Available: https://ieeexplore.ieee.org/abstract/document/7178872/

[16] K. D. N. and A. Patil, "Multimodal emotion recognition using cross-modal attention and 1d convolutional neural networks," in *Interspeech 2020*. ISCA, 2020, pp. 4243–4247. [Online]. Available: https://www.isca-speech.org/archive/interspeech_2020/n20_interspeech.html

[17] Y. Cimtay, E. Ekmekcioglu, and S. Caglar-Ozhan, "Cross-subject multimodal emotion recognition based on hybrid fusion," *IEEE Access*, vol. 8, pp. 168 865–168 878, 2020, conference Name: IEEE Access. [Online]. Available: https://ieeexplore.ieee.org/document/9195813

[18] T. Dalgleish and M. Power, *Handbook of Cognition and Emotion*. John Wiley & Sons, 2000-11-21, google-Books-ID: vsLvrhohXhAC. [Online]. Available: https://www.google.com.tr/books/edition/Handbook_of_Cognition_and_Emotion/vsLvrhohXhAC?hl=en&gbpv=1&dq=isbn:9780470842218&printsec=frontcover&pli=1

[19] C. Guanghui and Z. Xiaoping, "Multi-modal emotion recognition by fusing correlation features of speech-visual," *IEEE Signal Processing Letters*, vol. 28, pp. 533–537, 2021, conference Name: IEEE Signal Processing Letters. [Online]. Available: https://ieeexplore.ieee.org/document/9340264

[20] S. K. Bharti, S. Varadhaganapathy, R. K. Gupta, P. K. Shukla, M. Bouye, S. K. Hingaa, and A. Mahmoud, "Text-based emotion recognition using

deep learning approach," *Computational Intelligence and Neuroscience*, vol. 2022, p. e2645381, 2022, publisher: Hindawi. [Online]. Available: https://www.hindawi.com/journals/cin/2022/2645381/

[21] Z. Lian, J. Tao, B. Liu, J. Huang, Z. Yang, and R. Li, "Context-dependent domain adversarial neural network for multimodal emotion recognition." in *Interspeech*, 2020, pp. 394–398. [Online]. Available: https://www.iscaspeech.org/archive/interspeech_2020/lian20b_interspeech.html

[22] D. Priyasad, T. Fernando, S. Denman, C. Fookes, and S. Sridharan, "Attention driven fusion for multi-modal emotion recognition." [Online]. Available: http://arxiv.org/abs/2009.10991

[23] T. Mittal, U. Bhattacharya, R. Chandra, A. Bera, and D. Manocha, "M3er: Multiplicative multimodal emotion recognition using facial, textual, and speech cues," *Proceedings of the AAAI Conference on Artificial Intelligence*, vol. 34, pp. 1359–1367, 2020. [Online]. Available: https://doi.org/10.48550/arXiv.1911.05659

[24] W. Liu, J.-L. Qiu, W.-L. Zheng, and B.-L. Lu, "Multimodal emotion recognition using deep canonical correlation analysis." [Online]. Available: http://arxiv.org/abs/1908.05349

[25] T. Mittal, P. Guhan, U. Bhattacharya, R. Chandra, A. Bera, and D. Manocha, "Emoticon: Context-aware multimodal emotion recognition using frege's principle," in *Proceedings of the IEEE/CVF Conference on Computer Vision and Pattern Recognition (CVPR)*, June 2020. [Online]. Available: https://ieeexplore.ieee.org/document/9156904

[26] M. R. Makiuchi, K. Uto, and K. Shinoda, "Multimodal emotion recognition with high-level speech and text features." [Online]. Available: http://arxiv.org/abs/2111.10202

[27] Y.-T. Lan, W. Liu, and B.-L. Lu, "Multimodal emotion recognition using deep generalized canonical correlation analysis with an attention mechanism," in *2020 International Joint Conference on Neural Networks (IJCNN)*. IEEE, 2020-07, pp. 1–6. [Online]. Available: https://ieeexplore.ieee.org/document/9207625/

[28] H. Zhang, "Expression-EEG based collaborative multimodal emotion recognition using deep AutoEncoder," *IEEE Access*, vol. 8, pp. 164130–164143, 2020, conference Name: IEEE Access. [Online]. Available: https://ieeexplore.ieee.org/document/9187342

[29] S. R. Zaman, D. Sadekeen, M. A. Alfaz, and R. Shahriyar, "One source to detect them all: Gender, age, and emotion detection from voice," in *2021 IEEE 45th Annual Computers, Software, and Applications Conference (COMPSAC)*, 2021, pp. 338–343, ISSN: 0730-3157. [Online]. Available: https://ieeexplore.ieee.org/document/9529731

[30] X. Wu, W.-L. Zheng, and B.-L. Lu, "Investigating EEG-based functional connectivity patterns for multimodal emotion recognition." [Online]. Available: http://arxiv.org/abs/2004.01973

[31] M. S. Akhtar, D. Chauhan, D. Ghosal, S. Poria, A. Ekbal, and P. Bhattacharyya, "Multi-task learning for multi-modal emotion recognition and sentiment analysis," in *Proceedings of the 2019 Conference of the North American Chapter of the Association for Computational Linguistics: Human Language Technologies, Volume 1 (Long and Short Papers)*. Association for Computational Linguistics, 2019, pp. 370–379. [Online]. Available: https://aclanthology.org/N19-1034

[32] S. Nemati, R. Rohani, M. E. Basiri, M. Abdar, N. Y. Yen, and V. Makarenkov, "A hybrid latent space data fusion method for multimodal emotion recognition," *IEEE Access*, vol. 7, pp. 172948–172964, 2019, conference Name: IEEE Access. [Online]. Available: https://ieeexplore.ieee.org/document/8911364

[33] Z. Fang, A. He, Q. Yu, B. Gao, W. Ding, T. Zhang, and L. Ma, "FAF: A novel multimodal emotion recognition approach integrating face, body and text." [Online]. Available: http://arxiv.org/abs/2211.15425

[34] L. Sun, Z. Lian, J. Tao, B. Liu, and M. Niu, "Multi-modal continuous dimensional emotion recognition using recurrent neural network and self-attention mechanism," in *Proceedings of the 1st International on Multimodal Sentiment Analysis in Real-life Media Challenge and Workshop*, ser. MuSe'20. Association for Computing Machinery, 2020-10-15, pp. 27–34. [Online]. Available: https://doi.org/10.1145/3423327.3423672

[35] L. Cai, Y. Hu, J. Dong, and S. Zhou, "Audio-textual emotion recognition based on improved neural networks," *Mathematical Problems in Engineering*, vol. 2019, pp. 1–9, 2019. [Online]. Available: https://www.hindawi.com/journals/mpe/2019/2593036/

[36] M. Aydoğan and A. Karci, "Improving the accuracy using pre-trained word embeddings on deep neural networks for turkish text classification," *Physica A: Statistical Mechanics and its Applications*, vol. 541, p. 123288, 2020-03. [Online]. Available: https://linkinghub.elsevier.com/retrieve/pii/S0378437119318436

[37] Q.-T. Truong and H. Lauw, "VistaNet: Visual aspect attention network for multimodal sentiment analysis," *Proceedings of the AAAI Conference on Artificial Intelligence*, vol. 33, pp. 305–312, 2019-07-17. [Online]. Available: https://doi.org/10.1609/aaai.v33i01.3301305

[38] N. Ahmed, Z. A. Aghbari, and S. Girija, "A systematic survey on multimodal emotion recognition using learning algorithms," *Intelligent Systems with Applications*, vol. 17, p. 200171, 2023. [Online]. Available: https://www.sciencedirect.com/science/article/pii/S2667305322001089

[39] A. Gandhi, K. Adhvaryu, S. Poria, E. Cambria, and A. Hussain, "Multimodal sentiment analysis: A systematic review of history, datasets, multimodal fusion methods, applications, challenges and future directions," *Information Fusion*, vol. 91, pp. 424–444, 2023-03-01. [Online]. Available: https://www.sciencedirect.com/science/article/pii/S1566253522001634

[40] A. Solgi, A. Pourhaghi, R. Bahmani, and H. Zarei, "Improving SVR and ANFIS performance using wavelet transform and PCA algorithm for modeling and predicting biochemical oxygen demand (BOD)," *Ecohydrology & Hydrobiology*, vol. 17, no. 2, pp. 164–175, 2017-04-01. [Online]. Available: https://www.sciencedirect.com/science/article/pii/S1642359316300672

[41] J. Li, X. Wang, G. Lv, and Z. Zeng, "GraphMFT: A graph network based multimodal fusion technique for emotion recognition in conversation." [Online]. Available: http://arxiv.org/abs/2208.00339

Hussein Farooq Tayeb Alsaadawi is currently pursuing a Ph.D. at Firat University's Technology Faculty in the Department of Software Engineering, located in Elazig, Turkey. He completed his M.Sc. in the same department from 2015 to 2017, further solidifying his expertise in the field. Earlier, he earned his B.Sc. degree in Computer Science from Cihan University in Erbil, Iraq, between 2007 and 2011, demonstrating his early passion for the subject. In addition to his academic achievements, He holds a Technician Diploma in Electronic Engineering from Erbil Technical Institute in Iraq, which he obtained from 2000 to 2002. Following the completion of his diploma, he embarked on a successful career as a Software Technician in Iraq. He has published academic papers and international conference proceedings based on his valuable insights and research. His passion for software development, combined with his expertise in artificial intelligence, drives him to uncover groundbreaking solutions that will shape the industry's future.

Resul Das is a full professor in the Department of Software Engineering, Technology Faculty, Firat University. He graduated with B.Sc. and M.Sc. degrees from the Department of Computer Science at Firat University in 1999 and 2002, respectively. Then he received a Ph.D. degree at the Department of Electrical-Electronics Engineering at the same university in 2008. He served as both a lecturer and network administrator at the Department of Informatics at Firat University from 2000 to 2011. In addition, he has been an instructor of CCNA and CCNP and the coordinator of the Cisco Networking Academy Program since 2002. He worked between September 2017 and June 2018 as a visiting scholar at the Department of Computing Science at the University of Alberta, Edmonton, Canada supported by TÜBİTAK-BIDEB 2219 Post-Doctoral Fellowship. He has many journal papers and international conference proceedings. He served as Associate Editor for the Journal of IEEE Access and the Turkish Journal of Electrical Engineering and Computer Science-TUBITAK from 2018 to 2021. He became the 2% of the "World's Most Influential Scientists" list published by Stanford University researchers from 2020 to 2022. His current research areas include computer networks and security, cyber-security, software architectures, software testing, IoT/M2M applications, complex networks, graph visualization, knowledge discovery, and data fusion.

Research Article

Investigation of Equilibrium Optimizer to Solve Economic Dispatch with Practical Constraints

Y Venkata Krishna Reddy

Abstract— **Presently power demand keep on increasing due to rapid changes occurs in power industry. For that purpose establishing new generating is costlier rather than effectively utilize the available generating stations. In order to properly planning of power system generation sharing Economic Dispatch (ED) plays vital role. In this paper, Equilibrium Optimizer (EO) is used to solve the ED problem with effect of valve-point, prohibited operating zones (POZs), ramp rate up/down limits and pollution like practical constraints. In order to analyze the capability of the EO algorithm, the algorithm is applied to four test systems with 6 unit systems and the results are compared with other optimization algorithms. The comparative results proven that EO is better optimization technique to solve ED problem with practical constraints.**

Index Terms—   **Power Industry, Economic Dispatch, Equilibrium Optimizer, Valve-point, Prohibited operating zones, Ramp rate up/down limits.**

I. INTRODUCTION

THE SYSTEM which can deals with generation, transmission nd distribution to supply the energy to the consumers on economic basis is known as power systems. Electric power demand is increasing in the current context due to developments in both the industrial and public sectors. The main source of this electricity is primarily thermal plants are likely to meet load demand. In general, the cost of generating for any thermal plant will be proportional to the cost of fuel.

As a result, proper load sharing of generating units is essential to give lower generation costs. The Economic Dispatch (ED) problem is examined for this purpose in order to obtain optimal allocation of generation by all generating units while minimizing total fuel cost while meeting both the equality and inequality requirements. ED problems are typically complicated by practical limits of thermal units such as transmission network losses, valve-point loading, banned operating zones, and numerous fuels. The operational cost function is approximated by a single quadratic function in standard ED problems, and valve-point loading is neglected.

Y V KRISHNA REDDY, SV College of Engineering, Dept. of EEE, Tirupati, India. (e-mail: yvkrishnareddy36@gmail.com).

https://orcid.org/0000-0002-1832-2193

Typically, the Lambda Iteration approach is employed to solve the ED problem for proper thermal unit allocation at the lowest possible fuel cost. Therefore, proper distribution of producing units for large systems is problematic. To address this issue, researchers are looking for new methods that are similar to Particle Swarm Optimization (PSO) [1], Firefly Algorithm (FFA) [2], Quick Group Search Optimizer (QGSO) [3], Cuckoo Search Algorithm (CSA) [4] and Genetic Algorithm (GA). Because an ED problem in a practical power system is non-convex due to valvepoint loading, the applicability of traditional approaches is limited. Improved Differential Evolution (IDE) [5, 6], Tournament-based Harmony Search (THS) [7], and Oppositional based Grey Wolf Optimization (OGWO) [8] methods are utilized to tackle the ED problem with valvepoint loading.

However, note the discontinuities in the turbine-generator set performance characteristics, which are caused by valve-point (non-convex) loading in plants [9]. For tackling the ED with valve point effect (EDVPE) problem, hybrid approaches such as modified Sub-Gradient (MSG) and Harmony Search Algorithms hybrid GA-NSO [10] and MSG-HS [11] and methods are utilized.

Furthermore, instability in generation at certain levels of unit loading may be induced by physical restrictions or flaws. This issue can be overcome by employing the prohibited operating zones (POZ) paradigm [9] and switching the unit's generating level between any two. Its ramp rate restrictions for concurrent periods must not be exceeded [9]. Backtracking search algorithm (BSA) [12], PSO [13], Enhanced Random Drift PSO (RDPSO) [14], Exchange Market Algorithm (EMA) [15], Modified CSA [16] techniques are utilized to solve ELD with ramp rate limitations and POZs.

Despite the fact that ED reduces operational costs greatly, the environmental impact is still not addressed. By incorporating emission constraints into the ED problem, the problem is renamed the Economic Emission Dispatch (EED) Problem. For the EED problem with/without transmission losses, differential evolution (DE) [17], Glowworm Swarm Optimization (GSO) [18], MOEA [19], and Summation based Multi Objective DE (SMODE) [20] approaches are utilized. Approaches such as Multi objective BSA [21], multiobjective EA [22], new global PSO (NGPSO) [23] are used to combine fuel cost with emission as a specific objective problem.

Non-convex loading, emission, ramp rate restrictions, and POZs should all be considered while solving a practical ED problem, as it is extremely difficult to find an ideal solution. The Equilibrium Optimizer (EO) [24] approach was utilized in this article to tackle ED issues with numerous practical

operating restrictions such as valve-point effect, nonlinear emission, ramp-up/down, and POZs. The EO method quality is applied to four case studies for solving practical ED difficulties.

II.   PROBLEM FORMULATION

A.   Classical ED

The theoretical cost curve of classical ELD problem is as shown in the Figure 1.
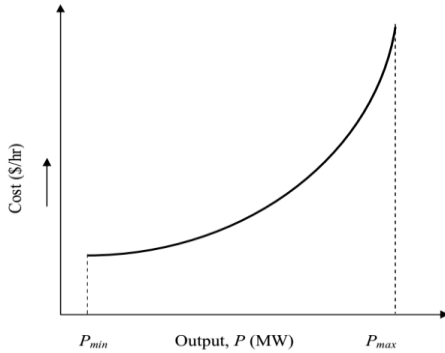
Fig.1 Convex Fuel cost function

The most simplified cost function of each generating unit i, can be represented as a quadratic function as: (
Minimize

$$F_T = \min f = \sum_{i=1}^{n} F_i(P_i) \qquad (\$/h) \tag{1}$$

$$F_i(P_i) = \sum_{i=1}^{N}(a_i P_i^2 + b_i P_i + c_i) \tag{2}$$

Equality Constraints:

$$\sum_{i=1}^{N} P_i = P_D + P_L \tag{3}$$

To calculate transmission losses the B-coefficient method used.

$$P_L = \sum_{i=1}^{N}\sum_{j=1}^{N} P_i B_{ij} P_j + \sum_{i=1}^{N} B_{0i} P_i + B_{00} \tag{4}$$

Inequality Constraints

$$P_{i\,min} \le P_i \le P_{i\,max} \tag{5}$$

Where Pimin and Pimax are the minimum and maximum real power generation limits of the ith generating unit.

B.   EDVPE

The ED problem cost objective function, considering the valve-point effects (EDVPE). Figure 2 shows the valve-point effect is incorporated in classic ED problem by superimposing the sine component model on the quadratic cost curve.

$$F_i(P_i) = a_i P_i^2 + b_i P_i + c_i + |e_i \sin(f_i(P_{min} - P_i))| \tag{6}$$
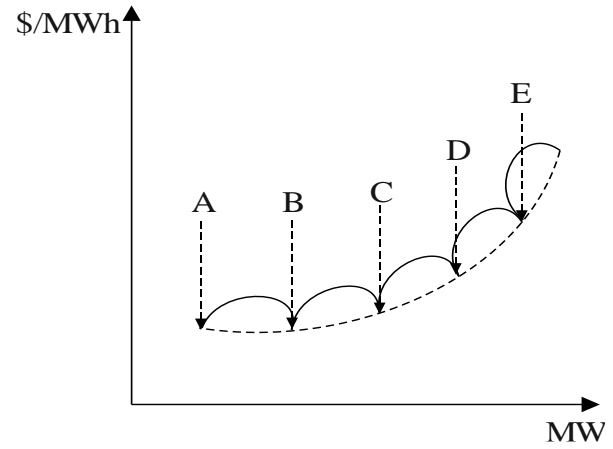
Fig. 2. Non-Convex Fuel cost function

C.   EDRPOZ

ED problem with ramp rate Limits and prohibited operating zones (POZs) treated as EDRPOZ. Figure 3 shows the model of Ramp-rate limits.

$$\begin{cases} P_i - P_{0i} \le UR_i \text{ if generation increases} \\ P_{0i} - P_i \le DR_i \text{ if generation decreases} \end{cases} \tag{7}$$
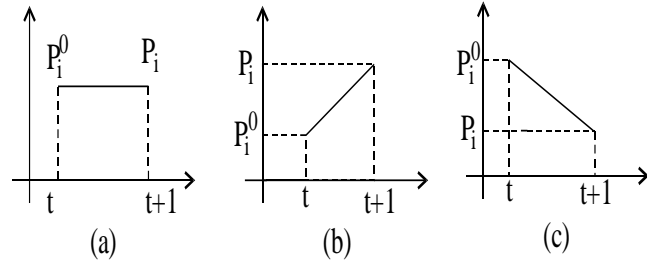
Fig. 3 Ramp rate limits of generating units

The new operation limits:

$$P_{i\,min,r} \le P_i \le P_{i\,max,r} \tag{8}$$

Where

$$P_{i\,min,r} = \max(P_{i\,min}, P_{0i} - DR_i)$$
$$P_{i\,max,r} = \min(P_{i\,max}, P_{0i} + UR_i) \tag{9}$$

These POZs can be included in the ED formulation as follows:

$$P_i = \begin{cases} P_{i\,min} \le P_i \le P_{i,1}^i \\ P_{i,j-1}^u \le P_i \le P_{i,j}^l \quad j = 2,....n_i \\ P_{i,n_i}^u \le P_i \le P_{i\,max} \end{cases} \tag{10}$$

Figure 4 clearly shows the POZs modeled in the cost curve.
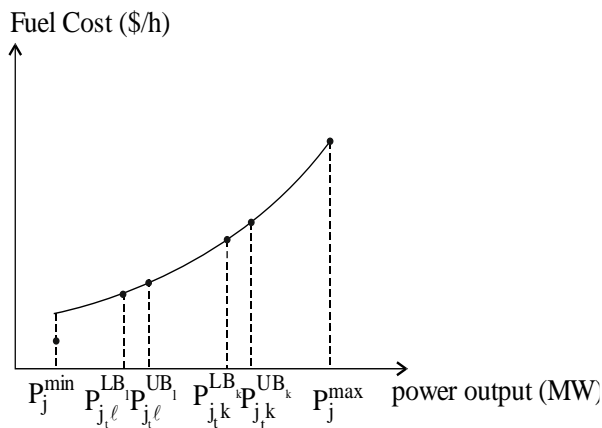
Fig. 4 Generator characteristics with POZs

D. EED

To reduce emissions along with the cost of generation considering the problem of environmental economic dispatch (EED). The fossil fuel power plants produce pollutants such as NO_X, CO_2 and SO_2 emissions which are usually represented by separate quadratic functions. Nevertheless, by combining all the pollutants as single emission introducing exponential function to the quadratic emission function as given in Equation (11) for overall emission level of the pollutants.

$$F = E(P_G) = \sum_{k=1}^{N_G} (\alpha_k P_{Gk}^2 + \beta_k P_{Gk} + \gamma_k) + \xi_{ck} \times \exp(P_{Gk} \lambda_k) \ (ton/h) \tag{11}$$

Weighted sum method: The fuel cost and emission objective problem is converted into single objective CEED problem given by Equation (12) by assuming weighting factor proportion to the importance of the objective.

$$Minimize \ F = W \times F_2 + (1-W) \times F_3 \tag{12}$$

III. EQUILIBRIUM OPTIMIZER

A. Faramarzi proposes an Equilibrium Optimizer (EO). In EO, each solution with its position acts as a search agents.

A. Initialization and evaluation of the functions

The initial positions were randomly determined according to the number of particles in the search space

$$C_i^{intial} = C_{min} + rand_i(C_{max} - C_{min}) \quad i = 1, 2, 3, ...n \tag{13}$$

B. Equilibrium pool and candidates (Ceq)

The state of equilibrium is known as the final state of EO convergence. In EO these candidates are selected four best particles based on their fitness value during the entire optimization process with other particles whose positions are in the mean of the four best particles described above. Such five particles were called candidates for equilibrium and used to construct an equilibrium pool.

$$C_{eq,pool} = \{C_{eq(1)}, C_{eq(2)}, C_{eq(3)}, C_{eq(4)}, C_{eq(ave)}\} \tag{14}$$

C. Exponential term (F)

The key updating rule for concentration is controlled by the exponential term F

$$F = e^{-\lambda(t-t_0)} \tag{15}$$

$$t = (1 - \frac{iter}{\max iter})^{(a_2 \frac{iter}{\max iter})} \tag{16}$$

To achieve convergence by increasing the quest pace and improving discovery and exploitation capabilities, t_0 is modelled as

$$t_0 = \frac{1}{\lambda} \ln(-a_1 sign(r - 0.5)[1 - e^{-\lambda t}]) + t \tag{17}$$

Now equation (15) can be rewritten as

$$F = a_1 sign(r - 0.5)(e^{-\lambda t} - 1) \tag{18}$$

D. Generation rate (G)

Generation rate is the most significant parameter used in equilibrium algorithm to increase the process of exploitation.

$$G = G_0 e^{-k(t-t_0)} \tag{19}$$

Where

$$G_0 = GPC(C_{eq} - \lambda C) \tag{20}$$

$$GP = \begin{cases} 0.5r1 & r2 \geq GP \\ 0 & r2 \leq GP \end{cases} \tag{21}$$

Finally, EO's updating law shall be as follows:

$$C = C_{eq} + (C - C_{eq}) * F + \frac{G}{\lambda V}(1 - F) \tag{22}$$

IV. RESULTS

A. Classical ED

In order to evaluate solution of classical ED problem generator practical constraints are not considered like valve-point effect, ramp limits and prohibited operating zones. But the transmission losses, equality and inequality constraints are considered for 6-unit test system [2] with power demand of 800 MW. The fuel cost function is convex function follows as Equation 1.

The simulation and comparison results for the given test system are presented in Table 1. Among all the methods, the proposed EO method is better interms of optimal cost and convergence characteristics shown in figure 5 for 25 trails.
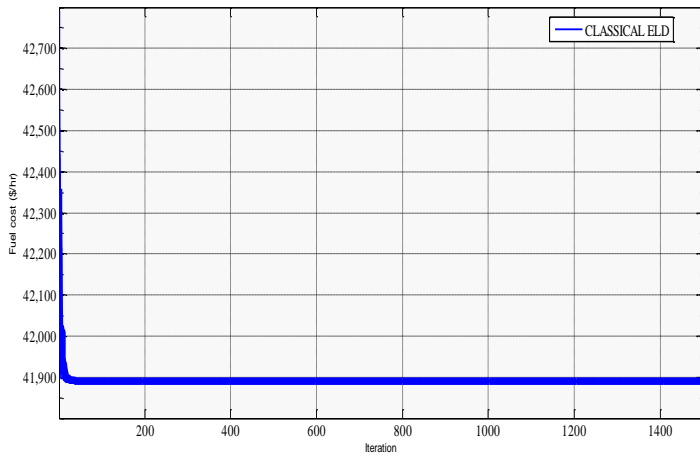
Fig. 5 Convergence characteristics of classical ED

Table 1: Comparison results for 6-unit to classical ED

	PSO [1]	FFA[2]	CSA[4]	EO
P_1 (MW)	32.67	32.5861	32.5863	33.9199
P_2 (MW)	14.45	14.4843	14.4843	14.4029
P_3 (MW)	141.73	141.548	141.548	141.2473
P_4 (MW)	136.56	136.045	136.045	135.6431
P_5 (MW)	257.37	257.664	257.664	257.3198
P_6 (MW)	242.54	243.009	243.009	242.6420
P_L (MW)	25.32	25.3309	25.3312	25.1749
P_T (MW)	825.32	825.3309	825.3312	825.1749
FC($/hr)	41896.66	41896.7	41896.9	41890.507
SD	--	--	--	0.44e-12

B. EDVPE

The cost function of the generation is represented by the Equation 6. The sinusoidal term added to convex cost function and resulting becomes non-convex cost function. The test system comprising six generating units [5] meets a power demand of 283.4 MW and includes valve-point effect and transmission loss.

The best and comparison results for test system are presented in table 2. Among all the methods the proposed EO method is better in terms of optimal cost and convergence characteristics shown in figure 6 for 25 trails.

Table 2: Comparison results for 6-unit to EDVPE

	GA-NSO[10]	MSG-HS[11]	PSO [11]	EO
P1(MW)	182.4784	199.6331	197.8648	199.5997
P2(MW)	48.3525	20.0000	50.3374	20.0000
P3(MW)	19.8553	23.7624	15.0000	23.8221
P4(MW)	17.1370	18.3934	10.0000	19.0903
P5(MW)	13.6677	17.1018	10.0000	18.1304
P6(MW)	12.3487	15.6922	12.0000	13.7463
PL(MW)	10.4395	11.1830	11.8022	11.0135
PT(MW)	293.839	294.5829	295.2022	294.0135
FC($/hr)	984.936	925.6406	925.7581	924.8883
SD	--	--	--	0.45e-12

Fig. 6 Convergence characteristics of EDVPE

C. EDRPOZ

EDRPOZ comprising six generators meets [11] a load demand of 1263 MW and includes loss, POZs and ramp up/down limits. The optimal and comparison results for EDRPOZ problem are presented in Table 3. The total operating cost during practical constraints is 15442.6753 ($/hr) and it is found to be lesser than the other methods reported in the literature. The convergence characteristics of 6 unit system with proposed method for EDRPOZ are shown in Figure 7 for 25 trails.

Table 3: Comparison results for 6-unit to EDRPOZ

	BSA [12]	EMA [15]	MCS[16]	EO
P1(MW)	447.4902	443.3872	447.5038	447.0649
P2(MW)	173.3308	173.2524	173.3182	173.1643
P3(MW)	263.4559	263.3721	263.4628	263.9481
P4(MW)	139.0602	138.9894	139.0653	139.0668
P5(MW)	165.4804	165.3650	165.4764	165.5847
P6(MW)	87.1409	87.0781	87.1347	86.5868
PL(MW)	12.9583	12.4430	12.9582	12.4154
PT(MW)	1275.95	1275.443	1276.958	1275.4164
FC($/hr)	15449.89	15443.07	15449.89	15442.675
SD	--	--	--	0.52e-12
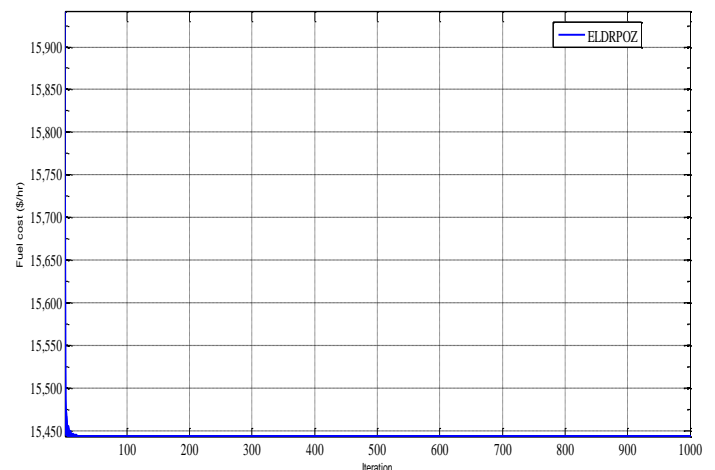
Fig. 7 Convergence characteristics of EDRPOZ

D. EED

The fossil fuel power plants produce pollutants such as NO_X, CO_2 and SO_2 emissions which are usually represented by separate quadratic functions. Nevertheless, by combining all the pollutants as single emission introducing exponential function to the quadratic emission function is given in Equation (11) for overall emission level of the pollutants. The fuel cost and emission objective problem is converted into single objective Economic Emission Dispatch (EED) problem by using the equation (12), assuming weighting factor proportion to importance of the objective.

Table 4: Optimal results for to EED by EO

Unit	Cost minimization	Emission minimization	EED
P1 (MW)	5.0000	40.9793	50.0000
P2 (MW)	30.3402	46.2677	17.9027
P3 (MW)	64.1857	54.2949	15.0798
P4 (MW)	102.4765	38.8797	12.2136
P5 (MW)	48.0259	54.3078	15.0798
P6 (MW)	35.1204	51.4338	18.6104
PTotal (MW)	285.1486	286.6741	284.6620
P loss (MW)	1.7486	3.2741	1.2620
Gcost ($/h)	604.9688	649.5788	598.9677
E (ton/h)	0.226023	0.1942	0.2242
SD	0.51e-12	0.49e-12	0.48e-12

The IEEE 30-bus 6-Unit system is considered as test system. Data is taken [16] with power demand of 283.4 MW. Table 4 represents the optimal results for test system for minimizing the cost, emission and combined economic emission with the help of EO. Table 5 provides comparison results for EED problem and figure 8, 9 and 10 represents convergence characteristics of test system.

Table 5: Comparison results for 6-unit system to EED

Methods	Fuel Cost Min. ($/Hr)	Emission Min. (ton/Hr)	CEED Min.($/Hr)
BSA [19]	605.9984	0.194203	608.9169
MOEA [21]	607.78	0.1942	NA
NGPSO [22]	605.9983	0.194178	623.8705
SMODE [23]	619.07	0.1942	NA
EO	604.9688	0.1942	598.9677
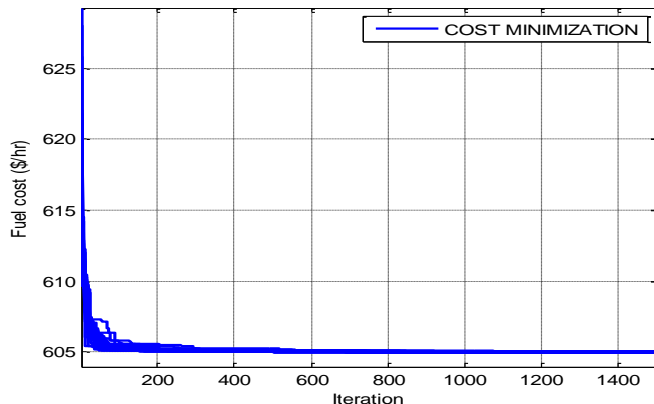
Fig. 8 Convergence characteristics of EED to cost minimization
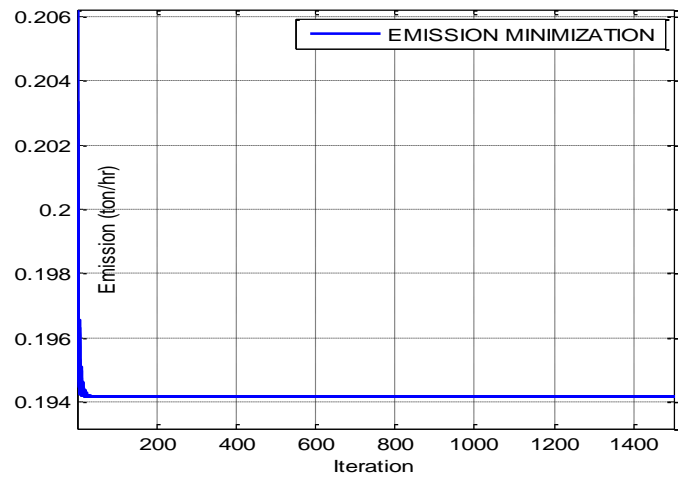
Fig. 9 Convergence characteristics of EED to emission minimization
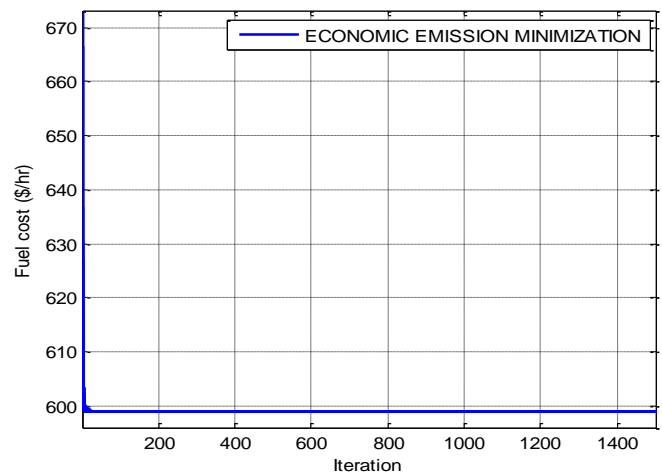
Fig. 10 Convergence characteristics of EED

V. CONCLUSION

A new optimization algorithm called Equilibrium Optimizer (EO) is used in this paper to solve the economic dispatch problem with realistic restrictions such as valve point effect, ramp rate up/down limits, prohibited operating zones and pollution. The EO has been used to evaluate four separate 6-unit test systems. The findings were consistent with other methods listed in the literature and showed that EO had quick convergence speed, better fuel cost outcomes, prevailing computational performance and more cognizant achievement. The suggested algorithm would be a viable solution to solve ED problem practical constraints. The proposed methodology is a potential approach in large-scale framework to solve complex non-smooth optimization problems.

REFERENCES

[1] Hardiansyah, Junaidi and Yohannes MS, "Solving Economic Load Dispatch Problem Using Particle Swarm Optimization Technique", *International journal of intelligent systems and applications*, Vol.12, pp.12-18, 2012.

[2] K. Sudhakara Reddy and M. Damodar Reddy, "Economic Load Dispatch Using Firefly Algorithm", *International Journal of Engineering Research and Applications*, Vol. 2, Issue4, pp.2325-2330, July-August 2012.

[3] Mohammad Moradi-Dalvand and Behnam Mohammadi-Ivatloo, "Continuous Quick Group Search Optimizer for Solving Non-Convex Economic Dispatch Problems", *Electric Power Systems Research (Elsevier Journal),* Vol. 93, pp.93–105, 2012.

[4] A.Hima Bindu and M. Damodar Reddy, "Economic Load Dispatch Using Cuckoo Search Algorithm", *International Journal of Engineering Research and Applications*, Vol. 3, Issue 4, pp. 498-502, Jul-Aug 2013.

[5] Shubham Tiwari, Ankit Kumar. 2013, Economic Load Dispatch Using Particle Swarm Optimization. IJAIEM, ISSN 2319 - 4847 Volume 2, Issue 4.

[6] Dexuan Zou, Steven Li. 2016, An improved differential evolution algorithm for the economic load dispatch problems with or without valve-point effects. Applied Energy 181 375–390.

[7] Mohammed Azmi Al-Betar, Mohammed A. Awadallah. 2016, Tournament-based harmony search algorithm for non-convex economic load dispatch problem. Applied Soft Computing.

[8] Moumita Pradhan, Provas Kumar Roy, Tandra Pal. 2017, Oppositional based grey wolf optimization algorithm for economic dispatch problem of power system. Ain Shams Engineering Journal

[9] Weerakorn, "Artificial intelligence in power system optimization", *CRC press, Taylor and Francis group*, 2013.

[10] Tahir Nadeem Malik, Azzam ul Asar "A new hybrid approach for the solution of nonconvex ED problem with valve-point effects", *Electric Power Systems Research* 80 (2010) 1128–1136.

[11] Celal Yas¸ "A new hybrid approach for nonconvex EDP with valve-point effect", *Energy.* 36 (2011) 5838-45.

[12] Mostafa Modiri-Delshad, "Backtracking search algorithm for solving economic diapatch problems with valve-point effects and multiple fuel optins", *Energy* 116 (2016) 637e649.

[13] Zwe-Lee Gaing "Particle Swarm Optimization to Solving the economic dispatch considering the generator constrints", *IEEE transactions on power systems*, vol. 18, no. 3, august 2003.

[14] Wael Taha Elsayed, Yasser G. Hegazy "Improved Random Drift Particle Swarm Optimization With Self-Adaptive Mechanism for Solving the Power Economic Dispatch Problem", *IEEE transactions on industrial informatics*, vol. 13, no. 3, june 2017.

[15] Naser Ghorbani and Ebrahim Babaei, "Exchange Market Algorithm for Economic Load Dispatch", Electrical Power and Energy Systems (Elsevier Journal), Vol. 75, pp.19–27, 2016.

[16] Jian Zhao and Shixin Liu, "Modified Cuckoo Search Algorithm to Solve Economic Power Dispatch Optimization Problems", IEEE/CAA journal of automatica sinica, Vol. 5, no. 4, pp,794-807, july 2018.

[17] MandaI, K., Chakraborty, N., "Differential Evolution based environmentally constrained Economic Dispatch", IEEE, (2008).

[18] Nelson Jayakumar, D., Venkatesh, P., "Glowworm swarm optimization algorithm with topsis for solving multiple objective environmental economic dispatch problem", Applied Soft Computing, 23: 375-386, (2014).

[19] M. A. Abido, "Multiobjective Evolutionary Algorithms for Electric Power Dispatch problem", IEEE transactions on evolutionary computation, Vol. 10, no. 3, pp.315-330, june 2006.

[20] Qu, B.Y., Liang, J.J., "Economic emission dispatch problems with stochastic wind power using summation based multi-objective evolutionary algorithm", Information Sciences, 351: 48-66 (2016).

[21] Mostafa Modiri-Delshad and Nasrudin Abd Rahim, "Multi-Objective Backtracking Search Algorithm for Economic Emission Dispatch Problem", Applied Soft Computing (Elsevier Journal), Vol. 18, pp.1-15, 2015.

[22] B.Y. Qu, J.J. Liang, Y.S. Zhu, Z.Y. Wang and P.N. Suganthan, "Economic emission dispatch problems with stochastic wind power using summation based multi-objective evolutionary algorithm", Information Sciences (Elsevier Journal), Vol.12, pp.1-19, 2016.

[23] Dexuan Zou, Steven Li, "A New Global Particle Swarm Optimization for the Economic Emission Dispatch with or without Transmission Losses", Energy Conversion and Management (Elsevier Journal), Vol.139, pp.45-70, 2017.

[24] Faramarzi et al "Equilibrium Optimizer: A Novel Optimization Algorithm", Elsevier 2019.

BIOGRAPHIES

Y. Venkata Krishna Reddy has four years' experience in teaching and 4 years of experience in research. Received M.tech in the specialization of Power Systems from JNTUACE, Anantapur in the year 2014. Awarded PhD degree in the year of 2019 at Sri Venkateswara University. Five times qualified in all India GATE entrance exam from 2012-2016. Presently he works as associate professor in SV College of engineering, tirupati. His research area is Power System Optimization and reactive power compensation.

Research Article

Design and analysis of L and LCL filters for grid-connected HNPC inverters used in renewable energy systems

Muhammet Cengiz, Turgay Duman

Abstract—With the widespread integration of renewable energy systems (RES) into the electric grid, maintaining power quality within specified limits has become a major focus. The total harmonic distortion (THD) value of the currents transferred to the grid and directly affecting power quality in RES such as grid-connected photovoltaic (PV) and fuel cells (FC) should not exceed 5%. To achieve this objective, various filter topologies are used to interface between the inverters, which are components of PV and FC systems, and the grid. Although there are numerous filter topologies, L and LCL-type passive filters are the most commonly used topologies in grid-connected systems. This study analyzes the L and LCL-type filter topologies for the H-bridge neutral point clamped (HNPC) inverter. Using MATLAB/Simulink®, a simulation of a 3 kW system employing L and LCL filters has revealed THD values of 1.56% and 0.07% for grid currents, respectively. Additionally, the HNPC inverter's efficiency has been determined at 98.46% in the LCL filter configuration. This study has been focused on modeling and comparing simulation results to investigate the harmonic attenuation capabilities of L and LCL filters, assess the maximum power transferred to the grid, and analyze their impact on grid currents.

Index Terms—HNPC inverter, L and LCL filters, power quality, PV system, sliding mode controller.

I. INTRODUCTION

ELECTRICAL energy, which constitutes approximately 20% of the global total energy consumption, is being demanded more and more each day, and it is expected that the total electrical energy demand will increase by more than 80% by 2050 [1]. Considering the reduction of traditional energy sources (coal, oil, etc.) used in energy production and the damage they cause to the environment, energy consumption is a major concern of today's society, and alternative energy sources are needed. Renewable energy technologies, particularly photovoltaic and fuel cell systems that generate clean and sustainable electricity from renewable energy sources such as solar, wind, and hydrogen, are regarded as one of the most important future solutions [2]. According to the reports issued by the International Energy Agency (IEA) and the International Renewable Energy Agency (IRENA), renewable sources are projected to contribute more than 80% to the overall energy production worldwide by 2050. Furthermore,

it is anticipated that the proportion of solar energy in total electricity production will increase to approximately 25%, and the percentage of hydrogen energy in total energy consumption will rise to around 13% [1], [3], [4].

PV and FC systems can generally be classified into two groups: grid-connected and stand-alone. Grid-connected PV (GCPV) systems are decentralized (distributed) power systems that can operate in parallel with the electricity transmission and distribution grid [5]. Parallel operation with the grid is the transfer of the power produced in excess of the needs of the loads in the system back to the electricity grid. Therefore, in contrast to standalone systems, GCPV systems do not need additional storage devices like battery packs, which lowers the cost of the system and makes it easier to maintain and reinstall [6], [7]. Furthermore, GCPV systems account for the vast majority of installed PV capacity when compared to stand-alone systems. Similarly, grid-connected FC systems (GCFC) are an important part of research and are widely discussed in areas such as air conditioning, electromechanical systems, lighting, and electronic devices [8]. To ensure the electrical grid's power quality, the more widely used GCPV and GCFC systems must meet certain specifications. The most important specification is to transfer a sinusoidal current to the grid with a total harmonic distortion value of no more than 5% [9], [10]. PV panels and FCs generate DC voltage. Fig. 1 depicts the overall grid connection structure of both systems.

Although the DC voltage generation logic of both sources differs, the components and power conversion principles required for grid integration are similar [2], [8]. To transfer a sinusoidal current from PV and FC systems to the grid, an inverter is required to convert the DC power produced by PV panels or fuel cells into AC power with a specific frequency and amplitude. Therefore, inverters are a critical component of RES such as PV and FC. Various inverter topologies used in PV applications have been presented in the literature [7]. Among these topologies, the HNPC inverter is widely used in grid-connected applications due to its advantages such as low THD, transformerless operation, high quality power conversion, and operation at high input voltages with low-capacity switches [11], [12]. On the other hand, grid-connected inverters modulated with pulse width modulation (PWM) techniques contain switching harmonic components in their output waveforms [13]. Therefore, inverters must be connected to the grid via a filter to provide sinusoidal current to the grid without harmonic distortion. Generally, three basic filter topologies are used at the inverter output, namely L, LC,

🟢 **Muhammet Cengiz** is with the Department of Electrical and Electronic Engineering, Engineering and Architecture Faculty, Erzurum Technical University, Erzurum, 25050, Turkey e-mail: muhammet.cengiz@erzurum.edu.tr

🟢 **Turgay Duman** is with the Department of Electrical and Electronic Engineering, Engineering and Architecture Faculty, Erzurum Technical University, Erzurum, 25050, Turkey e-mail: turgay.duman@erzurum.edu.tr

Fig. 1. General structure of grid connected system (PV or FC).

and LCL.

When selecting a suitable filter topology for grid -connected inverters, it is necessary to consider parameters such as size, cost, filter losses, and dynamic system properties, as well as effectively reducing harmonics [14]. The L filter contains only one component, which makes it have a simple topology and easy to design. However, it requires a very high inductance value for applications above a few kilowatts [15]. Using a high inductance value can make the system cumbersome and expensive, and it may also increase the filter's losses. Additionally, the system's dynamic response can be poor due to long voltage drops in the filter [16], [17]. The LC and LCL filter topologies are used to mitigate the disadvantages of using the L filter in high-capacity systems, such as size, cost, losses, and poor system dynamics. By increasing the capacitor value in the LC filter, the inductance value is decreased, and thus the disadvantages of the L filter mentioned above can be mitigated. However, in grid-connected systems, a high capacitor value is not quite preferred because it can cause problems such as sudden current peaks, grid side resonance due to reactive power requirements, and reliance on grid impedance for harmonic attenuation [17]. Therefore, L and LCL-type filter topologies are generally used in grid-connected systems [18], [19], [20].

LCL filters offer advantages over L filters such as improved harmonic performance, as well as lower size and cost [15], [21]. In addition, LCL filters are among the most widely used topologies in grid-connected inverters due to their advantages, such as lower ripple in the current injected into the grid and operating at a lower switching frequency [19]. However, LCL filters may suffer from resonances that occur due to reactive power requirements and must be damped to ensure system stability. Two types of damping methods, passive and active, are generally used to alleviate the resonance problem. The passive damping method can be implemented by adding a damping resistor in series with the LCL filter capacitor [21]. Although this method is simple, it reduces the harmonic attenuation performance of the LCL filter by causing additional

power losses due to the added resistance [20]. The active damping method is based on the concept of an imaginary resistor connected to the current control loop to eliminate power loss [22]. Although the imaginary resistor concept provides better harmonic attenuation performance, it increases control complexity and requires the use of an additional set of sensors. On the other hand, the active damping effect can also be achieved by controlling the grid current without the use of imaginary resistance [23]. The sliding mode control (SMC) method, which is used in grid current control and has advantages such as reducing control complexity, robustness against parameter changes, fast dynamic response, and ease of application, also overcomes the resonance problem without the need for additional damping methods [19], [20], [23].

This article is structured as follows: Section 2 gives an overview of the HNPC structure and control for single-phase grid connection. Sections 3 and 4 discuss the design phases of the L and LCL filters, respectively, and provide guidelines for determining filter component values. Section 5 presents simulation results for the grid connection states of L and LCL filters. Lastly, Section 6 presents the conclusions.

II. SINGLE-PHASE GRID-CONNECTED HNPC INVERTER

Power electronic devices, such as DC-DC converters and DC-AC inverters, must be used to transfer the DC power generated by the PV panel or FC to the electrical grid as maximum AC power. In recent years, researchers have focused on single-stage power processing systems that use only inverters as power converters, both to improve the overall efficiency of PV systems and to increase the power density of the inverters [24]. The single-phase grid-connected inverter block diagram of the system is shown in Fig. 2.

As depicted in Fig. 2, the HNPC inverter enables power transfer between the grid and the PV panel. The PV panel is treated as a constant DC source to simplify the system. The HNPC inverter is made up of two 3-level NPC inverter legs connected in parallel. Each NPC leg generates three different voltage levels at the output: $-V_{dc}/2$, $+V_{dc}/2$, and

Fig. 2. The single-phase grid-connected HNPC inverter.

Fig. 3. Graphical explanation of sliding mode control.
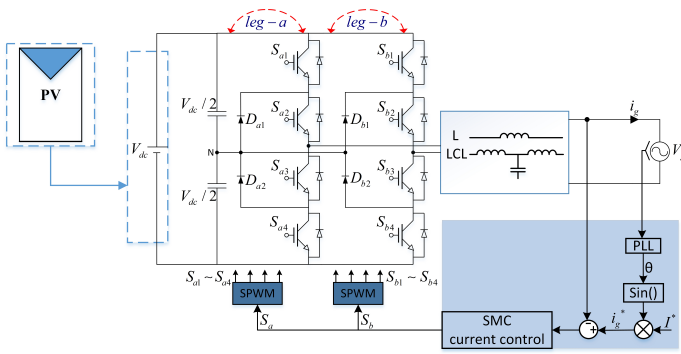
zero. Parallel connection of the NPC inverter legs results in the generation of five different voltage levels at the HNPC inverter output: $-V_{dc}, +V_{dc}, 0, -V_{dc}/2, +V_{dc}/2$. The switching states and voltage levels for the HNPC are given in Table 1. This inverter topology and suitable switching states have been discussed in the previous study [25].

TABLE I
SWITCHING STATES OF THE HNPC INVERTER

			Switching State					Output Voltage
Sa1	Sa2	Sa3	Sa4	Sb1	Sb2	Sb3	Sb4	Vab
1	1	0	0	0	0	1	1	V_{dc}
1	1	0	0	0	1	1	0	$\dfrac{V_{dc}}{2}$
0	1	1	0	0	0	1	1	
1	1	0	0	1	1	0	0	
0	1	1	0	0	1	1	0	0
0	0	1	1	0	0	1	1	
0	1	1	0	1	1	0	0	$-\dfrac{V_{dc}}{2}$
0	0	1	1	0	1	1	0	
0	0	1	1	1	1	0	0	$-V_{dc}$

On the other hand, in this study, SMC method, which is in the nonlinear controller group, was used for grid current control. The reference studies provide specifics on how to use the SMC control method for grid-connected inverter systems [26], [27]. The main idea of SMC is to bring the system state variables onto a pre-defined sliding surface through discontinuous control and to force them to move on this surface, and also to control them by approaching the origin point, as seen in Fig. 3. This concept requires the existence of a sliding surface and a control signal for its implementation. Generally, the sliding surface is constructed using state variable errors, and the sliding surface function, which is a linear combination of state variable errors, can be expressed as follows:

$$S(x) = \lambda x_1 + \dot{x}_1 \qquad (1)$$

where x_1 and $\dot{x}_1$ denote the state variable error and its derivative, respectively. λ is a positive constant called the sliding coefficient. The value of the sliding coefficient is a parameter that has an effect on the dynamic response of the system and should always be chosen as positive to ensure stability[27]. However, an excessively large λ value can jeopardize the stability of the system. Therefore, through trial and error and considering the switching frequency that determines the
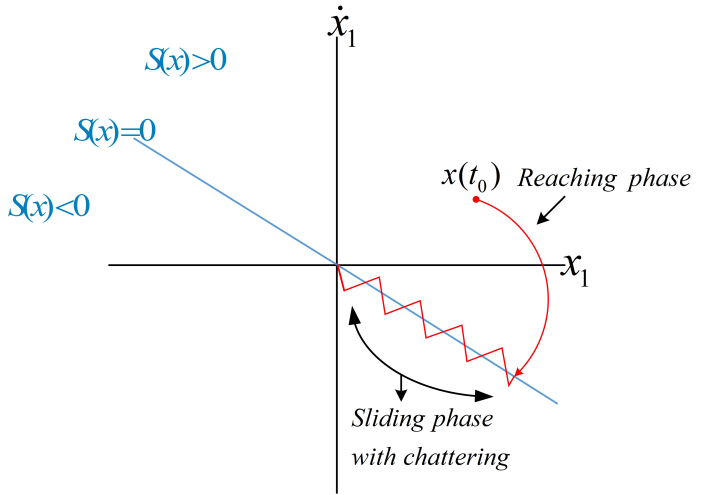
dynamics of the system, λ has been chosen as 5000 in this study. In grid-connected inverter systems, the main purpose is to control grid current. Therefore, x_1 can be determined as the error $(i_g{}^* - i_g)$ of the grid current. In addition, in order to weaken the resonance problem in the LCL filter mentioned in the introduction, the sliding surface can also be formed with the capacitor voltage error $(v_c - v_c{}^*)$. The adjustment of capacitor voltage results in automatic adjustment of grid current as a natural consequence.After determining the sliding surface function, the control signal that forces the state variables to act on the sliding surface must be determined. The structure of the control signal can be expressed as in Eq. (2):

$$u_{smc} = u_{eq} + u_{sw} \qquad (2)$$

where u_{eq} is the equivalent control signal that determines the system change on the sliding surface, and u_{sw} is the discontinuous switching control input that drives the state variables to the sliding surface and enforces the state variables to act on the sliding surface even in the presence of parameter changes and distortions. The equivalent control (u_{eq}) signal can be obtained by setting the derivative of the sliding surface function to zero $(\dot{S}(x) = 0)$. However, including the equivalent control part in the control signal increases overall computation time and control complexity [28]. Therefore, the use of a simpler discontinuous switching control signal is widely preferred [18], [27], [28]. In general, the discontinuous switching control signal connected to the sliding surface and with a control gain of 1 (one) can be expressed as in Eq. (3):

$$u_{smc} = u_{sw} = -\,\mathrm{sign}(S(x)) = \begin{cases} +1 & if \ S(x) < 0 \\ -1 & if \ S(x) > 0 \end{cases} \qquad (3)$$

where the sign() denotes the signum function [19], [23]. The chattering problem in practical applications can arise due to the discontinuous structure of the switching control signal, which switches between 1 and -1 values based on the sliding surface's sign [27]. As seen from Eq. (3), the control input is negative when the sliding surface is positive, and it is positive when the sliding surface is negative. Therefore, the control signal can be viewed as a switching function that changes its

value when the state variable's trajectory intersects the sliding surface. Furthermore, the chattering phenomenon observed in power converter applications has adverse impacts such as reduced control precision and power losses. Thus, minimizing chattering is crucial in SMC, and several techniques for reducing chattering have been proposed in literature [18], [20], [27]. One of the methods to reduce chattering is the boundary layer method. This method reduces chattering by passing the sliding surface function through a boundary layer of thickness ϕ. The signum function in the discontinuous switching control signal is then replaced by the $S(x)/\phi$ signal, which makes the control input continuous within the boundary layer and reduces chattering [26], [28]. As a result, the appropriate switching signals for the inverter are obtained by comparing the $S(x)/\phi$ signal with the triangle carriers.

A. Proportional-resonant (PR) control

The capacitor voltage reference ($v_c{}^*$) for the LCL filter connection state was successfully obtained using the excellent AC signal tracking capability of the PR control. The transfer function of the PR control is given in Eq. (4). When the grid current error is applied to the input of the transfer function, the output is $v_c{}^*$.

$$H_{PR}(s) = K_p + \frac{2K_r \omega_c s}{s^2 + 2\omega_c s + (2\pi f_g)^2} \tag{4}$$

where K_p is the proportional gain, K_r is the resonant gain, and w_c is the cut-off frequency. The dynamic and steady-state responses of the PR control are determined by adjusting the parameter values K_p and K_r. The derivation of proportional and resonant gains is analyzed in [23]. The gain values obtained according to the equations expressed in [23] are readjusted to improve the performance of the controller. Therefore, in this study, K_p and K_r were tuned to 3 and 1500, respectively. w_c is 1 rad/s.

III. L-TYPE FILTER DESIGN

Fig. 4 illustrates the circuit diagram of the L filter, which is placed between the inverter and the grid. The filter comprises of the filter inductance, denoted by L_i, and its internal resistance, r_i.
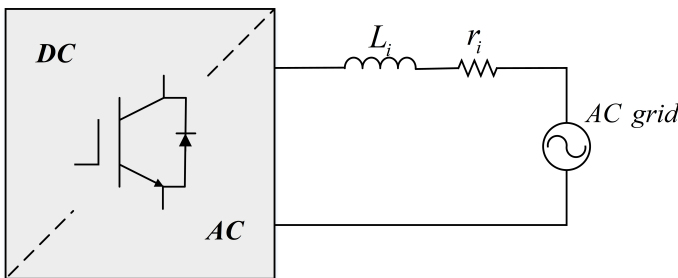
Fig. 4. L filter circuit diagram.

The inductance value (L_i) in the filter L can be determined by considering the current fluctuation on the inverter output side [16], [21]. The analysis of current ripple for all switch

states of the inverter is a difficult task. Therefore, it is necessary to obtain an equation that provides the maximum current fluctuation value while considering the inverter structure. As the HNPC inverter transfers power to the grid, the input voltage is higher than the grid voltage, indicating that the HNPC inverter is a buck-type inverter. To determine the inductance value, the HNPC inverter can be simplified to a half-wave buck converter model at the switching frequency, as illustrated in Fig. 5 [17]. In this model, the neutral point of the inverter and the neutral point of the grid are short-circuited, and the grid has a half-sinusoidal waveform.
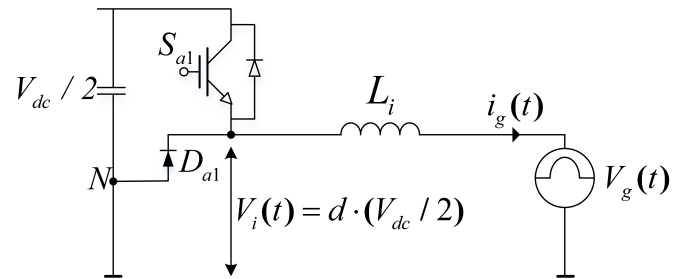
Fig. 5. Simplified HNPC inverter model.

The value of the inductance can be determined by using Eq. (5), which is derived from the analysis of the model in Fig. 5 in continuous current mode

$$L_i = \frac{\frac{V_{dc}}{2} - V_g}{2 \cdot \Delta I_L} \cdot \frac{d}{f_{sw}} \tag{5}$$

where d is the duty cycle, and the largest current ripple value (ΔI_L) occurs when the duty cycle is 50% [29]. Therefore, the inductance value is obtained as in Eq. (6).

$$L_i = \frac{\frac{V_{dc}}{2} - \frac{1}{2} \cdot \frac{V_{dc}}{2}}{2 \cdot \Delta I_L} \cdot \frac{1}{2 \cdot f_{sw}} = \frac{V_{dc}}{16 \cdot f_{sw} \cdot \Delta I_L} \tag{6}$$

The maximum amplitude value of the current ripple is calculated as in Eq. (7):

$$\Delta I_{L\,\max} = r \cdot \frac{P_i \cdot \sqrt{2}}{V_g} \tag{7}$$

where r denotes the ripple rate of the current transferred to the grid, and generally the current ripple rate is chosen as 10%–20% in LCL filter design [15], [30].

The L filter design process requires a balance between the need for a low value to maintain THD of the grid current within the limit set by international standards [31], and the need to avoid raising the inductance value too much, which would increase the filter size and cost. To strike this balance, the current ripple ratio was chosen as 10%, considering the impact of the inverter topology and control technique on the THD of the system. The system parameters used in the filter design are provided in Table 2. By using Eq. (6) and (7), the inductance value was calculated as $L_i = 3.85\, mH$.

Parameter	Value
Inverter output power (P_i)	$3\,kW$
DC bus voltage (V_{dc})	$500\,V$
Grid voltage amplitude (V_g)	$220\,V_{rms}$
Switching frequency (f_{sw})	$5\,kHz$

IV. LCL-TYPE FILTER DESIGN

The circuit diagram of the LCL filter placed between the inverter and the grid is shown in Fig. 6, where L_i denotes the inductance value on the inverter side, L_g denotes the inductance value on the grid side, and C_f denotes the filter capacitor. In addition, it symbolizes the r_i and r_g inductances' internal resistances.
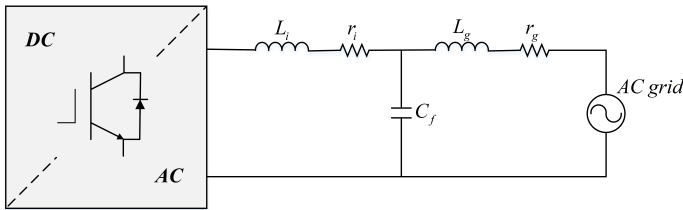
Fig. 6. LCL filter circuit diagram.

The inductance value on the inverter side is found with the help of Eq. (6) and (7). Considering the inductance value on the grid side, the current fluctuation rate was chosen as 20%.

While determining the filter capacitor value, the maximum power factor change acceptable by the grid is assumed to be 5%, and this value corresponds to 5% of the capacitor base value. Eq. (8) and (9) show the calculation of filter base values. The calculation of the filter capacitor value is given in Eq. (10).

$$Z_b = \frac{V_g^2}{P_i} \tag{8}$$

$$C_b = \frac{1}{2\pi f_g \cdot Z_b} \tag{9}$$

$$C_f = \%5 \cdot C_b \tag{10}$$

The inductance value on the grid side can be calculated using Eq. (11):

$$L_g = k \cdot L_i \tag{11}$$

where k denotes a constant correlation coefficient between the inverter and the grid-side inductances. This coefficient takes a value in the $0 < k \le 1$ range, and usually a value of 1 or close to 1 can be selected in high power applications.

To ensure that the LCL filter effectively suppresses harmonic distortion within the switching frequency range, it is necessary to meet the requirement statedin Eqs. (12):

$$10 f_g \le f_{res} \le \frac{1}{2} f_{sw} \tag{12}$$

where f_{res} is the resonant frequency of the filter and is expressed by Eqs. (13) [32].

$$f_{res} = \frac{\sqrt{\frac{L_i + L_g}{L_i \cdot L_g \cdot C_f}}}{2\pi} \tag{13}$$

By using above equations, the inductors and capacitor values have been calculated as $L_i = 1.62\,mH, L_g = 0.6\,mH, C_f = 9.87\,\mu F$, and $f_{res} = 2422.28\,Hz$.

V. SIMULATION RESULTS

In order to evaluate the effectiveness of L and LCL filter topologies with single-phase HNPC inverters in mitigating harmonic distortion and their impact on grid current, a modeling study was carried out using MATLAB/Simulink®. The simulation utilized system parameters and calculated filter values, which are presented collectively in Table 3.

Parameter	Value (L filter)	Value (LCL filter)
Inverter output power (P_i)	$3\,kW$	$3\,kW$
DC bus voltage (V_{dc})	$500\,V$	$500\,V$
Inverter-side inductance (L_i)	$3.85\,mH$	$1.62\,mH$
Grid-side inductance (L_g)	×	$0.6\,mH$
Filter capacitance (C_f)	×	$9.87\,\mu F$
Grid voltage amplitude (V_g)	$220\,V_{rms}$	$220\,V_{rms}$
Switching and grid frequencies (f_{sw}, f_g)	$5\,kHz, 50\,Hz$	$5\,kHz, 50\,Hz$
Sampling time (T_s)	$1\,\mu s$	$1\,\mu s$

Fig. 7 and 8 show MATLAB/Simulink®-based modeling of a single-phase grid-connected HNPC inverter circuit with L and LCL filters, respectively. In both models, the inverter topology (HNPC), switching technique (SPWM), and control method (SMC) are used similarly. In addition, as seen in Fig. 8, the control of the grid current with appropriate damping is provided by controlling the capacitor voltage. Therefore, proportional-resonant (PR) control, which has an excellent AC signal tracking feature, is used to generate the reference value of the capacitor voltage.

The waveforms of the grid voltage and current for both L and LCL filters are illustrated in Fig. 9. It can be observed that the current transferred to the grid experiences fewer fluctuations with an LCL filter connection as compared to an L filter connection. It is evident that in both filter topologies, the grid current follows a sinusoidal waveform and remains in-phase with the grid voltage. By aligning the grid current and voltage, the power factor can be improved such that it approaches or equals one, thereby decreasing the consumption of reactive power.

In the L and LCL filter connection states, the active power transferred to the grid with the fundamental frequency (50 Hz) component is shown in Fig. 10. In the case of an L filter connection, 2943 W of active power is transferred to the grid, while in the case of an LCL filter connection, 2954 W of active power is transferred. Both filter topologies result in nearly zero reactive power due to their design. The LCL filter provides superior harmonic attenuation, resulting in lower amplitudes of harmonic components (excluding the fundamental frequency)
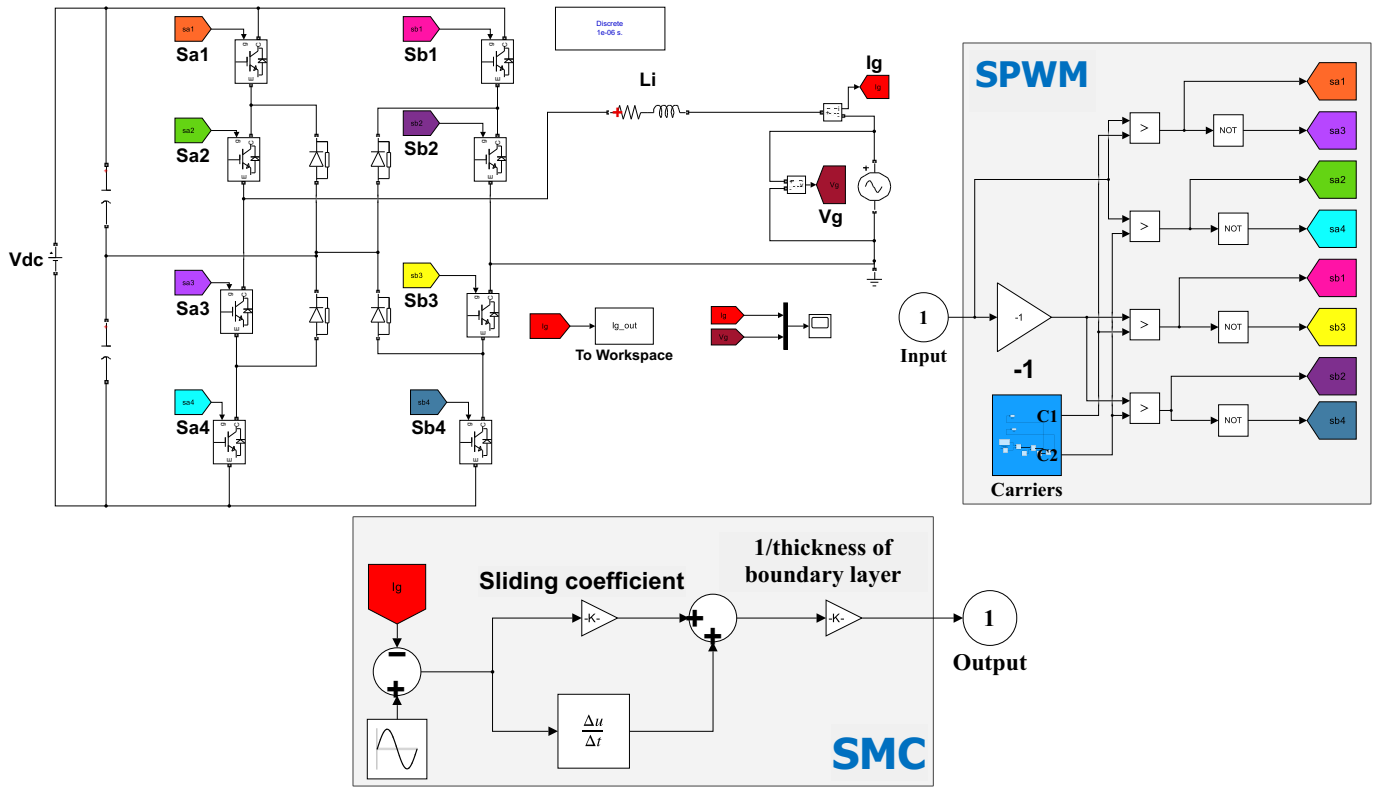
Fig. 7. L filter simulink model.
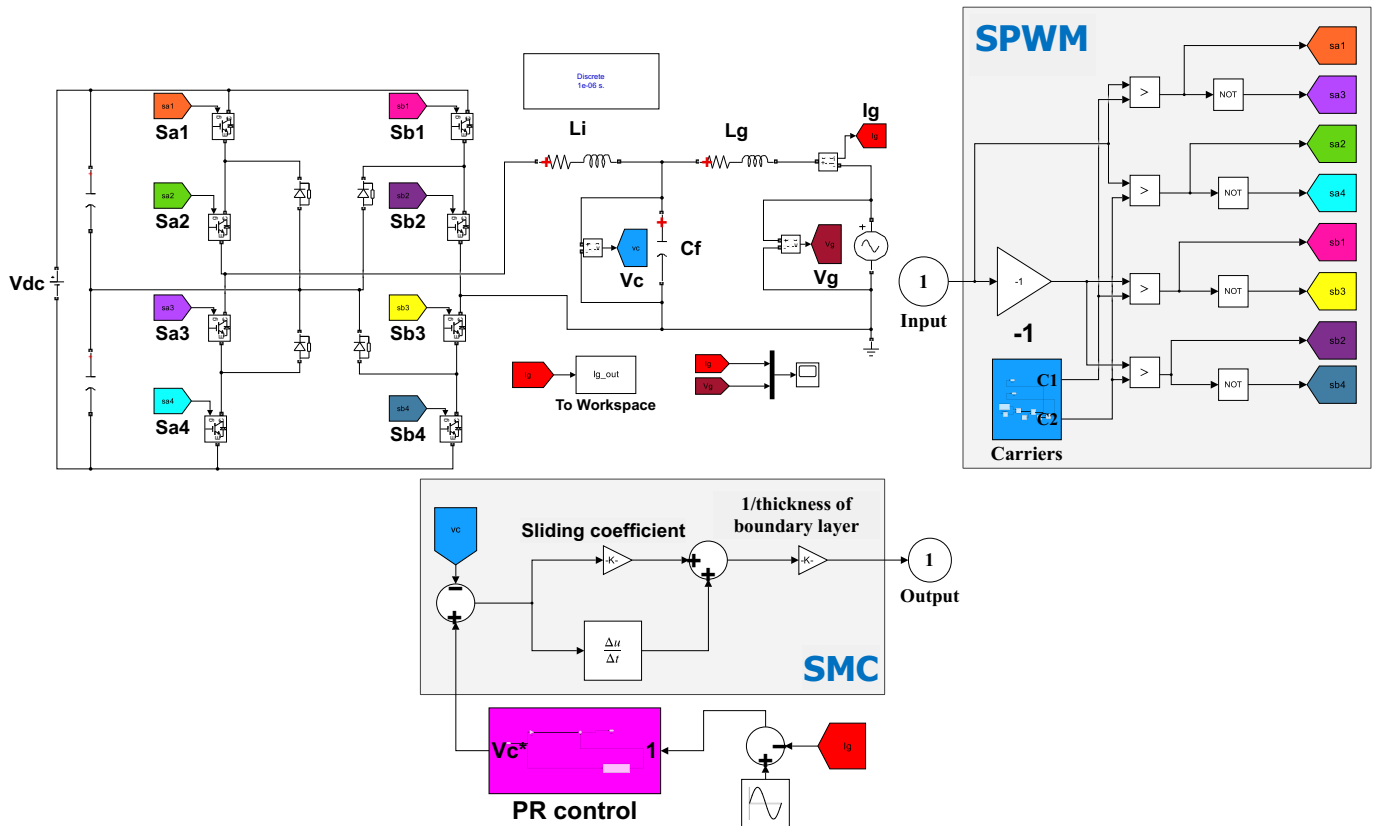
Fig. 8. LCL filter simulink model.
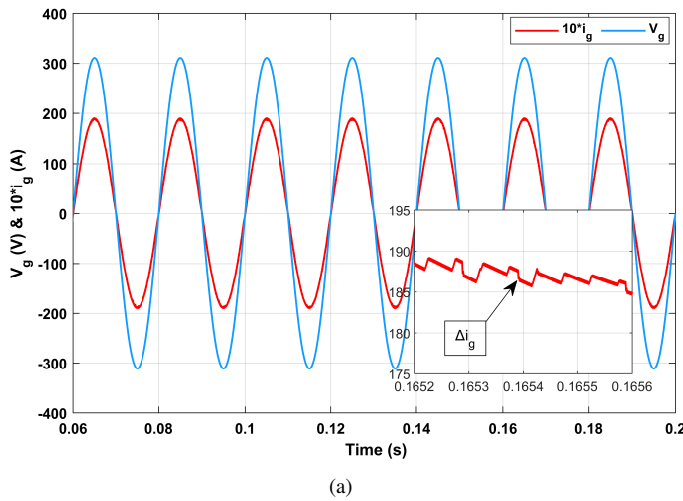
(a)
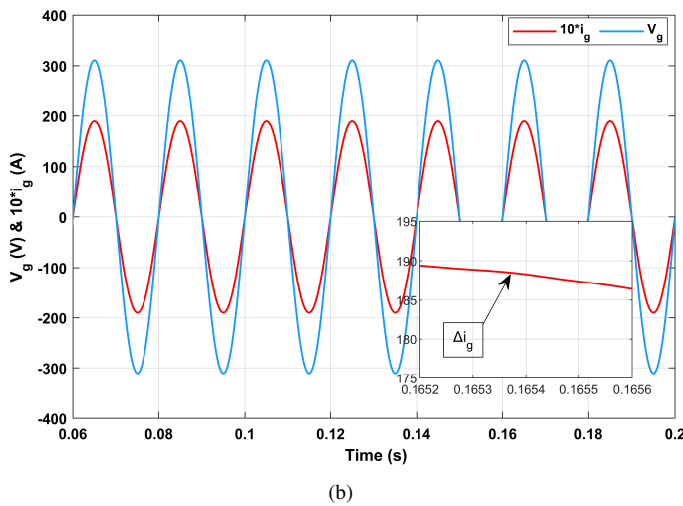
(b)

Fig. 9. Grid current and voltage waveforms a) for L filter b) for LCL filter.
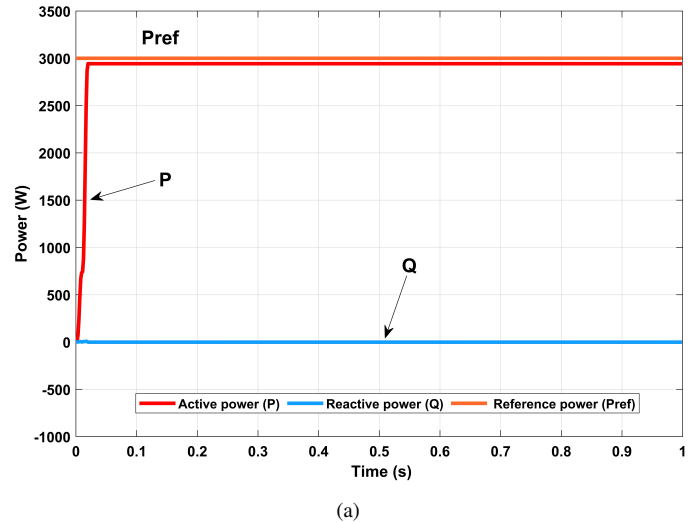
(a)
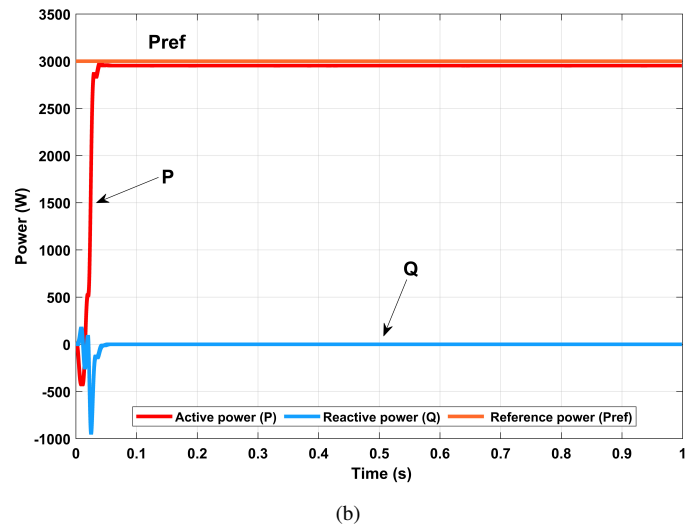
(b)

Fig. 10. Active power transferred to the grid a) for the L filter b) for the LCL filter.

and higher amplitudes of the fundamental frequency component. As a result, the LCL filter enables greater transmission of active power to the grid when compared to the L filter.

The FFT analysis tool in Power GUI was used to perform THD analysis of the grid current for both L and LCL connection states, and the results are presented in Fig. 11. The figure illustrates that the THD values of the grid current for L and LCL connection states are 1.56% and 0.07%, respectively. Moreover, it is apparent that the grid current in both cases, particularly with the LCL filter, consists of odd harmonic components, whose amplitudes are significantly smaller than those of the fundamental frequency components.

The comparison of L and LCL filters based on the obtained results is given in Table 4. Although LCL filters require an additional damping method or control of the capacitor voltage due to the resonance problem, they are seen to be advantageous in terms of harmonic attenuation, efficiency, and grid current fluctuation. In addition, the fact that they require a lower inductance value compared to L filters reduces power loss and contributes to the efficiency of the system.

TABLE IV
COMPARISON OF L AND LCL FILTERS.

Comparison category	L filter	LCL filter
Harmonic attenuation performance	Good	Very good
Current fluctuation	Acceptable	Low
Resonance damping	Not applicable	Naturally
THD value of grid current	1.56%	0.07%
Inverter efficiency	98.1%	98.46%

VI. CONCLUSION

In this study, two filter topologies, L and LCL, commonly used in grid-connected renewable energy systems, were an-

(a)

(b)
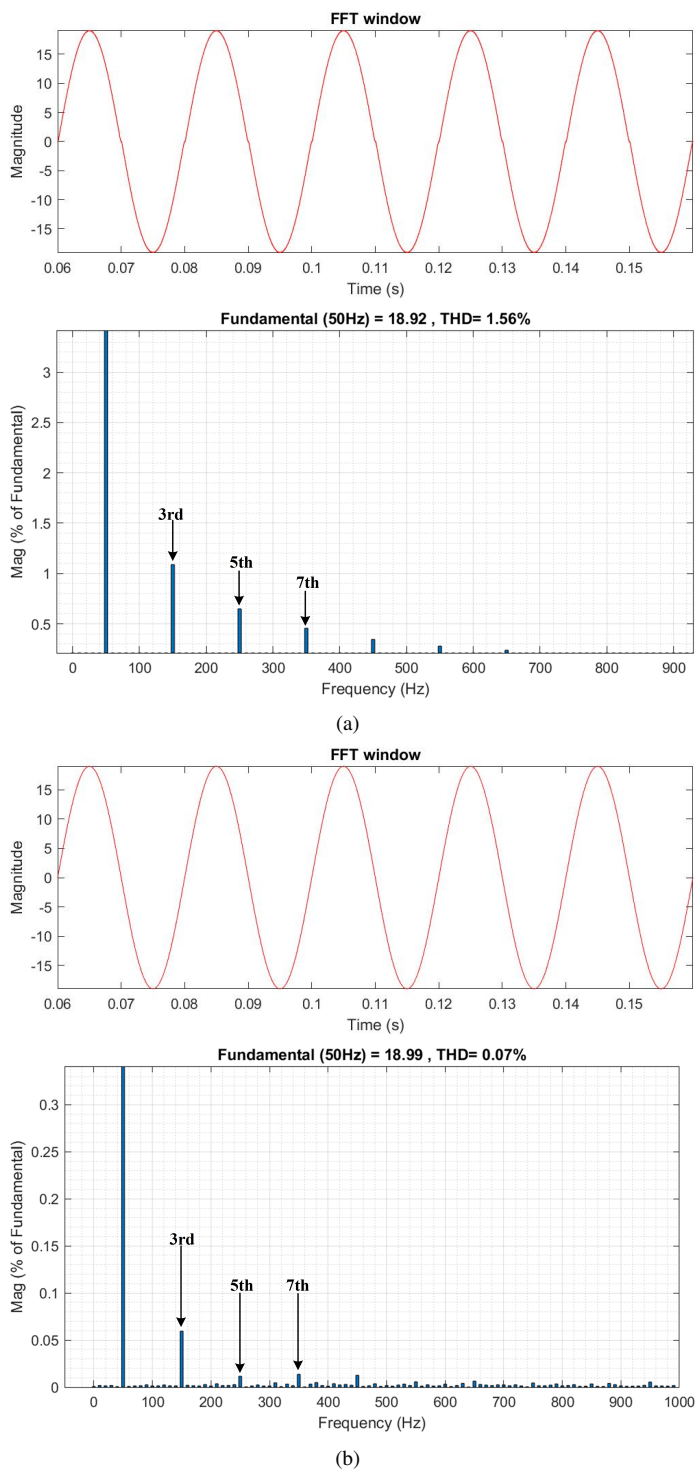
Fig. 11. Grid current THD analysis a) for L filter b) for LCL filter.

alyzed.Both filter topologies were designed for the HNPC inverter, and their harmonic attenuation performances were compared, along with their effects on the current and power transferred to the grid. In order to make the analysis more realistic, all components (inverter topology, switching technique, control method, parameters used in the control method, simulation configuration) that could affect the results were kept similar in both filter types. The simulation results showed

that the THD value of the grid current was within the limits specified by international standards (IEEE 1547, IEC 61727) for both filter topologies. However, the LCL filter exhibited better harmonic attenuation performance with a lower inductance value compared to the L filter. In addition, the LCL filter provided lower current fluctuation and allowed more active power transfer to the grid. The resonance problem in the LCL filter is naturally dampened by controlling the capacitor voltage without the need for an additional damping method. Furthermore, the grid current was successfully controlled via the control of the capacitor voltage. The HNPC inverter used in this study has a multi-level output, which inherently results in a lower THD value compared to other inverter topologies. As a result, with the use of a suitable control method, it can be applied in an L filter topology that does not require a high inductance value, while still ensuring that the THD value remains within the limits specified by international standards.

The study does not provide a detailed description of the control method. In future work, a comprehensive analysis of the entire system and the grid current will be conducted, along with a thorough explanation of the control method.

REFERENCES

[1] I. E. Agency, *World Energy Outlook 2022*, 2022.
[2] F. Blaabjerg, D. M. Ionel, Y. Yang, and H. Wang, "Renewable energy systems: Technology overview and perspectives," *Renewable Energy Devices and Systems with Simulations in MATLAB® and ANSYS®*, pp. 1–16, 2017.
[3] I. R. E. Agency, *Future of Solar Photovoltaic: Deployment, investment, technology, grid integration and socio-economic aspects (A Global Energy Transformation: paper)*, 2019.
[4] H. Noh, K. Kang, and Y. Seo, "Environmental and energy efficiency assessments of offshore hydrogen supply chains utilizing compressed gaseous hydrogen, liquefied hydrogen, liquid organic hydrogen carriers and ammonia," *International Journal of Hydrogen Energy*, vol. 48, no. 20, pp. 7515–7532, 2023.
[5] M. H. Mohamed Hariri, M. K. Mat Desa, S. Masri, and M. A. A. Mohd Zainuri, "Grid-connected pv generation system—components and challenges: A review," *Energies*, vol. 13, no. 17, 2020.
[6] I. Sefa and N. Altin, "Grid interactive photovoltaic inverters-a review," *Journal of the Faculty of Engineering and Architecture of Gazi University*, vol. 24, no. 3, 2009.
[7] S. Kouro, J. I. Leon, D. Vinnikov, and L. G. Franquelo, "Grid-connected photovoltaic systems: An overview of recent research and emerging pv converter technology," *IEEE Industrial Electronics Magazine*, vol. 9, no. 1, pp. 47–61, 2015.
[8] M. İnci and Ömer Türksoy, "Review of fuel cells to grid interface: Configurations, technical challenges and trends," *Journal of Cleaner Production*, vol. 213, pp. 1353–1370, 2019.
[9] M. Obi and R. Bass, "Trends and challenges of grid-connected photovoltaic systems – a review," *Renewable and Sustainable Energy Reviews*, vol. 58, pp. 1082–1094, 2016.
[10] N. Rasekh and M. Hosseinpour, "Lcl filter design and robust converter side current feedback control for grid-connected proton exchange membrane fuel cell system," *International Journal of Hydrogen Energy*, vol. 45, no. 23, pp. 13 055–13 067, 2020.
[11] T. Duman, S. Marti, M. A. Moonem, A. A. R. Abdul Kader, and H. Krishnaswami, "A modular multilevel converter with power mismatch control for grid-connected photovoltaic systems," *Energies*, vol. 10, no. 5, 2017.
[12] E. Kabalcı, "Review on novel single-phase grid-connected solar inverters: Circuits and control methods," *Solar Energy*, vol. 198, pp. 247–274, 2020.
[13] X. Ruan, X. Wang, D. Pan, D. Yang, W. Li, and C. Bao, *Control techniques for LCL-type grid-connected inverters*. Springer, 2018.
[14] C. Gurrola-Corral, J. Segundo, M. Esparza, and R. Cruz, "Optimal lcl-filter design method for grid-connected renewable energy sources," *International Journal of Electrical Power Energy Systems*, vol. 120, p. 105998, 2020.

[15] M. Liserre, F. Blaabjerg, and S. Hansen, "Design and control of an lcl-filter-based three-phase active rectifier," *IEEE Transactions on Industry Applications*, vol. 41, no. 5, pp. 1281–1291, 2005.

[16] Y. Kim, H. Cha, B.-M. Song, and K. Y. Lee, "Design and control of a grid-connected three-phase 3-level npc inverter for building integrated photovoltaic systems," in *2012 IEEE PES Innovative Smart Grid Technologies (ISGT)*, 2012, pp. 1–7.

[17] S. V. Araujo, A. Engler, B. Sahan, and F. L. M. Antunes, "Lcl filter design for grid-connected npc inverters in offshore wind turbines," in *2007 7th Internatonal Conference on Power Electronics*, 2007, pp. 1133–1138.

[18] F. Sebaaly, H. Vahedi, H. Y. Kanaan, N. Moubayed, and K. Al-Haddad, "Sliding mode fixed frequency current controller design for grid-connected npc inverter," *IEEE Journal of Emerging and Selected Topics in Power Electronics*, vol. 4, no. 4, pp. 1397–1405, 2016.

[19] H. Komurcugil, S. Ozdemir, I. Sefa, N. Altin, and O. Kukrer, "Sliding-mode control for single-phase grid-connected LCL-filtered vsi with double-band hysteresis scheme," *IEEE Transactions on Industrial Electronics*, vol. 63, no. 2, pp. 864–873, 2016.

[20] S. Ozdemir, N. Altin, H. Komurcugil, and I. Sefa, "Sliding mode control of three-phase three-level two-leg npc inverter with lcl filter for distributed generation systems," in *IECON 2018 - 44th Annual Conference of the IEEE Industrial Electronics Society*, 2018, pp. 3895–3900.

[21] A. Reznik, M. G. Simões, A. Al-Durra, and S. M. Muyeen, "*lcl* filter design and performance analysis for grid-interconnected systems," *IEEE Transactions on Industry Applications*, vol. 50, no. 2, pp. 1225–1232, 2014.

[22] Y. Jia, J. Zhao, and X. Fu, "Direct grid current control of lcl-filtered grid-connected inverter mitigating grid voltage disturbance," *IEEE Transactions on Power Electronics*, vol. 29, no. 3, pp. 1532–1541, 2014.

[23] N. Altin, S. Ozdemir, H. Komurcugil, and I. Sefa, "Sliding-mode control in natural frame with reduced number of sensors for three-phase grid-tied lcl-interfaced inverters," *IEEE Transactions on Industrial Electronics*, vol. 66, no. 4, pp. 2903–2913, 2019.

[24] Y. Yang and F. Blaabjerg, "Overview of single-phase grid-connected photovoltaic systems," in *Renewable Energy Devices and Systems with Simulations in MATLAB® and ANSYS®*. CRC Press, 2017, pp. 41–66.

[25] T. Duman and M. Cengiz, "Comparative analysis of thd performances of different carrier based pwm techniques for single phase 5-level npc multilevel inverter." in *International Conference on Innovative Academic Studies (ICIAS 2022)*, 2022, pp. 937–944.

[26] S. Bayhan and H. Komurcugil, "A sliding-mode controlled single-phase grid-connected quasi-z-source npc inverter with double-line frequency ripple suppression," *IEEE Access*, vol. 7, pp. 160 004–160 016, 2019.

[27] H. Komurcugil, S. Biricik, S. Bayhan, and Z. Zhang, "Sliding mode control: Overview of its applications in power converters," *IEEE Industrial Electronics Magazine*, vol. 15, no. 1, pp. 40–49, 2021.

[28] F. Bagheri, H. Komurcugil, O. Kukrer, N. Guler, and S. Bayhan, "Multi-input multi-output-based sliding-mode controller for single-phase quasi-z-source inverters," *IEEE Transactions on Industrial Electronics*, vol. 67, no. 8, pp. 6439–6449, 2020.

[29] R. W. Erickson and D. Maksimovic, *Fundamentals of power electronics*. Springer Science Business Media, 2007.

[30] P. Gakhar and M. Gupta, "Harmonic mitigation in a transformer less grid connected solar pv system using modified lcl filter," in *2018 3rd International Conference and Workshops on Recent Advances and Innovations in Engineering (ICRAIE)*, 2018, pp. 1–4.

[31] A. Karafil, "Tek fazlı Şebeke bağlantılı eviricilerde l, lcl ve llcl tipi filtre tasarımı[design of l, lcl and llcl type filter for single phase grid connected inverters]," *Karadeniz Fen Bilimleri Dergisi*, vol. 12, no. 1, pp. 448 – 460, 2022.

[32] K. A. El Wahid Hamza, H. Linda, and L. Cherif, "Lcl filter design with passive damping for photovoltaic grid connected systems," in *IREC2015 The Sixth International Renewable Energy Congress*, 2015, pp. 1–4.

Muhammet Cengiz was born in Erzurum, Turkey, in 1994. In 2018, he graduated from Erzurum Atatürk University with a bachelor's degree in Electrical and Electronics Engineering. He is currently a master's student at Erzurum Technical University's Department of Electrical and Electronics Engineering and has been working as a research assistant in the same department since 2022. His current research interests include power electronics, multi-level power converters, sliding mode control, and renewable energy systems.

Turgay Duman was born in Erzurum located in the eastern region of Turkey. He studied Electrical and Electronic Engineering and earned a Bachelor's degree in Engineering from Ataturk University in 2010. He worked as an Electrical Engineer at Information Technologies and Communication Authority in 2011 in Erzurum, Turkey. He recieved his Master's and Ph.D degrees in Electrical Engineering from The University of Texas at San Antonio in 2014 and 2019, respectively. His research areas include power electronics, renewable energy systems, multi-level power converters, real-time simulations, and large sacale PV systems. He is currently working as an assistant professor at Erzurum Technical University.

Research Article

Detection of Various Diseases in Fruits and Vegetables with the Help of Different Deep Learning Techniques

Sevil Ozcan and Emrullah Acar

Abstract— **Fruit and vegetable diseases have an important place in the food sector in terms of sustainable agricultural policies. Therefore, these diseases reduce the productivity of the crop and adversely affect the food supply. These deteriorations in fruits and vegetables are not desired by the consumer. When these deteriorations are encountered, it not only causes loss of reputation for tradesmen, but also causes serious economic losses. In this context, it is thought that the use of deep learning techniques will be useful in detecting diseased products in agriculture. While the fruit or vegetable is still in the harvest period, it can be determined whether the product is diseased or not by looking at the leaves. Thus, the precautions that can be taken during the harvest period will ensure the production of quality and healthy products. In this study, it was aimed to detect 10 different diseases in tomato and strawberry using two different deep learning techniques (CNN and Resnet50). Our data set consists of 1055 tomato and 1238 strawberry images. In the next step, a total of 2293 images were increased to 13758 images by using image augmentation techniques. As a result, 67.1% success was achieved with the help of CNN architecture. In the following periods, it is aimed to obtain better performance rates with better and sufficient hardware by using an isolated and balanced distributed data set.**

I. INTRODUCTION

VEGETABLES AND fruits, one of the most important issues in the food industry, constitute an important and large part of the plant production cycle. Fruits and vegetables

SEVIL OZCAN, is with Department of Electrical Engineering University of Batman University, Batman, Turkey,(e-mail: bajece@hotmail.com).

https://orcid.org/0000-0002-2306-6008

EMRULLAH ACAR, is with Department of Electrical Engineering University of Batman University, Batman, Turkey,(e-mail: bajece@hotmail.com).

https://orcid.org/0000-0002-2306-6008

getting sick is one of the factors that the consumer does not want to encounter, which is the end point of consumption. When this situation occurs, the tradesman who offers the diseased product to the end consumer loses his reputation in the eyes of the consumer. These sick products, which are not preferred by the end consumer, return to the tradesmen as a serious economic loss. Producers who cannot carry out the necessary intervention and precaution activities suffer economic losses due to increasing product losses. This damage is reflected from manufacturers to retailers and food wholesalers. Spoils occurring in fruit and vegetable products are generally at the expense of the final consumer. It causes the product to be cautious to the point where it spoils. As with many plant products, vegetable and fruit diseases also cause deformities. Similar to this situation, image processing techniques used in the detection of various diseases such as tumor cell detection; Just as it detects diseases based on shape changes in organs in the human body, this condition can also be detected in fruits and vegetables. Thus, it is thought that precautions can be taken during the production phase [1]. There are very limited resources in the literature for disease detection of fruits and vegetables. One of the first studies in the field of disease detection of fruits and vegetables was carried out by Wen and Tao (1997). It has developed a system that grades fruit according to color, surface and size defects in accordance with OECD standards in order to estimate fruit quality and offer fresh market opportunities. In this proposed study, they developed a system that automatically grades color and size and thus separates damaged fruits. Their study is based on a model that assumes that fruits and vegetables have a spherical structure with diameters that vary depending on their size and shape. Additionally, it can analyze more than five vegetables or fruits per second for each grade [2].

The first steps in the field of disease detection and quality control in vegetables and fruits represent great progress for the food industry in general. In the 21st century, where technology is increasingly advanced, the study of Wen and Tao (1997) was the first step in this field. In the food industry, effective solutions have continued to be developed to control and continuously improve the quality of fruits and vegetables produced.

Deep learning and artificial intelligence (AI) technologies have become the most important tools used in the detection of fruit diseases in recent years. Improved image processing techniques and deep learning algorithms allow producers and retailers to evaluate the quality and condition of fruits much more

precisely. For example, Convolutional Neural Network (ESA/CNN) is a deep learning model. This model can detect diseases and defects on vegetables and fruits. After the system carries out this learning task, it can predict the defect and disease of a diseased vegetable or fruit. This is especially useful for large-scale farming operations. Because farmers and agricultural workers do not need to individually control thousands or even millions of fruits. Some of the studies conducted in this field in the literature are as follows:

Jolly & Raman (2017), using computer vision in their study, recorded the highest accuracy ranging between 85.93% and 95.31% through SVM and K-NN for disease and diagnosis in apples [3]. Aslan (2021) proposed the detection of diseases in peach trees using a convolutional neural network (CNN) in his study titled "Detection of Peach Diseases with Deep Learning". This method was implemented using a pre-trained AlexNet model and tested on a dataset containing real disease images from the TRB1 region. 99.30% accuracy was achieved in the experiments [4]. In the study by Terzi et al. (2023), a new CNN model consisting of 15 layers was developed, and the performance rate of the model consisting of 1028 images was obtained as 96.10% [5]. Sevli's work (2023), "Detection of Apple Plant Diseases with Deep Learning", includes agricultural sustainability and the importance of deep learning in combating diseases. By applying an ESA-based classification to the data set consisting of 1821 images, 98.76% accuracy was achieved [6]. Acar et al. (2022) used various machine learning techniques in the detection of plant diseases caused by pathogens. As a result, they achieved high performance [7].

The main purpose of this study is to easily detect fruit and vegetable diseases. For the purpose of the study, ResNet50 and Convolutional Neural Networks (CNN), which are deep learning architectures, were used and a system that can detect disease was designed. The performance rates of these two architectures were compared and it was determined that the most successful result was obtained in the model trained using Convolutional Neural Networks (CNN). The contributions of this study, which aims to detect fruit and vegetable diseases, to the literature are as follows;

a) Prevention of fruit and vegetable diseases,

b) Preventing economic damages from production to the end consumer,

c) With the proposed architecture, a new approach has been proposed for strawberry and tomato diseases for the first time.

II. MATERIAL AND METHOD

A. Dataset Collection

In the literature, there are very few studies using image recognition techniques to detect tomato and strawberry diseases together. The reasons for this situation are; the current data set is not sufficient and there is no comprehensive data set to ensure the diversity of the study. In this study, 1055 tomatoes and 1238 strawberries; a total of 2293 images of one type of fruit and one type of vegetable were employed. By applying data augmentatıon operations such as rotation, cropping, zooming, inverting and contrasting to the images in the data set, the total number of images was increased from 2293 to 13758. There are 7 disease classes for strawberry and 3 classes for tomato in the disease data set. These are 3 vegetable diseases for tomatoes: Tomato blight, Tomato leaf mold and Tomato spider mites [8]. For strawberry, it is seen as Strawberry angular leaf spot, Strawberry anthracnose, Strawberry flower blight, Strawberry gray mold, Strawberry leaf spot, Strawberry fruit powdery mildew and Strawberry leaf powdery mildew [9]. Figure 1 shows images for two sample classes.
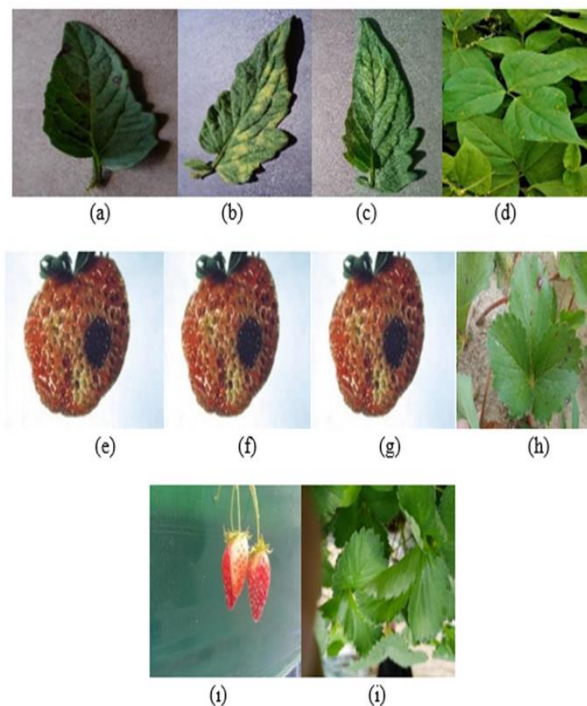
Fig.1. Sample images of Strawberry and Tomato diseases. (a) Tomato Blight, (b) Tomato Leaf Mold, (c) Tomato Spider Mites, (d) Strawberry Angular Leaf Spot, (e) Strawberry Anthracnose, (f) Strawberry Blossom Blight, (g) Strawberry Gray Mold, (h) Strawberry Leaf Spot, (ı) Strawberry Powdery Mildew Fruit, (i) Strawberry Powdery Mildew Leaf

B. The Recommended System Architecture

The proposed system architecture consists of four different stages, as seen in the block diagram in the figure.

(a) Obtaining Image Dataset (Image Augmentation),

(b) Image Preprocessing (Filtering),

(c) Deep Learning (CNN and ResNet)

(d) Classification Metrics (Accuracy, Precision, Recall, F1-Score)
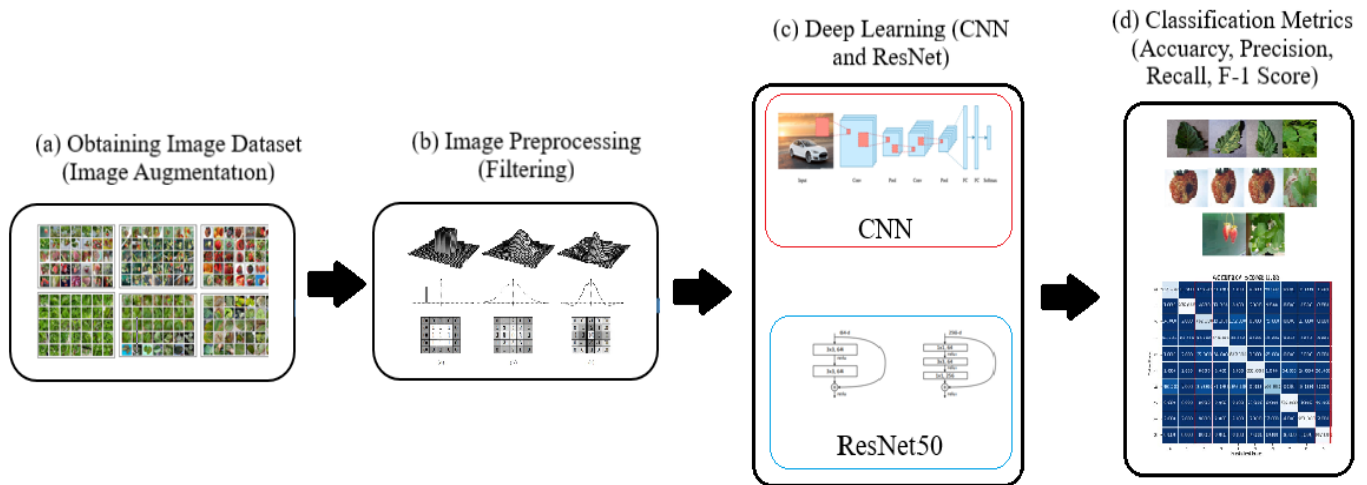
Fig.2. The Recommended System Archıtecture

III. METHOD

A. Deep Learning

In general, deep learning can be defined as an artificial intelligence method that is created by combining multiple artificial neural networks and is generally used in processes such as image recognition. In 2006, it has been shown by the supervised propagation method how the feedforward neural network provides learning [10]. The term deep learning was first used by Igor Aizenberg et al. in 2000. It was used by [11]. The concept of "Deep" in the expression Deep Learning refers to the amount of layers in the network. As the number of layers in a deep learning architecture increases, the network becomes deeper. This provides computers with the ability to perform larger calculations and makes it easier for computers to learn. Two separate deep learning algorithms were used in this study. These; Convolutional Neural Networks (CNN) and ResNet50. The main difference between these algorithms is the number of layers and model structure.

1) Convolutıonal Neural Networks (CNN)

One of the most successful models for feature extraction on image data is Convolutional Neural Networks (CNN). CNN can learn down to the deepest features of images. Pre-trained deep learning models can be used to solve many different problems, especially since they are trained on large and diverse data sets. Slightly tuning ("fine-tuning") the weights of these models to solve a specific problem often makes it possible to achieve high performance with less data. In this case, the final layers of the model are usually rearranged on a problem-specific basis and

the model is retrained with fewer iterations on the new data set. The advantage of this approach is to save calculation time and get better results with less data.

2) ResNet50

It is a deep learning architecture frequently used in image detection and classification. ResNet, which has 23 million parameters and consists of approximately 152 layers, aims to improve the bottleneck in learning. Figure 3 shows the "redundant" blocks that provide bottlenecks for ResNET50 and ResNET architectures [12]. There are four parameters to evaluate the performance of the models. These; F-1 score, recall, accuracy and precision [13-14].
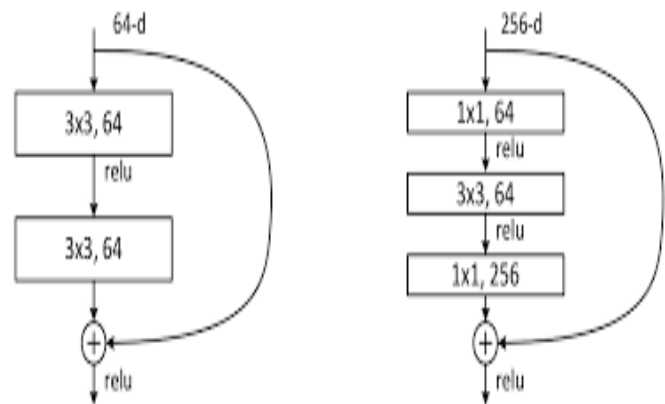
Fig.3. A deeper residual function building block in the ResNet structure and a "bottleneck" building block in ResNet-50[15]

IV.   RESULTS AND DISCUSSION

Two different deep learning architectures (CNN and ResNet50) were utilized in this study. 10 layers were then preferred for the CNN model created and the training phase of
this model lasted 18 hours in 15 epochs. The training phase of ResNet model lasted 8 hours in 15 epochs.
The models created were developed on a Microsoft Windows Server 2019 x64 bit operating computer with Microsoft Visual Studio 1.81 Intel Xeon E7-8893 v4 CPU 3.20 Ghz. Python has been a preferred programming language because it is relatively low effort and fast compared to other programming languages. In this study, software was developed using the TensorFlow backend engine and Keras library in the Microsoft Visual Studio 1.81 environment.
After that, 1055 tomato and 1238 strawberry images in the training data set were subjected to data augmentatıon (rotation, cropping, zooming, inverting and contrasting). In total, 13758 images were obtained from 2293 images.
Later, a 10-layer CNN model was employed for the data obtained from data augmentatıon. The training time of the CNN model took 18 hours and the process repeated in 15 epochs. After training, the model was tested with images in the test data set, which constitutes 1/4 of the data set. Finally, a performance of 67.1% was achieved for the CNN model.

The loss and performance graphs of the CNN model in the training result are as in Figure 4.
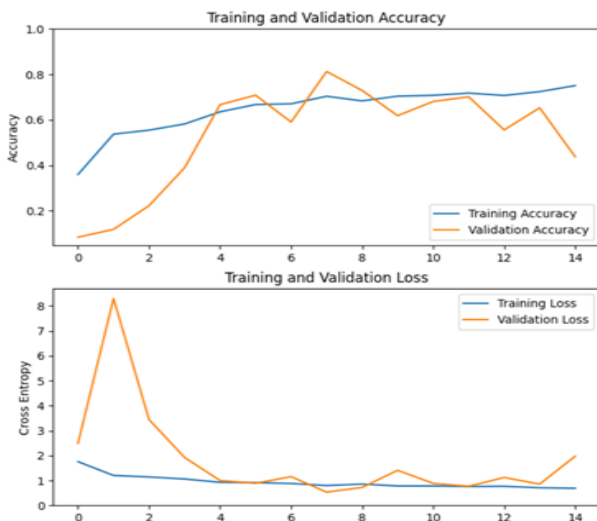
Fig.4. CNN Model Loss and Accuracy Graphs

Again, in this study, there was a model training phase lasting 8 hours in 15 epochs using the ResNet50 model, which is another deep learning architecture. Similarly, testing was carried out with the images in the test data set and a performance of 52.3% was achieved. The loss and accuracy graphs of the training result of the ResNet50 model are given in Figure 5.
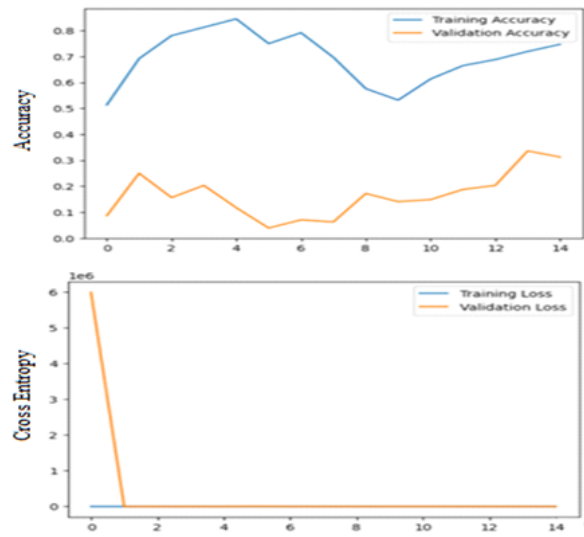
Fig.5. ResNet50 Model Loss and Accuracy Graphs

Test results and performance metrics of the CNN and ResNet50 models are as in Table I.

TABLE I

THE PERFORMANCE METRICS OF CNN AND RESNET50 MODELS

MODEL	Accuracy	Precision	Recall	F1-Score
ResNet50	52.3 %	0.56	0.49	0.52
CNN	67.1%	0.73	0.59	0.65

Finally; when the images in the test data set are introduced to the proposed model, which has completed the training phase, it detects the relevant disease and prints it on the screen. Figure 8 shows the CNN model screen output that detects an example tomato leaf mold disease.

In this part, the results of two different deep learning architectures are given in Table 1. While the accuracy value of the test data applied to the CNN model was determined as 67.1%; In the Resnet50 model, this value was found to be 52.3%.

Fig.6. Screenshot of real-time sick fruit recognition system

If we talk about the reasons for the low performance rates of this study; it can be due to that the unbalanced distribution of the data belonging to the classes in the data set, the limited and low number of epochs due to the insufficiency of the video card, the server insufficiency, and the large number of classes in the data set and the similarity of these classes to each other. Moreover, the processing time comparison of CNN and ResNet50 models is shown in Table II.

TABLE II
THE PROCESSING TIME COMPARISON OF CNN AND RESNET50 MODELS

MODEL	Epoch	Duratıon
CNN	15	18 hours
ResNet50	15	8 hours

A comparison of some studies with different inheritances in the literature is presented in Table III. There is no study with a similar structure to the data set in this proposed study. Therefore, it is only possible to compare it with other types of data.

TABLE III
COMPARISON WITH OTHER STUDIES

Study	Method	Data Type	Accuracy
Jolly&Raman (2017)[3]	SVM+K-NN	Apple	85.93%
Aslan (2021) [4]	CNN+AlexNet	Peach	99.30%
Terzi, Özgüven ve Yağcı (2023)[5]	CNN	Grape	96.10%
Sevli (2023)[6]	CNN	Apple	98.76%
Proposed Study	CNN	Tomato+Strawberry	67.1%

V. CONCLUSION

Vegetable and fruit diseases affect all consumers, from the producer to the final consumer. In the proposed work, it was aimed to detect diseases of fruits and vegetables and intervene in the early period, prevent serious economic losses and provide fresh market opportunities to consumers. In this context, CNN and ResNet50 models from deep learning architectures were preferred. In this study, 7 strawberry and 3 tomato disease classes were determined and the data set was used. Disease images were trained on two deep learning models and tested after this training. By making the application prepared in this study ready for real-time tests, it is aimed to create a video-based identification system with better hardware and more distinguishable data sets in the future.

In this work, the success of the models employed was compared with each other. These models were prepared for real-time application and more successful results could have been obtained with better hardware by using more isolated data. Moreover, it is envisaged that a video-based detection system can be created to detect vegetable and fruit diseases in mobile systems used in production lines or packaging systems. In addition, by developing the system designed in this study, it is possible to recognize the product in pre-harvest and not yet germinated fruit leaves. An application related to fruits and vegetables that all consumers can use in daily life will be examined comprehensively and it will be determined whether this application works on smartphones and whether it can be used without requiring touch. Such research will make a significant contribution to the prevention of fruit diseases and the economic damage from production to the end consumer.

VI. REFERENCES

[1] Nakano, K. (1997). Application of neural networks to apple color grading. Computer and Electronics in Agriculture, 18 (2–3), 105–116.

[2] Zhang, B., Huang, W., Li, J., Zhao, C., Fan, S., Wu, J., & Liu, C. (2014). Computer vision principles, developments and applications for external quality control of fruits and vegetables: A review. International Food Research. Elsevier Ltd. https://doi.org/10.1016/j.foodres.2014.03.012

[3] Jolly, P., & Raman, S. (2017). Analysis of Surface Defects in Apples Using Gabor Properties. In - Papers 12th International Conference on Signal Display Technology and Internet-based systems, SITIS 2016 (pp. 178-185). Institute of Electrical and Electronics Engineers Inc. https://doi.org/10.1109/SITIS.2016.36

[4] Aslan, M. (2021). Derin Öğrenme ile Şeftali Hastalıkların Tespiti. Avrupa Bilim ve Teknoloji Dergisi, (23), 540-546.

[5] Terzi, İ., Özgüven, M. M., & Yağcı, A. (2023). Derin Öğrenme Teknikleri ile Bazı Üzüm Çeşitlerinin Tespiti. Turkish Journal of Agriculture-Food Science and Technology, 11(1), 125-130.

[6] Sevli, O. (2022). Elma Bitkisi Hastalıklarının Derin Öğrenme İle Tespiti. International Euroasia Congress on Scientific Researches and Recent Trends 9, Antalya.

[7] Acar, E., Ertugrul, O. F., Aldemir, E., & Oztekin, A. (2022). Automatic identification of cassava leaf diseases utilizing morphological hidden patterns and multi-feature textures with a distributed structure-based classification approach. Journal of Plant Diseases and Protection, 129(3), 605-621.

[8] Banot, Mrs S. and PM, Dr. M. (2016). A fruit detection and grading system based on image processing. IJIREEICE, 4 (1), 47-52.

[9] Yapay Zeka ve Derin Öğrenme A-Z: TENSORFLOW https://www.udemy.com/course/yapayzeka/

[10] G.E. Hinton, "Learning multiple layers of representation," Trend Cogn. Sci., vol. 11, no. 10, pp. 428-434, Oct.2007

[11] I. N. Aizenberg, N. N. Aizenberg, and J. Vandewalle, "Multiple- Valued Threshold Logic and Multi- Valued Neurons," in Multi- Valued and Universal Binary Neurons, Boston, MA: Springer US, 2000, pp. 25-80.

[12] Targ, S. , Almeida, D., Lyman, K.(2016). Resnet in Resnet: Generalızıng Resıdual Archıtectures, Workshop track - ICLR 2016.

[13] Örenç, S., Emrullah, A., & Özerdem, M. S. (2022). Utilizing the ensemble of deep learning approaches to identify monkeypox disease. *Dicle Üniversitesi Mühendislik Fakültesi Mühendislik Dergisi*, *13*(4), 685-691.

[14] Turk, O., Ozhan, D., Acar, E., Akinci, T. C., & Yilmaz, M. (2022). Automatic detection of brain tumors with the aid of ensemble deep learning architectures and class activation map indicators by employing magnetic resonance images. *Zeitschrift für Medizinische Physik*.

[15] S. Targ, D. Almeida, K. Lyman, Resnet in Resnet: Generalızıng Resıdual Archıtectures, Workshop track - ICLR 2016. Vs He, K., Zhang, X., Ren, S., Sun, J., (2015). Deep Residual Learning for Image Recognition, Microsoft Research. arXiv:1512.03385v1 [cs.CV] 10 Dec 2015.

BIOGRAPHIES

SEVİL ÖZCAN Diyarbakır City, in 1996. She received the B.S. degrees in electrical and electronics engineering from the Dicle University, Diyarbakır, Turkey, in 2019. She is currently a graduate student in the Department of Electrical and Electronics Engineering at Batman University. Her research interests include digital image processing, machine learning and deep learning applications.

EMRULLAH ACAR received the B.S. degree in electrical and electronics engineering from Çukurova University, Adana, Turkey, in 2009, the M.S. degree in biomedical engineering from Istanbul Technical University, Istanbul, Turkey, in 2010, and the M.S. and Ph.D. degrees in electrical–electronics engineering from Dicle University, Diyarbakır, Turkey, in 2012 and 2017, respectively. He is currently an Associate Professor of electrical–electronics engineering with Batman University and also the head of the electronics division. His research interests include digital image processing, machine learning, and remote sensing applications. Dr. Acar received awards and honors include The Scientific and Technological Research Council of Turkey (TUBITAK) Grant, Erasmus Mobility Grant, Sweden, Internship Grant, Germany and Visiting Researcher, Czech Republic.

Research Article

Analysis and Compensation of Dead Time Harmonics Based on Time Compensation Strategy in the Single-Phase Full-Bridge Inverters

Umutcan Polat and Deniz Yildirim

Abstract—A short period, called dead time, is implemented to prevent power switching devices from shoot-through in voltage-source inverters (*VSI*). While adding dead time is required in the switching signals, it also causes negative effects on inverter operation such as distortion at output voltage due to significant number of harmonic components, and reduction in voltage magnitude of fundamental components. Eventually, the negative effects caused by dead time have to be compensated with compensation schemes. Different modulation schemes, which are called unipolar and bipolar switching, can be implemented in *VSI*, which in return might change the dead time effect. Although analysis of bipolar switching on the dead time effect has been implemented, analysis of unipolar switching is not addressed by most. In this paper, the effect of dead time on unipolar sinusoidal pulse width modulation (*SPWM*) is analyzed, the principle of the proposed compensation strategy is described in detail and the time compensation method with unipolar *SPWM* scheme is implemented using microprocessor-STM32F407G. The technique is intensively simulated and the evaluated through experimental results on resistive and resistive-inductive loads by comparing uncompensated and compensated states. Simulation and experimental results are presented to demonstrate and confirm the validity of the proposed dead-time compensation method.

Index Terms—Dead time compensation method, Dead time effect, Single phase full bridge inverter, Time compensation method, Unipolar switching.

I. INTRODUCTION

INVERTERS have become an indispensable converter for many industrial application areas where they are widely used in the control of various applications such as traction systems, electric vehicles, renewable energy integration with utility grid and several industrial systems. Wide spread use of inverters have increased recently and inverter technologies are developing gradually [1]. In real applications, power semiconductor switches used in power electronics circuits are not ideal, i.e., they have finite turn-on and turn-off times during switching transitions. In order to prevent synchronous conduction of upper and lower switches of the same leg at the same time, certain time delay called dead time [2]- [4] is inserted to the driving signals of these switches on the same leg to allow enough time to turn off one switch before other

switch receives turn on signal which ensures safe operation [5]. On the other hand, this blanking time causes problems in the system operation such as distortion of the output voltage and current waveform to contain a large number of harmonic components and reduction in fundamental output voltage and high switching frequency [6], [7]. As the frequency increases, this negative effect increases even more [3], [8] which is called as dead time effect. According to IEEE 519, the total harmonic distortion of the output voltage should not be more than %5. In off-grid systems, an *LC* filter is used to suppress harmonics and THD values of the output voltage and current remains below the level determined by the standards. However, it is difficult to suppress the output voltage distortion caused by dead time with these output filters because of increase in filter size and cost. Therefore, dead time compensation method become important to reduce these negative effects on voltage source inverter. Dead time compensation methods are classified as shown in Figure 1 where they can be divided into three parts such as time compensation method, average voltage compensation method and repetitive control method, respectively.
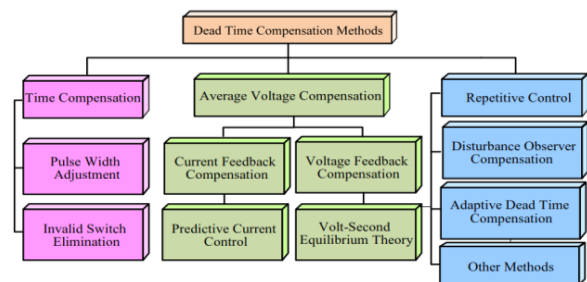
Fig. 1: Dead time compensation methods [3].

While one such category of the methods is based on the averaging voltage theory, other method is based on determination of output current polarity. The time compensation approach which is also known as pulse width adjustment method is the most extensively utilized method due to faster and more accurate results. In order to compensate for the effect of dead time, the turn-on or turn-off time of the power devices are altered by changing pulse-width as increasing or decreasing according to direction of output current and voltage in one period [3], [6]. In this method, pulse width can be increased or decreased following the detection of output current direction which is shown in Figure 2.

Umutcan Polat is with the Department of Electrical Engineering, Istanbul Technical University, Istanbul, Turkey, (e-mail: polatu19@itu.edu.tr).
https://orcid.org/0000-0001-7701-146X
Deniz Yildirim is with the Department of Electrical Engineering, Istanbul Technical University, Istanbul, Turkey, (e-mail: yildiri1@itu.edu.tr). https://orcid.org/0000-0001-6216-6290
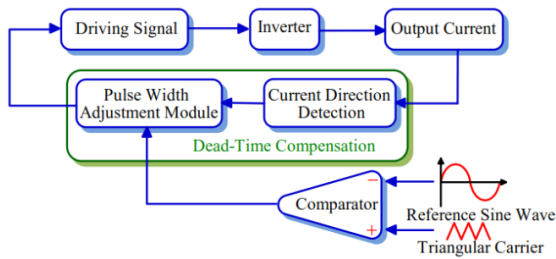
Fig. 2: The schematic diagram of pulse width adjustment method [3].

When the advantages of this method are examined, the output voltage is compensated about zero error and this method depends on direction of output current and voltage which results in simple structure. However, any uncertainty in the zero-crossings of the current adversely affects the compensation. Since the direction of the current is also decisive in the compensation, this is one of negative features of pulse width adjustment method and it strains the memory of the microcontrollers for operating in every period requiring significant amount of computational resources [3]. Several studies regarding dead time compensation method have been presented in the literature. The method proposed by authors [4] demonstrates novel distorted voltage compensation method to eliminate the effect of dead time on zero-current clamping phenomenon. The novel compensate strategy is represented for six-switch three-phase output inverter in [9] by using the direction of the current in each phase and error voltage occurred due to dead time is compensated by increasing or decreasing of the switching conduction period. The protection algorithm, which ensures two switches are not conducted at the same time, is applied on circuit by the author [10] and the dead time is defined within algorithm from the beginning. In literature [11], the fifth and seventh current harmonics are generated in the stationary reference frame because of dead time and sixth current harmonics are generated in the D-Q reference frame. The distortion of output waveforms caused by dead time is compensated by using a proportional integral (PI) current regulator in synchronous frame. In literature [12], a modified pulse width modulation method is proposed to reduce common-mode voltage in case of effect of dead time. In addition, the direct pulse compensation of the dead time is proposed by authors [13]. The aim of this study is to reduce dead time-imposed voltage distortion by superimposing a square wave on the triangle wave. The frequency of the triangle carrier and the square wave is the same and the amplitude of the square wave equals the dead time. In literature [14], the effect of dead time on a three-level neutral-point clamp (NPC) voltage source converter is examined in detail. The self-balancing space vector pulse-width modulation (SVPWM) is applied for improving the effect of dead time and it provides cost effective. In terms of continuous and discontinuous pulse-width modulation, the effect of dead time is discussed in [15] which includes minimum and maximum pulse width effects. In literature [16], novel dead-time space vector pulse-width modulation technique is presented for controlling voltage source inverter. In this study, the proposed algorithm has been

altered to ensure that the duty cycle is independent of carrier frequency and sampling time. In terms of optimum dead time, the method proposed by the authors [17] predict optimum dead time based on load current and eliminate body-diode conduction. In [18], the proposed compensation method using the controller output has been presented and in [19], adaptive dead time compensator is carried out by calculating the feed-forward compensation duty cycle. In order to fully mitigate low order harmonics caused by dead time effect, multiple resonant controllers and repetitive controllers is used by authors [20] - [23]. In [24], the dead time compensation algorithm has been suggested by using filter. However, the bandwidth of the current controller can be limited due to low pass filter (*LPC*). In [25] - [27], a more complex mathematical model of *VSI* is carried out, considering the effect of parasitic capacitance on output voltage and the compensation formula is derived according to parasitic capacitance. Generally, the studies mentioned above are carried out by using bipolar *SPWM* which is easier to analyze and a direct time compensation method can be applied. However, unipolar *SPWM* has advantages compared to bipolar *PWM* technique, such as obtaining lower *THD* values, helping the selection of semiconductor switches with lower nominal value depending on the *dv/dt* value in real applications, and harmonic frequencies present at two times the switching frequency at load [28], [29]. Despite all the advantages, analysis of the effect of dead time on unipolar *SPWM* could hardly be found in literature. In this paper, analysis of the effect of dead time on unipolar *SPWM* is carried out and time compensation method is applied on unipolar *SPWM* single phase full bridge inverter. The experimental and simulation results for compensated and uncompensated states are obtained at resistive *(R)* and resistive-inductive *(RL)* loads in fixed dead time and the results are compared according to *THD* values. The analysis of the effect of dead time on unipolar *SPWM* and the usefulness of applying the compensation method to the circuit at *R* and *RL* loads are confirmed by simulation and experimental results.

II. ANALYSIS OF DEAD TIME EFFECT ON VOLTAGE SOURCE INVERTER

A. Model of Single-Phase Full Bridge Inverter

A single-phase full bridge inverter is shown in Figure 3 where V_{DC} is the DC input voltage, C_{input} is input capacitor, *S1-S4* are power switches with four freewheeling diodes connected in reverse and parallel to the power switches, L_f is filter inductor, C_f is filter capacitor and load.
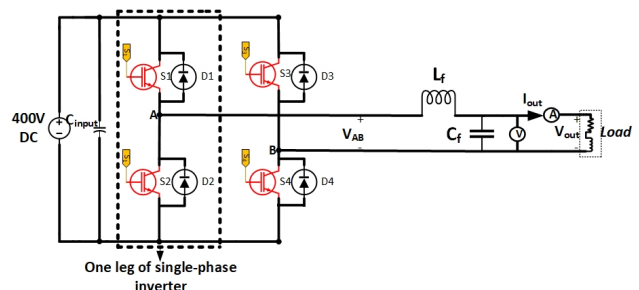
Fig. 3: The circuit model of single-phase full bridge inverter.

B. Dead time effect

When *S1* and *S2* power switches are ideal, these switches can be altered simultaneously from on to off at the same time. However, power switches used in voltage source converter (Mosfet, IGBT etc.) do not have ideal characteristic. In practice, it is seen that *S1* and *S2* power switches have turn-on and turn-off time delays. For this reason, turn-on of the power switch is delayed by a few second or vice versa in order to avoid the simultaneous conduction of the power devices in the same phase leg. This case indicates the necessity of dead time in H bridge-type *PWM* voltage source converters in order to ensure safe operation. In addition, dead time is also known as blanking time and normally a few microseconds [6]. The representation of dead time on gate signals is shown in Figure 4.
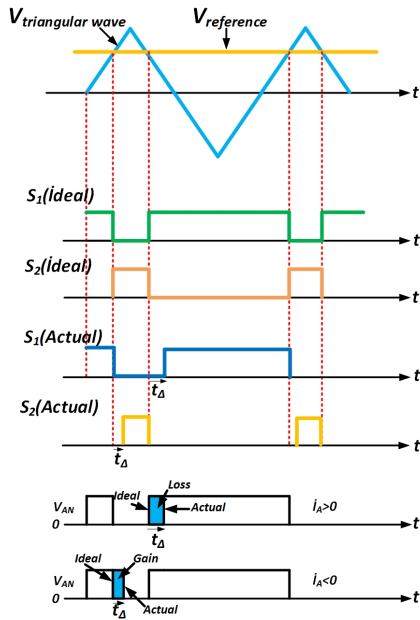
Fig. 4: The representation of dead time on gate signals.

PWM (Pulse-Width Modulation) is generated within microcontroller using a counter instead of triangular waveform which is known as carrier signal. It is more convenient to use the triangular waveform in Figure 4 to better illustrate the effect of dead time. In Figure 4, the voltage waveforms of one leg of single-phase inverter V_{AN} show in more detail for the state of *S1* and *S2* switches. During the dead time, both switching elements stop to conduct, the output current flows through the anti-parallel diodes which are determined as D_1 and D_2 due to the continuous current. As mentioned in Figure 4, anti-parallel diodes are turned on depending on the direction of the current. If output current is positive ($I_A > 0$), diode(D_2) is turned on and the output terminal will show a negative voltage. If output current is negative ($I_A < 0$), diode (D_1) is turned on and the output terminal will show a positive voltage. It can be seen that the conduction time of the output voltage waveform decreases when the output current is greater than zero compared to ideal waveform. In case of $I_A < 0$, this case opposite of $I_A > 0$. That is, the conduction time of the output voltage waveform increases when the output current is less than zero compared to ideal waveform.

C. Dead time effect of unipolar SPWM
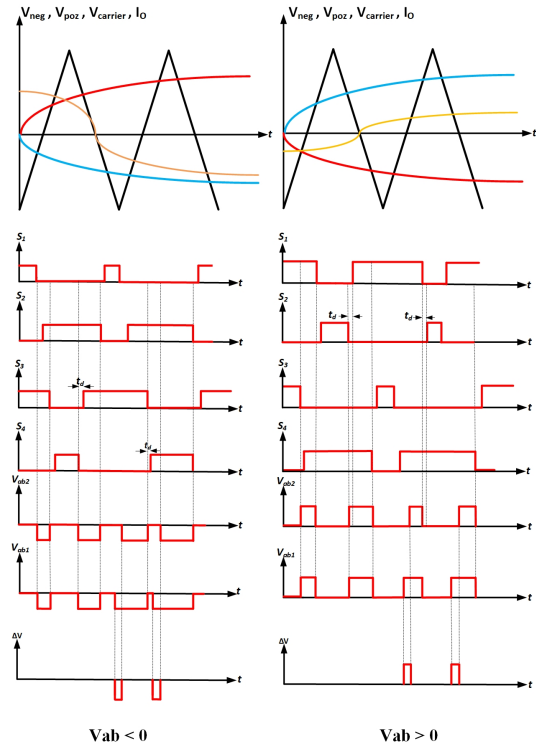
Fig. 5: Dead time effect with different voltage and current polarity.

As mentioned above, dead time effect analysis of unipolar *SPWM* is different than bipolar *SPWM*. Figure 5 shows dead time effect of unipolar *SPWM*. To analysis dead time effect, it necessary to ideal, actual gating waveform with dead time and output voltage in both cases. While load is ohmic-inductive, gate signals and output voltage waveforms are given in Figure 5. The above-mentioned graphs are drawn from the starting points of the T/2 and periods to a certain point. When these graphs are analyzed, it will be possible to find out how the variation of the output voltage between the ideal state and the actual state for a period due to dead time effect. In addition, variation of output voltage is known as error voltage. When analyzing Figure 5, it is sufficient to examine four situations depending on output voltage and output current for one fundamental period. Thus, these situations are $V_{ab} > 0, I > 0$; $V_{ab} > 0, I < 0$; $V_{ab} < 0, I > 0$; $V_{ab} < 0, I < 0$, respectively [16]. In case of $V_{ab} > 0, I > 0$, this situation can be explained in two steps. S_1 is turned off while S_4 is turned on, the output current flows through S_4 and D_2. Thus, actual output voltage V_{ab2} is zero during dead time t_d. S_4 is turned off while S_1 is turned on, the output current flows through S_1 and D_3. Thus, actual output voltage V_{ab2} is zero during dead time t_d. When the actual voltage V_{ab2} is compared with ideal voltage, it is seen that the actual voltage diminishes two pulses with dead time t_d and magnitude of V_{DC}. In case of $V_{ab} > 0, I < 0$, S_1 is turned off while S_4 is turned on or S_1 is turned on while S_4 is turned off, the output current flows through D_4 and D_1. Thus, actual output voltage V_{ab2} is V_{DC} during dead time t_d. When the actual voltage V_{ab2} is compared with ideal voltage, it is seen that the actual voltage no diminishes with dead time t_d

and magnitude of V_{DC}. In case of $V_{ab} < 0, I > 0$, S_2 is turned off while S_3 is turned on or S_2 is turned on while S_3 is turned off, the output current flows through D_3 and D_2. Thus, actual output voltage V_{ab2} is $-V_{DC}$ during dead time t_d. When the actual voltage V_{ab2} is compared with ideal voltage, it is seen that the actual voltage no diminishes with dead time t_d and magnitude of V_{DC}. That is, the output voltage is unaffected by the dead time. In case of $V_{ab} < 0, I < 0$, this situation can be explained in two steps. S_2 is turned off while S_3 is turned on, the output current flows through S_3 and D_1. Thus, actual output voltage V_{ab2} is zero during dead time t_d. S_3 is turned off while S_2 is turned on, the output current flows through S_2 and D_4. Thus, actual output voltage V_{ab2} is zero during dead time t_d. When the actual voltage V_{ab2} is compared with ideal voltage, it is seen that the actual voltage diminishes two pulses with dead time t_d and magnitude of $-V_{DC}$. In the light of this information, inductor current direction is shown in Figure 6 as six diagrams.

(a) $V_{ab} > 0, I > 0$ (S_4, D_2)   (b) $V_{ab} > 0, I > 0$ (S_1, D_3)

(c) $V_{ab} > 0, I < 0$ (D_1, D_4)   (d) $V_{ab} < 0, I < 0$ (S_3, D_1)

(e) $V_{ab} < 0, I < 0$ (S_2, D_4)   (f) $V_{ab} < 0, I > 0$ (D_2, D_3)
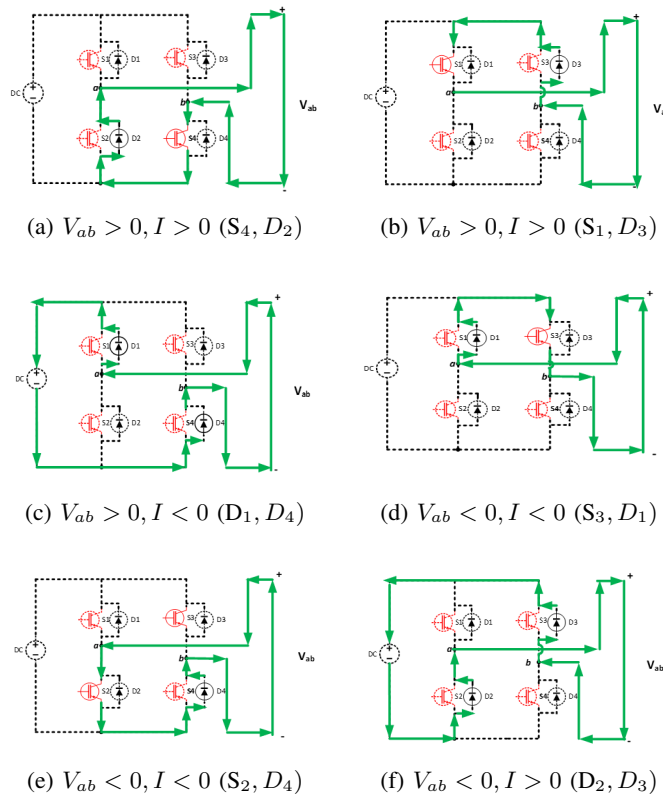
Fig. 6: Conducting devices based on polarity of output voltage and output current.

Considering the above analysis, the following assumptions need to be made to formulate the effect of dead time quantitatively [30]. First of all, the carrier frequency of the circuit must be sufficiently greater than the fundamental frequency. Secondly, the inverter output current is virtually sinusoidal, and voltage variation occurs almost equidistantly. Lastly, switching components should have a minimal reverse storage time which is negligible. According to the analysis and assumptions above, the error voltage is calculated based on the ideal voltage and the actual voltage with dead time as follows:

$$\Delta V = \Delta V_1 - \Delta V_2 = +2f_c t_d V_{DC} \qquad I_{out} > 0, V_{ab} > 0 \quad (1)$$

$$\Delta V = \Delta V_1 - \Delta V_2 = -2f_c t_d V_{DC} \qquad I_{out} < 0, V_{ab} < 0 \quad (2)$$

where V_{DC} is the DC input voltage, f_c is the switching frequency, and t_d is the dead time.

III. SIMULATION RESULTS

The simulation of a full-bridge single-phase inverter circuit is carried out in uncompensated state and compensated state for *RL* and *R* load at a certain dead time period. Sinusoidal Pulse Width Modulation technique is used to control the a full-bridge single-phase inverter circuit. This circuits are simulated in Power Simulation (PSIM) software. Waveforms of the output voltage and output current are obtained and total harmonic distortion values are calculated for both cases. The results obtained for compensated and uncompensated state are compared and evaluated.

A. Power stage and control structure of circuit

In the first step, the full bridge single-phase inverter circuit is modeled at resistive load for uncompensated state and compensated state. The simulations of the power circuit are performed using PSIM. In addition, the open loop operation of the circuit is examined by generating switching signals with *SPWM* method. In this simulation, DC input voltage and low pass filter values are 400V, 3.60mH, 15μF, respectively. *LC* filter values are calculated depending on the amount of fluctuation of inductance current, switching frequency and DC bus voltage. The power and control circuit of single-phase full bridge inverter with resistive load are shown in Figure 7.
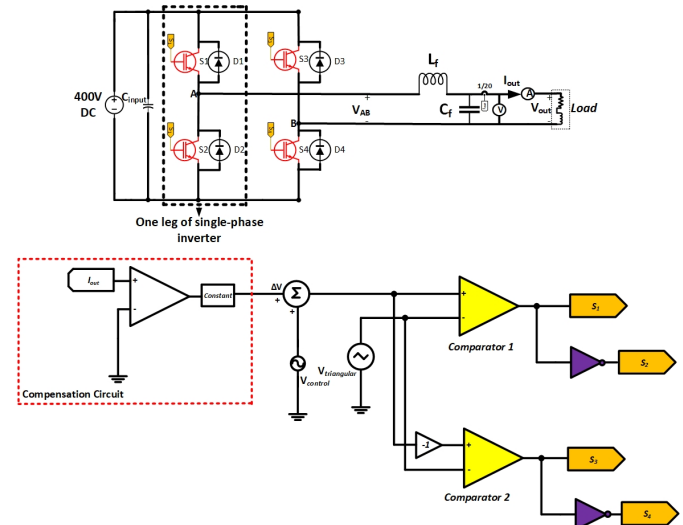
Fig. 7: Power and control circuit of single-phase full bridge inverter.

B. Compensated circuit

As mentioned before, time compensation methods are used to reduce this negative effect. According to this method, if the pulse width is changed at the zero points of the current, the distortion of the output waveforms is reduced. Thus, *THD* values are reduced. That is, the reference signal must

change for the compensation to be applied to the circuit in this simulation. In this simulation, this method is applied by designing the following formula.

$$V_{control,update} = \begin{cases} V_{control} + \Delta V & \text{if } I_{\text{out}} > 0 \\ V_{control} - \Delta V & \text{if } I_{\text{out}} < 0 \end{cases} \quad (3)$$

where, $V_{control}$ is the reference signal of the inverter circuit in the uncompensated state and ΔV is the error voltage as seen in formulas (1) and (2). This error voltage should be added to $V_{control}$ to determine the new reference signal. Thus, this signal is updated and *PWM* signals are sent to the respective MOSFETs for compensation according to the polarity of the output current.

C. Uncompensated and compensated state with resistive load

Figure 8 shows the output voltage and output current when the full bridge inverter was connected to a 100Ω resistive load, both in the absence of dead time compensation and in its presence. In the uncompensated state, it can be observed that the output current remains at zero for a longer duration compared to the compensated state due to the effect of the dead time. As a result, the output voltage is more significantly affected at that instant. In light of this information, it is anticipated that there will be an increase in harmonic distortion values (*THD*) in the uncompensated state will be higher than in the compensated state. The simulation results also support this hypothesis. As depicted in Figure 8, the *THD* value of the output voltage decreases by 41.01% at a resistive load in the compensated state. Thus, the adverse effects of the dead time are mitigated to a significant extent using the compensation method.

(a)

(b)
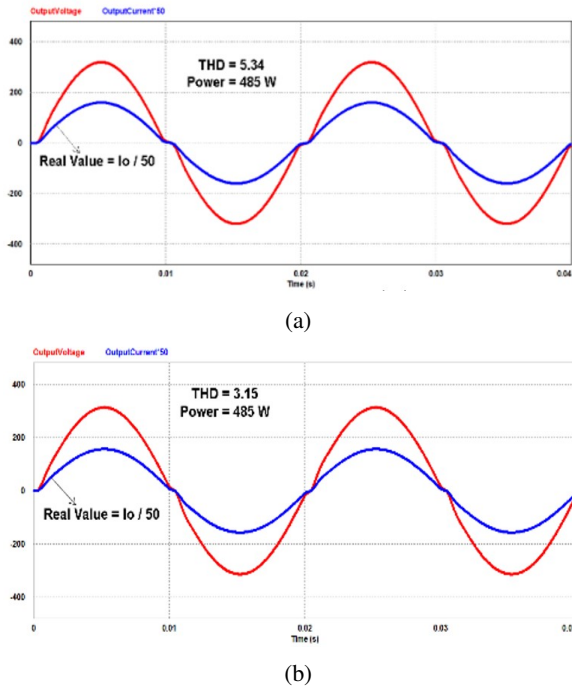
Fig. 8: Output voltage and output current waveforms with resistive load; (a) Uncompensated state; (b) Compensated state.

D. Uncompensated and compensated state with resistive-inductive load

Figure 9 shows the output voltage and output current when the full bridge inverter was connected to an 85Ω and 143mH resistive-inductive load, both without and with dead time compensation. Comparing Fig. 9(a) with Fig. 9(b), the compensation method provides a significant decline of about 31.54% in the distortion caused by dead time.

(a)

(b)
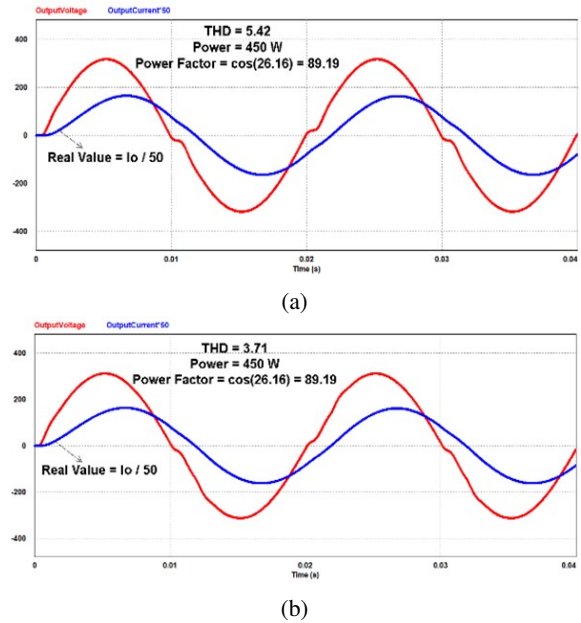
Fig. 9: Output voltage and output current waveforms with resistive-inductive load;(a) Uncompensated state; (b) Compensated state.

IV. EXPERIMENTAL RESULTS

Experimental tests with the single-phase full bridge inverter were carried out for resistive and resistive-inductive load at compensated and uncompensated state. The operating parameters of the inverter and component list are given in Table 1.

A. General working blocks of designed system

In Figure 10, a comprehensive block diagram illustrates the experimental setup utilized for the inverter testing. This diagram encompasses various crucial components such as the DC input voltage, capacitors, optocouplers, and isolated DC sources. Central to this setup is the microcontroller, which oversees the general functioning and synchronization of the components. Moreover, the inclusion of an isolated current sensor adds to the precision of the system by providing real-time current measurements. The inverter power circuit, an essential part of the structure, ensures the necessary power conversion, while an output low-pass filter has been incorporated to refine the output quality. To offer a more tangible perspective, Figure 11 visually represents the inverter's power circuit as implemented in a controlled laboratory environment.

TABLE I: Keysystem specifications and component list of the inverter circuit.

Parameters	Symbols	Values	Component List	
Input Voltage	V_{in}	400V	Mosfet	FGH20N60SFD-600V/20A
Output Voltage	V_{out}	220V$_{rms}$	Inductors	3.60mH
Input Current	I_{in}	1.4A max	Optocoupler	TLP350
Output Current	I_{out}	0-3A	Output Capacitor	4μF
Switching Frequency	$f_s = 1/T_s$	20kHz	Input Electrolytic Capacitor	470μF
Dead Time	t_d	$1\mu s$ (2% of T$_s$)	Input Ceramic Capacitor	2.2μF
Line Frequency	f_L	50Hz	Microcontroller	STM32F407G
Filter Inductance	L	3.60mH	Comparator	LM311N
Filter Capacitive	C	15μF	Current Transducer	LEM HX05- NP
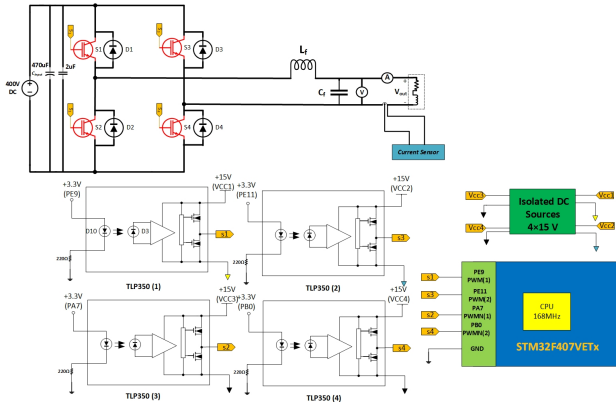
Fig. 10: Block diagram of full bridge single-phase inverter.
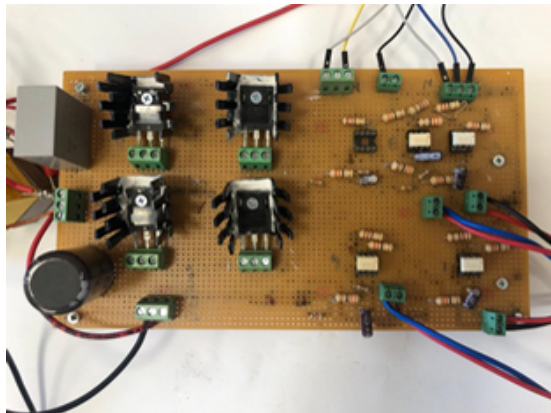
Fig. 11: Full bridge inverter circuit with power circuit.

counter and the sine table values, depending on whether the dead time is compensated or not, where the flow diagram of the *SPWM* algorithm is given in Figure 12.
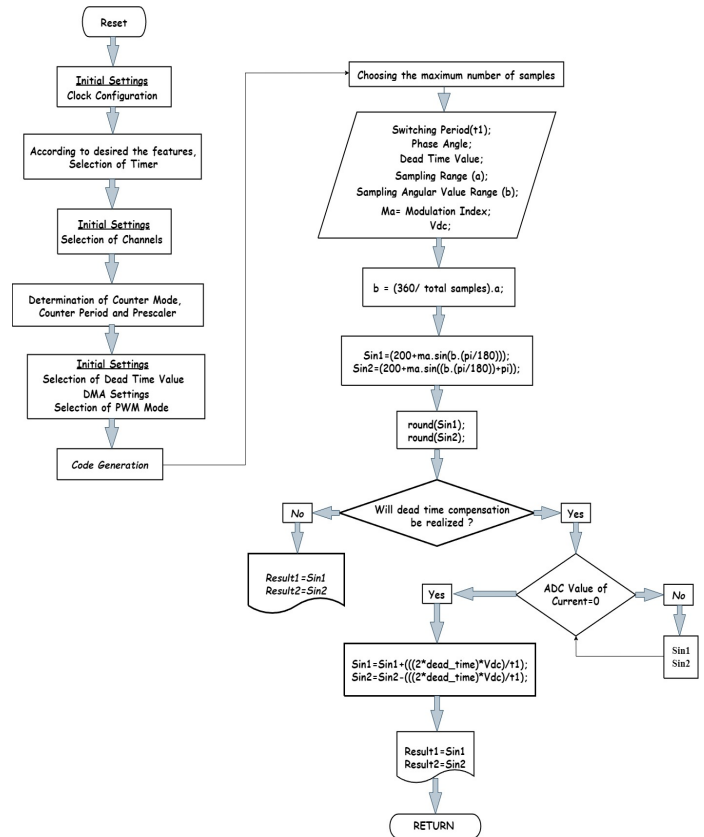
Fig. 12: The Flow Diagram of *SPWM* Generation.

B. Software design

Control signals of mosfet are generated using digital *SPWM* algorithm running on a high-performance microcontroller [31]. Firstly, various adjustments are arranged easily at the beginning such as counter mode, clock configuration and dead time value by using microcontroller development tool as desired. Then, it is created a sine table by writing the relevant codes and used the functions of the timers. The reason is that the microcontroller uses the counter instead of the triangle wave. Finally, necessary signals will be generated by comparing the

C. Uncompensated and compensated state with resistive load

In case of experimental study, Figure 13 shows the output waveforms and *THD* values of the output voltage at uncompensated and compensated states in case of a resistive load. When comparing Figure 13(a) and 13(b), it can be seen that the compensated method decreases the distortion caused by dead time by about 34.46%. In addition, the relation between the output voltage and *THD* values for the resistive load in the uncompensated and compensated states is shown in Figure 14.

(a)   (b)

(c)   (d)
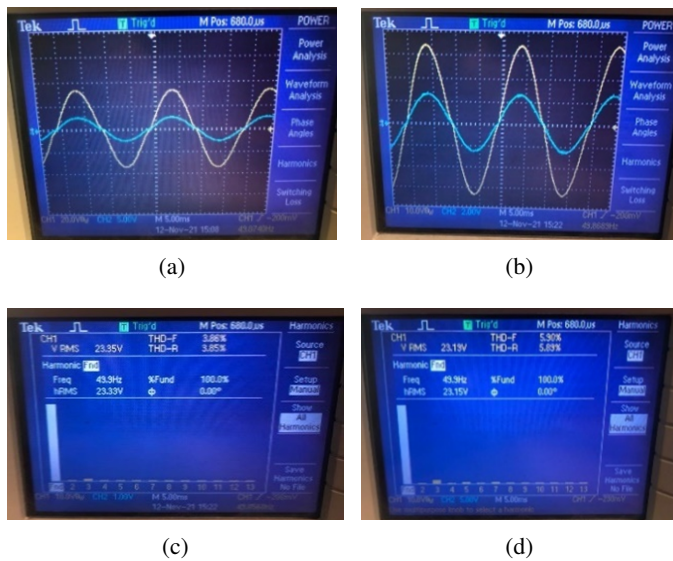
Fig. 13: Output voltage and output current waveforms with resistive load; (a) Compensated state; (b) Uncompensated state; (c) THD value in compensated state; (d) THD value in uncompensated state.
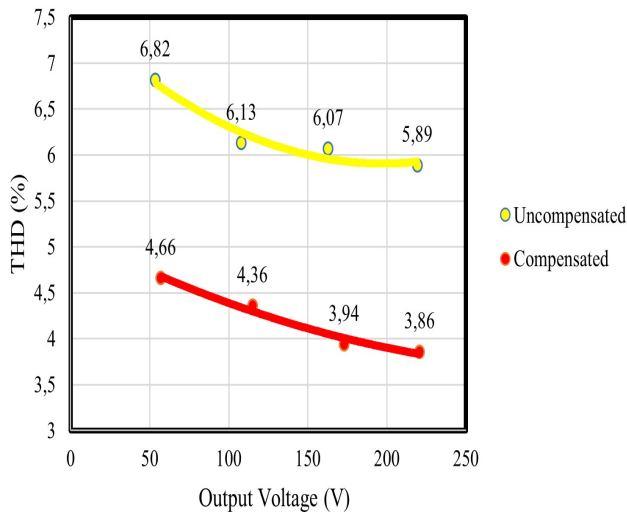
Fig. 14: Relation between THD and output voltage in resistive load.

D. Uncompensated and compensated state with resistive-inductive load

Figure 15 provides a clear representation of the output waveforms, offering a detailed view of the differences in total harmonic distortion (*THD*) measurements between the compensated and uncompensated states when subjected to a resistive-inductive load. Upon closely observing Figure 15, it becomes evident that there's a significant reduction in the *THD* value associated with the output voltage in the compensated state. Specifically, the reduction is around 25.24% when compared with its uncompensated counterpart. This observation underscores the effectiveness and potential benefits of the method we've employed. Furthermore, if we direct our attention to Figure 16, it presents an intriguing

overview of the relationship dynamics between the output voltage and *THD* values. This relationship becomes even more apparent when assessing an resistive-inductive load across both states, offering a comparative perspective between the uncompensated and compensated scenarios.

(a)   (b)

(c)   (d)
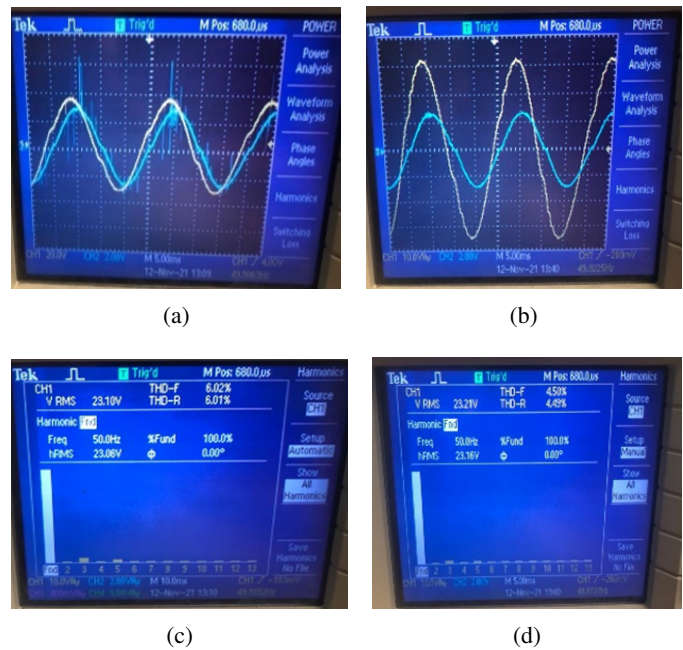
Fig. 15: Output voltage and output current waveforms with resistive-inductive load; (a) Uncompensated state; (b) Compensated state; (c) THD value in compensated state; (d) THD value in uncompensated state.
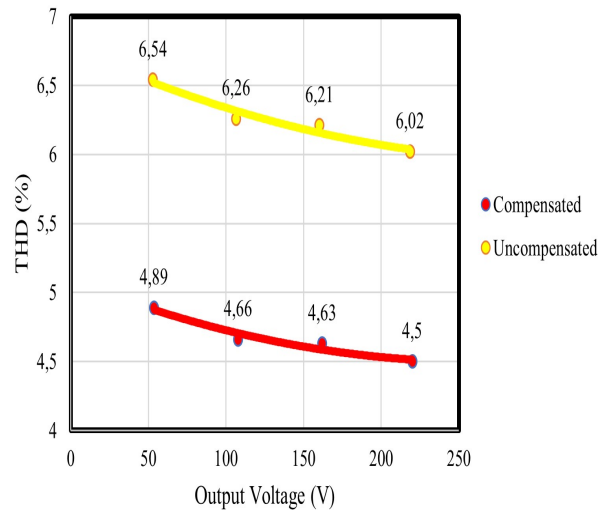
Fig. 16: Relation between THD and output voltage in resistive-inductive load.

Under the given conditions where the DC input voltage is set at 400 V, Table 2 provides a comprehensive overview of the results from experimental evaluations. These results give insights into the performance differences between the uncompensated and compensated states across varying load conditions, specifically focusing on resistive and resistive-inductive loads.

TABLE II: Experimental measurement results for 2% (1 μs) dead time.

State	Uncompensated State		Compensated State	
Load	Resistive	Resistive-inductive	Resistive	Resistive-inductive
Input Current (A)	1.235	1.18	1.313	1.178
Output Voltage (V)	219.2	218.5	220.7	220
Output Current (A)	2.164	2.31	2.176	2.304
THD_V (%)	5.89	6.02	3.86	4.50

V. CONCLUSION

In this paper, the dead time effect of unipolar sinusoidal pulse width modulation for full bridge single-phase inverter is thoroughly analyzed and a method is proposed to compensate dead time in *SPWM* controlled inverter. The variation of output voltage distortion for compensated and uncompensated states is examined and tested for resistive and resistive-inductive load by simulations as well as by experiments. From the results one can observe from the experimental and simulation result that the time compensation method for a dead time of 2% result in a reduction of *THD* value of inverter output voltage. According to simulation results, *THD* value of the output voltage is decreased as 41.01% at R load and 31.54 % at *RL* load. On the other hand, *THD* value of the output voltage is decreased as 34,46% at *R* load and 25,24% at *RL* load in the experimental results. It can be seen from the results that the dead time compensation methods are important part for power converter, which directly affects the output performance, stability and reliability of the control system. Experimental and simulation results demonstrate the usefulness of the compensation method and show that time compensation method has simple control logic and can be realized conveniently and easily. The output voltage of the inverters approaches the sinusoidal wave as the *THD* values decrease and the results confirm to validity of the time compensation method in both simulation and the experimentation.

REFERENCES

[1] Çamur S., Arifoğlu B., Beşer E. Kandemir and Beşer E. "Design and Application of a Novel Structure and Topology for Single-Phase Five Level Inverter", Wseas Transactions on Electronics, 2006.

[2] Zhang, J. and Luo, F. L. "An accurate approach of dead-time compensation for three-phase DC/AC inverter." 2009 4th IEEE Conference Industrial Electronic, doi: 10.1109/ICIEA.2009.5138745.

[3] Ji, Y.; Yang, Y.; Zhou, J.; Ding, H.; Guo, X.; Padmanaban, S. Control Strategies of Mitigating Dead-time Effect on Power Converters: An Overview. Electronics 2019, 8, 196. doi:10.3390/electronics8020196.

[4] Choi, J., and Sul, S. "A new compensation strategy reducing voltage/current distortion in PWM VSI systems operating with low output voltages. IEEE Transactions on Industry Applications, 31, 1001-1008,1995.

[5] Cao, F., Liu, J., and Zhang, Y. "A switching strategy of dead-time elimination for pulse width modulation converters. 2015 IEEE 2nd International Future Energy Electronics Conference (IFEEC), 1-14.

[6] Zammit, D., Apap, M., and Staines, C.S. "Dead time compensation in h-bridge inverters," International Journal of Industrial Electronics and Drives, vol. 4, DOI 10.1504/IJIED.2018.090411, no. 1, pp. 56–68, 3 2018.

[7] Jeong, S., and Park, M. "The analysis and compensation of dead-time effects in PWM inverters," in IEEE Transactions on Industrial Electronics, vol. 38, no. 2, pp. 108-114, April 1991, doi: 10.1109/41.88903.

[8] Narmatha, R., and Govindaraj, T. "Inverter Dead-Time Elimination for Reducing Harmonic Distortion and Improving Power Quality", International journal of Asian Scientific Research, vol.3, April 2013.

[9] Ikegami, S., Hoshi, N., and Haruna, J., "Experimental verification of dead-time compensation scheme for pulse width modulation scheme on six-switch two three-phase output inverter," 2014 17th International Conference on Electrical Machines and Systems (ICEMS), 2014, pp. 1420-1424, doi: 10.1109/ICEMS.2014.7013709.

[10] Weerakoon, D., Sandaruwan, B., De Silva, R., Abeyratne, S. and Rathnayake, D. "A novel dead-time compensation scheme for PWM VSI drives," 2016 IEEE International Conference on Information and Automation, 2016, doi: 10.1109/ICIAFS.2016.7946570.

[11] Hwang, S. and Kim, J. "Dead Time Compensation Method for Voltage-Fed PWM Inverter," in IEEE Transactions on Energy Conversion, vol. 25, no. 1, pp. 1-10, March 2010, doi: 10.1109/TEC.2009.2031811.

[12] Aizawa, N., Kikuchi, M., Kubota, H. Miki, I. and Matsuse, K. "Dead-time effect and its compensation in common-mode voltage elimination of PWM inverter with auxiliary inverter," The 2010 International Power Electronics Conference, doi: 10.1109/IPEC.2010.5543867.

[13] Liu, Y.; Huang, Q.; Dong, C. The direct pulse compensation of dead-time of APF. Procedia Eng. 2011, 15, 5355–5362.

[14] P. J. P. Vinod and P. P. N. Tekwani. "Pulse-based dead-time compensation method for self- balancing space vector pulse width-modulated scheme used in a three-level inverter-fed induction motor drive," IET Power Electron., vol. 4, no. January 2010, pp. 624–631, 2011.

[15] B. Welchko, S. Schulz, and S. Hiti, "Effects and compensation of deadtime and minimum pulse-width limitations in two-level PWM voltage source inverters," in Proc. 2006 IEEE Ind. Appl. Conf., 8–12 Oct. 2006, vol. 2, pp. 889–896.

[16] T. Abhiram, P. S. Reddy and P. V. N. Prasad, "Integrated dead-time SVPWM algorithm for indirect vector controlled two-level inverter fed induction motor drive," 2017 International Conference on Information, Communication, Instrumentation and Control (ICICIC), 2017, pp. 1-6, doi: 10.1109/ICOMICON.2017.8279073.

[17] J. S. Yu, G. Jin, S. L. Cheng and W. T. Ng, "Digital dead-time control for an integrated tri-mode buck-boost DC-DC converter," 2015 9th International Conference on Power Electronics and ECCE Asia (ICPE-ECCE Asia), 2015, pp. 1768-1771, doi: 10.1109/ICPE.2015.7168017.

[18] S.-H. Hwang and J.-M. Kim, "Dead time compensation method for voltage-fed PWM inverter," IEEE Trans. Energy Convers., vol. 25, no. 1, pp. 1–10, Mar. 2010.

[19] M.A. Herran, J.R. Fischer, S.A. Gonzalez, M.G. Judewicz, and D.O. Carrica, "Adaptive dead-time compensation for grid-connected PWM inverters of single-stage PV systems," IEEE Trans. Power Electron., vol. 28, no. 6, pp. 2816–2825, Jun. 2013.

[20] K. Zhou, D. Wang, Y. Yang, and F. Blaabjerg, "Periodic Control of Power Electronic Converters ", ser. Energy Engineering. Institution of Engineering and Technology, 2016.

[21] Z. Tang and B. Akin, "Suppression of dead-time distortion through revised repetitive controller in PMSM drives," IEEE Trans. Energy Convers., vol. 32, no. 3, pp. 918–930, Sept. 2017.

[22] Y. Yang, K. Zhou, H. Wang, and F. Blaabjerg, "Harmonics mitigation of dead time effects in PWM converters using a repetitive controller," in Proc. of APEC, pp. 1479–1486, Mar. 2015.

[23] X. Chen, X. Ruan, D. Yang, W. Zhao, and L. Jia, "Injected grid current quality improvement for a voltage-controlled grid-connected inverter," IEEE Trans. Power Electron., vol. 33, no. 2, pp. 1247–1258, Feb. 2018.

[24] Hengbing Zhao, Q. M. J. Wu and A. Kawamura, "An accurate approach of nonlinearity compensation for VSI inverter output voltage," in IEEE Transactions on Power Electronics, vol. 19, no. 4, pp. 1029-1035, July 2004, doi: 10.1109/TPEL.2004.830072.

[25] Li C., Gu Y., Li W., He X., Dong Z., Chen G., Ma C., Zhang L. "Analysis and compensation of dead-time effect considering parasitic capacitance and ripple current", 2015 IEEE Applied Power Electronics Conference and Exposition(APEC),2015,pp.1501-1506.

[26] N. Urasaki, T. Senjyu, T. Kinjo, K. Uezato, T. Funabashi and H. Sekine, "Dead-time compensation strategy for permanent magnet synchronous motor drive taking zero current clamp and parasitic capacitor effects into account", 30th Annual Conference of IEEE Industrial Electronics Society, 2004.IECON2004,2004,pp.2718-2723Vol.3.

[27] Z. Zhang and L. Xu, "Dead-time compensation of inverters considering snubber and parasitic capacitance," IEEE Trans. Power Electron., vol. 29, no. 6, pp. 3179–3187, Jun. 2014.

[28] Namboodiri, A. "Unipolar and Bipolar PWM Inverter", IJIRST –International Journal for Innovative Research in Science Technology vol. 1, December 2014, ISSN (online): 2349-6010.

[29] Endiz, M. and Akkaya, R. "Matlab / Simulink ile Bipolar ve Unipolar PWM Kontrol Tekniklerinin Karşılaştırmalı Olarak İncelenmesi Comparative Study of Bipolar and Unipolar PWM Control Tech-

niques using Matlab / Simulink", no 24, pp. 309–313, 2021, doi: 10.31590/ejosat.900868.

[30] Yuan, G., Luo, S., Zhou, S., Zou, X., and Zou, K. "Low-order harmonics analysis and suppression method for 400Hz single-phase VSI," 2015 IEEE Applied Power Electronics Conference and Exposition (APEC), 2015, pp. 2341-2345, doi: 10.1109/APEC.2015.7104675.

[31] STMicroelectronics,"RM0090 Reference manual", STM32F407/417 datasheet, Oct.2012 [Revised Feb. 2021].

BIOGRAPHIES

Umutcan Polat was born in Istanbul, Turkey. He received bachelor's degree in electrical engineering from Yildiz Technical University in 2018. Polat received Master's degree from Istanbul Technical University (ITU) in 2022. Now, Polat is currently PhD student at Istanbul Technical University and he works as a Research Assistant in the Department of Electrical Engineering at Istanbul Technical University (ITU). His research areas include on power converters, electrical machines and renewable energy systems.

Deniz Yildirim was born in Istanbul, Turkey. He received bachelor's degree in electrical engineering from Istanbul Technical University in 1989 and master's degree and PhD degrees in Electrical Engineering from university of Colorado at Boulder in 1993 and 1999, respectively. His research areas include power converters, electrical machines, and utility interactions of renewable energy (solar and wind power) sources. He has various industrial consulting experience in FEM analysis, solar potential calculation, electronic circuit design, inverters, and electromechanical component design. He is currently an Assistant Professor of Electrical Engineering in Istanbul Technical University, Istanbul, Turkey.

Research Article

Evaluation of the relevance of LED lamp selection based on manufacturer-declared parameters

Jelena Dikun, Vilma Jakubauskiene

Abstract—**The purpose of this study was to evaluate the relevancy of LED lamp parameters to ordinary customers as well as to find out which parameters are more or less significant for the purchasers. It was found that the majority of customers have some difficulties understanding the luminous parameters of LED lamps but are aware of the efficiency and advantages of these artificial light sources. In order to propose the selection guide for LED lamps, the MCDM (Multiple-Criteria Decision-Making) techniques were applied. The proposed algorithm consists of eight steps and covers all LED lamp parameters declared by the manufacturer.**

Index Terms—**Artificial Light Sources, Efficiency, LED lamps, Luminous parameters, Multiple-Criteria-Decision-Making.**

I. INTRODUCTION

IN THE MODERN WORLD, light-emitting diode (LED) lamps are actively used to illuminate domestic and industrial premises and are confidently replacing other types of lamps, such as halogen, luminescent and incandescent lamps. By 2026, the LED lamps market is expected to grow by 211 percent compared to 2020, when LED lamp production reached US$75.8 billion [1]. The high growth of LED bulb production is based on the cogent advantages of its luminous and electric parameters in comparison to other types of lamps [2]. The main parameters such as rated power (P), efficiency (η), luminous flux (Φ), and life-time (LT) of four light bulbs commonly used in home applications are presented in Table 1.

As can be seen from Table 1, LED lamps provide the highest quality artificial lighting and are more economical than other types of lamps using different physics to produce the light.

TABLE I
THE COMPARATIVE PARAMETERS OF GENERALLY USED LIGHT BULBS

	Incandescent lamp	Halogen lamp	Luminescent lamp	LED lamp
Life time, T, houres	1000	2000	8000-20000	> 50 000
Efficiency η, lm/W	10	30	60	≈95
Average luminous flux, Φ, lm	Power, W			
400	40	30	9	4
650	60	40	12	5
900	75	52	15	8
1200	100	67	20	10
1600	150	87	23	15

Approximately 3.5 times longer than luminescent lights, 25 times longer than halogen lamps, and 50 times longer than incandescent bulbs is the lifespan of an LED lamps.

The amount of luminous flux depends on the amount of power consumed. The more power an artificial light source uses, the more luminous flux is produced. In this rating, both LED and luminescent lamps show satisfaction results, although the LED lamp's consumption of electric power for producing the same amount of luminous flux is around twice as low. The low and worst results of this parameter are demonstrated by halogen and incandescent lamps accordingly. A halogen lamp requires 78 watts to produce a luminous flux of 1600 lumens, while an incandescent bulb consumes twice as much energy.

Another important indicator is the efficiency of the artificial light source. The efficiency of the incandescent lamp is the lowest, while the values of the luminescent, halogen, and LED light sources are 60 percent, 30 percent, and 95 percent, respectively. The efficiency of an artificial light source is defined [3] as the ratio of the light flux produced by this source to the electrical power consumed from the electric grid and expressed in lm/W. Due to the development of semiconductor technology and materials science, the efficiency of LED light sources is approximately doubling every three years [4]. According to EU regulation [3], the light bulb efficiency should not be less than 85 lm/W.

Nowadays, the prices for electricity in Lithuania for residential consumers are on average 0.24 Eur./kW [5].

Jelena Dikun, is with Department of Engineering and Informatics of Higher Education Institution, Klaipeda, Lithuania, (e-mail: j.dikun@kvk.lt).

https://orcid.org/0000-0001-6243-1779

Vilma Jakubauskiene, is with Department of Engineering and Informatics of Higher Education Institution, Klaipeda, Lithuania (e-mail: v.jakubauskiene@kvk.lt).

https://orcid.org/0009-0003-1248-6300

According to Eurostat report [8], the amount of electricity consumed by the average consumer for lighting is 9 to 12 % of total consumption. Therefore, it is preferable and advised to utilize LED lighting. As the recommended standard efficacy for other types of lamps presented in Table 1 is below 85 lm/W, only LED artificial light sources will be addressed in this article.

However, the LED bulbs proposed by manufacturers have different numerical values for the same parameters, such as life span, efficiency, and luminous flux, and thus it is important to find out how and on what basis ordinary buyers choose a certain light source.

In these latter days, there are a sufficient number of studies dealing with lamp-choosing aspects for domestic usage. The study [6] shows that the main motives for using LED lamps are price, quality, energy savings and consumption, reliability of LED lamps, compatibility of LED lamps with lighting fixtures, brand, product availability, and environmental friendliness. Three key factors led researchers to select LEDs: increased lamp life, reduced energy use, and lower utility costs [7]. According to the study [8], 34% of respondents are extremely well knowledgeable on the benefits of LEDs, 60% are just somewhat informed, and 6% hardly know anything. This study also asserts that three factors—brightness, low energy consumption, and durability—have an effect on the selection of LED lamps. However, which parameters play a decisive role when choosing a light source or in what order these parameters are evaluated by purchasers is not specified. Moreover, there is not enough research to clarify the choice of lamp based on the parameters specified by the manufacturer.

In order to specify how ordinary customers are aware of the parameters of the LEDs indicated on the package, a survey was conducted in the home-use store. 1115 people were interviewed during the survey. The questions and answers are from the interview presented in Table 2.

TABLE II
QUESTIONNARIE RESULTS ABOUT AWARENESS OF THE LED LAMP PARAMETERS

Questions	Answers			
	Yes	No	Fragmentarily	Unaware
Do you know which parameters of a light bulb you should pay attention to before buying it?	28%	33%	29%	10%
Do you understand the physical parameters of the LEDs indicated on the package?	16%	18%	59%	7%
Are you aware of which parameters must be shown on the bulb light package?	30%	55%	14%	6%
Do you use internet sources to ensure the right choice of lamp?	57%	13%	27%	3%

The review results in Table 2 demonstrate that 72% of respondents found it difficult to identify the primary lamp specifications, and 84% of consumers did not clearly comprehend what the parameters of lamps meant. Seventy percent of the participants lacked precise knowledge of the requirements for the manufacturer's label on the package of light bulbs. Also still, the majority of respondents (57%) research lightbulbs online before making a purchase. But the internet can't always provide accurate information regarding lamp parameters, so everyone should be cautious and make sure the sources they rely on are reliable [9]. Consumers who are looking for precise information regarding lamp parameters should make use of reliable websites, manufacturer specifications, and articles that have undergone expert review [10].

The purpose of this study is to evaluate the importance of the LED bulb parameters declared by the manufacturers and to determine which lamp's specified parameters and in which sequence are more or less preferred when choosing an affordable artificial light source using MCDM (Multiple-Criteria Decision-Making) techniques.

II. THE PARAMETERS OF LIGHT BULBS DECLARED BY MANUFACTURERS

The information designated on the lamp's package should comply with the regulation [3]. Manufacturers often include information about a lamp that falls into one of two categories on the package. One of these is the lamp's electrical specifications, including the rated voltage (U, V), wattage (P, W), and grid frequency (f, Hz) to which it can be connected.

The luminous parameters of a lamp are a different set of parameters [11]. These comprise a lamp luminous flux (Φ), the light source's lifetime (LT), color temperature (TC), color rendering index (CRI), and light beam angle (LBA). A list of LEDs lamp from one of the stores is shown in Table 2. Lamps from the same manufacturer are identified by the same capital letter, and that companies' product line is identified by a numerical index. The Table 3 displays the rated specifications for each artificial light source that the customer may see on the package.

Rated power (P, W). The amount of energy consumed by the lamp to produce light is indicated by its rated power.

Visible light is a small part of the spectrum of electromagnetic radiation in the range from 360 to 830 nm that causes a visual sensation in the human eye. The amount of visible light emitted by a lamp is called the *luminous flux (Φ).* This parameter is measured in lumens (lm) and is related to the power of the lamp, but, as can be seen from Table 2, it does not have a linear relationship with the rated power of a lamp.

The *efficiency* of a lamp is its most crucial component. Efficiency is defined as the luminous flux (Φ) to lamp power (P) consumption ratio.

Also, manufacturers indicate the energy efficiency class (EEC) of the lamp. *The EEC* label provides details about an electrical appliance's energy usage so that customers may choose the best model of lamp. This is underlined on the label by the use of colors on the arrows, where green denotes maximum efficiency and red denotes the lowest performance level. For the lamps, the energy efficiency classes are separated into seven categories, with values stated as letters from A to G and indicating the efficiency range of artificial light sources [12]. The efficiency of Class A lights is 210 lm/W. The ranges of 185-210, 160-185, 135-160, 110-135, and 85-110 lm/W, respectively, show the efficacy of artificial light sources with

classes B, C, D, E, and F. The class G lamp has the lowest efficiency, which is 85 lm/W.

Colour temperature (TC) describes the tone of the light that a light bulb emits. Between 1000- and 10,000-degrees Kelvin are used to quantify TC. It is very important that customers select a lamp with the proper colour temperature when lighting a space. The TC has a significant impact on the human psyche because different colours of light induce different feelings, moods, and associations. The lighting manufacturers use a variety of colours to make the light that is emitted look pleasing to the eye [13]. The impact of light's colour temperature on a person's physical and mental health can be either beneficial or harmful. A light that is between 2300 and 3000 K in temperature is better for the eyes and more relaxing. According to research [14], exposure to light with a TC of 5000–6000 K elevates blood pressure, heart rate, and levels of both physical and mental activity. To avoid health case deterioration, it is recommended to reside in a high-TC environment for no more than 3-5 hours per day. The TC range of artificial light sources within 2200–3000K is best for human vision.

Another important characteristic of a lamp is the *colour rendering index (CRI).* The CRI is a luminous parameter of an artificial light source that indicates how accurately that light source displays the natural colours of the illuminated object [15]. The CRI range is defined from 0 to 100. If CRI is 0, then all objects have the same colour. If the CRI is 100, then the light source transfers to the observer the true colours of the object. The low CRI that cannot simulate day-light colours decreases serotonin production in the human brain and causes serotonin syndrome. The higher the CRI of the artificial light source, the better the colour rendering. A study [16] shows that for the avoidance of vision problems, it is recommended to use luminaries with sufficient colour rendering of at least 80.

The spread of light from the light source is defined as the *light beam angle (LBA)* and measured in degrees. LBA determines the area illuminated by the light: with a higher LBA, more area is illuminated, and with a lower LBA, a smaller area is lightened [17]. The light will be more evenly dispersed but will have less luminous flux with wider beam angles. Conversely, greater light intensity will distribute less light at narrower angles.

TABLE III
LED LAMP' PARAMETERS DECLARED BY MANUFACTURES

Code/index	Rated Power P, W	Luminous Flux Φ, lm	T_C, K	Light Beam Angle LBA, ^{0}	Energy Efficiency Class EEC			Price, Eur	Lifetime LT, years	CRI
					Letter	Efficiency η lm/W	Average Efficiency η_{av} lm/W			
A1	7,5	806	2700	360	D	135-160	147,5	10,99	1,7	95
A2	4	470	4000	360	E	110-135	122,5	5,99	1,7	80
A3	6,5	806	2700	360	E	110-135	122,5	6,49	1,7	80
B1	5,9	806	2700	360	D	135-160	147,5	9,29	1,7	90
B2	8	806	2700	360	F	85-110	97,5	4,79	1,7	80
B3	10,5	1521	2700	150	D	135-160	147,5	12,99	1,7	90
B4	8,5	1055	4000	150	E	110-135	122,5	9,79	1,7	80
B5	12,5	1521	2700	150	E	110-135	122,5	8,79	1,7	80
B6	10	1055	2700	150	F	85-110	97,5	5,79	1,7	90
B7	7,5	806	4000	150	F	85-110	97,5	4,79	1,7	80
C1	8,8	806	4000	360	F	85-110	97,5	4,79	10	80
C2	11	1060	4000	360	F	85-110	97,5	5,79	10	80
C3	13,2	1521	4000	360	F	85-110	97,5	8,79	10	80
D1	10	1065	4000	220	F	85-110	97,5	4,79	2,85	85
D2	13,5	1521	6400	220	E	110-135	122,5	6,99	2,85	85
D3	10	1055	3000	220	E	110-135	122,5	6,99	2,85	85
D4	10	860	3000	200	E	110-135	122,5	3,29	2,85	85
D5	12	960	3000	240	E	110-135	122,5	3,79	2,85	85
D6	12	1060	3000	240	E	110-135	122,5	8,99	2,85	85
D7	15	1340	2700	360	A	210	210	5,49	2,85	85
D8	18	1901	6400	360	A	210	210	6,49	1,7	85
D9	15	1500	6400	360	A	210	210	5,49	1,7	85
D10	15	1350	4000	360	E	110-135	122,5	5,49	1,7	85
D11	18	1900	3000	120	A	210	210	6,49	2,3	85
D12	15	1340	3000	360	A	210	210	6,49	1,7	85

The room should be evenly and brightly illuminated throughout by the LB with an LBS of 360 degrees. The narrow LBA light bulb (from 10 to 46 degrees) emits light that only illuminates the designated region of the room. The lamps, presented in the Table 2 are classified [18] as having wide (100-1300) and very wide (1300 or more degree) LBA. LBs with a narrow LBA are used for the illumination of working places. If there are several working places in the room, the number of LB with narrow LBA should be increased in accordance with the number of working places. For ordinary areas, it is preferable to use artificial light sources with a wide LBA that help to decrease their amount as well as save electric energy consumption.

III. MATHEMATICAL MODEL FOR THE LIGHT SOURCE SELECTION

In order to determine the level of importance of lamp parameters that influence choice and to propose the selection algorithm for LED lamps, the Multiple-Criteria Decision-Making (MCDM) technique was used. The MCDM method was applied to the lamps, whose parameters are presented in Table 3.

The MCDM clearly assesses numerous competing factors in decision-making. The equations used in this section were published in [19]. Using the MCDM method, a $n \times m$ working table is created in which the first column, in the form of an X quantity, contains alternatives that can affect the final decision. For this study, quantity X is the number of LED lamps offered by the store (Table 3).

$$X = \{x_i\}, \quad i = 1, n; \quad n = |X| \tag{1}$$

Here: X-is the quantity of proposed lamps;
  n - the number of proposed lamps.

The quantity R represents the criteria for lamps that are written in the first row of Table 4 and includes price (Pr), average efficiency (η_{av}), rated power (P), luminous flux (Φ), colour temperature (T_C), colour rendering factor (CRI), light beam angle (LBA), and lifetime (LT). The listed criteria are arranged in order from the most significant to the least significant. The significance of criteria was determined according to interview results (Table 2) and based on the studies [6-8].

$$R = \{r_j\}, \quad j = 1, m; \quad m = |R| \tag{2}$$

Here: R-is the quantity of proposed criteria;
  m - the total number of proposed criteria.

Therefore, the working table should consist of n rows and m columns.

At the next stage of the analysis, the weight of each criterion is calculated. As the number of criteria m is less than [20] for the weight determination, the simplified equation (3) is used:

$$\omega_j = \frac{2 \cdot (m - j + 1)}{m \cdot (m + 1)} \tag{3}$$

Here: ω_j-is the weight of j criterion.

If all the criteria for the customer are equivalent, that is, he cannot decide which of the criteria is greater or less important for him, then the weights of all criteria are calculated as follows:

$$\omega_j = \frac{1}{m} \tag{4}$$

For both weighted or equivalent criterion case, the correctness of the criteria weight calculation is checked by accepting that the sum of all weights must be equal to one:

$$\sum_{j=1}^{m} \omega_r = 1 \tag{5}$$

The following phase of the analysis includes the calculations of the values of the local priority vector (LPV) using one of the formulas (6) or (7). The LPV quantitatively describes the set of features, i.e., a set of criteria inherent in one object, i.e., an alternative. The calculated NPV values u_{ij} are entered in Table 4 through the slash. The choice of formula (6) or (7) is carried out according to the rule: a) if an increase in indicators among alternatives according to one or another criterion leads to an improvement in quality, formula (6) should be used; b) if the increase in indicators among alternatives for one or another criterion leads to a deterioration in quality, formula (7) is used:

$$u_{ij} = \frac{c_{ij} - c_{ij}^{min}}{c_{ij}^{max} - c_{ij}^{min}} \cdot 100\% \tag{6}$$

$$u_{ij} = \frac{c_{ij}^{max} - c_{ij}}{c_{ij}^{max} - c_{ij}^{min}} \cdot 100\% \tag{7}$$

Here: u_{ij}-is LPV defined for the u_{ij} element of Table 3, %;
  c_{ij}-the weighted value j criterion of the alternative i;
  c_{ij}^{max} and c_{ij}^{min} is a maximum and minimum values of weighted criterion j.

Finally, the vector of global priorities (VGP) is obtained. The VGP is the ultimate goal of multi-criteria analysis and determines the only possible solution from the total set of proposed alternatives. The values of the GPV are defined as $V=\{vi\}, i=1, n$ and calculated using equation (8):

$$v_i = \sum_{j=1}^{m} u_{ij} \cdot \omega_i \tag{8}$$

Here: ω_i-is the weight of i alternative.

The determination of the optimal value of VGP with the designation of the number of the optimal alternative, that is, the desirable solution of selection, is carried out using a set of expressions (9):

$$v_{opt} = \max\{v_i\}; \quad i_{opt} = k; \quad x_{opt} = x_k \tag{9}$$

Here: v_{opt}-is optimal value of VGP;
  k-is the number of optimal alternatives.

IV. MODELLING RESULTS AND DISCUSSIONS

Table 4 presents the results of selecting a single artificial light source from a set of 25 LED lamps according to the parameters declared by the manufacturers. Bold blue and red mark the lowest and highest values of the criteria within one alternative, as well as the values of the LPV in points. LPV criteria Pr., P, and TC were calculated using equation (7), that is, guided by the principle that the greater the value of the criterion, the worse for the purchaser. For all other criteria, namely η, Φ, CRI, LBA, and LT, equation (6) was applied, since the higher the value of the criterion, the better this product is for the customer. The value of LPV is written with a slash and, in some cases, has values equal to either 0 or 100 points. 0 points for an alternative under the condition "the more the better" and 100 points for the condition "the more the worse" mean that the criterion of this alternative has the lowest possible value within the range of one criterion. Conversely, a score of 0 for the "the more the worse" alternative and a score of 100 for the "the more the better" alternative indicates the highest declared value of the criterion.

As a result of calculations, it has been defined that when applying criteria weighted by priorities (the weight of each individual criterion differs from the weights of all other criteria) and equivalent criteria weights, the selection result is the same.

This is an alternative x20 with an alphanumeric code of D7. In the category of criteria "the more, the worse," alternative D7 has a price equal to 5.49 euros, which is 1.4 times more than the designated minimum of 3.29 euros. The TC parameter is equal to the minimum value of 2700K, and the rated power is 3.75 times greater than the minimum. As mentioned earlier, the amount of luminous flux Φ depends on the power P, so to achieve a luminous flux of 1340 lm, which is only 1.4 times less than the designated maximum value of 1901 lm, this amount of energy is adequate. It should also be noted that the alternative D7 has an efficiency class of A, that is, the highest of all the proposed. Therefore, practically all electrical energy will be converted to light. The luminous flux Φ criterion belongs to the category "the more, the better." In the "the more, the better" category, the LBA parameter is equal to the maximum possible of 360 degrees, while the life-time LT of the D7 alternative is 2.85 years, which is significantly less than the maximum of 10 years. However, it should be noticed that the lamp's LT is primarily dependent on the number, frequency, and duration of its switching cycles. Therefore, the low value of this criteria obtained as a result of the simulation should not confuse the purchasers. The CRI parameter has an average of 85 units, which is quite high for the narrow range of this alternative, from 95 to 80.

TABLE IV
MCDM ANALYSIS' RESULTS

			Criteria $R=\{r_j\}$, $j=1$, $m=8$								VGP[1]	VGP[2]
			j_1	j_2	j_3	j_4	j_5	j_6	j_7	j_8		
Alternatives $X=\{x_i\}$, $i=1$, $n=25$			Pr, Eur	η_{av}	P, W	Φ, lm	T_C, K	CRI	LBA, ^{0}	LT, years		
			ω_1	ω_2	ω_3	ω_4	ω_5	ω_6	ω_7	ω_8		
i	x_i	Code/ index	0,222/ 0,125	0,194/ 0,125	0,167/ 0,125	0,139/ 0,125	0,111/ 0,125	0,083/ 0,125	0,056/ 0,125	0,028/ 0,125		
1	x_1	A₁	10,99/20,6	147,5/44,4	7,5/75,0	806/23,5	2700/100,0	95/100,0	360/100,0	1,7/0,0	54	58
2	x_2	A₂	5,99/72,2	122,5/22,2	4/100,0	470/0,0	4000/64,9	80/0,0	360/100,0	1,7/0,0	50	45
3	x_3	A₃	6,49/67,0	122,5/22,2	6,5/82,1	806/23,5	2700/100,0	80/0,0	360/100,0	1,7/0,0	53	49
4	x_4	B₁	9,29/38,1	147,5/44,4	5,9/86,4	806/23,5	2700/100,0	90/66,7	360/100,0	1,7/0,0	57	57
5	x_5	B₂	4,79/84,5	97,5/0,0	8/71,4	806/23,5	2700/100,0	80/0,0	360/100,0	1,7/0,0	51	47
6	x_6	B₃	12,99/0,0	147,5/44,4	10,5/53,6	1521/73,4	2700/100,0	90/66,7	150/12,5	1,7/0,0	45	44
7	x_7	B₄	9,79/33,0	122,5/22,2	8,5/67,9	1055/40,9	4000/64,9	80/0,0	150/12,5	1,7/0,0	37	30
8	x_8	B₅	8,79/43,3	122,5/22,2	12,5/39,3	1521/73,4	2700/100,0	80/0,0	150/12,5	1,7/0,0	42	36
9	x_9	B₆	5,79/74,2	97,5/0,00	10/57,1	1055/40,9	2700/100,0	90/66,7	150/12,5	1,7/0,0	49	44
10	x_{10}	B₇	4,79/84,5	97,5/0,00	7,5/75,0	806/23,5	4000/64,9	80/0,0	150/12,5	1,7/0,0	42	33
11	x_{11}	C₁	4,79/84,5	97,5/0,00	8,8/65,7	806/23,5	4000/64,9	80/0,0	360/100,0	10/100,0	49	55
12	x_{12}	C₂	5,79/74,2	97,5/0,00	11/50,0	1060/41,2	4000/64,9	80/0,0	360/100,0	10/100,0	46	54
13	x_{13}	C₃	8,79/43,3	97,5/0,00	13,2/34,3	1521/73,4	4000/64,9	80/0,0	360/100,0	10/100,0	41	52
14	x_{14}	D₁	4,79/84,5	97,5/0,00	10/57,1	1065/41,6	4000/64,9	85/33,3	220/41,7	2,85/13,9	47	42
15	x_{15}	D₂	6,99/61,9	122,5/22,2	13,5/32,1	1521/73,4	6400/0,0	85/33,3	220/41,7	2,85/13,9	39	35
16	x_{16}	D₃	6,99/61,9	122,5/22,2	10/57,1	1055/40,9	3000/91,9	85/33,3	220/41,7	2,85/13,9	49	45
17	x_{17}	D₄	3,29/100	122,5/22,2	10/57,1	860/27,3	3000/91,9	85/33,3	200/33,3	2,85/13,9	55	47
18	x_{18}	D₅	3,79/94,8	122,5/22,2	12/42,9	960/34,2	3000/91,9	85/33,3	240/50,0	2,85/13,9	53	48
19	x_{19}	D₆	8,99/41,2	122,5/22,2	12/42,9	1060/41,2	3000/91,9	85/33,3	240/50,0	2,85/13,9	43	42
20	x_{20}	D₇	5,49/77,3	210/100,0	15/21,4	1340/60,8	2700/100,0	85/33,3	360/100,0	2,85/13,9	68	63
21	x_{21}	D₈	6,49/67,0	210/100,0	18/0,0	1901/100,0	6400/0,0	85/33,3	360/100,0	1,7/0,0	57	50
22	x_{22}	D₉	5,49/77,3	210/100,0	15/21,4	1500/72,0	6400/0,0	85/33,3	360/100,0	1,7/0,0	59	51
23	x_{23}	D₁₀	5,49/77,3	122,5/22,2	15/21,4	1350/61,5	4000/64,9	85/33,3	360/100,0	1,7/0,0	49	48
24	x_{24}	D₁₁	6,49/67,0	210/100,0	18/0,0	1900/99,9	3000/91,9	85/33,3	120/0,00	2,3/7,2	61	50
25	x_{25}	D₁₂	6,49/67,0	210/100,0	15/21,4	1340/60,8	3000/91,9	85/33,3	360/100,0	1,7/0,0	65	59

VGP[1]- is the vector of global priorities under weighted criteria
VGP[2]- is the vector of global priorities under equilibrium criteria

IV. CONCLUSION AND RECOMMENDATION

During the study, it was found that selecting an appropriate LED lamp for residential use becomes challenging because most consumers lack a thorough awareness of factors like the luminous qualities of artificial light sources. The majority of respondents make a choice, paying attention to price, wattages, and efficiency, while other luminous parameters of lamps declared by manufacturers are little known or unknown at all. The CRI, Φ, TC, and LBA are complicated concepts for many common customers, despite the fact that they have a direct impact on how an illuminated item is physically perceived by the human eye. In order to optimize the possible options from the set of proposals, a mathematical model of "Multiple-Criteria Decision-Making " analysis was proposed. The MCDM method allows one to select one lamp with optimal parameters from the proposed N items and identify parameters that are questionable or do not have a significant impact on the final choice, such as power rating P, CRI, and LT. It is reasonable to consider the energy efficiency class (EEC) at the beginning of the selection process. In the second step, it is useful to determine the desired power (P) and luminous flux (Φ) of the light bulb.

Additionally, because the CRI parameter for LED lamps has a fairly limited range from 80 to 95, it is not essential to specifically regard one because it should be equal to or greater than 80. Another parameter that should not be taken into consideration is the lifetime (LT) of the lamp because, as mentioned above, it depends on the frequency of the lamp's commutation.

Summarizing the study, the authors propose an LED lamp selection algorithm in several steps. This LED lamp selection guide is offered according to the above conclusions, covers all the criteria involved in modelling, and includes the following steps:

1. Determine an admissible price.
2. Make sure that the electrical efficiency class is in the range [A; C].
3. Review the rated power; it should be as low as possible.
4. Check the luminous flux: it should be no less than 806 lm.
5. Make sure the color temperature does not exceed 4000K.
6. Verify that the CRI is not less than 80.
7. Review the light beam angle: it should be higher than 240 degrees.
8. Examine the lifetime: the bigger the number of hours, the better.

REFERENCES

[1] G. B. Nair, S. J. Dhoble, „The Fundamentals and Applications of Light-Emitting Diodes, Woodhead Publishing Series in Electronic and Optical Materials, 2021, Pages 253-270.

[2] B.-S.Wu, Y. Hitti, S. MacPherson, V. Orsat, M. G. Lefsrud, "Comparison and perspective of conventional and LED lighting for photobiology and industry applications", Environmental and Experimental Botany, 2020, Volume 171, 103953.

[3] EU COMMISION REGULATION (EU) 2019/2020 SLR & 2019/2015, "The Ecodesign for Energy-Related Products and Energy Information (Lighting Products) Regulations 2021, No.1095;

[4] M.E. Emetere, L.P. Bologi, S.E. Sanni, O.R. Chidi, D. Femi-Pidan and E.E. Okoro, 2021, "A review on electrical bulbs and its improvement over time: Saving energy or life?", Published under licence by IOP Publishing Ltd; DOI 10.1088/1757-899X/1107/1/012144;

[5] Ignitis Group, Private elelctricyti supply, https://ignitis.lt/en/electricity-home

[6] Orose Leelakulthanit, National Institute of Development Administration, Thailand, (2014), The Factors Affecting The Adoption Of LED Lamps, International Business & Economics Research Journal – July/August 2014 Volume 13, Number 4.

[7] M. Ganeshalingam, R. Hosbach, L. Zavodivker, B. F. Gerke, C.L.S. Kantner, and H. Stratton, (2022), Consumer Purchasing Behavior and Usage of Lighting in the Residential Sector, Energy Efficiency Standards Department Energy Analysis and Environmental Impacts Division, Lawrence Berkeley National Laboratory.

[8] Dr.S.Padmini, (2020), Consumer Perception and Purchasing Behavior towards LED Lights, IOSR Journal of Business and Management (IOSR-JBM) e-ISSN: 2278-487X, p-ISSN: 2319-7668. Volume 22, Issue 5. Ser. IV (May. 2020), pp. 18-32, www.iosrjournals.org

[9] Boothby, C., Murray, D., Polovick Waggy, A., Tsou, A., Sugimoto, C.R., (2021), Credibility of scientific information on social media: Variation by platform, genre and presence of formal credibility cues, Quantitative Science Studies, 2021, № 3, p. 845-863.

[10] Allen, E., S., Burke, J., M., Welch, M., E., Rieseberg, L., H., (1999), How reliable is science information on the web? Nature. 1999 Dec 16;402(6763):722. doi: 10.1038/45370.

[11] S. Kitsinelis and S. Kitsinelis, (2015), "Light Sources: Basics of Lighting Technologies and Applications 2nd Edition", CRC Press; 2nd edition, 2015.

[12] European Commission - Press release, (2021), "Simpler EU energy labels for lighting products applicable from 1 September", Brussels, 31 August 2021.

[13] R. Shahidi, R. Golmohammadi, M. Babamiri, J. Faradmal, and M. Aliabadi, (2021), "Effect of warm/cool white lights on visual perception and mood in warm/cool color environments", EXCLI J. 2021; 20: 1379–1393.

[14] A. Jiang, X. Yao, S. Westland, C. Hemingray, B. Foing and J. Lin, "The Effect of Correlated Colour Temperature on Physiological, Emotional and Subjective Satisfaction in the Hygiene Area of a Space Station", 2022, Int J Environ Res Public Health, 19(15): 9090.

[15] CIE 13.3, (1995), Method of Measuring and Specifying Colour Rendering Properties of Light Sources (E).

[16] C. Ticleanu, "Impacts of home lighting on human health", Lighting Research and Technology, 2021, Volume 53, Issue 5, pp. 453–475.

[17] CIE 2015. CIE S 025/E:2015. Test Method for LED Lamps, LED Luminaires and LED Modules. Vienna: CIE.

[18] IEC TR 61341:2011," Method of measurement of center beam intensity and beam angle(s) of reflector lamps"

[19] A. T. de Almeida, C. A. V. Cavalcante, M. H. Alencar, R. J. P. Ferreira, A.T. de Almeida-Filho, T.V. Garcez,(2015), "Multicriteria and Multiobjective Models for Risk, Reliability and Maintenance Decision Analysis", International Series in Operations Research and Management Science. Springer, 2015.

[20] Lopez, L., M., Ishizaka, A., Qin, J., Alvarez-Carrillo, P., A., (2023), Multi-Criteria Decision-Making Sorting Methods: Applications to Real-World Problems, Academic Press; 1st edition.

BIOGRAPHIES

Jelena Dikun, Klaipeda, in 1970. She received the B.S. and M.S. degrees in electrical engineering from the University of Klaipeda, Lithuania, in 2011 and 2013, respectively.

From 2012 to 2014, she was a research assistant with the electromagnetic pollution project at Klaipeda University. At present, she works as a lecturer for a Higher Education Institution in the Engineering and Informatics Department, as well as for Klaipeda University in the Engineering Department. She is the author of 20 articles. Her research interests include light technology, electrical materials, and technical measurements in electrical engineering.

Vilma Jakubauskiene, Klaipeda, in 1965. She received the B.S. and M.S. degrees in mathematics from the University of Vilnius, Lithuania, in 1988 and she received the M.S. degrees in computer science engineering from the University of Technology of Kaunas. At present, she works as a lecturer for a Higher Education Institution in the Engineering and Informatics Department. She is the author of 10 articles. Her research interests include Methods of teaching mathematics in the age of technology and distance learning environments.

Research Article

Real-Time Digital Simulator Design for Differential Drive Mobile Robot using FPGA

Mehmet Rıza Saraç, Omur Aydogmus

Abstract—**This paper presents a real-time simulation of a differential drive mobile robot (DDMR). The permanent magnet DC motors that drive the robot's left and right wheels were modeled and executed in real-time on a Field Programmable Gate Array (FPGA) based co-simulator platform, interfacing with the Webots robot simulator, which simulates the DDMR on the PC side. The electrical parameters, which are not available in robot simulators, were simulated and measured by the proposed co-simulator system in real-time under various environmental conditions and trajectories of the robot. Parameters such as current, voltage, and torque were measured instantaneously, enabling a more realistic simulation. Additionally, the cycle time of the robot simulator was determined to be 32 ms, and the developed FPGA-based simulation operated at approximately 2000 times the speed of the robot simulator. The results demonstrate the applicability of the developed platform in robotic applications.**

Index Terms—**Co-simulator, Digital Twin, FPGA, Mobile robot, Real-time digital simulator.**

I. INTRODUCTION

OVER time mobile robots have increasingly become integrated into our daily lives, taking on different forms and playing significant roles in various sectors [1]. They have proven their adaptability in industrial production [2], medical applications [3], agricultural processes [4], space exploration [5], and various other fields. As technology advances, it is evident that mobile robots have the potential to overcome challenges and stimulate innovation in different areas [6].

Mobile robots are typically divided into two main categories: wheeled robots [7] and legged robots [8]. Additionally, there are various approaches to combining wheeled and legged components to create different types of robots [9]. Wheeled mobile robots exhibit variations in wheel type, quantity, and assembly configuration. Designs range from standard types to mecanum, omni, and spherical wheels, as well as differential and steering wheels, depending on the connection configuration [10].

However, constraints such as time and cost make it impractical to work directly with mobile robots. Many applications require preliminary work to be done in a simulation environment. Various robot simulation platforms, such as Gazebo, Webots, Coppeliasim, and Isaac Sim, have been developed for

this purpose. These simulators are considered a practical and effective approach for developing control strategies, but not all simulators are suitable for simulating electrical variables like current and voltage. These simulators typically focus on kinematic and dynamic modeling using physics engines [11].

As an alternative, simulation techniques, especially Hardware-in-the-Loop (HIL) simulations, are becoming increasingly popular in various systems, including robotics [12], automotive [13], power systems [14], and aircraft systems [15]. For instance, a backstepping control regulator has been implemented for PUMA 560 using the FPGA-in-the-loop option on the Xilinx Zedboard Zynq FPGA with the Hardware Description Language (HDL) Coder tool [16]. Another study focused on optimizing solution times for real-time use of inverse kinematics in articulated robots, developing and testing an optimization algorithm compatible with FPGA architecture [17]. Furthermore, a discussion on the application of FPGA-based HIL simulation to computer vision in an unmanned aerial vehicle is presented in [18].

A review of the existing literature shows that there is a significant gap in robot simulators that do not include electrical models. This paper proposes a novel solution using an FPGA architecture to simulate models of electric motors with high-speed processing. In this study, FPGA-based models for the drive motors of a DDMR were designed and executed in real-time with an FPGA-based co-simulator. In the proposed system, the angular velocities and currents of the motors were transmitted to a PC-based robot simulator platform, while voltage and torque information was received as feedback to the FPGA environment. As a result, the motors were operated in the FPGA environment and seamlessly integrated with the PC-operated robot. This innovative approach successfully addresses the gap in traditional robot simulators and improves the existing system by incorporating the previously ignored electrical model component.

This paper is organized as follows: It begins with an introduction that provides information about mobile robots and FPGA-based HIL systems. The next section presents the hardware side of the study, which includes FPGA. In the third section, the robot simulator and control concept are discussed. The experimental results are analyzed in the fourth section. Finally, the paper concludes with a summary section that recaps the main findings and explores their implications for future research.

II. FPGA HARDWARE DEVELOPMENT

Real-time simulators use fixed time step algorithms for calculations. This approach requires Dommel's method to bee

Mehmet Rıza Saraç is with the Department of Mechatronics Engineering, Technology Faculty, Firat University, Elazig, TURKEY e-mail: mrsarac@firat.edu.tr

Omur Aydogmus is with the Department of Mechatronics Engineering, Technology Faculty, Firat University, Elazig, TURKEY e-mail: oaydogmus@firat.edu.tr

TABLE I
INTEL CYCLONE V SE 5CSEBA6U23I7NDK FPGA RESOURCES

Resource	Description	Value
LEs (K)	Logic Elements	110
ALMs	Adaptive Logic Modules	41,910
Reg	Registers	116,036
MLAB (Kb)	Memory	621
M10K (Kb)	Memory	5,570
DSP	DSP Blocks	112
18x18 Mult.	18x18 Multipliers	224
PLL	Phase Locked Loop (Fractional)	6
DLL	Delay Locked Loop	4
Global Clock	Clock Networks	16
GPIO	General Purpose I/O	288

Fig. 1. PMDC motor simulator module of digital twin system

used for systems including nonlinear components like inductors and capacitors [19]. Simulator input signal is interpreted as a sequential arrays step functions. Every simulation step requires previous calculation results as boundary conditions. This requires previous simulation step to be completed and the results saved before the evaluation of next step. To compete with required calculation work load, high speed and high performance equipments need to be used. This performance can be achieved by software using high speed μP with combination of real-time operation systems or by hardware approach. Hardware development is mainly used for Very large-scale integration (VLSI) electronic components. However, VLSI manufacturing is a hard and painful process permitting very limited changes after tape-out process.

FPGA-based systems has great advantages for hardware development and permitting hardware changes even after end product is sold. In this study DE10-Nano development board was selected for its popularity. DE10-Nano development board is a Solution on Chip (SoC) development platform produced by Terasic company. Platform designed around Intel Cyclone V 5CSEBA6U23I7 SoC device which contains dual core ARM Cortex-A9 hardware processor and FPGA fabric with resources listed in the Table I [20].

The development board has an onboard Analog-Digital Converter (ADC) system based on Linear Technology LTC2308. The ADC has a resolution of 12 bits, operates at a speed of 500 KSPS, and 8 analog input channels. It supports a 4-wire Serial Peripheral Interface (SPI) connection interface with a maximum operating frequency of 40 MHz. Proposed FPGA-based real-time digital simulator system also includes an interface board for analog signal inputs and outputs. The analog interface board also contains Digital-Analog Converter (DAC) systems which the development board does not include. The DDMR simulated for this study has two DYNAMIXEL XL430-W250-T servo motors with gear ratio of 258.5:1. The proposed real-time simulator was designed to simulate Permanent Magnet Direct-Current (PMDC) motors. To simulate gear box mechanical loading of servo motors used by robot, additional mechanical load was configured with parameter inputs of real-time simulator. The load torque on the shaft of servo motors are simulated by Webots simulator and received as T_i signal by real-time simulator.

The real-time simulator was designed to accept eight input signals which four of them are supply voltage and torque
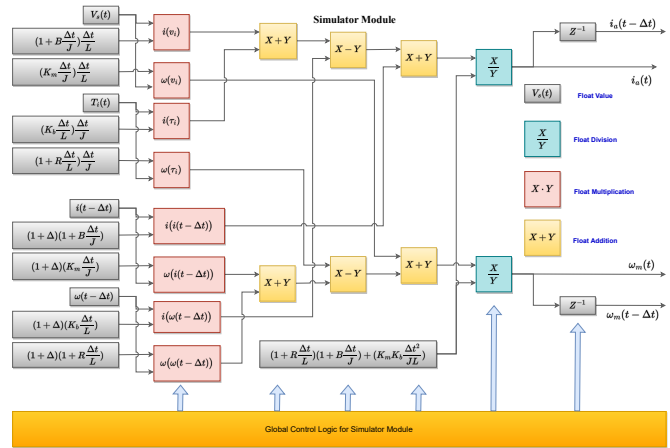
inputs for both left and right motors. Other input signals are parameter inputs for simulator assumed to be same for both motors which are B_L, J_L, K_M, and K_B. ADC inputs for supply voltages and torque inputs were privileged and configured to be read at every ADC read sequence.

The real-time simulator has eight channels to be read and with the read speed of 500 Kilo samples per Second (KSPS) each channel will have a 62.5 KSPS of speed. To increase sampling ratio a privilege system was used. The system read sequence has four privileged inputs and the only one of the four parameter input channels in ADC read sequence. This asymmetric read sequence enables a speed rate of 100 KSPS for privileged channels and only 25 KSPS speed for parameter inputs. All required ADC channels were read in 10 μs and after this read sequence was completed and a signal asserted within simulator as simulation step signal.

FPGA hardware development was made by using Intel Quartus Prime Lite edition software freely available from manufacturers web page. For hardware development Verilog hardware description language (HDL) is used and Intel floating point IP library was used for floating calculations. The development board generate a clock signal of 50 MHz and fed FPGA at three different pins. A hardware Phase Locked Loop (PLL) unit was used to generate required clock signals required by proposed real-time simulator. To configure and read from ADC system an SPI module was developed to communicate with LTC2308 ic. This module requires 40 MHz clock signal to operate which was generated by PLL module. A module was also designed to control reset signal. The analog interface board contain DAC channels which use parallel interface to communicate with development board. A module was developed with in FPGA for PI interface used by DAC channels.

The real-time simulator contains three main modules which operate at 50 MHz required for simulation. There was two motor simulator modules as depicted in Fig. 1 operating in parallel to simulate right and left motors of robot. The real-time simulator also contains a module as depicted in Fig. 2 as parameter module which is used to calculate required coefficients for motor simulator modules from parameter input
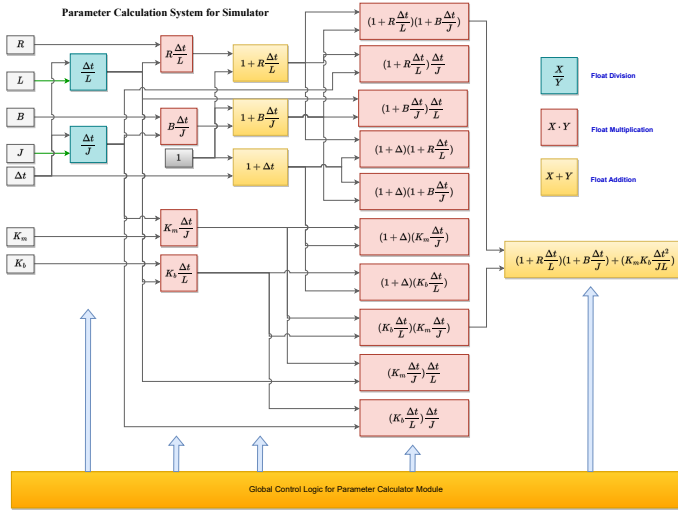
Fig. 2. Parameter calculation module of digital twin system

Fig. 4. Control system of motor voltage

Fig. 3. RTDS and Webots robot simulator connection block diagram

signals.

The motor simulator modules get main input signals and calculate output signals I_a and ω_m by using coefficients calculated by *Parameter Calculation* module. Both modules were designed to perform calculations with in 10 μs as it is also one ADC read cycle. However the changes in main input signals can be seen after one simulation cycle, the change in parameter inputs were using an additional simulation cycle to be ready for use by main simulator module which means at least two cycles were required for the the change of parameters to effect the output signals.

III. ROBOT SIMULATOR AN CONTROL CONCEPT

In this study, the Webots robot simulator was employed for the physical calculations of the robot. Open Dynamics Engine (ODE) was employed as the default physics engine in WEBOTS to perform physics calculations. Additionally, the definitions of the Turtlebot3 were utilized in the pre-defined PROTO file, created from WEBOTS components. The connection between this simulator (PC-side) and the Real Time Digital Simulator (RTDS) (FPGA-side) co-simulator was established using Python, which utilized the *pydwf* library to facilitate communication with Analog Discovery 2 devices. Within the Python program, a subprogram generated angular velocity information to be applied to the motors for robot movement. As illustrated in Fig. 3, Analog Discovery 2

devices served as analog input and output modules for data exchange.

The angular velocity values generated by the robot control algorithm were transmitted to the Webots robot simulator. Torque and angular velocity references from Webots were combined with armature current and angular velocity feedback information from the real-time co-simulator. These inputs were then used to calculate the supply voltage value for the digital motors. To derive this voltage value, in Eq. 2. is formulated by substituting the load torque, $T_L(t)$, for the input torque, $T_i(t)$, in Eq. 1. The calculation of the supply voltage value, crucial for motor application, involves a fixed value of 128 ms for Δt, as specified in the equation. However, given that Δt can vary during the simulation, it is treated as a variable and measured for use in the calculations.

$$\omega(t) = \frac{(1+\Delta t)\left[(1+\Delta t\frac{R}{L})\omega(t-\Delta t) + \frac{\Delta t K_m}{J}i(t-\Delta t)\right]}{(1+\Delta t\frac{R}{L})(1+\Delta t\frac{B}{J}) + \Delta t^2 \frac{K_m K_b}{JL}}$$
$$+ \frac{(1+\frac{R\Delta t}{L})\frac{\Delta t}{J}T_i(t) + \frac{\Delta t^2 K_m}{JL}V(t)}{(1+\Delta t\frac{R}{L})(1+\Delta t\frac{B}{J}) + \Delta t^2 \frac{K_m K_b}{JL}} \quad (1)$$

$$V(t) = \frac{(1+R\frac{\Delta t}{L})(1+B\frac{\Delta t}{J}) + K_m K_b\frac{\Delta t^2}{JL}}{K_m\frac{\Delta t^2}{JL}}\omega(t)$$
$$+ \frac{(1+R\frac{\Delta t}{L})\frac{\Delta t}{J}}{K_m\frac{\Delta t^2}{JL}}T_i(t)$$
$$+ \frac{(1+\Delta t)}{K_m\frac{\Delta t^2}{JL}}K_m\frac{\Delta t}{J}i(t-\Delta t)$$
$$- \frac{(1+\Delta t)}{K_m\frac{\Delta t^2}{JL}}(1+R\frac{\Delta t}{L})\omega(t-\Delta t) \quad (2)$$

The calculations, as depicted in Eq. 2, are executed within the motor voltage control system illustrated in Fig. 4. These computations were performed to generate the supply voltage values applied to the motors. The obtained voltage and load torque values were transmitted to the real-time simulator through the Analog Discovery 2 device. Utilizing this information, the real-time simulator simulated the motors, generating
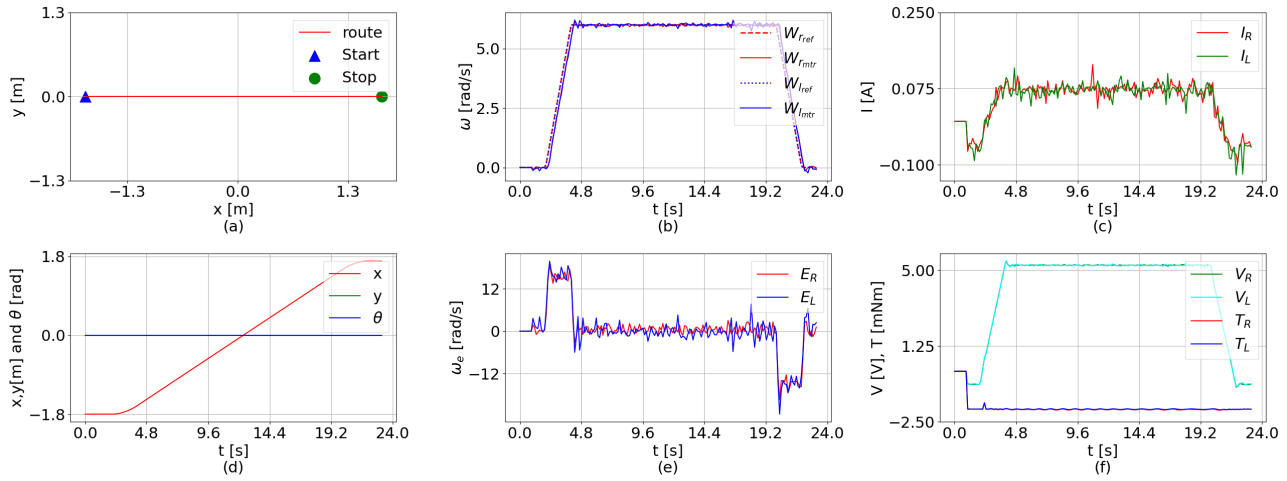
Fig. 5. Results for robot simulation for linear trajectory on a surface with inclination of 0.1 for $x = 0$ axis rad and 2 kg of payload; a) trajectory followed by robot, b) speed references and simulated speed value for motors, c) armature currents for both motors, d) position and orientation of robot, e) error values for both motors angular speed values, f) simulated load torque and supply voltages for motors
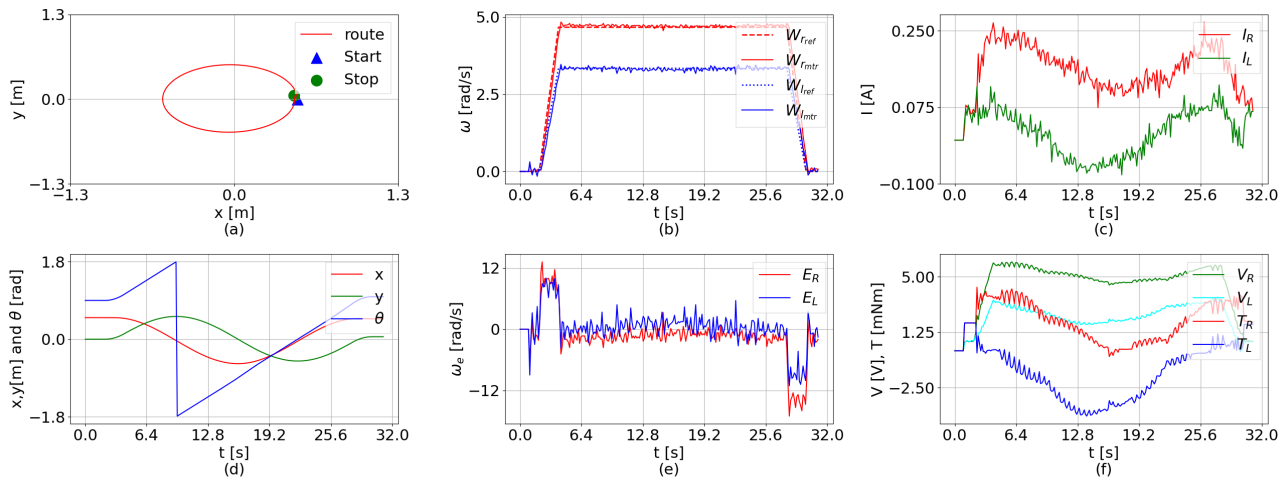
Fig. 6. Results for robot simulation for circular trajectory on a surface with slope of 0.1 rad for $y = 0$ axis and 2 kg of payload; a) trajectory followed by robot, b) speed references and simulated speed value for motors, c) armature currents for both motors, d) position and orientation of robot, e) error values for both motors angular speed values, f) simulated load torque and supply voltages for motors

angular velocity and armature current signals. Subsequently, these calculated values were relayed back to the Python-based control program. The program also undertakes the task of saving these values to show the experimental results.

IV. EXPERIMENTAL RESULTS

A. Linear trajectory

The results shown in Fig. 5 are obtained for a robot carrying a 2 kg payload on a plane with a positive slope of 0.1 rad in the x-axis. As depicted in Fig. 5a, the robot travels approximately 4 meters linearly along the x-axis. The robot covered the distance between the start point and the end point in approximately 24 seconds. Fig. 5b demonstrates that the left and right motors accurately follow the reference velocity signals. The armature currents of the motors are illustrated in Fig. 5c. The robot's x, y position, and rotation information

on the z-axis θ are presented in Fig. 5d. Since the robot moves linearly, its rotation on the z-axis is zero. The error signals at angular velocities are shown in Fig. 5e. The high values in the error signals in the acceleration and deceleration regions are attributed to the control step time of the Webots simulator, which is 130 ms. The voltage signals obtained at the controller output and the torque values measured from the robot wheels are analyzed in Fig. 5f. As seen, the torque values are negative as the robot descends the ramp. In this case, both motors should operated in forward-braking (regenerating) mode. However the total load torque of motor is the sum of both servo systems load torque and the load of the gearbox inside servo system. For lower speed of robot, the motors were operating in forward-braking mode and the armature current is reversed. But for higher speeds of robot, the required torque for the gearbox increased and motors needs to compensate additional torque by working at forward-motor quarter. The
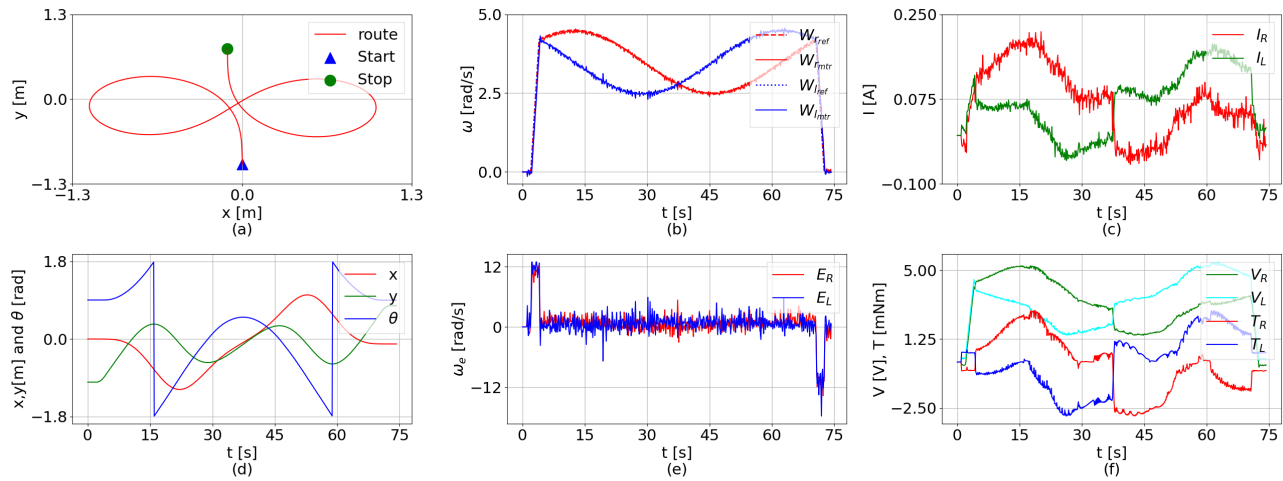
Fig. 7. Results for robot simulation for infinite symbol trajectory on a surface with inclination of 0.1 rad for $x = 0$ axis; a) trajectory followed by robot, b) speed references and simulated speed value for motors, c) armature currents for both motors, d) position and orientation of robot, e) error values for both motors angular speed values, f) simulated load torque and supply voltages for motors

motors driving the robot are connected to the wheels through a reducer. Thus, the torque at the output of the reducer and the armature current patterns of the motors are dissimilar as shown in Fig. 5.

B. Circular trajectory

As a different operation, the plane is set to a 0.1 rad slope in the y-axis. Subsequently, the robot is operated on a circular trajectory with a radius of 0.5m under the same load conditions. The graphs obtained under these conditions are presented in Fig. 6. The circular trajectory along which the robot moves is shown in Fig. 6a. Since the robot moves counter-clockwise, Fig. 6b illustrates that the left wheel rotates slower than the right wheel. In Fig. 6c, between 12-19 seconds, the left motor operates in regenerative mode, drawing negative current. This is because, at that moment, the motor continues to run at a positive speed. Fig. 6d depicts the robot rotating on the z-axis for a total of one revolution, oriented in the same direction. The error signals are presented in Fig. 6e, and voltage and torque signals are given in Fig. 6f.

C. Infinite symbol trajectory

Finally, the robot is moved along a trajectory that resembles an infinity symbol. In Fig. 7, the robot is unloaded, and the plane is rotated on the x-axis by 0.1 rad in the positive direction to obtain a slope. The starting position of the robot is (0,-1), and the end position is (0,0.75). The trajectory of the robot is shown in Fig. 7a. Examining Fig. 7b reveals that the angular velocities of the motors are driven by sine and cosine references. In Fig. 7c, it can be observed that, at some points, the motor operates the generator mode by drawing negative current, performing a braking operation. In this case, the position and angle information of the robot is given in Fig. 7d. Additionally, control error signals are shown in Fig. 7e. Fig. 7f illustrates the voltages applied to the motor and the measured torque signals. Notably, both the left and right motors brake by producing negative torque in different regions.

V. Conclusion

A study is presented to address a missing aspect of robot simulators, namely the electrical modeling of motors. In the proposed system, motor models were developed in real-time within the FPGA environment. This model was integrated with a PC-based robot simulator, introducing a new method to address deficiencies in robot simulation. In the study, the PC side of the robot simulator was responsible for the robot's dynamic features, while the FPGA-based co-simulator side took on the real-time operation of the electrical and mechanical models of the motors.

Upon examining the results of the study, it can be said that satisfactory outcomes were achieved. This work demonstrates the real-time feasibility of electrical analyses through the development of an additional module for robot simulators. As a future study, there are plans to create an FPGA-based robot simulator by establishing a system similar to the physical motor of the robot simulator discussed in this study.

References

[1] M. U. Farooq, A. Eizad, and H.-K. Bae, "Power solutions for autonomous mobile robots: A survey," *Robotics and Autonomous Systems*, vol. 159, p. 104285, 2023.

[2] G. Fragapane, D. Ivanov, M. Peron, F. Sgarbossa, and J. O. Strandhagen, "Increasing flexibility and productivity in industry 4.0 production networks with autonomous mobile robots and smart intralogistics," *Annals of operations research*, vol. 308, no. 1-2, pp. 125–143, 2022.

[3] G. Fragapane, H.-H. Hvolby, F. Sgarbossa, and J. O. Strandhagen, "Autonomous mobile robots in hospital logistics," in *IFIP International Conference on Advances in Production Management Systems*. Springer, 2020, pp. 672–679.

[4] L. Emmi, E. Le Flécher, V. Cadenat, and M. Devy, "A hybrid representation of the environment to improve autonomous navigation of mobile robots in agriculture," *Precision Agriculture*, vol. 22, pp. 524–549, 2021.

[5] F. Luo, Q. Zhou, J. Fuentes, W. Ding, and C. Gu, "A soar-based space exploration algorithm for mobile robots," *Entropy*, vol. 24, no. 3, p. 426, 2022.

[6] P. K. Panigrahi and S. K. Bisoy, "Localization strategies for autonomous mobile robots: A review," *Journal of King Saud University-Computer and Information Sciences*, vol. 34, no. 8, pp. 6019–6039, 2022.

[7] G. Boztas and O. Aydogmus, "Implementation of pure pursuit algorithm for nonholonomic mobile robot using robot operating system," *Balkan Journal of Electrical and Computer Engineering*, vol. 9, no. 4, pp. 337–341, 2021.

[8] O. Aydogmus and M. Yilmaz, "Comparative analysis of reinforcement learning algorithms for bipedal robot locomotion," *IEEE Access*, pp. 1–1, 2023.

[9] S. Zhang, J.-t. Yao, Y.-b. Wang, Z.-s. Liu, Y.-d. Xu, and Y.-s. Zhao, "Design and motion analysis of reconfigurable wheel-legged mobile robot," *Defence Technology*, vol. 18, no. 6, pp. 1023–1040, 2022.

[10] L. Tagliavini, G. Colucci, A. Botta, P. Cavallone, L. Baglieri, and G. Quaglia, "Wheeled mobile robots: state of the art overview and kinematic comparison among three omnidirectional locomotion strategies," *Journal of Intelligent & Robotic Systems*, vol. 106, no. 3, p. 57, 2022.

[11] J. Yoon, B. Son, and D. Lee, "Comparative study of physics engines for robot simulation with mechanical interaction," *Applied Sciences*, vol. 13, no. 2, p. 680, 2023.

[12] I. Tejado, J. Serrano, E. Pérez, D. Torres, and B. M. Vinagre, "Low-cost hardware-in-the-loop testbed of a mobile robot to support learning in automatic control and robotics," *IFAC-PapersOnLine*, vol. 49, no. 6, pp. 242–247, 2016.

[13] Y. Chen, S. Chen, T. Zhang, S. Zhang, and N. Zheng, "Autonomous vehicle testing and validation platform: Integrated simulation system with hardware in the loop," in *2018 IEEE Intelligent Vehicles Symposium (IV)*, 2018, pp. 949–956.

[14] A. Hadizadeh, M. Hashemi, M. Labbaf, and M. Parniani, "A matrix-inversion technique for fpga-based real-time emt simulation of power converters," *IEEE Transactions on Industrial Electronics*, vol. 66, no. 2, pp. 1224–1234, 2019.

[15] C. Qi, F. Gao, X. Zhao, A. Ren, and Q. Wang, "A force compensation approach toward divergence of hardware-in-the-loop contact simulation system for damped elastic contact," *IEEE Transactions on Industrial Electronics*, vol. 64, no. 4, pp. 2933–2943, 2017.

[16] A. Fekik, H. Khati, A. T. Azar, M. L. Hamida, H. Denoun, I. A. Hameed, and N. A. Kamal, "Fpga in the loop implementation of the puma 560 robot based on backstepping control," *IET Control Theory & Applications*, 2023.

[17] S. Dereli and R. Köker, "Hardware design of fpga-based embedded heuristic optimization technique for solving a robotic problem: Ic-pso," *Arabian Journal for Science and Engineering*, pp. 1–15, 2023.

[18] E. Moréac, E. M. Abdali, F. Berry, D. Heller, and J.-P. Diguet, "Hardware-in-the-loop simulation with dynamic partial fpga reconfiguration applied to computer vision in ros-based uav," in *2020 International Workshop on Rapid System Prototyping (RSP)*. IEEE, 2020, pp. 1–7.

[19] H. W. Dommel, "Digital computer solution of electromagnetic transients in single-and multiphase networks," *IEEE Transactions on Power Apparatus and Systems*, vol. PAS-88, no. 4, p. 388–399, April 1969.

[20] *Cyclone V Device Overview*, May 2018.

Mehmet Rıza SARAÇ is a research assistant in the Department of Mechatronics Engineering at the University of Firat, where he has been a faculty member since 2011. He graduated with B.Sc. degree from the Department of Electrical - Electronics Engineering at Inonu University in 2002 and M.Sc. degrees from the Department of Mechatronics Engineering at the Firat University in 2016. Then he completed his Ph.D. degree at the Department of Mechatronics Engineering at the same university in 2023. His current research areas include computer hardware, hardware development, FPGA-based system design, and embedded system design.

Omur Aydogmus is a professor at Firat University, Faculty of Technology, specializing in Mechatronics Engineering. He earned his M.Eng. and Ph.D. degrees in electrical and electronics engineering from Firat University, Elazig, TURKIYE. His research primarily centers on collaborative robots, the integration of artificial intelligence in robotics, electric motor drive systems, and industrial automation applications. He has published numerous papers in peer-reviewed journals and conferences, and he has also received several grants for his research. He is a highly respected researcher in the field of mechatronics engineering, and his work has made contributions to the development of new and innovative technologies in robotics and industrial automation.

Research Article

Document Classification with Contextually Enriched Word Embeddings

Raad Saadi Mahmood, Gokhan Bakal and Ayhan Akbas

Abstract—The text classification task has a wide range of application domains for distinct purposes, such as the classification of articles, social media posts, and sentiments. As a natural language processing application, machine learning and deep learning techniques are intensively utilized in solving such challenges. One common approach is employing the discriminative word features comprising Bag-of-Words and n-grams to conduct text classification experiments. The other powerful approach is exploiting neural network-based (specifically deep learning models) through either sentence, word, or character levels. In this study, we proposed a novel approach to classify documents with contextually enriched word embeddings powered by the neighbor words accessible through the trigram word series. In the experiments, a well-known web of science dataset is exploited to demonstrate the novelty of the models. Consequently, we built various models constructed with and without the proposed approach to monitor the models' performances. The experimental models showed that the proposed neighborhood-based word embedding enrichment has decent potential to be used in further studies.

Index Terms—Text classification, Deep Learning, LSTM, Word2Vec, N-grams

I. INTRODUCTION

THE complexities of human language and the ambiguous nature of word meanings within various contexts pose a significant challenge for machines attempting to learn the precise meanings of words and accurately extract important classifications. However, with the aid of context and textual data, or through human intervention in creating the necessary contexts, models can be trained to process text more effectively, especially through the use of deep learning or neural networks in natural language processing. These techniques have proven to be useful in a range of language classification applications, including spam detection, question classification, and news classification.

To enable accurate predictive development in language and text processing, algorithms have been developed to identify specific words with unique meaning scopes and to establish

RAAD SAADI MAHMOOD is with the Department of Computer Engineering, Engineering Faculty, Cankiri Karatekin University, Cankiri, Turkey e-mail: (irqrsm82@gmail.com) https://orcid.org/0000-0003-0879-1989

GOKHAN BAKAL is with the Department of Computer Engineering, Engineering Faculty, Abdullah Gul University, Kayseri, Turkey e-mail: (gokhan.bakal@agu.edu.tr) https://orcid.org/0000-0003-2897-3894

AYHAN AKBAS is with the Insttite for Communication Systems, University of Surrey, Guildford, UK e-mail: (a.akbas@surrey.ac.uk) https://orcid.org/0000-0002-6425-104X

relationships between words within text sentences. By developing specialized lists of text and relationships between words, models can be trained to more accurately predict classification outcomes and improve their usefulness.

In the field of natural language processing, deep learning techniques such as recurrent neural networks have demonstrated high accuracy in predicting text. These models are able to memorize and recall previous words and information by storing them in hidden layers and maintaining communication between them to recognize relationships. To achieve this, words are converted into vectors and the text is represented by a bag of words. The text length and units are relatively small and closely related within the model.

This article proposes a method for classifying documents, as illustrated in Fig. 1, by following a series of steps.
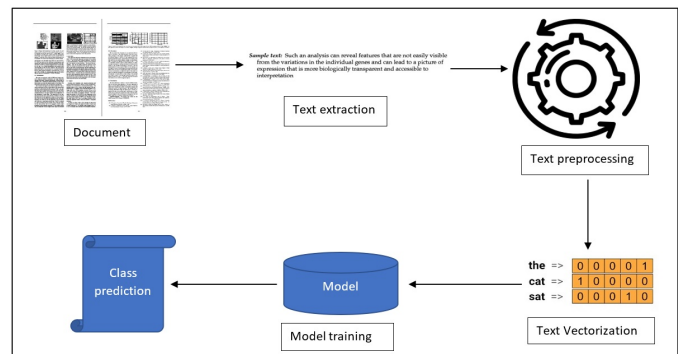
Fig. 1: Document classification model training method

II. RELATED WORK

This article presents a review of previous studies on the use of the single word2vec with n-grams and LSTM models, either independently or in combination, followed by a comparison of their results. Some of these studies include Trappey, Hsu, Trappey and Lin, who utilized a Bayes-based approach with ML and n-grams to classify patent documents with a small dataset of 114 documents achieving a precision rate of approximately 90%, but the model was not suitable for large datasets with 200 words per document. They employed the Back-propagation Network (BPN) algorithm for this purpose [1]. Aghila also employed a small dataset that used feature selection in document classification between single-page documents and 400-page documents. Their approach demonstrated an

accuracy rate of 87% to 98% on the multi-dataset, and they recommended using the combined method for Naïve Bayes and other ML algorithms [2].

Regarding word2vec, Joulin, Grave, Bojanowski, and Mikolov proposed the use of Word2vec in document processing, utilizing images of documents, tags, titles, and captions with 60 and 200 hidden layers. They employed the fastText model with bigram and word vectors, resulting in 97% accuracy with trigram while increasing the model's speed by 600x. However, this study trained with small text documents [3]. Chen and Sokolova detailed embedding algorithms in text processing and analysis of medical and scientific texts, including a dataset of 1000 texts categorized as positive and negative. Their study demonstrated that the Word2vec method is more reliable than Doc2Vec in terms of processing and results [4].

In the realm of natural language processing, several studies have explored the effectiveness of n-grams [5]. Marafino, Davies, Bardach, Dean, and Dudley utilized the SVM algorithm to process n-grams and extract relations. They also combined the n-gram method with feature extraction and achieved accuracy ranging from 0.86 to 0.98, precision of 0.90 to 0.95, and F1 of 0.88 to 0.95. However, this method was tested on a very small dataset of diverse files, including sound and video files [6].

Regarding the LSTM algorithm, numerous studies have investigated its effectiveness. Graves and Schmidhuber found that bidirectional networks outperformed unidirectional ones, and that LSTM was faster and more accurate than standard RNNs and MLPs. In a study by Graves, Fernández, and Schmidhuber, the authors examined the use of long memory in monophonic and biophonic sound classification, and found that bidirectional LSTM outperformed both unidirectional LSTM and traditional RNNs [7], [8].

One of the most significant studies in this field is by Xiao, Wang, and Zuo, who proposed an efficient method for patent document classification. Their approach involves training a patent text classification model using Word2vec and LSTM on a patent dataset, and addressing the dimensional disaster issue caused by traditional methods. They vectorized a dataset of 50,000 using Word2vec, and compared their model's performance with KNN and CNN. Their results showed that LSTM+Word2vec achieved the highest accuracy rate of 93.48%, while normal LSTM achieved 87.7%, CNN+Word2vec achieved 81.18%, CNN achieved 80.59%, and KNN achieved 33.51%. Notably, their approach outperformed other studies that dealt with small amounts of words and datasets in training and testing [9].

III. METHODS BACKGROUND

This study encompasses the following methods and models:

A. Natural Language Processing (NLP)

One of the sub-fields of artificial intelligence, stemming from linguistics and computer science, is concerned with methods of interactions and language processing between computers or machines, human language, and methods of communication. The central issue is how computers can analyze and process vast amounts of language data, including the nuances of human language, so that machines can accurately predict and understand the information and ideas contained in documents. Challenges in natural language processing (NLP) include speech recognition, natural language understanding, and natural language generation. NLP combines computational linguistics, which is modeling based on human language rules, with statistical models, machine learning, and deep learning models. NLP content has three categories that are common in text processing: count-based, prediction-based, and sequential [10]. The first category relies on word frequencies with the assumption that common words in a document have fixed meanings, the second models probabilistic relations between words, and the third is based on the assumption that the sequence or stream of words has a fixed meaning for the document. Nowadays, there are many smart applications that are the basis for some computer or smartphone applications, such as digital assistants [11], speech-to-text dictation software [12], customer service chatbots [13], and other consumer amenities that can process large amounts of text quickly, even in real-time. Among its applications:

- Language recognition [14],
- Distinguish words [15],
- Clarify the meaning of the word [16],
- Identify specific entities [17],
- Sentiment analysis [18],
- Natural language generation [19]

B. Text preprocessing

Preparing models for text classification is a challenging task, as it requires training models to handle textual data in its raw form [20]. Therefore, preprocessing is necessary to reduce the complexity of the data and transform it into a suitable format. This involves extracting texts, words, and data from the text corpus, and transforming them into a variable length vector representation using a dictionary. One of the three common NLP models, namely sequential, prediction-based, or count-based, is then used to process and predict the words. Sequential methods assume that words in a text corpus are linearly related and extract the sequence of words or their stream from the texts. Prediction-based methods, on the other hand, are based on probabilistic relations between words. Finally, count-based methods rely on the frequency of words in a text corpus, assuming that common words have fixed meanings. To prepare the data for our method, we need to carry out the following operations in the training phase:

1) Extract text: The initial stage of training models for text classification is word processing, which is of paramount importance. This is followed by the stage of text processing and filtering to exclude all general words, commonly known as "stop words," which add little or no value to the text or context and are widely used with an unspecified meaning that does not contribute to classification. Additionally, the context of the text is examined, which depends on the sequence of words in sentences or sentence structure. As a result,

the characteristics derived from this analysis strengthen the accuracy and effectiveness of the classification subject.

2) Lemmatization: The second stage of text preprocessing involves converting each word to its base form, while taking into consideration its context, in order to preserve its meaning. This process is followed by tokenization, which further enhances the form of the text.

3) Tokenization: In natural language processing, the process of substituting words with unrelated values called "tokens" is used to facilitate processing and internal system of models, without the need to carry the original words in scope. This process involves splitting the words of a text into units, which may involve splitting individual words, letters, or even numbers.

4) N-gram: This study focuses on utilizing NLP modeling for the analysis of a sequence of N-words (number of words) in a given text. The text serves as a base for creating word grams through NLP modeling. One-gram, or unigram, refers to a single-word sequence. In the case of the aforementioned statement, each word can be considered a single-gram word. Two-gram, or bi-gram, refers to a sequence of two words. Similarly, three-gram, or tri-gram, pertains to sequences containing three words, as depicted in Fig. 2.
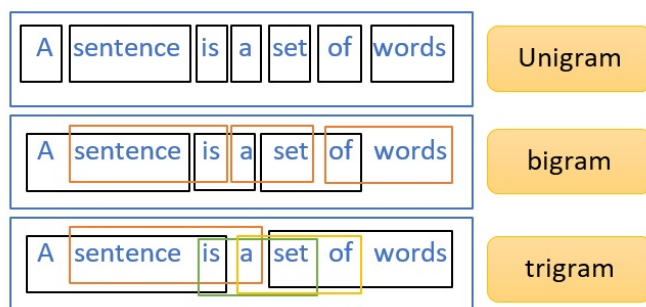
Fig. 2: N-grams

5) Classification: In order to prepare a model for text classification, it is crucial to limit the texts that are used to train the model. This involves selecting characteristics that increase the model's experience and reducing errors that may occur during training, such as overlapping topics or repeated words in different fields. To accomplish this, the examination and selection of characteristics using neural convolutional networks have proven effective in filtering and selecting the most relevant features for classification training.

This study focuses on integrating two models, Word2vec and LSTM, to perform the task of classification. This represents an important application of deep learning and natural language processing. The Word2vec model is responsible for processing words and identifying useful words and phrases embedded in the text. The selected phrases and words are considered important for classifying texts, regardless of their convergence to the integrated topic or the specific words used in the document.

On the other hand, the LSTM algorithm predicts the classification based on the proximity of words or the presence of close words (three words or more) and the balance of

the words included in the text, such as whether it is an electrical or medical document. Together, these two models can accurately predict the classification of texts based on their unique characteristics and embedded features.

6) Recurrent neural networks: RNN, a type of network utilized in the field of deep learning, adopts a conventional approach to handling data and constructing ideas. Upon each data processing event, the network generates new ideas from scratch in a traditional manner. However, the issue with this approach is the failure to maintain previous ideas, which can decay over time. To address this issue, a network cell is introduced to facilitate the exchange of information between cells, and a recurrent neural network can be conceptualized as multiple copies of a network cell, with each copy transmitting a message to its successor. The basic structure of a recurrent neural network resembles that of a chain, and it is used for processing data. This concept has been discussed in a study by Adhikari et al. [21].

7) Word2vec: In order to train a classification model, it is necessary to represent words in a numerical format, and these numerical representations must be vectorized so that the model can utilize them based on the relationship between the words. The word2vec algorithm, which is included in the Genism library and utilizes two neural network layers, is used to produce high-quality vectorized representations of words, known as word embeddings, with high efficiency and similarity. Word embeddings are used to represent words in vector form for numerical computation. The word2vec algorithm is designed to target sentences in text in order to generate word embeddings based on the context of the words and their meanings.

Word2vec algorithm consists of two methods: the Skipgram method, which takes a word as input and predicts the surrounding context as output (Fig.3), and the CBOW (Continuous Bag of Words) method, which takes a sentence context as input and predicts the word as output (Fig.4). These methods are then used to generate context for the classification model through word embeddings [4].
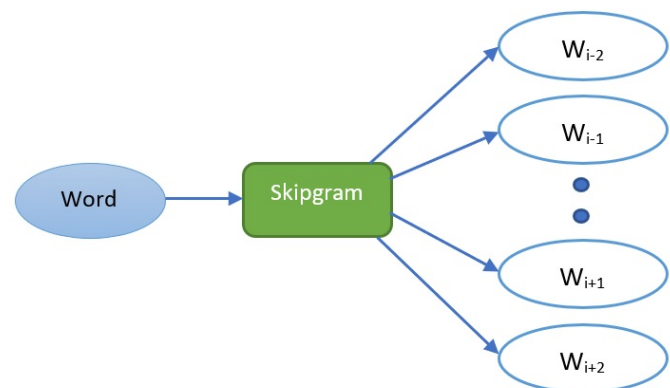
Fig. 3: Skipgram method

8) LSTM: LSTM is a widely-known recurrent neural network that is capable of learning long-term dependencies in data. It comprises four layers that interact with each other. The data flows through its units and allows for a few linear
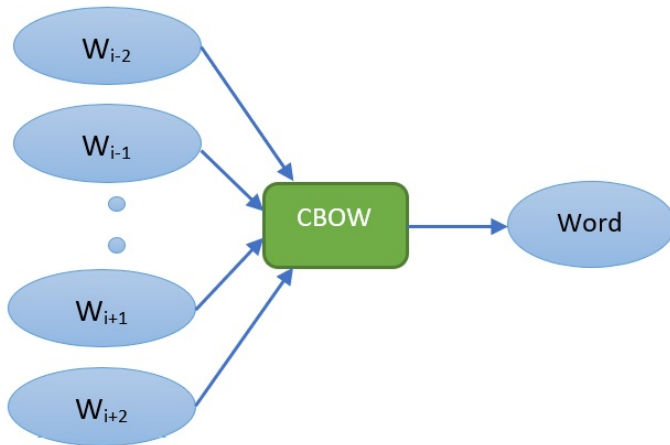
Fig. 4: CBOW method

interactions. By evaluating the combination of corpus, LSTM hyperparameters, and tokenized text, sequential models can accurately classify topics and achieve high performance according to evaluation metrics.

LSTM network has the ability to store previous data and use it during current processing and calculations. This means that the connection between nodes in the hidden layers remains throughout the processing time, which makes the model more effective.

LSTM addresses the issue of vanishing gradients by implementing improvements such as the forget gate, modifying activation functions, and utilizing memory units to enhance connections. Additionally, LSTM maintains the sequence information of text and produces good results on features by considering context, as illustrated in Fig. 5.

This study utilizes word2vec and LSTM with word embeddings to classify documents. The performance of this approach is compared to that of a standalone LSTM model, as well as a combination of LSTM and word2vec, and a combination of LSTM and word embeddings generated after embedding neighboring words.
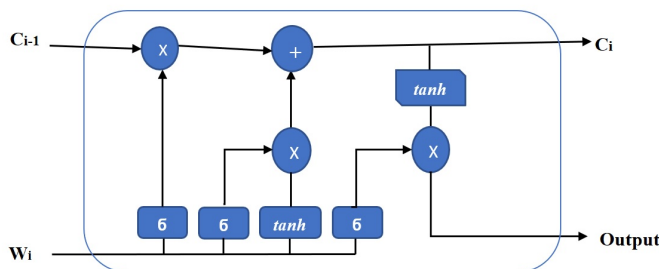
Fig. 5: LSTM model

9) Word embeddings: Our study proposes an approach to generating a dense vector representation of words that captures their meaning by employing the word2vec algorithm, which employs two main training algorithms, CBOW and Skipgram, to learn word embeddings. The proposed approach

involves integrating LSTM with CBOW and evaluating the performance, followed by integration with Skipgram and performance evaluation. Subsequently, the approach employs the word embeddings generated by both algorithms and evaluates their performance using trigram words, while also generating a neighboring words matrix instead of relying on a dictionary [4].

10) Dataset: The Web of Science (WOS) is a dataset for document classification that comprises 46,985 documents belonging to 134 categories, which are further classified under 7 parent categories, as illustrated in Fig. 6.
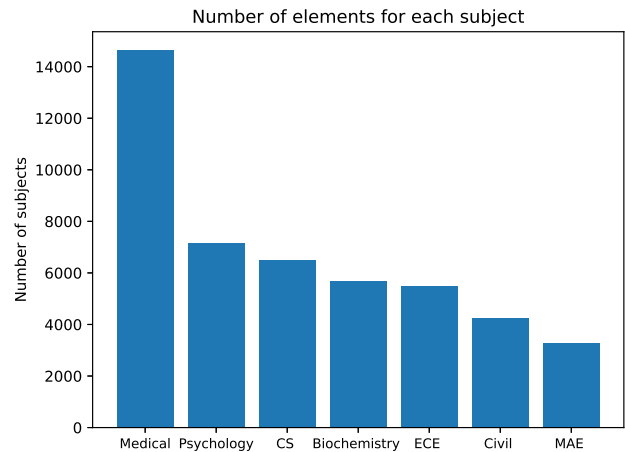
Fig. 6: WOS dataset

IV. METHODOLOGY

The principal motivation of this study is to investigate the effect of contextual information obtained by neighbor words via trigram sequences in textual input for the classification task. First, we generate the trigram word series through the input documents. Then, based on the most discriminative/essential trigram elements, we extract the neighboring words accessed by the shared words/terms in each trigram element. To test our proposed approach, we created two distinct experimental scenarios: **plain models**, where we built regular classification models using general word embeddings, and **neighborhood models**, where we constructed models utilizing neighboring word embeddings. As considered in the proposed novel neighborhood model, we train our word embedding models to gain general word embeddings using *SkipGram* and *Continues-Bag-of-Words* algorithms. Following this step, we extract all the trigram word series and compute the average word embeddings based on the neighboring terms identified through the shared words in the trigrams. Next, we added the calculated neighboring word embeddings to each target word to contextually enhance the embedding of the target word. In the final step, we exploited the updated word embeddings by integrating them into the embedding layer of our LSTM model to perform the classification task.

A. *Preparing data*

The dataset contains raw data along with its errors. Prior to training the model, it is necessary to clean the data by examining and validating empty and irregular records. This is followed by applying lemmatization and tokenization to the document texts, and then splitting the data into test and train sets. Subsequently, the first model is trained using the cleaned text data and the results are evaluated for comparison with other models.

B. *Vectorization*

Once the data is cleaned and contextual information is retained, it needs to be converted into a vectorized form to enable the classification model to process it effectively. Subsequently, the models are integrated with word embeddings. The second model is integrated with the CBOW algorithm while the third model is integrated with Skipgram, and both are tested and evaluated. The results are presented in Table I.

	SKIPGRAM	CBOW	neighbor WORD
First Model	☐	☐	☐
Second model	☐	☒	☐
Third model	☒	☐	☐
Fourth model	☐	☒	☒
Fifth model	☒	☐	☒

TABLE I: Models methods (single model and combined models)

C. *Model-vec-word embedding*

In this approach, a list of embedded words is prepared to train two separate LSTM models using two methods of Word2vec, Skipgram, and CBOW. This process produces two lists of word embeddings that are used to train two different LSTM models. The performance of the two models is then evaluated to determine which one is better in terms of context and word embeddings. Firstly, the LSTM model is trained with Skipgram vectors, then another LSTM model is trained with CBOW vectors, and finally, the test results are evaluated. This method involves using a model to create vectors that represent the relationships between words and a large number of other words. The Skipgram and CBOW methods both train the model on a large number of words.

D. *Neighbor word embeddings*

After incorporating word embeddings through both Skipgram and CBOW methods, the models become more precise in their selection of words and have a broader range of words in their embeddings. However, to improve the accuracy of classification predictions, the models need to have greater accuracy and depth in understanding the relationships between words, thereby narrowing the field between the words. This can be achieved by focusing on the relationships between neighboring words, which can be deduced through the context of similar texts that the models can be trained on. This will narrow the range and number of words, reducing them to the nearest three or more adjacent words. A list of these adjacent

TABLE II: Definition of TP, FP, TN, and FN

		Prediction	
		Positive	Negative
Truth	Positive	True Positive	False Positive
	Negative	False Negative	True Negative

words can be compiled and used to train models that minimize the possibilities that may affect the correct classification.

V. EVALUATION

The main concept in classification is to evaluate the models to determine their accuracy and reliability in classification analysis. By reviewing the models' performance, we can identify the most accurate and reliable model for our classification tasks. The results obtained from training and testing the models can be used to assess their performance.

To evaluate the performance of classification models, the confusion matrix is commonly used. This matrix includes four terms, namely true positive (TP), true negative (TN), false positive (FP), and false negative (FN). Based on the confusion matrix, various metrics can be calculated, such as accuracy, precision, recall, F1-score, and others, as shown in Table. II.

The model prediction results are tested and trained, then divided the results in four areas as follows:

- True Positive: The correct model classification of Positive results (Positive).
- False Negative: The incorrect model classification of Positive results (Negative).
- False Positive: The incorrect model classification of Negative results (Positive).
- True Negative: The correct model classification of Negative results (Negative).

These results will measure the metrics as follows:

1) Precision is a ratio calculated between the number of positive samples correctly classified and the total number of samples classified as positive (either correctly or incorrectly). The precision of the model measures how accurately it classifies a sample as positive. Precision is calculated usingEqn 1:

$$Precision = \frac{TP}{TP + FP} \qquad (1)$$

2) Recall is a measured ratio that assesses the model's ability to detect positive samples. A higher recall ratio indicates a greater number of positive samples detected. The model's recall is calculated as the ratio between the number of positive samples correctly classified as positive and the total number of positive samples. It is measured using 2:

$$Recall = \frac{TP}{TP + FN} \qquad (2)$$

Accuracy is one of the metrics used to measure the overall performance of a model across all classes. It is calculated as the ratio of correct predictions to the total number of predictions, as shown in 3.

$$Accuracy = \frac{TP + TN}{TP + TN + FP + FN} \quad (3)$$

F1-score: It is a measure for evaluating the predictive abilities of a model and assessing its performance by combining two important, competing measures: precision and recall. Currently, this evaluation method is widely used in model assessment, as demonstrated in Eqn. 4.

$$F_1 = 2 \times \frac{Precision \times Recall}{Precision + Recall} \quad (4)$$

The objective of this study is to attain high values in the aforementioned performance metrics for evaluating the models. A high F1-score is obtained when precision and recall are both high, leading to accurate class prediction. To further improve the performance metrics, the models are enhanced using a combined method.

VI. RESULTS

This experiment involved analyzing texts of 50,000 words per document, as presented in Table I. The study compared the performance of five models trained with Skipgram or CBOW word embeddings. The results showed significant differences in Accuracy, Recall, and F1-score when comparing the performance of the LSTM model as a single model to the combined models. To improve the models, the study used neighboring words for model enhancement and analyzed the predictions.

When evaluating the performance of the LSTM model as a single model, the results showed an accuracy of 0.8126 and an F1-score of 0.8130. When combined with CBOW, the accuracy improved to 0.8724, and the F1-score was 0.8722. However, the best results were obtained by combining LSTM with Skipgram, with an accuracy of 0.8790 and an F1-score of 0.8790, making it the most accurate model in the study. To save time and increase accuracy, the combined models were also evaluated, which showed an accuracy of 0.8721 and 0.8769 for CBOW and Skipgram, respectively, and an F1-score of 0.87.

The models were assessed based on Accuracy, Precision, Recall, and F1-score metrics, and the results are presented in Table III:

Method	Accuracy	Precision	Recall	F1_score
LSTM single model	0.8126	0.8194	0.8067	0.8130
LSTM with CBOW	0.8724	0.8781	0.8664	0.8722
LSTM with Skipgram	0.8790	0.8841	0.8739	0.8790
LSTM with CBOW neighbor word	0.8721	0.8764	0.8681	0.8722
LSTM with Skipgram neighbor word	0.87691	0.8833	0.8708	0.8770

TABLE III: Comparison of single and combined methods

The single LSTM method curve shows unmatching accuracy between test and train, but combined methods show higher

matching, LSTM + Skipgram method shows higher matching in the accuracy curve and higher performance, but the LSTM + Skipgram neighbor word shows the lower loss result between methods, as shown in Fig. 7. The Skipgram algorithm produces pretrained word vectors that capture a wealth of linguistic information from vast text corpora. LSTM's ability to incorporate these pretrained vectors as initial embeddings provides the model with a knowledge base of semantic relationships and word similarities. This, in turn, facilitates faster convergence and better generalization. Since Skipgram's ability to consider surrounding words leads to the generation of contextually rich word embeddings, the LSTM model using Skipgram yields relatively more accurate performance scores. Therefore, the superior performance of LSTM with Skipgram in our study can be attributed to the synergy between LSTM's sequential learning capabilities and Skipgram's context-aware word embeddings. This combination enables the model to grasp text structure, adapt to varying lengths, handle polysemy, and leverage pretrained word vectors, resulting in improved overall performance.
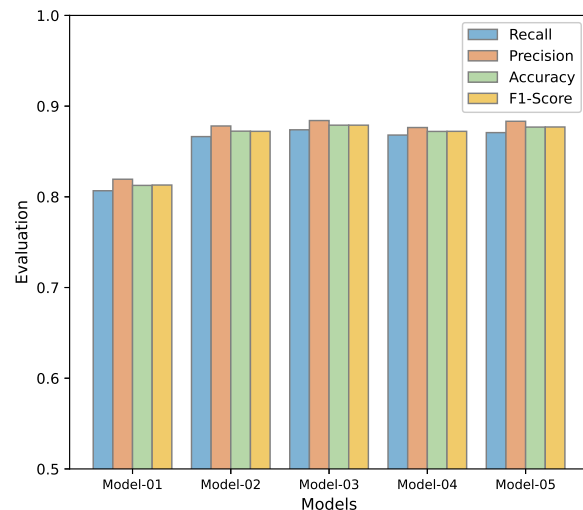
Fig. 7: Models evaluation

VII. CONCLUSION

The Documents classification plays an important fundamental role in research and in text classification field. Documents diverse have features that show no single algorithm can perform as accurate in classification fields, however the combined methods serve more accurate with higher performance in classification fields without limiting the studies state-of-the-art depend on single methods or algorithms.

LSTM as one of the NLP classifiers performs better than other NLP classifiers, and in combination with other methods, it has a very high performance. For example, the word2vec method creates appropriate words from context or creates context from words, then gathers these words in a new dataset to train the LSTM model and make the prediction more accurate, as shown in Table III.

The LSTM model approved the best results in Deep learning classification models determining memory, and combined with the word2vec methods, the neighbor word relation may need more development to rise in accuracy and precision.

The single pre-model, as a result of its evaluation, proved that it was trained on text word vectors only and without any relationship between them, which left the words in the memory of this model without any relationship between them as the accuracy decreased in words that shared similar classifications.

The second and third models were trained under a relationship consisting of text vectors formed by methods such as Skipgram and CBOW, where a relationship is formed between words within the memory of the model, and here the model is trained more clearly in the relationship and context between words, where the relationship between words depends on the production of vectors. While Skipgram relies on the word to establish context and yields more accurate evaluation results, as we have observed previously, it's clear that focusing on context is the key to training a model with superior accuracy in classification. In the case of CBOW, as mentioned earlier, the context is utilized to predict the specific word, and this context remains in memory. This can make it easier for the model to make accurate classifications.

It is required to delve deeper into the relationship between words and context. There can exist relationships in texts between words, specifically with adjacent words, which narrows down the range of words within the context or text. This reduced context is used for training the new model, resulting in reduced processing time and improved classification accuracy.

VIII. PRACTICAL IMPLICATIONS & FUTURE DIRECTIONS

The proposed study's findings have significant practical implications for document classification and natural language processing. Firstly, employing contextually enriched word embeddings, specifically trigram word series, presents a promising approach for enhancing document classification models' effectiveness. This approach leverages contextual information, providing more nuanced and precise text representations.

Beyond this, the demonstrated potential of the proposed approach can lead to opportunities to improve document classification across various domains. Researchers and practitioners can address text classification challenges in subfields like information retrieval, sentiment analysis, and content recommendation with greater precision and effectiveness by utilizing the power of these enriched embeddings. In practical terms, this study presents a valuable contribution to the development of more context-aware document classification models.

From the outcomes, there are two stimulating directions for prospective research as listed below:

- **Dynamic Neighborhood-Based Approaches:** *Investigating dynamic approaches, where the context window dynamically adjusts to the specific requirements of different document types, could further improve the adaptability and accuracy of classification models.*

- **Interplay with Pretrained Models:** *Exploring how contextually enriched word embeddings complement or enhance the performance of pre-trained language models could be valuable. Combining these approaches might result in state-of-the-art document classification systems.*

REFERENCES

[1] A. J. Trappey, F.-C. Hsu, C. V. Trappey, and C.-I. Lin, "Development of a patent document classification and search platform using a back-propagation network," *Expert Systems with Applications*, vol. 31, no. 4, pp. 755–765, 2006.

[2] G. Aghila *et al.*, "A survey of na\" ive bayes machine learning approach in text document classification," *arXiv preprint arXiv:1003.1795*, 2010.

[3] A. Joulin, E. Grave, P. Bojanowski, and T. Mikolov, "Bag of tricks for efficient text classification," *arXiv preprint arXiv:1607.01759*, 2016.

[4] Q. Chen and M. Sokolova, "Specialists, scientists, and sentiments: Word2vec and doc2vec in analysis of scientific and medical texts," *SN Computer Science*, vol. 2, pp. 1–11, 2021.

[5] G. Bakal and O. Abar, "On comparative classification of relevant covid-19 tweets," in *2021 6th International Conference on Computer Science and Engineering (UBMK)*. IEEE, 2021, pp. 287–291.

[6] B. J. Marafino, J. M. Davies, N. S. Bardach, M. L. Dean, and R. A. Dudley, "N-gram support vector machines for scalable procedure and diagnosis classification, with applications to clinical free text data from the intensive care unit," *Journal of the American Medical Informatics Association*, vol. 21, no. 5, pp. 871–875, 2014.

[7] A. Graves, S. Fernández, and J. Schmidhuber, "Bidirectional lstm networks for improved phoneme classification and recognition," in *Artificial Neural Networks: Formal Models and Their Applications–ICANN 2005: 15th International Conference, Warsaw, Poland, September 11-15, 2005. Proceedings, Part II 15*. Springer, 2005, pp. 799–804.

[8] A. Graves and J. Schmidhuber, "Framewise phoneme classification with bidirectional lstm and other neural network architectures," *Neural networks*, vol. 18, no. 5-6, pp. 602–610, 2005.

[9] L. Xiao, G. Wang, and Y. Zuo, "Research on patent text classification based on word2vec and lstm," in *2018 11th International Symposium on Computational Intelligence and Design (ISCID)*, vol. 1. IEEE, 2018, pp. 71–74.

[10] C. C. Aggarwal and C. C. Aggarwal, "Machine learning for text: An introduction," *Machine learning for text*, pp. 1–16, 2018.

[11] P. Milhorat, S. Schlögl, G. Chollet, J. Boudy, A. Esposito, and G. Pelosi, "Building the next generation of personal digital assistants," in *2014 1st international conference on advanced technologies for signal and image processing (atsip)*. IEEE, 2014, pp. 458–463.

[12] H.-H. Chiang, "A comparison between teacher-led and online text-to-speech dictation for students' vocabulary performance." *English Language Teaching*, vol. 12, no. 3, pp. 77–93, 2019.

[13] E. Adamopoulou and L. Moussiades, "Chatbots: History, technology, and applications," *Machine Learning with Applications*, vol. 2, p. 100006, 2020.

[14] D. Martinez, O. Plchot, L. Burget, O. Glembek, and P. Matějka, "Language recognition in ivectors space," in *Twelfth annual conference of the international speech communication association*, 2011.

[15] T. Pedersen and R. Bruce, "Distinguishing word senses in untagged text," *arXiv preprint cmp-lg/9706008*, 1997.

[16] M. Bevilacqua, T. Pasini, A. Raganato, and R. Navigli, "Recent trends in word sense disambiguation: A survey," in *Proceedings of the Thirtieth International Joint Conference on Artificial Intelligence, IJCAI-21*. International Joint Conference on Artificial Intelligence, Inc, 2021.

[17] D. Nadeau and S. Sekine, "A survey of named entity recognition and classification," *Lingvisticae Investigationes*, vol. 30, no. 1, pp. 3–26, 2007.

[18] W. Medhat, A. Hassan, and H. Korashy, "Sentiment analysis algorithms and applications: A survey," *Ain Shams engineering journal*, vol. 5, no. 4, pp. 1093–1113, 2014.

[19] E. Reiter and R. Dale, "Building applied natural language generation systems," *Natural Language Engineering*, vol. 3, no. 1, pp. 57–87, 1997.

[20] B. Kolukisa, B. K. Dedeturk, B. A. Dedeturk, A. Gulsen, and G. Bakal, "A comparative analysis on medical article classification using text mining & machine learning algorithms," in *2021 6th International Conference on Computer Science and Engineering (UBMK)*. IEEE, 2021, pp. 360–365.

[21] A. Adhikari, A. Ram, R. Tang, and J. Lin, "Rethinking complex neural network architectures for document classification," in *Proceedings of the 2019 Conference of the North American Chapter of the Association for Computational Linguistics: Human Language Technologies, Volume 1 (Long and Short Papers)*, 2019, pp. 4046–4051.

Biographies

Raad Saadi Mahmood earned his BSc in Computer Science from Baghdad University in 2004 and his MSc in Electronics and Computer Engineering from Cankiri Karatekin University in 2023 . With 18 years of experience as a Senior Programmer, he has provided technical support at the Midland Refineries Company, specifically in the Technical Branch of the Measuring Department in Iraq. Mahmood's primary focus is on enhancing industrial systems using AI.

Gokhan Bakal received his PhD and MSc degrees in Computer Science from the University of Kentucky, USA in 2019 and 2014, respectively. He is currently working as an Assistant Professor in the Computer Engineering Dept. at Abdullah Gul University. His research areas are Text Mining, Machine and Deep Learning, Bioinformatics, and Computational Drug Discovery.

Ayhan Akbas holds BSc and MSc degrees in Electrical and Electronics Engineering, both obtained from the Middle East Technical University in 1991 and 1995, respectively. He earned his PhD degree from the Department of Computer Engineering at TOBB University of Economics and Technology. With over 20 years of experience in the field of Information Technology, Dr. Akbas has occupied both technical and managerial roles at multinational companies. He worked as Assistant Professor at THK University, Cankiri Karatekin University and Abdullah Gül University. Currently, he is pursuing his career at Universiy of Surrey, Guildford, UK. His areas of interest are Wireless Sensor Networks, IoT, 6G, Wireless Communication, and Machine Learning.

Research Article

Analysis of the Effect of Switching Frequency on Acoustic Noise in External Rotor Brushless DC Motors

Bugra Er, Berk Demirsoy, Ahmet Fenercioglu

Abstract— **Electric motors are widely used in various industries and are subject to specific acoustic noise standards depending on their applications. Despite their superior performance compared to brushed motors, brushless motors generate acoustic noise due to their mechanical, electrical, and electronic components. This study investigates the effect of changing the switching frequency through the driver on the acoustic noise of an external rotor brushless DC motor. Tests were conducted on a surface-mounted magnetic brushless motor with different switching frequencies, and detailed information about the control board governing the brushless motor was provided. Sound intensity and harmonic measurements were conducted with a dB meter in an anechoic quiet room. Changing the switching frequency also affects the motor speed, so two different measurements were taken during the study. In one test, the BLDC motor speed was kept constant, while in the other, the Duty cycle ratio was kept constant for measurements. An increase in the switching frequency was observed to reduce motor noise. However, this increase also leads to losses in the switching components, resulting in a temperature increase. The speed of the external rotor brushless DC motor was kept constant by adjusting the Duty cycle while changing the switching frequency. Increasing the switching frequency in the range of 12-28 kHz reduced the measured acoustic noise while causing temperature increases in different frequency ranges. The study's results indicate that the existing BLDC motor and driver system provide optimum performance in terms of acoustic noise and temperature in the 16-18 kHz range.**

Index Terms— **Acoustic noise, BLDC motor, Switching frequencies.**

I. INTRODUCTION

BLDC(Brushless Direct Current) motor has a high starting torque and is often preferred in variable-speed

Buğra Er, is Kormas Elektrikli Motor A.Ş. TOSB OSB, Kocaeli, Turkey, (e-mail: bugraer@kormas.com).

https://orcid.org/0000-0002-3982-5654

Berk Demirsoy, is Kormas Elektrikli Motor A.Ş. TOSB OSB, Kocaeli, Turkey, (e-mail: berkdemirsoy@kormas.com).

https://orcid.org/0009-0003-3489-7346

Ahmet Fenercioğlu, is Department of Mechatronic Engineering, Bursa Technical University, 16310, Bursa Turkey, (e-mail: ahmet.fenercioglu@btu.edu.tr).

https://orcid.org/0000-0002-1522-6868

applications. It can minimize mechanical wear, noise, and temperature without brushes [1]. Due to the absence of brush friction, it emits lower acoustic noise.

The control algorithm for BLDC motors is considerably complex compared to brushed DC motors [2]. The rotor position needs to be detected and commutation must be performed. Hall-effect sensors are used for rotor position sensing [3]. By evaluating the data from three sensors, the BLDC motor triggers the appropriate phase for operation. Control of switching angles is essential, especially during acceleration. The signal applied to the switching elements contains PWM (Pulse Width Modulation) signals. The switching frequency of this PWM signal is of great importance. Parameters related to the time constant are directly related to the switching frequency and rotor frequency [4].

BLDC motor is classified into two categories based on its mechanical structures: bearing, housing, rotor, and stator assembly, and BLDC motor control approaches [5]. While BLDC motor parameters remain constant during system operation, practical applications involve continuously changing parameters such as mechanical load and friction [6]. Factors like friction among these mechanical elements can contribute to mechanical noise [7]. Additionally, conditions such as the influence of bearing, shaft vibration, and rotor eccentricity can also generate noise [8]. In this context, mechanical factors and noise are significant considerations in BLDC motor systems. The electrical noise sources in the BLDC motor system are illustrated in Figure 1 [9].
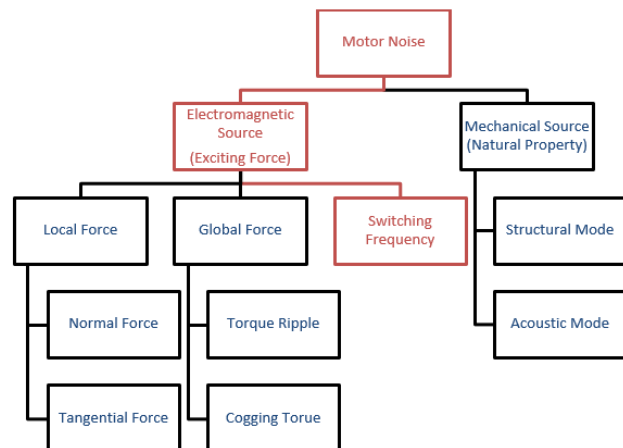
Fig 1. BLDC motor noise

These sources include factors such as motor power and switching frequency, which contribute to motor noise. Additionally, the motor mechanics, depending on the mechanical design, can directly influence the sound. Electromagnetic sources can also impact the noise level in BLDC motor design [10]. Holding torque and torque fluctuations are other factors that affect the sound and are examined as a separate field. Acoustic noise refers to unwanted audible sound and is of significant importance as it emanates from a vibrating object. Current variation and the fundamental frequency of acoustic noise originating from the current cause electromagnetic noise in the BLDC motor's commutation frequency [11]. In this study, the designed board in Altium Designer software includes ST Microelectronics components, an IPM (Intelligent Power Module), and an STM32G030 microcontroller. Real-time drive parameters can be analyzed and manipulated through Keil u5. By gradually changing the switching frequency from 12kHz to 28kHz, the motor speed, motor sound, motor current, and motor phase signals were examined.

II. EXTERNAL ROTOR BLDC MOTOR AND DRIVER DESIGN

Acoustic noise in a system containing a motor is influenced by electromagnetic, mechanical, aerodynamic, and electrical sources [12]. Electromagnetic noise and vibration on the motor can be affected by factors such as stator shape and slot opening, phase imbalances, high airgap harmonics, and the magnetic saturation of the used core. Mechanical noise and vibration are influenced by the motor's assembly, while aerodynamic noise and vibration can be related to airflow in the motor's ventilation channels [13-14]. Additionally, reducing electromagnetic noise in BLDC motors relies on reducing torque ripple [15]. Various factors can contribute to torque ripple in electric motors, including cogging torque, non-ideal back-EMF (Electromotive Force) waveform, PWM current harmonics, and phase commutation. At high speeds, the system's inertia can compensate for torque ripple, but at low speeds, torque ripple can cause unacceptable levels of vibration and acoustic noise [16]. To reduce acoustic noise related to torque ripple, studies have been conducted on the number of poles and cogging torque in BLDC motor designs. Cogging torque can hinder the smooth operation and desired speed of the motor, leading to acoustic noise. The number of poles in the BLDC motor design has an impact on its acoustic noise [17]. Table 1 below provides the system parameters of the BLDC motor and the driver.

Table I
SYSTEM PARAMETERS OF THE MOTOR AND DRİVER

	Input Voltage	310 V_{DC}
Motor	Number of Poles/Slots	18/20
	Phase resistance	3.2 Ω
	Phase inductance	10.42mH
Driver	Inverter Type	Six-Step Driver
	Control Signal	PWM
	Switching Frequency	Variable frequency
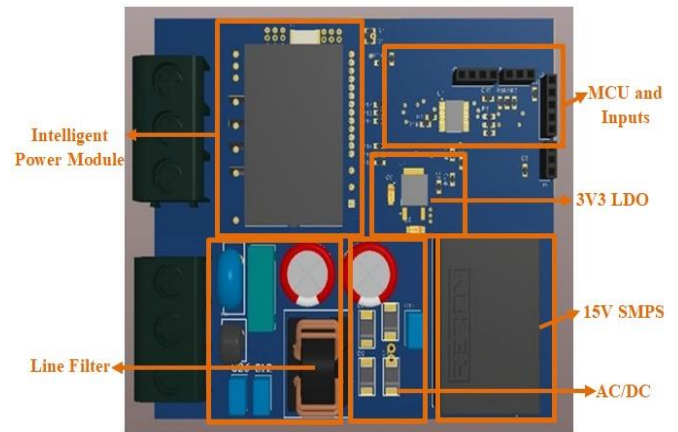
Fig 2. BLDC motor driver

The BLDC motor driver is a necessary component in the control of BLDC motor systems. In this study, an IPM is used as the power stage. The IPM has a rating of 600V and 15A, and it includes the necessary pins for the IGBT driver, IGBT, and bootstrap structure. The switching elements represented by the symbol 'S' in the design are implemented as IGBTs. The power supply of the system is determined as 220V_{AC}, and AC-DC conversion is performed using bridge diodes. Then, a switched-mode power supply is used to obtain 15V. A 3V regulator is available for the STM32 microcontroller and the Hall-effect sensors used in the STM32 series. The 3V regulator and IGBT drivers are powered by the 15V power supply. The control circuit consists of the microcontroller and the system inputs. The driver circuit is responsible for distributing the energy from the source to the motor phases according to the signals from the control circuit. The relevant components are shown in Figure 2 on a PCB design using Altium Designer. The structure of the motor driver sections provided in Figure 2 is detailed in Figure 3 and Figure 4.
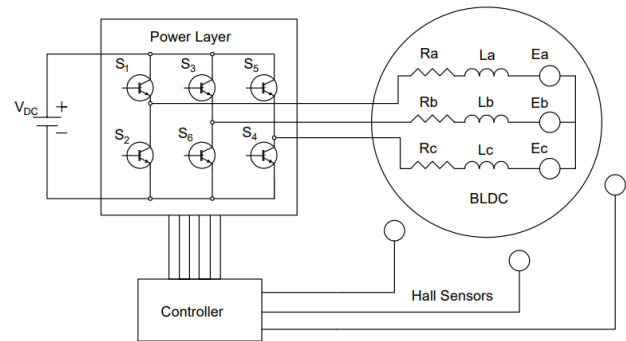
Fig 3. Driver diagram

The diagram provided in Figure 3 depicts the use of Hall sensors to detect the rotor position, which is then communicated to the controller to transmit the necessary signals to the power layer [18]. By transmitting 6 PWM signals, the control of three half-bridge structures is achieved. Each half-bridge structure controls one phase of the motor. The diagram represents a three-phase motor configuration. The back-EMF of each phase has a trapezoidal waveform [19]. The trapezoidal signals between phases have a phase difference of 120 electrical degrees [20].
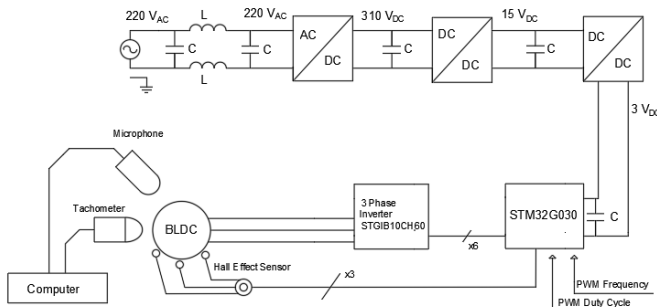
Fig 4. Schematic diagram of the experimental setup

III. ACOUSTIC MODEL AND TESTING

Figure 4 illustrates the schematic diagram of the test system. The system operates with a 220V AC input, which is then converted to DC 310V through a line filter and rectifier supply. The control layer obtains 15V and 3V DC voltages, which are utilized for powering the controller and hall sensors. Based on the rotor position detected by the hall sensors, control signals are transmitted to the power layer for BLDC motor control through 310V DC switching. A tachometer is employed in the system to measure the BLDC motor speed. By varying the switching frequency and duty cycle, sound measurements are performed and recorded via the BLDC motor driver and BLDC motor system.
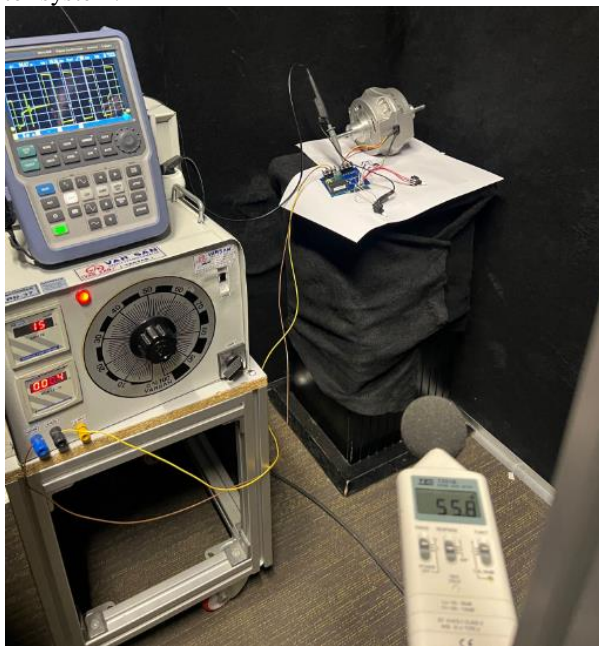
Fig 5. Acoustic noise test environment of BLDC motor system

To investigate the acoustic noise characteristics, measurements are conducted at different motor speeds using the test setup shown in Figure 5. For noise measurement, a vertical sound level meter is placed 1 meter away from the motor. The motor speed is obtained using a BLDC motor tachometer. The options for frequency response include A and C weighting. We conducted the measurements using the A-weighting frequency response, which is closer to the sensitivity of the human ear. The experiment was performed with a sound level meter that

has a sensitivity of 0.1 dB. The measurement system comprises a sound level meter, a BLDC motor, an AC power supply, and a computer. The utilized sound level meter complies with the IEC 60804-2000 Type 1 standard and has a measurement error of less than 0.5 dB. The microphone used for noise measurement is vertically positioned at a distance of 1 meter from the motor [10]. The same 1-meter measurement distance has also been applied in motor studies conducted in the HVAC field. Acoustic noise was measured in accordance with ISO 3741 standard at four different points horizontally, 1 meter away from the BLDC motor.

The tests were conducted in a 10m² anechoic room, where the motor was not operational but the power sources connected to the motor were active. Anechoic materials and sound insulators were used to ensure sound isolation. In the absence of motor operation, a sound measurement of 36 dB was obtained from the system. Rohde & Schwarz oscilloscope and interfaces were utilized for controlling the system's key frequency and phase diagrams. Variac was used as the power source in the system for voltage and current monitoring. It has no visible effect on the phase plots. During the BLDC motor testing, the waveform at a 50% duty cycle and a switching frequency of 20 kHz with a peak value of 310 Vdc is shown in Figure 6. Figure 7 represents a representation of the switching frequency within the phase signal.
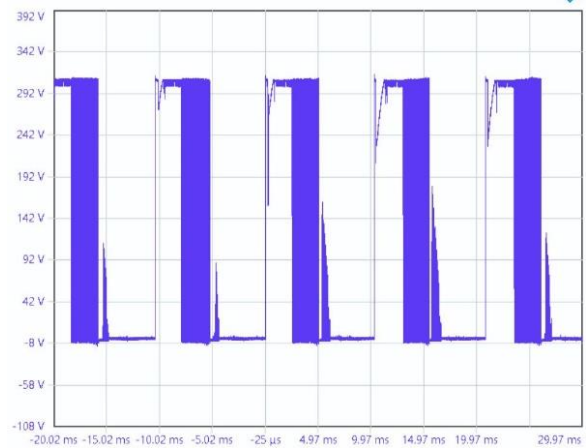
Fig 6. BLDC motor phase signal (%50 PWM 20kHz)
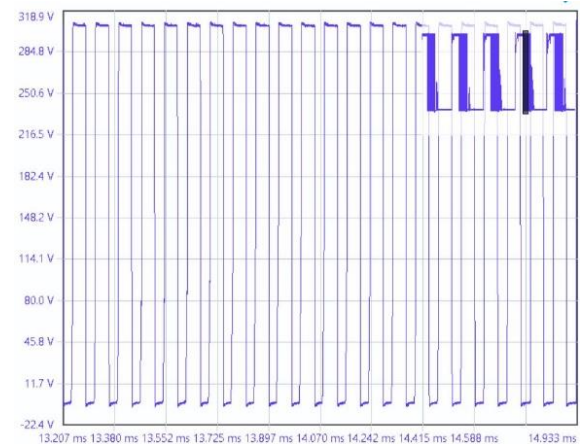
Fig 7. Extended version of BLDC motor signal

The motor was operated at switching frequencies ranging from 12 kHz to 28 kHz during the experiments. During the tests, the

applied PWM values to the BLDC motor, system voltage, noise level, current consumption of the system, and BLDC motor speed were measured. Additionally, the motor frequency corresponding to the speed was obtained.

%50 Duty Cycle Test Data
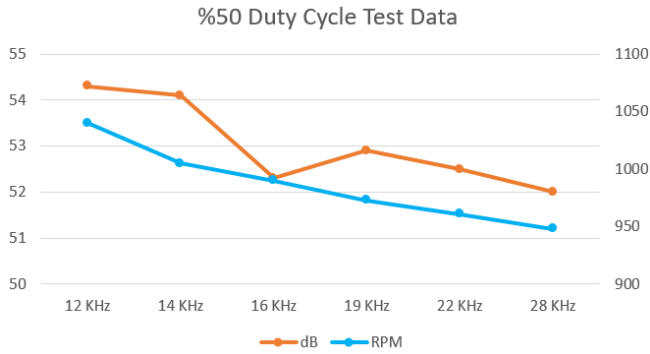
Fig 8. Noise graph with %50 Duty Cycle BLDC motor variable switching frequency and RPM

%70 Duty Cycle Test Data
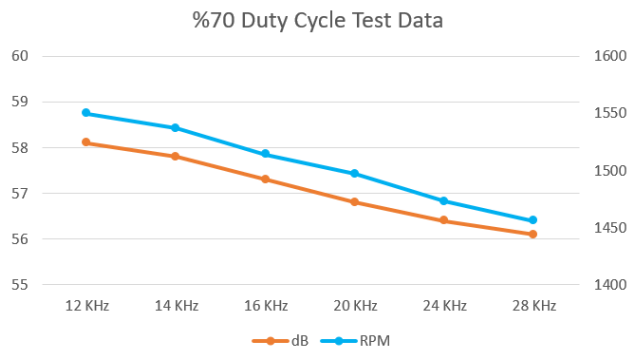
Fig 9. Noise graph with %70 duty cycle BLDC Motor variable switching frequency and RPM

In the graphs obtained in Figure 8 and Figure 9, the variation in motor RPM(Revolutions per Minute) is observed as the switching frequency is changed. During the tests, measurements were taken as the switching frequency increased, and the decrease in motor speed was plotted on the graph as the noise level in dB. As the frequency increases, the motor speed decreases, leading to a reduction in mechanical noise. The graphs obtained in Figures 10 and 11 show the change in acoustic noise as the switching frequency changes while keeping the motor speed constant.

%50 Duty Cycle Test Data
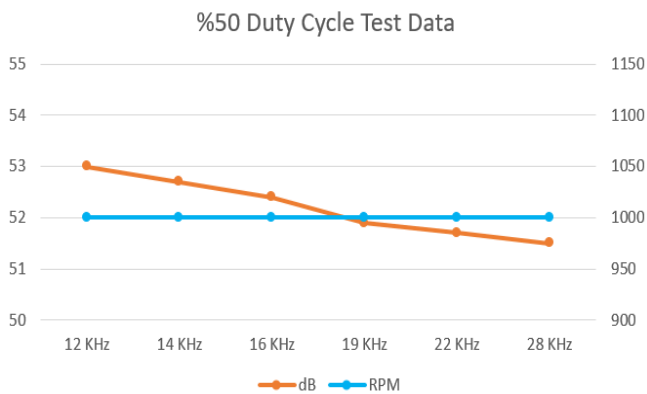
Fig 10. Noise graph with BLDC Motor variable switching frequency and duty cycle, constant 1000RPM

On the horizontal axis, the switching signals ranging from 12kHz to 28kHz are applied to the motor drive, and the resulting noise levels in dB are given on the vertical axis. The increase in motor speed contributes to an increase in the mechanically generated sound level. In tests conducted with different duty cycle values, the minimum amount of acoustic noise varies. In Figure 11 and Figure 12, the acoustic noise graph is presented for variable switching frequencies while maintaining a constant speed.

%70 Duty Cycle Test Data
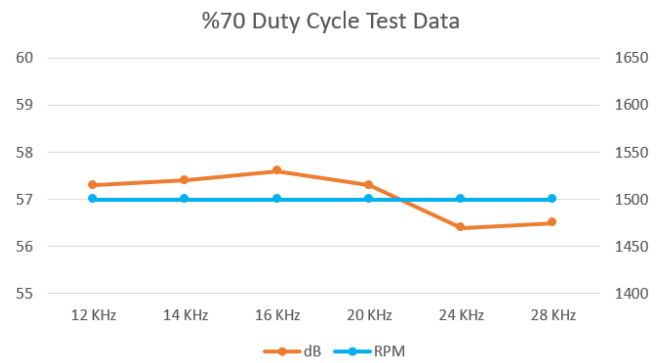
Fig 11. Noise graph with BLDC Motor variable switching frequency and duty cycle, constant 1500 RPM
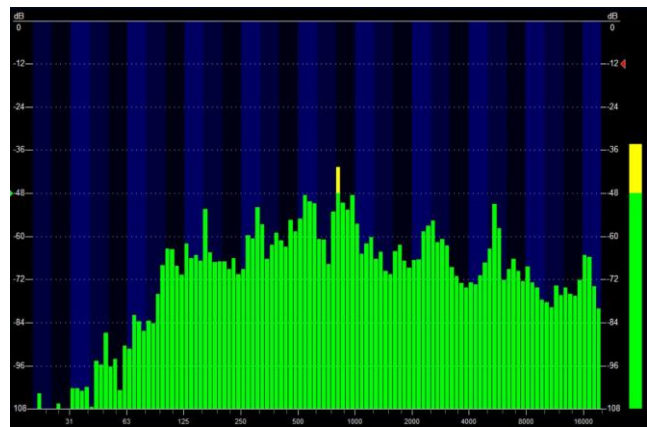
Fig 12. Display of acoustic noise frequency for 28khz

Figures 12, 13, 14, and 15 provide data on acoustic noise frequencies. These graphs illustrate how reducing the switching frequency affects the frequency of acoustic noise. The horizontal axis represents the frequency of acoustic noise, while the vertical axis indicates the sound intensity in dB. For example, in Figure 12, when the switching frequency is 16 kHz, it is observed that the levels of acoustic noise drop to as low as 8 kHz in Figure 15. These findings indicate that as the switching frequency decreases, acoustic noise approaches a range perceptible to the human ear, considering the audible frequency range. However, increasing the switching frequency, while potentially shifting acoustic noise to frequencies beyond the human ear's perception, necessitates considering the electrical stress and temperature values on components when making such a decision.
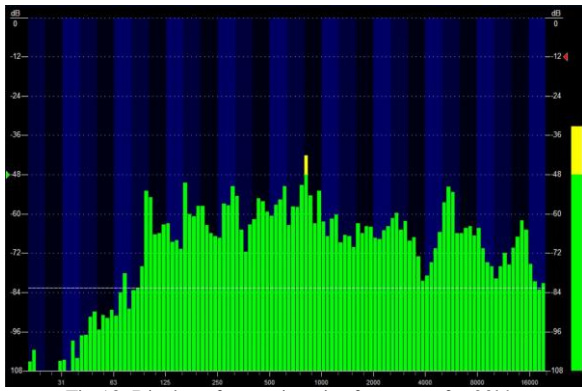
Fig 13. Display of acoustic noise frequency for 20khz
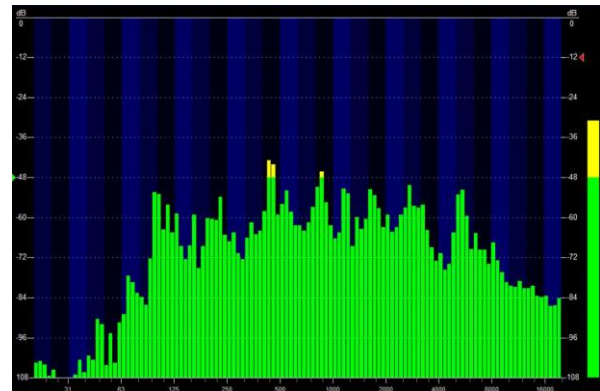
Fig 15. Display of acoustic noise frequency for 12khz
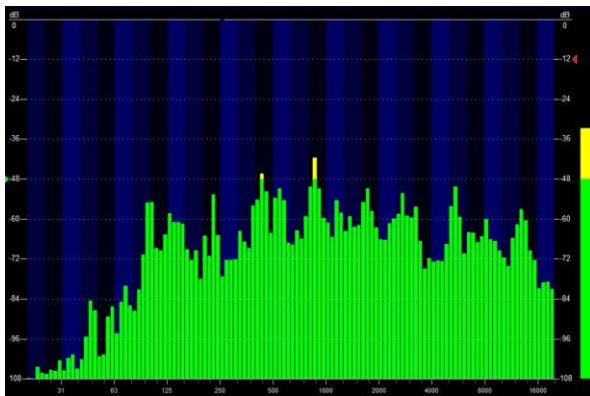
Fig 14. Display of acoustic noise frequency for 16khz

Fig 16. IPM temperature graph at tested switching

TABLE II
SYSTEM PARAMETERS

	12kHz	14kHz	16kHz	19kHz	22kHz	28kHz
Step Times (sec)	200	200	200	200	200	200
Output Power (W)	55.9	55.9	55.9	55.9	55.9	55.9
Output Frequency (Hz)	166	166	166	166	166	166
Transmission and Switching Loss (W)	0.28	0.31	0.34	0.39	0.44	0.50
Total Loss (W)	0.28	0.31	0.34	0.39	0.43	0.50
Junction Temperature (°C)	57.80	61.30	64.90	70.54	76.44	84.86

The switching frequency has a significant impact on the motor speed. Additionally, the operating sound of the motor is directly related to the switching frequency. Figure 16 presents the temperature map of the IPM (Intelligent Power Module) for a switching frequency of 12kHz. The losses occur in the switching elements due to their internal resistances and switching losses. These losses directly affect the temperature of the IPM. Various simulation programs are available for component manufacturers to simulate power modules or products. ST Microelectronics provides the STpowerStudio program specifically for IPM modules. Table 2 provides input data for switching frequencies, motor frequencies, and input

voltage, along with their respective durations. Each case was subjected to a 200-second simulation, during which no significant temperature changes were observed. Subsequently, temperature data was obtained using these inputs and calculated for the STGIB10CH60S IPM product using the program, resulting in the generation of graphs. These graphs are presented in Figure 17. The results obtained from the tests highlight the importance of correctly selecting the switching frequency.
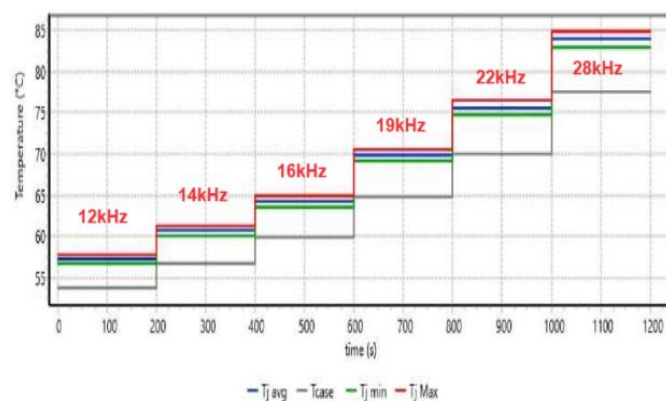
Fig 17. IPM at switching frequency changes

VI. CONCLUSIONS

This research focuses on examining the impact of frequency variations on the efficiency, cost, and reliability of BLDC motors. Speed control was achieved by applying PWM signals to switching elements based on rotor position information. Frequency changes were measured using a scale recorder powered by an STM32F031 Microcontroller. The experiments revealed that lower frequencies yielded better results under high load conditions. In balanced load conditions, determining the optimal frequency is a priority. Oscilloscope data, presented with various graphs ranging from 12 kHz to 28 kHz, clearly illustrate the variation of the switching frequency in phase-neutral graphs. Data collected from motor experiments are also shared. Sound intensity and harmonic measurements were conducted with a dB meter in an anechoic quiet room. Changing the switching frequency also affects the motor speed; hence, two different measurements were conducted during the study. In one test, the BLDC motor speed was kept constant, while in the other, the Duty cycle ratio was maintained at a constant level for measurements. An increase in the switching frequency is shown to reduce motor noise. However, this increase also leads to increased losses in the switching components, resulting in a temperature rise. The speed of the external rotor brushless DC motor was kept constant by adjusting the Duty cycle while changing the switching frequency. Increasing the switching frequency in the range of 12-28 kHz reduced motor speed while decreasing the measured acoustic noise. However, temperature increases were observed in different frequency ranges. The study's results demonstrate that the existing BLDC motor and driver system provide optimum performance in terms of acoustic noise and temperature in the 16-18 kHz range. These findings can serve as a valuable source of information for industry professionals looking to optimize the performance of BLDC motors.

REFERENCES

[1]   M.R. Hazari, E. Jahan, M.E. Siraj, M.T.I. Khan, A.M. Saleque. "Design of a Brushless DC (BLDC) motor controller." In 2014 International Conference on Electrical Engineering and Information & Communication Technology. IEEE, 2014, pp 1-6.

[2]   P. Yedamale. "Brushless DC (BLDC) motor fundamentals." Microchip Technology Inc, vol. 20.1, 2003, pp 3-15.

[3]   R.M. Pindoriya, A.K. Mishra, B.S. Rajpurohit, R. Kumar. "An analysis of vibration and acoustic noise of BLDC motor drive." In 2018 IEEE Power & Energy Society General Meeting (PESGM), 2018, pp 1-5.

[4]   P. Mishra, A. Banerjee, M. Ghosh, S. Gogoi, P.K. Meher. "Implementation and validation of quadral-duty digital PWM to develop a cost-optimized ASIC for BLDC motor drive." Control Engineering Practice, vol. 109, 104752, 2021.

[5]   K. Nakata, M. Sanada, S. Morimoto, Y. Takeda. "Noise reduction for switched reluctance motor with a hole." Proceeding Power Converters Conference, vol. 3, 2002, pp 971-976.

[6]   E. Serdar, Izci D., Yilmaz M. "Efficient speed control for DC motors using novel Gazelle simplex optimizer." IEEE Access, 2023, pp. 105830 – 105842.

[7]   X.T. Bai, Y.H. Wu, K. Zhang, et al. "Radiation noise of the bearing applied to the ceramic motorized spindle based on the sub-source decomposition method." J. Sound Vib., 410, 2017, pp 35-48.

[8]   D.J. Kim, H.J. Kim, J.P. Hong, et al. "Estimation of acoustic noise and vibration in an induction machine considering rotor eccentricity." IEEE Trans. Magn, vol. 50, 2, 2014, pp 857-860.

[9]   H.J. Lee, S.U. Chung, S.M. Hwang. "Noise source identification of a BLDC motor." Journal of mechanical science and Technology, vol. 22, 2008, pp 708-713.

[10]   A. Lelkes, J. Krotsch, R.W. De Doncker. "Low-noise external rotor BLDC motor for fan applications in Conference Record of the 2002 IEEE Industry Applications Conference." IEEE, vol. 3, 2002, pp 2036-2042.

[11]   A. Sathyan, N. Milivojevic, Y.J. Lee, M. Krishnamurthy, A. Emadi. "An FPGA-based novel digital PWM control scheme for BLDC motor drives." IEEE Transactions on Industrial Electronics, vol. 56. 8, 2009, pp 3040-3049.

[12]   D.H. Cho, K.J. Kim. "Modeling of electromagnetic excitation forces of an induction motor for vibration and noise analysis." Proceeding of the KSME Autumn A, 18 (2), 1997, pp 372-377.

[13]   S. Nau, H. Mello. "Acoustic noise in induction motors: causes and solutions." IEEE 2000 Petroleum and Chemical Industry Technical Conference, 2000, pp 253-263.

[14]   B. Weilharter. "Noise Computation of Induction Machines." 2012.

[15]   S. Zuo, F. Lin, X. Wu. "Noise analysis, calculation, and reduction of external rotor permanent-magnet synchronous motor." IEEE Trans. Ind. Electron., vol. 62.10, 2015, pp 6204-6212.

[16]   T.M. Jahns, W.L. Soong. "Pulsating torque minimization techniques for permanent magnet AC motor drives-a review." IEEE Transactions on industrial electronics, vol. 43. 2, 1996, pp 321-330.

[17]   K.S. Kim, C.M. Lee, G.Y. Hwang, et al. "Effects of the number of poles on the acoustic noise from BLDC motors." Springer J. Mech. Sci. Technol., vol. 25. 2, 2011, pp 273-277.

[18]   A. Glowacz. "Thermographic fault diagnosis of ventilation in BLDC motors." Sensors, 21(21), 2021, 7245.

[19]   K.T. Chau, C.C. Chan, C. Liu. "Overview of permanent magnet brushless drives for electric and hybrid electric vehicles." IEEE Transactions on Industrial Electronics, vol. 55, 6, 2008, pp 2246-2257.

[20]   P.C. Desai, A. Emadi. "A novel digital control technique for brushless DC motor drives Current control." IEEE Electronics Machine Drives Conference, 2005, pp 326-331.

BIOGRAPHIES

Buğra ER received the B.Sc. and M.Sc. degrees from Suleyman Demirel University, department of electrical education, Isparta, Turkey in 2020, 2023 respectively. He is currently a R&D engineer of Kormas Electric in Kocaeli, Turkey. His main research interests include electrical motor driver design and CANbus, HVAC control design, PCB design, permanent magnet synchronous motors and Brushless DC motors driver, power electronics for automotive applications.

Berk Demirsoy received his B.Sc. education in the Department of Electrical and Electronics Engineering at Sakarya University in 2021, and he is currently pursuing his M.Sc. in the Department of Electrical and Electronics Engineering at Sakarya Applied Sciences University. Sakarya, Turkey. He is currently a R&D engineer of Kormas Electric in Kocaeli, Turkey. His main research interests include electrical motor design and verification with FEM analyses, permanent magnet

synchronous motors, Brushless DC motors, induction motors, switched reluctance motors and power electronics applications.

Ahmet Fenercioğlu received the B.Sc. and M.Sc. degrees from Marmara University, department of electrical education, İstanbul, Turkey in 1994, 1996 respectively and the Ph.D. degree from Gazi University, Ankara, Turkey, in 2006. He is currently a Professor of Mechatronics Engineering Department at Bursa Technical University in Bursa, Turkey. His main research interests include electrical motor design and verification with FEM analyses, permenant magnet synchronous motors, induction motors, switched reluctance motors, power electronics and eddy current applications.

Publication Ethics

The journal publishes original papers in the extensive field of Electrical-electronics and Computer engineering. To that end, it is essential that all who participate in producing the journal conduct themselves as authors, reviewers, editors, and publishers in accord with the highest level of professional ethics and standards. Plagiarism or self-plagiarism constitutes unethical scientific behavior and is never acceptable.

By submitting a manuscript to this journal, each author explicitly confirms that the manuscript meets the highest ethical standards for authors and coauthors

The undersigned hereby assign(s) to *Balkan Journal of Electrical & Computer Engineering* (BAJECE) copyright ownership in the above Paper, effective if and when the Paper is accepted for publication by BAJECE and to the extent transferable under applicable national law. This assignment gives BAJECE the right to register copyright to the Paper in its name as claimant and to publish the Paper in any print or electronic medium.

Authors, or their employers in the case of works made for hire, retain the following rights:

1. All proprietary rights other than copyright, including patent rights.
2. The right to make and distribute copies of the Paper for internal purposes.
3. The right to use the material for lecture or classroom purposes.
4. The right to prepare derivative publications based on the Paper, including books or book chapters, journal papers, and magazine articles, provided that publication of a derivative work occurs subsequent to the official date of publication by BAJECE.
5. The right to post an author-prepared version or an of ficial version (preferred version) of the published paper on an i nternal or external server controlled exclusively by t he author/employer, pr ovided that (a) such posting is noncommercial in nature and the paper is made available to users without charge; (b) a copyright notice and full citation appear with the paper, and (c) a link to BAJECE's official online version of the abstract is provided using the DOI (Document Object Identifier) link.

CONTENTS